DISSERTATION

CLOUD-RESOLVING MODELING OF AIR-SEA INTERACTIONS OVER THE WESTERN PACIFIC

Submitted by

Alexandre Araújo Costa

Department of Atmospheric Science

In partial fulfillment of the requirements

For the Degree of Doctor of Philosophy

Colorado State University

Fort Collins, Colorado

Summer 2000

UMI Number: 9986267

COLORADO STATE UNIVERSITY

May 19, 2000

WE HEREBY RECOMMEND THAT THE DISSERTATION PREPARED UNDER OUR SUPERVISION BY ALEXANDRE COSTA ENTITLED CLOUD-RESOLVING MODELING OF AIR-SEA INTERACTIONS OVER THE WESTERN PACIFIC BE ACCEPTED AS FULFILLING IN PART REQUIREMENTS FOR THE DEGREE OF DOCTOR OF PHILOSOPHY.

Committee on Graduate Work

Roger A. Pielke

David A. Krueger

William R. Cotton

Adviser

Department Head

ABSTRACT OF DISSERTATION

CLOUD-RESOLVING MODELING OF AIR-SEA INTERACTIONS

OVER THE WESTERN PACIFIC

A cloud-resolving model (CRM) was used to simulate convection over the Western Pacific, during the Tropical Ocean Global Atmosphere Coupled Ocean – Atmosphere Response Experiment (TOGA-COARE). Simulations were performed either using prescribed sea surface temperatures (SSTs) or coupling the atmospheric model to an upper-ocean model (UOM).

An uncoupled control simulation (CONTROL) was performed in which observed, time-evolving, SSTs were used as a lower boundary condition. The CRM was able to properly represent the evolution of the observed cloud systems. The similar statistics within an ensemble of multiple realizations of CONTROL (ENS1 to ENS4) confirmed its robustness.

Sensitivity experiments using the uncoupled CRM were carried out, in which the sea surface temperature was increased (SST+) or decreased (SST-) by one degree Celsius and the same evolving large-scale forcing used in CONTROL. The convective-stratiform partition of the cloud systems was altered; the convective part being favored in SST+ and the stratiform part favored in SST-.

In order to investigate the influence of inhomogeneous surface forcing, sinusoidal SST perturbations of different wavelengths were superimposed onto the observed SST in the uncoupled CRM. The inhomogeneous forcing changed the organization of the cloud systems in space and time.

The CRM-UOM with high vertical resolution in the upper oceanic levels was used to investigate air-sea interactions in 10-day long simulations, representing two different regimes of COARE convection. Simulated atmospheric and oceanic fields were

realistic. The model simulated the formation of precipitation-produced, stable freshwater lenses at the top of the ocean mixed layer, with a variety of horizontal dimensions and lifetimes. The simulated fresh anomalies showed realistic features, such as a positive correlation between salinity and temperature, the development of a surface jet in the direction of the wind and downwelling (upwelling) on its downwind (upwind) edge. The dataset generated by the coupled model was used to investigate the influence of SST changes in the apparent heat source and apparent moisture sink profiles.

Finally, two 70-day coupled simulations were performed, with and without the salinity effect. No evidence was found that, at least in such timescale, the salt-stratification helps the maintenance of high SSTs over the Western Pacific.

Alexandre Araújo Costa
Department of Atmospheric Science
Colorado State University
Fort Collins, CO 80523
Summer 2000

ACKNOWLEDGMENTS

Even if I were a more talented writer, it would be impossible to find the words to express my gratitude to the number of people who contributed to the success of this research project. First of all, I would like to thank my advisor William Cotton for being tremendously supportive in every meaning one can find to this word. Roger Pielke, David Randall, Steve Rutledge and David Krueger are acknowledged for offering part of their precious time to serve on my committee. Along with Bill Cotton, Roger Pielke, Bob Walko and Hongli Jiang provided a substantial help without which the completion of this work would not be possible.

Ligia Bernadet was a key factor for my coming to CSU and she is thanked for all her help before and after the long trip from Brazil. Pier Vidale and Kesia Trench, and their little ones (Irene and Caterina) are thanked for becoming my family in Fort Collins. I think this says it all.

Being a Physicist, having taken courses like Quantum Mechanics and Relativity in the past, I could not find a better environment to assimilate the "atmospheric thinking". The entire Department Faculty is acknowledged, particularly Mike Montgomery, Wayne Schubert, Richard Johnson, Steve Cox, Chin-Ho Moeng, Steve Rutledge, Roger Pielke, David Randall and Bill Cotton for the exciting courses I attended.

Working in Bill's group was a pleasurable experience. Special thanks go to Brenda Thompson, who was able to keep smiling while I bothered her almost every day. Along others, I had great discussions with Sue van der Heever, Brian Gaudet, Chris Golaz, and Travis Ashby, who also provided the necessary distraction from work, which alleviates the spirit.

The Brazilian community living in Fort Collins, including several Brazilians also pursuing their degrees in CSU, are acknowledged for soothing the separation from my home country, its culture, uses and habits.

The distance was no obstacle for the unimaginable support I received from my dear parents, my parents-in-law and my entire family.

At last, but definitely not least, if there is some merit in this dissertation, more than half must be given to my beloved wife, Ana Célia Barbosa. Without her, the journey would be much more extenuating and even worse, solitary. Ana and our precious daughter, Bárbara, teached me as much as the Atmospheric Science faculty during the last three and a half years. We had great times. We had hard times. Above all, we were together.

This research was supported by the *Conselho Nacional de Desenvolvimento Científico e Tecnológico* (CNPq, Brazil) and by the National Oceanic and Atmospheric Administration under grant NA67RJ0152.

TABLE OF CONTENTS

LIST OF FIGURES

LIST OF TABLES

Chapter 1

INTRODUCTION

" Lasciate ogne speranza, voi ch'intrate"
(Dante Alighieri, Italian poet)

"Abandon every hope, who enter here"

In this dissertation, the author addresses the issue of the air-sea coupling in the atmospheric deep convective regime over the tropical oceans. Although the tropical waters do not resemble any kind of hellish landscape, a reason exists for the use of the well-known "invitation" to Dante's *Inferno* to open this Introduction. It is important to clarify such a reason, before the reader "abandons his/her hope" and give up reading the almost 300 pages that are proceeded.

The famous citation from Alighieri's Divine Comedy does not concern an eventual lack of interesting material in this research. Neither it is a reference to the fact that the author has expiated your sins elaborating it.

The study of tropical convection and its coupling to oceanic processes is, certainly, a complicated subject. Nonetheless, the object of this research revealed, along with its complexity, a vivid internal harmony, making the search for results exciting, and the analysis work, captivating. The souls in Dante's *Inferno* were tied to their terrible destiny, for penitence. The author of the present dissertation, impassioned by its subject, also felt, in a certain way, like a voluntary and fortunate prisoner.

Since tropical convection plays a determinant role in the global atmospheric circulation, it is crucial to understand the driving mechanisms for deep convection and the feedbacks associated with it.

Over the tropics, especially over the ocean, air-sea interaction processes are recognized as a key factor driving convection. It is well known that the atmosphere responds to the heat flux at the surface, which is a function of the sea surface temperature (SST). At least on a large scale, rising motion tends to occur over warmer SSTs while sinking motion is expected over colder SSTs. Although such a relation between SST and tropical convection is recognized to exist (e.g., Webster 1994), the actual mechanisms by which the surface forcing impacts the organization of cloud systems have not been sufficiently explored.

Several theories have been proposed to explain how convection and SSTs are related in the tropics. Ramanathan and Collins (1991) proposed that thick cirrus clouds formed in association with deep convection eventually shield the sea surface from the solar radiation and thereby regulate the SSTs ("thermostat" hypothesis). However, satellite data analysis by Fu et al. (1992) showed no evidence of relations between SST variations and cirrus clouds changes. They concluded that the large-scale circulation governs the evolution in the cirrus field. Recent cloud-resolving model simulations by Wu and Moncrieff (1999) support this conclusion. Although contributing important insights on the dependence of the cloud and water vapor feedbacks on SSTs, the results by Wu and Moncrieff (1999) still leave many open questions. For instance, how do variations in the SST field influence the characteristics of convective systems that are relevant for the parameterization of cloud processes in GCMs, such as the mass flux, the convective-stratiform partition and the fractional cloud area?

Numerical studies of stratocumulus to cumulus transition show that enhanced surface fluxes associated with warming SSTs can have a dramatic effect on the dynamics of the marine stratocumulus layer (Krueger et al., 1995; Wyant et al., 1997). In those studies, it has been shown that CRMs and/or large-eddy simulation (LES) models are able to represent cumulus convection and small cloud coverage associated with warm SSTs, and large cloud coverage and stratiform clouds connected to cold SSTs. Of course, both the horizontal and vertical scales involved in the deep convective and the marine stratocumulus regimes are not the same. However, despite such a difference, one could ask, is tropical deep convection influenced in a similar manner by a scenario of SST warming or cooling?

Observations over the tropical Pacific show that the SST field is far from being homogeneous, and that horizontal temperature gradients as large as 1°C may occur in less than 10km (Hagan et al., 1997). Several studies show that inhomogeneous surface forcing can be very important impacting atmospheric circulations and, therefore, driving convection (Pielke et al., 1991; Avissar and Chen, 1993; Lynn et al., 1998). Thus, it is necessary to determine to what extent the average SST and SST inhomogeneities affect the collective properties of convective systems.

Also, there are many open questions related to the coupling of the atmosphere and the ocean on small timescales. This includes the western Pacific warm pool (WPWP) variability on spatial scales of hundreds of kilometers and less, the control of the hydrographic fields by local and remote forcing associated with cloud systems, possible air-sea feedbacks associated with this variability, etc.

This research focuses on cloud-resolving simulations of tropical convection over the WPWP, using data from the Tropical Ocean Global Atmosphere – Coupled Ocean Atmosphere Response Experiment (TOGA-COARE). Three cases are investigated, including a 70-day period that comprised different regimes over the warm pool, from calm winds and suppressed convection to active, organized deep convection associated with a westerly wind burst (WWB). The main tool used in this research was a coupled model, consisting of a two-dimensional cloud-resolving model (CRM) coupled to an upper-ocean model (UOM).

The outline of this dissertation is as follows. Chapter 2 reviews important background information related to this research, including the role of tropical convection, air-sea interactions in the tropics, hydrographic characteristics of the WPWP and cloud-resolving modeling. Chapter 3 presents the experimental data collected during TOGA-COARE, used to initialize, nudge and/or validate the atmospheric and oceanic models. Chapter 4 provides a description of the atmospheric modeling tool, as well as discusses the data ingestion procedure. In Chapter 5, results are presented from simulations performed using a cloud-resolving model and prescribed SSTs, including sensitivity experiments regarding SST increase or decrease and non-uniform SST fields (sinusoidal SST patterns with various wavelengths). Chapter 6 describes the features of the ocean model and shows the coupling process between the two models. In Chapter 7, results of coupled simulations are presented, with distinction to the characterization of the oceanic variability, resulting from the non-uniform atmospheric forcing. In Chapter 8, the results from both uncoupled and coupled simulations are used to show how ocean-atmosphere interaction can influence the heating rates associated with the release of latent heat by convective systems. Chapter 9 analyses the response of the surface latent and sensible heat fluxes to small-scale processes, including correlations between atmospheric and oceanic fields. In Chapter 10, the combined ocean-atmosphere model is used to simulate the evolution of the coupled system during a 70-day period, including phases of active and suppressed convection. In addition, a sensitivity test is performed, in order to assess the influence of the salt-stratification in the upper oceanic layers to the thermal structure of the WPWP. Concluding remarks and suggestions for future research are presented in Chapter 11.

Chapter 2

BACKGROUND

"O mar não é tema: tema é o ar do mar." "The sea is not a theme: the air from the sea is."

(José Alcides Pinto, Brazilian poet)

Poetry is obviously not meant to be exact. In reality, both tropical meteorology and oceanography are recognizably important to understand global processes. It is true, however, that the air-sea interaction in the tropics is a richer subject than its individual components.

This Chapter focuses on background information regarding atmospheric and ocean processes over the tropics, in general, and over the warm pool, in particular. It will become clear how difficult is to treat in isolation the "sea" or the "air", and often the "air from the sea" will be addressed, instead. Chapter 2 comprises four sections. First, tropical convection is discussed, including air-sea interactions. Second, one particular tropical oscillation, namely the Madden-Julian or Intraseasonal Oscillation (MJO, ISO) is reviewed. Following, a discussion is presented on the vertical and horizontal structure of the upper-ocean at the western Pacific. Finally, a review of cloud-resolving models, as tools for investigating tropical convection, is shown.

2.1 – Tropical Convection

Although the ultimate power source for motions at the Earth's atmosphere is obviously the Sun, much of the energy that propels the global atmospheric circulation is realized due to the diabatic heating associated with deep convection in the tropics. In order to compensate the radiative deficit at high latitudes, and to maintain the thermal "equilibrium" of the planet, heat must be transported poleward by the atmosphere and the ocean. At low latitudes, the observed mean winds converge toward the equator at low levels and diverge aloft (according to Palmén and Vuroela 1963, the maximum poleward mass flux in the upper-level leg of the Hadley cell is located near 200 mb). Hence, in the atmosphere, in order to be transferred to higher latitudes, energy is first carried to the upper levels of the tropical troposphere by convective motions.

Latent heat release is the major source of energy for atmospheric motions in the tropical atmosphere. In parallel, the smallness of the Coriolis parameter frees the tropical winds from geostrophic balance (although the Earth's rotation is not unimportant). Atmospheric motions in the tropics are highly diabatic and ageostrophic.

2.1.1. Tropical field experiments

Several field experiments were carried out in the past decades, in order to furnish data to verify and stimulate the development of hypotheses on the physical mechanisms that operate in the tropical atmosphere. Garstang and Fitzjarrald (1999) present a comprehensive list of field experiments over tropical regions, from the 20s to the early 90s. Table 2.1 shows some of the experiments listed by Garstang and Fitzjarrald (1999) plus other field campaigns carried out during mid and late 90s.

Field Experiment	Date	Location
BOMEX (Barbados Oceanographic and Meteorological Experiment)	1969	Barbados
ATEX (Atlantic Tropical Experiment)	1969	Eastern Atlantic
VIMHEX (Venezuela International Meteorological and Hydrological Experiment)	1969 1972	Venezuela
GATE (Global Atmospheric Research Program – Atlantic Tropical Experiment)	1974	Eastern Atlantic
WAMEX (West African Meteorological Experiment)	1975	West Africa
COPT(Convection Profonde Tropicale)	1981	Central Africa
ARME (Anglo/Brazil Amazon Region Micrometeorological Experiment)	1983-1985	Amazon
ABLE I (Atlantic Boundary Layer Experiment)	1984	Western Atlantic
ABLE II (Amazon Boundary Layer Experiment)	1985 1987	Amazon
DECAFE (Dynamique et Chemie de l'Atmosphère en Forêt Equatoriale)	1986	West Africa
EMEX (Equatorial Mesoscale Experiment)	1986-1987	North of Australia
AMEX (Australian Monsoon Experiment)	1986-1987	Northern Australia
ABRACOS (Anglo-Brazilian Amazonian Climate Observation Study)	1990	Amazon
TOGA-COARE (Tropical Ocean-Global Atmosphere - Coupled Ocean-Atmosphere Response Experiment)	1992-1993	Western Pacific
Ceará Experiment	1994	Northeast Brazil
EMAS (Experimento de Mesoescala na Atmosfera do Sertão)	1995	Northeast Brazil
MCTEX (Maritime Continent Thunderstorm Experiment)	1995	North of Australia
SCSMEX (South China Sea Monsoon Experiment)	1998	South of Southeast Asia
LBA (Large Scale Biosphere-Atmosphere Experiment)	1999-2000	Amazon

Table 2.1 – Field experiments over tropical regions.

Field experiments such as BOMEX and ATEX attempted budget calculations. VIMHEX contributed models of the tropical cumulus cloud and subcloud layers over the continent under undisturbed conditions (e.g., Garstang and Betts, 1974). WAMEX shed light over the characteristics of African squall lines.

Since tropical convection plays a determinant role in the global atmospheric circulation, it is crucial to understand the scale interactions between convective activity and large-scale weather systems. That was one of the major objectives of the Global Atmospheric Research Program's (GARP) Atlantic Tropical Experiment (GATE), which was conducted in 1974. In order to investigate the mechanisms by which deep cumulus convection is organized by the larger scales and how the resulting convective activity affects the synoptic motions that can be resolved in large-scale models, GATE comprised five subprograms: synoptic, boundary-layer, convection, radiation, and oceanography. GATE's achievements included, according to Garstang and Fitzjarrald (1999) a better understanding of: 1) the characteristics of the fluxes of heat, water vapor, and momentum across the air-sea interface; 2) the control of convection by low-level convergence; 3) the interaction between the cloud and subcloud layers; etc.

During the 80s, many field experiments in the tropics focused on the characteristics of the boundary-layer, and were directed toward environmental issues. For instance, ARME concentrated on the hydrological budget over the Amazon rain forest. The ABLE experiments were conceived to study the atmospheric chemistry of the lower troposphere over the Atlantic Ocean (ABLE I) and the Amazon region (ABLE II). Similarly, the atmospheric chemistry over the Congo forests was investigated during DECAFE.

In the early 90s, an international scientific effort on a scale that exceeded the implementation of GATE took place. The decade-long Tropical Ocean-Global Atmosphere (TOGA) program was augmented with the completion of the Coupled Ocean-Atmosphere Response Experiment (COARE).

Along other several TOGA-COARE motivations, there were climate issues. Since it was suggested that the rise of warm events in the Pacific Ocean could be triggered by westerly wind anomalies over the western side of the basin (e.g., Barnett, 1977; Gill and Rasmussen, 1983), increasing efforts have been made to understand the mechanisms that rule such anomalies. The occurrence of the strong 1982-1983 El Niño event, following the development of westerly wind anomalies to the west, as described by Philander (1990), contributed to turn the attention of the scientific community to the Western Pacific. It is now recognized that the Western Pacific warm pool (WPWP) is a crucial center-of-action for the El Niño/Southern Oscillation (ENSO) phenomena. COARE's scientific goals went beyond those of GATE and aimed to describe and understand (Webster and Lukas, 1992): 1) the principal processes responsible for the coupling of the ocean and the atmosphere in the western Pacific warm-pool system; 2) the principal atmospheric processes that organize convection in the warm-pool region; 3) the oceanic response to combined buoyancy and wind-stress forcing in the western Pacific warm-pool region; and 4) the multiple-scale interactions that extend the oceanic and atmospheric influence of the western Pacific warm-pool system to other regions and vice versa.

The understanding of the processes over the WPWP was extremely poor just less than a couple of decades ago. Although the existence of a major tropical variability on the timescale of 30-60 days was already recognized (Madden-Jullian oscillation, MJO, first described by Madden and Jullian, 1971), the presence of important air-sea interactions over that region was ignored. In fact, even the knowledge of the hydrographic characteristics of the WPWP was limited at that time. For instance, it was believed that the mixed-layer of the Western Pacific was very deep; a view surpassed by the analysis of data from the Western Equatorial Pacific Ocean Circulation Study (WEPOCS, e.g., Lukas and Lindstrom, 1991). Only the completion of TOGA-COARE provided the opportunity to investigate the warm pool processes in depth.

Indeed, as pointed out by Godfrey et al. (1998), TOGA-COARE answered many questions regarding the dynamics of the coupled system over the WPWP. COARE encompassed a rich panorama, comprising: 1) The evolving structure of the atmosphere (e.g., McBride et al., 1995; Ding and Suni, 1995; Lin and Johnson, 1996a,b; Frank et al., 1996; Johnson and Lin, 1997; Brown and Zhang, 1997) and the ocean (e.g., Bradley et al., 1993; Cechet, 1993; Eldin et al., 1994; You, 1995; Anderson et al., 1996; Cronin and McPhaden, 1997; Soloviev and Lukas, 1997a,b; Ohlmann et al., 1998; Inall et al., 1998); 2) The behavior of the surface fluxes, and their relationships with atmospheric and ocean parameters (e.g., Bradley, 1994; Fairall et al., 1996a,b; Jabouille et al., 1996; Sun et al., 1996; Song et al., 1996; Saxen and Rutledge 1998); 3) The organization of convection and precipitation (e.g. Mapes and Houze, Jr., 1995; Mori, 1995; Chen et al., 1996; Chen and Houze, Jr., 1997; Short et al., 1997; Rickenbach and Rutledge, 1998; Hildebrand, 1998; Roux, 1998; DeMott and Rutledge, 1998a,b; LeMone et al., 1998; Lewis et al., 1998). Also, several aspects of short-term air-sea interactions were explored thanks to the COARE dataset (Wang et al., 1996; Lau and Sui, 1997; Feng et al., 1998; Li et al., 1998).

Recognizably, a key question to improve the understanding of tropical convection is the role of microphysical processes. Recently, other field experiments were carried out in the tropics, addressing this issue, including the microphysical studies carried out during the Ceará Experiment (Costa et al., 2000), along with EMAS, which characterized convection over the semi-arid region of Northeast Brazil, and the MCTEX (Keenan et al., 2000), over northern Australia. The objectives of MCTEX were primarily related to cloud processes, including: 1) Examine the lifecycle of convection from the initiation process through mesoscale organisation of the deep precipitating system; 2) Quantify microphysical processes in convective and stratiform regions with emphasis on the relative importance of coalescence and ice processes; 3) Study cloud electrification mechanisms, especially couplings between ice phase precipitation and the occurrence of strong electric fields; 4) Provide an improved basis for cloud parameterizations in numerical models; 5) Document the radiative properties of convectively-generated cirrus; 6) Quantify the water budget of island thunderstorms; 7) Improve algorithms for rainfall estimation from ground-based and spaceborne sensors; 8) Develop improved short-range forecasting techniques for convective systems; and 9) Investigate the effects of the surrounding ocean on island thunderstorm development and the response of the ocean to convective activity.

As in the 80s, meteorological experiments concerning environmental issues were also performed during the 90s, particularly over the Amazon region, as ABRACOS and LBA. ABRACOS focused on the effects of deforestation in the atmospheric boundary-layer. LBA, a much larger experiment, comprised objectives as 1) To quantify, understand and model the physical, chemical and biological processes controlling the energy, water, carbon, trace gas, and nutrient cycles found within Amazonia and to determine how these link to the global atmosphere; 2) To quantify, understand and model how the energy, water, carbon, trace gas and nutrient cycles respond to deforestation, agricultural practices and other land use changes, and how these responses are influenced by climate; 3) To predict the impacts of these responses both within and beyond Amazonia under future scenarios of changes in land use and climate; 4) To determine the exchanges between Amazonia and the atmosphere of key greenhouse gases and species regulating the oxidizing potential of the atmosphere and to understand the processes regulating these exchanges; and 5) To provide quantitative and qualitative information to support sustainable development and ecosystem protection policies in Amazonia, in the context of both its regional and global functioning.

Those field campaigns contributed substantially to the current knowledge on tropical meteorology. As part of their contribution, data from most of the meteorological experiments over the tropics has been used extensively in cloud-resolving modeling, as will be discussed later in this chapter.

2.1.2. Tropical convection and air-sea interactions

Air-sea interaction processes are recognized as a key factor to drive tropical convection. It is well known that the atmosphere responds to the heat flux at the surface, related to the sea surface temperature (SST) and that rising motion tends to occur over warmer SSTs while sinking motion is expected over colder waters.

Based on observations, Riehl (1954) suggested that deep convection tends to occur within the 28°C SST isotherm. Lots of controversy persists on the relation between the SST magnitude and the intensity of convection, however.

Gadgil et al. (1984) found that cloudiness and SST are well correlated over relatively cold waters, but not for warmer SSTs. Their calculations show an almost linear dependence between the maximum cloudiness and the SST below the 28°C threshold, and virtually no dependence above that value. They suggested that high SSTs are a necessary but not sufficient condition for sustained deep convection, and that above 28°C, SST ceases to be a critical factor determining cloudiness.

In agreement with previous studies (including Riehl's), Graham and Barnett (1987) showed that, over broad regions of the Pacific and Indian oceans, SSTs greater than 27.5°C are required for large-scale deep convection to occur. In their analysis, above that SST value, surface divergence emerged as the primary determinant whether is deep convection present or absent. The large frequency of SSTs around 28°C in those regions led Graham and Barnett (1987) to assume that value as a equilibrium SST value (and 30°C as an upper SST limit) under convective conditions. They suggested that evaporative cooling and blocking of solar radiation could act as regulating factors for the SSTs.

Later, a theory of a cirrus-based "thermostat" for the SSTs would be proposed by Ramanathan and Collins (1991). Since the ocean below cloudy air receives less solar radiation, it tends to cool, while heating occurs in clear regions. Long-lived optically-thick cirrus clouds that reflect significant amounts of solar radiation, generated as a byproduct of deep convection, would be responsible by changes in the ocean radiation budget.

In opposition to Ramanathan and Collins (1991), Fu et al. (1992) found no relation between cirrus and SSTs. They also criticized the "local thinking" behind the cirrus-thermostat theory, arguing that air-sea interaction should be strongly non-local.

Local relationships between SST and deep convection were found in other data analysis, as the one by Waliser and Graham (1993). Over the western Pacific, they found that the intensity (or frequency) of organized convection rises sharply as SSTs increase from 26.5 to 29.0°C, peaks at 29.5°C and declines at higher temperatures (very little organized convection occurs in association with SSTs above about 30°C). They argued that suppressed convection could allow unusually warm SSTs, although large regions with very high SSTs could not be maintained in equilibrium given negative feedbacks of deep convection on SST warming. Of course, the negative correlation between SST and convective activity at higher temperatures (> 29.5°C) cannot be explained by the mechanisms associated with the positive correlation at lower temperatures. Apparently, causality changes by that SST threshold.

As it became clear that no simple framework could explain the intricate relationship between tropical convection and SST, Waliser and Graham (1993) proposed that the regulation of the surface temperature of tropical oceans is made by an "imperfect thermostat". In fact, as SSTs increase, the atmospheric column is destabilized and, in turn, convection results in decreased surface insolation, suggesting that an ëquilibrium state" could be reached. However, according to Waliser and Graham's point of view, internally generated atmospheric variability produces fluctuations in convection regardless of the SSTs. Such variability would disturb the system, preventing the SST-convection equilibrium to be maintained, particularly on a short time scale, shaping an imperfect regulation. In their paper, however, the authors were not able to explain why very warm SSTs occur not only in regions where convection is suppressed (Northwestern Australia, Arabian Sea), but also where organized convection is common (as in the western Pacific), and why there is a more modest reduction in convection at high SSTs over the warm pool than in other regions.

Webster (1994) also discussed the regulation of SSTs by convection and introduced new ingredients. Arguing that the ocean-atmosphere interaction goes beyond radiational and evaporational regulation, he calls for the inclusion of the effect of freshwater flux in the conceptual model of SST regulation. Since deep convection produces a large freshwater flux, Webster postulates that, due to the stabilizing effect of precipitation in the upper ocean, radiant heating is limited to a fresh, shallow layer. As a consequence, radiative controls alone could not restrict SST increases. A more comprehensive discussion of the importance of the salinity budget to the generation and maintenance of high SSTs over the western Pacific will be presented later in Section 2.3.

2.1.3. Scale interactions and convection organization in the tropics

Convection is essentially a multi-scale process. It involves, at one extreme, the large-scale circulations that establish the environment in which convection develops, on spatial scales of thousands of kilometers and timescales of several weeks to months. At the opposite extreme, microphysical processes, which interact closely with radiation, occur on spatial scales of microns and timescales of less than one second. In the middle, turbulence, cloud-scale and mesoscale circulations are found. The complex interaction among large-scale, mesoscale, cloud-scale, and microphysical processes makes it virtually impossible to explicitly model all those processes in the same context. For instance, the highest resolution general circulation models (GCMs) and numerical weather prediction (NWP) models cannot resolve small scale phenomena, as the individual drafts that in fact account for the convective fluxes, and such subgrid-scale processes have to be parameterized.

Large-scale regulation of convection is made, in first instance, by the meridional and zonal circulations associated with the Hadley and Walker cells (Bjerknes 1966, 1969; Schneider and Lindzen 1977), along with the seasonal and interannual variability in those flow fields. In addition, transient features of the large-scale circulations in the tropics are also major modulators of convective activity, including the Madden-Julian Oscillation (MJO, discussed in detail in the next Section), and high-frequency tropical waves (Yanai et al. 1968; Wallace 1971; Maruyama 1971; Rao and Ramana-Murty 1972; Kiladis and Wheeler 1995). The mean, interannual, seasonal (including monsoonal), low- and high-frequency intraseasonal features act on the local convergence/divergence of heat and moisture and on the large-scale transport of moisture into and latent heat out of regions of convective activity.

The large-scale flow strongly determines the evolution of convection but, in turn, convection acts on the large scale, stabilizing the tropical troposphere, exciting waves and, as pointed out by Riehl and Simpson (1979), providing the vertical heat transport required in the equatorial trough to balance the heat budget of the planet.

A prominent feature of convection is its organization on the mesoscale. Mesoscale structures have much larger spatial scales and much longer life cycles than individual clouds. Convection, for instance, is often organized in cloud ensembles containing multiple cells. For instance, tropical convective clouds over the Pacific, Atlantic and Indian oceans are commonly grouped in distinctive cloud clusters, or mesoscale convective systems (MCSs).

Large-scale bands of clouds, such as the ones associated with the Intertropical Convergence Zone (ITCZ) show mesoscale features embedded into them. The importance of appropriate large-scale conditions to the development of organized deep convection was verified by McBride and Gray (1980). They performed a composite examination of MCSs in the tropics, and concluded that the convergence associated with the ITCZ was the major forcing of such systems over the eastern Atlantic and western Pacific. Also, data analysis from GATE by Frank (1978) showed that large-scale convergence precedes the formation of MCSs by several hours.

Along with the large-scale forcing, surface and radiative processes are recognizably important to the development of convection and both are strongly connected to the diurnal cycle. Sui et al. (1997a) classified the diurnal variations in convection over TOGA-COARE into three stages: warm morning cumulus, afternoon convective showers and nocturnal convective systems. As discussed by Hall and Vonder Haar (1999), several mechanisms were proposed to explain the diurnal variation of convection over tropical oceans, but all hypotheses are far from being universally accepted.

Based on a review of works by Leary and Houze (1979), Liou (1986), and Houze (1989), Waliser and Graham (1993) showed that convective systems comprise: 1) Narrow ascent regions ($10^2 km^2$) of deep cumulonimbi, with intense precipitation, producing net heating over the entire tropospheric column; 2) A larger region (10^2 – $10^4 km^2$) of precipitating mid- to high-level stratiform cloud that produces net heating in the upper troposphere and net cooling in the lower troposphere; and 3) A much larger region (10^4 – $10^6 km^2$) of cirrus clouds near the tropopause. A similar perspective is presented by Moncrieff and Klinker (1997). According to them, mesoscale convective systems (MCSs) or cloud clusters have two primary interacting scales: a heavily precipitating convective region, with a characteristic scale of the order of 10km, and a lightly precipitating stratiform region, with a characteristic scale of the order of 100km.

Several researchers discussed the distinct behavior and role of the convective and stratiform components of mesoscale systems. Houze (1993) defined stratiform and convective precipitation in terms of the vertical velocity scales. In stratiform regions, there is often ascending motion in the upper troposphere and downward motion in the lower troposphere, which accounts for the heating profile described previously. In addition, the vertical air motion is small compared to the fall velocity of the hydrometeors. Those characteristics of stratiform regions contrast with the ones of their convective counterparts, in which ascending motion dominates except in the near-surface downdrafts and the air motion is often comparable to the terminal velocity of water particles.

How do observed tropical convection systems divide into convective and stratiform components? Observations of precipitating systems over the Western Pacific described by Yuter and Houze (1998), show that even over a period of active convection, the convective cells never occupy more than a small fraction of the area. Radar observations during TOGA-COARE by Short et al. (1997) suggest that stratiform columns are more frequent (71%) than convective columns (29%). The convective columns, however, are the primary contributors to the total rainfall (74% versus 26% stratiform). Short et al. (1997) also show that the convective-stratiform partitioning is highly case-dependent, with more organized systems showing a greater contribution from the stratiform component.

The structure of the tropical cloud systems is rather complex. As pointed out by Yuter and Houze (1998), the nature of the convective activity over the Western Pacific is variable, including a shallow cumulus, vigorous cumulonimbus clouds, deep cloud clusters, and long-lived convective systems called "super-clusters". The dominant form of the organization of convection depends on the environmental conditions (for instance, the wind shear). A recent publication by Johnson et al. (1999) shows that data from TOGA-COARE provided evidence of a significant population of cumulus congestus, establishing a third mode in the cloud configuration, along shallow cumuli and cumulonimbi. The trimodal distribution of cloudiness is accompanied by trimodal distributions of cloud detrainment and divergence.

2.2 – The Madden-Julian Oscillation

The most important large-scale intraseasonal variability in the tropics (and particularly over the western Pacific warm pool) corresponds to a 30-60 day cycle, first described by Madden and Julian (1971). The spatial structure of the so-called Madden-Julian Oscilation (MJO) comprises a circulation cell in the zonal direction, restrained meridionally to low latitudes, and with maximum amplitude over the equator. A detailed description of the MJO is given by Madden and Julian (1971, 1972, 1994), Krishnamurti et al. (1973), Weickermann et al. (1985), Lau and Chen (1986), Knutsen et al. (1986), Hendon and Salby (1994), Salby and Hendon (1994), Kayano and Kousky (1999) and others.

The perturbations associated with the MJO move eastward, with a speed of propagation that is smaller over the western Pacific and Indian Ocean than over the Atlantic and eastern Pacific. Philander (1990) claims that the average propagation speed of the MJO is of the order of 10 ms^{-1}. However, Lau and Chan (1985) found that the most significant mode of intraseasonal variability of tropical convection has a dipolar structure (zonally oriented), which propagates eastward at a speed of approximately 4-5 ms^{-1}. In agreement with Lau and Chan's study, data analysis by Hendon and Salby (1994) also found that convective anomalies associated with the MJO propagate eastward at about 5ms^{-1} over the Eastern Hemisphere.

The MJO is particularly coupled to atmospheric convection over the western Pacific (according to Philander 1990, the MJO has a strong effect on cloudiness over that region and the Indian Ocean but a much weaker effect on cloudiness over other regions of strong convective activity, such as the Amazon basin). Modulation of convection by the MJO has been found by several researchers. According to Lau and Chan (1985), fluctuations in the monthly averaged outgoing longwave radiation (OLR) over the western and central Pacific are mostly modulated on a timescale of 40-50 days. Empirical orthogonal function (EOF) analysis of OLR data by Lau and Chan (1988) shows dominant variations on the intraseasonal (period of 40-50 days), annual and interannual timescales. Hendon and Salby (1994), Salby and Hendon (1994) and Hendon and Liebmann (1994) showed that convective anomalies associated with the MJO (at wavenumbers 1-3 – predominantly 2 – and oscillation periods of 35-95 days) are confined to the warmest waters of the Indian and western Pacific oceans, evolving through a cycle of amplification and decay. Data from TOGA-COARE revealed that deep convection often occurs over the western Pacific in association with westerly wind bursts (WWBs), with a phase lag of the order of a couple weeks between the peak convective activity and the peak near-surface winds (Lin and Johnson, 1996a)

Several mechanisms have been proposed to explain the occurrence of the MJO, however none of the proposed theories have been completely successful in explaining its characteristics.

Since such intraseasonal variability is markedly periodic, the most obvious first attempt for a MJO theory would be based on wave dynamics. Madden and Julian (1971) first suggested that the oscillation would be equatorial Kelvin-type waves. Cheng (1977) and Lim and Cheng (1983) have shown, however, that observations of the speed of propagation of the MJO were not compatible with predictions based on the theory of the dynamics of Kelvin waves. Murakami et al. (1986) added that the phase relations between the zonal winds and geopotential heights in the MJO were not the same as in a Kelvin-type wave.

A more complex wave-based mechanism was proposed by Lau and Peng (1987) who applied the concept of wave-CISK to the MJO. Several features of the observed oscillation were qualitatively reproduced in their simulations from a wave-CISK based model. However, although Kelvin and Rossby waves were observed in association with convection (e.g., Madden 1986), as in Lau and Peng's simulations, large discrepancies were also found. For instance, the speed of eastward propagation of their disturbances was at least twice as large as the observed value.

Another mechanism was proposed by Neelin et al. (1987) and Emanuel (1987), based on wind-evaporation feedbacks. The theory is based upon the superposition of anomalous easterly (westerly) winds to the east (west) of the region of rising motion to "basic state" easterlies. The combination of those features would produce increased winds to the east and weakened winds to the west. The resulting enhanced evaporation to the east would force the pattern of ascending motion to be displaced eastward.

The theory of the wind-evaporation feedback has strong limitations. For instance, as pointed out by Philander (1990), the theory does not explain the zonal scale of the phenomenon. Observations from TOGA-COARE (e.g., Lin and Johnson, 1996a) revealed that over the western Pacific, the evaporation is actually small before the passage of the convective disturbance associated with the MJO, and large during the convectively active period and under the following westerly wind anomaly (WWB).

There are indications that air-sea coupling might be involved as a driver mechanism for the MJO. Kawamura (1988) showed that the SST in the western Pacific exhibits a significant intraseasonal variability, coupled to the convective activity, and modulated on a timescale of 30-60 days. In particular, SSTs above normal were found to the east of the eastward-propagating convective disturbance. Kawamura (1991) points out that the existence of high SSTs to the east of the convective anomaly provides favorable conditions for the large-scale disturbance to propagate eastward. Such a point of view is shared by Jones et al. (1998) who show that in regions to the east of the convective anomaly associate with the MJO, surface downward shortwave radiation surpasses cooling by evaporation, and positive SST anomalies tend to develop. In contrast, convectively active regions exhibit a large evaporation and a small downward solar radiation flux, developing negative SST anomalies. Jones et al. (1998) suggest the existence of a feedback between convection associated with the MJO and the intraseasonal changes in the SST.

2.3 – Stratification and Variability in the Warm Pool

The upper layers of the western Pacific exhibit a unique vertical and horizontal structure associated with the complex atmospheric forcing, particularly with heavy precipitation. In this Section, several aspects of the warm pool stratification and horizontal variability are discussed.

2.3.1 – Ocean buoyancy

It is well known that the density of the seawater depends on pressure, temperature and salinity. Neglecting the influence of pressure, which is reasonable for shallow processes, the sea water density can be approximated as a function of temperature and salinity only.

$$\rho = \rho(T,S) \tag{2.1}$$

The coefficients of thermal expansion and saline contraction are defined respectively as:

$$\alpha = -\rho^{-1}\left(\frac{\partial\rho}{\partial T}\right) \tag{2.2}$$

$$\beta = -\rho^{-1}\left(\frac{\partial\rho}{\partial S}\right). \tag{2.3}$$

Linear approximations useful at temperatures above 5°C and atmospheric pressure are shown in Equations (2.4) and (2.5), from Kraus and Businger (1994). While β varies only slightly with temperature, α changes with a factor about 4 in the range of temperature found in the world ocean.

$$\alpha \cong (77.5 + 8.70T)\cdot 10^{-6}\ {}^{\circ}\mathrm{C}^{-1} \tag{2.4}$$

$$\mathrm{b} \equiv (779.1 - 1.66T)\cdot 10^{-6}\ {}^{\circ}\mathrm{C}^{-1}, \tag{2.5}$$

where the temperature is given in °C.

Based on the definition of these coefficients, Gill (1982) suggests that the buoyancy of an ocean parcel can be given by:

$$B = \alpha T - \beta S. \tag{2.6}$$

What are the interface processes that influence the buoyancy in the ocean mixed-layer? Any process adding heat to the ocean from above tends to increase the buoyancy of the parcels at the surface, contributing to enhance the ocean stability. On the other hand, the removal of heat at the surface tends to destabilize the ocean. We also may consider the influence of mechanically forced mixing due to the wind that contributes to reduce temperature and salinity gradients, and, therefore, reduces the ocean stability. Webster (1994) summarized the main processes that can alter the ocean stability and we reproduce his result in Table 2.2.

Process	Effect on Ocean Buoyancy/Stability
Solar Radiation	Increases buoyancy/ increases stability
Incoming LW	Increases buoyancy/ increases stability
Outgoing LW	Decreases buoyancy/ decreases stability
Latent Heat Flux	Decreases buoyancy/ decreases stability
Sensible Heat Flux	Decreases buoyancy/ decreases stability
Precipitation	Increases buoyancy/ increases stability
Wind	Decreases stability by mechanically forced mixing

Table 2.2 – Influence of surface processes in the upper-ocean stability. Adapted from Webster (1994).

Radiative fluxes are very important to ocean mixed-layer processes and, in fact, radiant heating is the largest term in the heat budget of the WPWP - Western Pacific warm pool - (Ohlmann et al., 1998). Longwave radiation processes in the ocean can be treated as surface processes, but the same cannot be done to shortwave radiation. Solar radiation actually penetrates the atmosphere-ocean interface and directly heats the water beneath the ocean surface through flux convergence caused by absorption.

Unlike other types of surface, the ocean albedo is highly variable. The reflectivity depends on the incident angle, thus the ocean albedo depends on the sun elevation, the cloud coverage and the roughness of the sea surface, which varies with the wind speed

(Kraus and Businger, 1994). The solar radiation absorption is also highly variable, showing a strong spectral dependence. Clear water is mostly transparent in the blue-green region of SW spectrum, with attenuation increasing as the wavelength increases and approaches the near-infrared spectral region. However, according to several authors (Jerlov, 1976; Smith and Baker, 1981; Kirk, 1994), the subsurface light field changes if the absorption and / or scattering properties of the aqueous media are modified by the presence of particles in suspension (biomass and detrital materials).

It has been recognized that mixed layer chlorophyll concentration significantly influences attenuation of the in-water light field at the WPWP and that important feedbacks in the upper-ocean can be regulated by biological activity (Ohlmann et al., 1998). Based on observations regarding the variability of mixed-layer phytoplankton pigment concentrations, that alter the solar radiation absorption at the WPWP, Siegel et al. (1995) suggest that there is an important biogeochemically regulated feedback that may play some role in enhancing the rate at which the WPWP returns to its normal state following a westerly wind burst event.

Over tropical oceans, precipitation contributes opposite effects to the upper-ocean stability: freshening, which promotes stabilization; and cooling (because rainwater is often cooler than the tropical SSTs), which tends to destabilize the near-surface layers. The salinity effect, however, is about one order of magnitude greater than the thermal effect, and, therefore, the first dominates.

The way which the winds influence the upper-ocean stratification is rather complex. Chu (1993) identified two different regimes of correlation between the time rate of change of the SST and the ocean mixed-layer depth, depending on the wind forcing.

Under weak wind forcing, the mixed-layer turbulent kinetic energy (TKE) is not sufficient to allow entrainment of cool water from below, and warming tends to occur due to solar heating, such that the thinner the mixed-layer the more efficient is the warming. On the other hand, under the influence of strong winds, the export of heat at the bottom of the mixed-layer associated with cool water entrainment eventually overcomes the heating above, and the mixed layer tends to cool, such that the thicker the mixed-layer less efficient the cooling. The formation of the so-called "barrier layer" and the role of the westerly wind bursts on the stratification of the mixed-layer at the WPWP will be discussed later in this Chapter.

Many authors assume that the buoyancy changes due to the salinity flux are unimportant. However, Webster (1994) shows there are several regions where the salinity budget is as important as the heat fluxes to modify the ocean stability. Let the ratio between the temperature and the salinity terms in the buoyancy flux:

$$R = \left| \frac{\alpha Q_T}{\beta S(P-E)} \right| \tag{2.7}$$

where Q_T takes into account the latent heat flux, the sensible heat flux due to turbulent transport and precipitation, and the radiative fluxes. As it can be seen in Figure 2.1, in several regions of the world ocean, this ratio is small, and the two buoyancy fluxes are comparable. This is what happens at the WPWP and other tropical regions, due to heavy rainfall, and at polar regions, due to melting of sea ice.

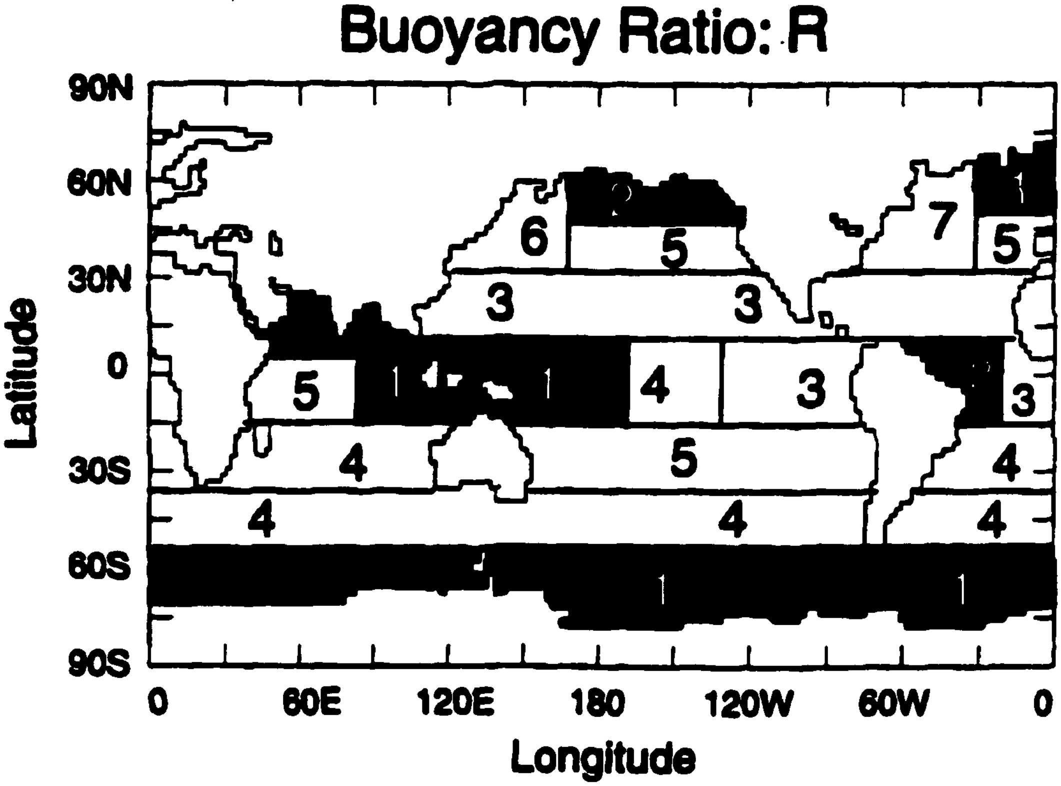

Figure 2.1 – Ratio of the impact on upper ocean buoyancy of heating and salinity effects (R). Regions where R is order unity are shaded. In some tropical regions (western Pacific, western Atlantic and northeastern Indian oceans), the freshwater flux is so great that the heating and salinity effects are at or near parity. From Webster (1994)

2.3.2 – Vertical structure of the warm pool: barrier-layer, warm layer and cool skin

As discussed earlier, the SST at the WPWP seems to be regulated by two opposite mechanisms; both associated with atmospheric deep convection. Cloud coverage blocks part of the incoming solar radiation, and strong winds that occur during certain events tend to enhance latent and sensible heat fluxes, as well as to increase mixing. These two effects would work to maintain a relatively cool SST. In opposition, the large freshwater flux due to precipitation can support a relatively shallow mixed-layer that tends to achieve a high temperature. A detailed description of the shallow WPWP mixed-layer (only 30m deep on average) was made by Lindstrom et al. (1987) and Lukas and Lindstrom (1991).

Since the buoyancy flux associated with precipitation is large in the WPWP, the isothermal layer is often deeper than the mixed-layer and this is a key factor to maintain the warm SSTs. The existence of a salt-stratified layer between the mixed-layer and the bottom of the isothermal layer prevents the entrainment of cool water from below in the mixed-layer. Such a salt-stratified layer acts as a "barrier" for heat fluxes because the stability associated with that region resists mixing, as pointed out by Anderson et al. (1996). Godfrey and Lindstrom (1989) called that region the "barrier-layer". You (1998) defines the barrier-layer as the vertical distance difference between a halocline and a thermocline, in which there is very little temperature change but a large salinity change.

Approximately no heat fluxes occur when any water from the near-isothermal layer penetrates the mixed-layer above or vice-versa (Sprintall and Tomczack, 1992). Due to the presence of the barrier-layer, cooling by entrainment is allowed only during very strong wind events. Therefore, entrainment might not be considered a continuous process as suggested by Niiler and Stevenson (1982), but instead intermittent.

Fig. 2.2 is a schematic diagram depicting the barrier layer theory by Lukas and Lindstrom (1991). During a wind burst, the momentum flux at the surface increases the ocean TKE, such that turbulence erodes the salt-stratification and the mixed layer extends down to the top of the thermocline. Eventually, precipitation and surface heating form a shallow, fresh and warm mixed-layer decoupled from deeper waters due to the presence of the barrier-layer. Delcroix et al. (1992) points out that the dynamics of such a system is controlled by a combination of several factors (winds, precipitation and currents). Along with radiation, those factors are all important to determine the depth of the mixed-layer and the thickness of the underlying barrier-layer.

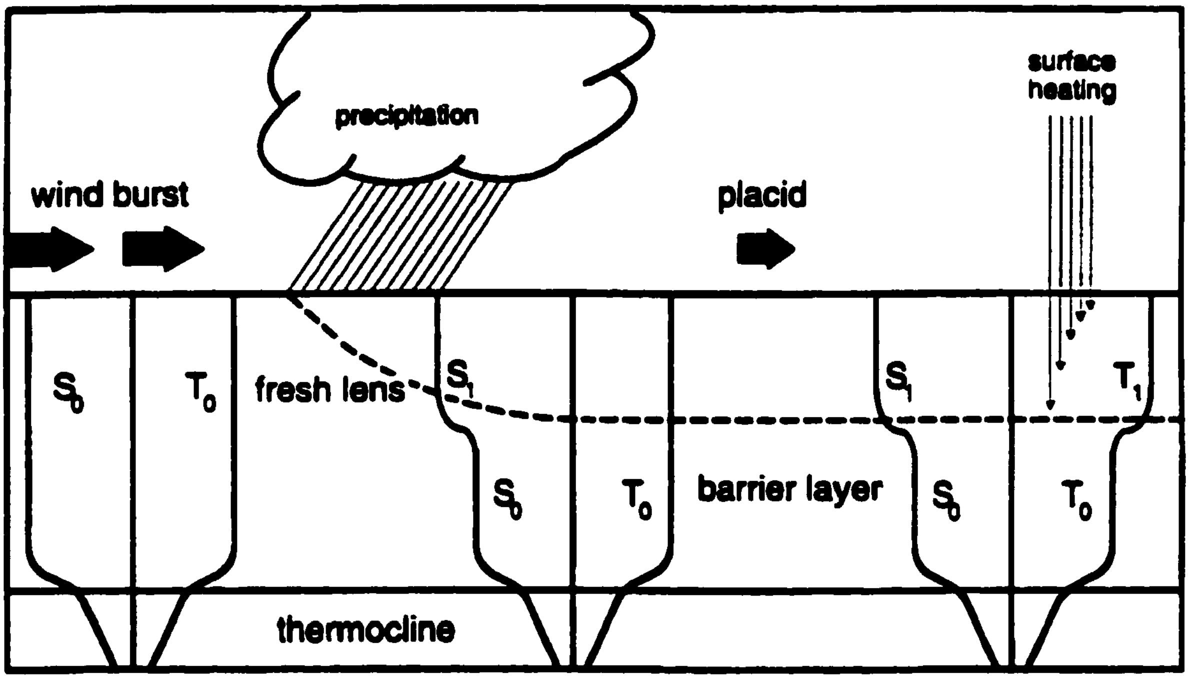

Fig. 2.2 – Conceptual model of the barrier-layer theory. From Anderson et al. (1996)

Even though the barrier-layer theory provides a satisfactory explanation for many characteristics of the ocean mixed-layer at the WPWP, as its shallowness, for example, some details of the barrier-layer formation process are still unclear. You (1998) described an observed barrier-layer during TOGA-COARE and showed that, although its formation is determined by heavy precipitation, there are different mechanisms through which the barrier-layer actually develops.

Suppressed fluxes lead to very interesting consequences at the ocean surface layer. Since vertical mixing between the ocean surface and deeper layers is diminished, it allows the shallow, cool fresh water to persist at the surface. In addition, any heat input at the surface would continuously raise the temperature of the upper ocean if it were not advected away from that region, because the net flux at the bottom of the mixed-layer is always close to zero and the heat gained becomes trapped above. It may eventually lead to an increase of the temperature at the ocean surface. During daytime, if the winds are light, the turbulent mixing may be suppressed by the heating near the surface associated with the incoming solar radiation. Hence, the upper layer becomes decoupled from the mixed-layer below, and its temperature may rise rapidly (Kraus and Businger, 1994). Only strong winds can overcome this stabilizing influence.

A slight temperature increase in already warm regions may alter significantly the saturation mixing ratio at the surface and, therefore, change the latent heat flux substantially. For instance, at the WPWP, where the SSTs are high (28-30°C), increasing the temperature only one degree results in a saturation mixing ratio increase on the order of 1.5 g/kg, possibly accounting for an enhancement of the latent heat flux on the order of tens of Wm^{-2}. Also, due to the fact that the Stefan-Boltzmann law comprises a fourth power of the absolute temperature, a one degree variation of the skin-SST enhances the upward radiative flux by about 6 Wm^{-2}. Clayson et al. (1995) actually found a net increase in the upward heat flux of 27 Wm^{-2}, suggesting even higher variations of the skin-SST.

In fact, the so-called warm-layer effect can be very substantial. Model estimates by Fairall et al. (1996a) using COARE data suggest that for a clear day with a $1ms^{-1}$ wind speed at the 10m atmospheric level, the peak afternoon warming is of the order of 3.8K and the warm-layer depth is of the order of 70cm. If the wind speed increases to $7ms^{-1}$, the warm-layer deeps to 19m and the temperature variation decreases to only 0.2K, and there is virtually no warm-layer effect in that case. According to Soloviev and Lukas (1997), during TOGA-COARE, skin-SSTs as high as 33.25°C were observed. Fairall et al. (1996) points out that, on average, the warm-layer effect accounts for a change of about $4Wm^{-2}$ in the heat flux at the ocean surface, but that it can be as high as $50Wm^{-2}$ at noon. Webster et al. (1996) point out that the diurnal variation of the skin-SST is in fact comparable to the difference between the temperature of the WPWP during El Niño and La Niña. Therefore, one must expect that such influences are in fact substantial enough to drive and/or modify atmospheric circulations on short timescales.

In addition to the warm-layer effect, in order to achieve an accurate calculation of the SSTs, one has to include the so-called cool-skin effect. Saunders (1967) describes the basic physics of the cool skin, which is associated with molecular diffusion of heat at the millimeter scale at the ocean surface that makes the skin-SST a few tenths of a degree cooler than the bulk temperature of the ocean. Fairall et al. (1996a) examined the cool-skin effect in detail at the WPWP and their model estimates, based on observations at the WPWP during COARE, resulted in an average cool-skin effect of 0.3K at night and 0.18K at noon. Webster et al. (1996) discussed the importance of an accurate representation of the skin-SST to determine upward sensible heat, latent heat, and longwave radiation fluxes.

2.3.3 – Horizontal variability at the WPWP

Because the WPWP fresh layer produced by precipitation events is so shallow, its heat capacity is much smaller than that of the top mixed-layer in most of the ocean water masses. Therefore, it responds quickly to changes in downward shortwave radiative flux, cloud cover and precipitation.

Observations show that the horizontal structure of the WPWP is highly variable. Soloviev and Lukas (1997) analyzed ship measurements and found sharp frontal interfaces of width 1-100m and separation 0.2-60km, several of them associated with precipitation-produced freshwater lenses. Due to the influence of the wind, most of the interfaces were anisotropic. Similar findings were obtained by Hagan et al. (1997) from aircraft measurements. They observed horizontal temperature gradients of the order of one degree in less than 10km, related to clouds and precipitation (cloud shadows and freshwater anomalies).

Indications are that the highly variable horizontal thermohaline structure of the WPWP has a two-way coupling with the atmospheric variability. Significant horizontal gradients in skin-SST can be induced or dissipate on relatively short time scales by horizontal variations in the atmospheric fields, but in turn may generate cloud scale and mesoscale circulations, which trigger and influence cloud systems and precipitation. Those interactions are going to be investigated in the following chapters.

2.4 – Cloud-Resolving Models

Lato sensu, cloud-resolving models (CRMs) are atmospheric numerical models that can resolve circulations at the cloud scale. A more restrictive definition of a CRM is given by Randall et al. (1996): "a model with sufficient resolution to resolve (at least crudely) the structures of individual clouds (e.g., cumulus clouds), run over a spatial domain large enough to contain many clouds and for a time long enough to include many cloud life cycles". While the terminology "CRM" focuses on the model resolution, an alternate expression ("cloud ensemble model", CEM) emphasizes the relatively large domain and long integration period, which permit realizations of "ensembles" of clouds in space and time.

Early CRMs were used to investigate interactions between cumulus clouds and circulations on the mesoscale (Yamasaki 1975), the response of cumulus ensembles to an imposed forcing (Soong and Ogura 1980; Soong and Tao 1980; Tao and Soong 1986; Tao et al., 1987), cloud-cloud interactions (Tao and Simpson 1984) and subcloud layer processes (Krueger 1988). However, in those simulations, domain sizes were often limited (tens of kilometers), as well as the simulated periods (of the order of hours), due to computer limitations.

Today, two-dimensional and even three-dimensional multi-day cloud-resolving simulations can be performed using model domains of hundreds of kilometers, which provides a wide range of applications. Cloud-radiation interactions were investigated by Liu and Moncrieff (1998), Li et al., (1999) and Wu et al. (1999). Quasi-equilibrium states of tropical convection were simulated by Sui et al. (1994), Grabowski et al. (1996a), Xu and Randall (1999) and Tao et al. (1999). Cloud-, meso-, and large-scale circulations were simultaneously resolved (in two-dimensions) by a CRM with a very large number of horizontal grid points by Grabowski (1998).

As pointed out by Randall et al. (1996), one major application for CRMs is the development of physically based parameterizations for general circulation models (GCMs), in conjunction with single-column models (SCMs). A detailed description of an approach to physically based parameterizations combining observations, CRMs and SCMs is shown in Figure 2.3, adapted from Moncrieff et al. (1997).

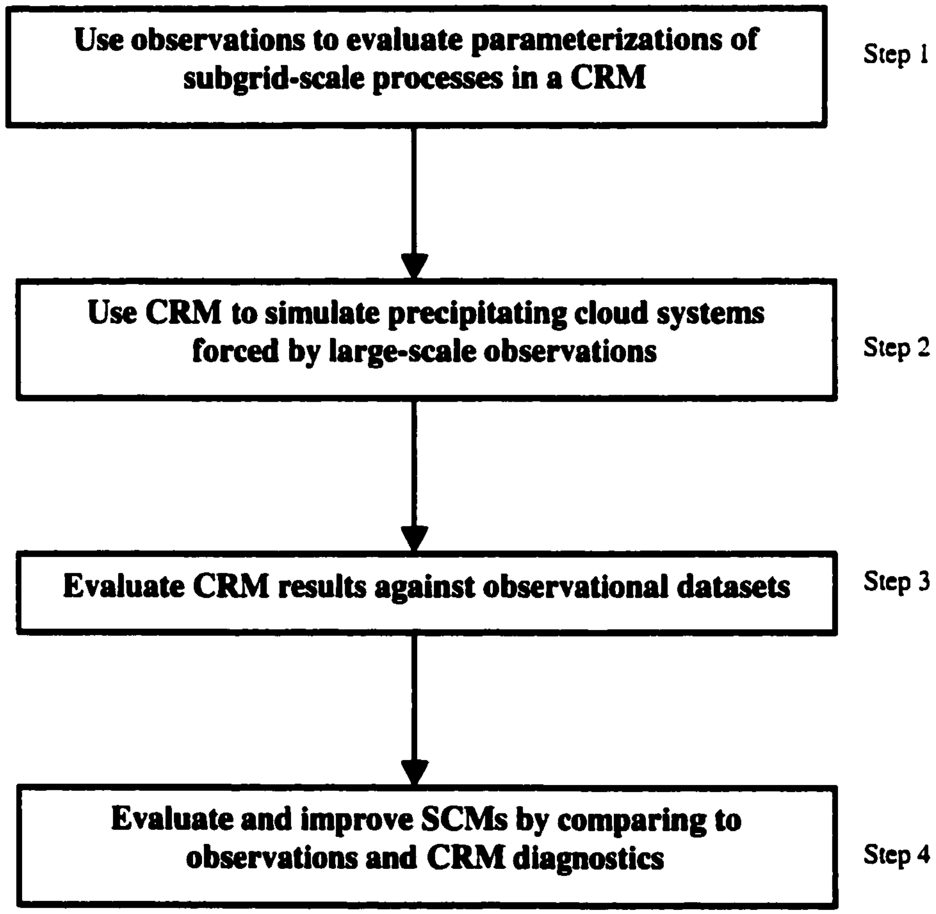

Figure 2.3 - Four-step approach to physically based parameterizations, which combines observations, cloud-resolving models, and single-column models. Adapted from Moncrieff et al. (1997).

Observations from field experiments over tropical regions, such as GATE and TOGA-COARE provide the data required to simulate cloud systems using a CRM. Several studies based on cloud-resolving simulations of tropical convection using data from those experiments have been published lately. Wang et al. (1996) used the Goddard Cumulus Ensemble (GCE) Model and the TOGA-COARE bulk flux algorithm (Fairall et al., 1996a) to simulate the development of a squall line during COARE. The same case was studied by Trier et al. (1996). Grabowski et al (1996b) simulated different convective regimes during GATE using an anelastic cloud model (Clark, 1977; 1979). A similar study was perfomed by Xu and Randall (1996). Wu et al. (1998, 1999) performed long-term (39 days) simulations of cloud systems formed during TOGA COARE between 5 December 1992 and 12 January 1993. Recently, standardized cloud-resolving model experiments using the COARE dataset were organized by the GEWEX cloud systems study (GCSS) Working Group #4. Krueger et al. (1997) and Krueger and Lazarus (1999) compared the results produced by several 2-D and one 3-D CRM in a multi-day simulation of TOGA-COARE convection, and showed that the different models produced similar statistics. Simulations for the same case were performed by Su et al. (1999) and Li et al. (1999).

Examples of how CRMs can be used to help the development of parameterizations of convection in global models can be found in Xu (1995) and Alexandre and Cotton (1998). In both papers, convective-stratiform partition of cloud systems was assessed explicitly.

Although CRMs have been successfully validated against observations, every model has its own uncertainties, related to the numerical schemes and parameterizations, as radiation, turbulence and microhysics. Grabowski et al. (1999) showed that, at least in their simulations, microphysics alone affects the results modestly, but the combined influence of radiation and microphysics can alter the convective response significantly. Using two different ice parameterizations in long-term TOGA-COARE cloud-resolving simulations, Wu et al. (1999) found important changes in the cloud fractional area and albedo that modified the radiative budget.

Other uncertainties in cloud-resolving simulations are related to the model dimensionality, domain size, spatial resolution, etc. Sensitivity experiments have been carried out by several researchers, in an attempt to address those issues. The sensitivity of cloud-resolving simulations to spatial resolution was analyzed by Grabowski et al. (1998), who found a strong influence of the grid spacing at the upper-level cloud coverage. Concerning the model dimensionality, an early publication by Tao et al. (1987) showed that the mean dynamic, thermodynamic and cloud fields were very similar in their 2-D and 3-D simulations. Later, Grabowski et al. (1998) and Donner et al. (1999) compared results from 2-D and 3-D GATE simulations, and found similar conclusions. Also, the model intercomparison performed by the GCSS Working Group #4 showed that the several 2-D CRMs and the only 3-D CRM exhibited similar behavior (Krueger and Lazarus, 1999). Two-dimensional cloud-resolving simulations of convection have shortcomings. For instance, the three-dimensional structure of cloud systems cannot be represented and downdrafts tend to be exaggerated because of the lack of a degree of freedom. Also, 2-D simulations exhibit a larger variability in most of the fields associated with the cloud ensemble, as well as a different behavior of the CAPE and CIN. However, despite its limitations, 2-D CRMs still have a major advantage over their 3-D counterparts: since they are computationally less expensive, larger domains and longer simulation periods can be used. For several applications, 2-D CRMs are still the optimum tool to investigate collective properties of convection.

Other important issue about cloud-resolving simulations over tropical oceans is what degree of sophistication is necessary in the representation of the upper-ocean. For example, although simulating real cases, Grabowski et al. (1996a), Wang et al. (1996) and Sui et al. (1999) used constant SSTs in space and time. That assumption is not realistic, especially for multi-day or multi-week simulations, since observations show significant changes in the SSTs associated with the diurnal cycle, evaporation and precipitation. Even the use of time-evolving, spatially uniform temperatures is not completely realistic, because observations by aircrafts (e.g., Hagan et al., 1997) and vessels (e.g., Wijesekera et al., 1999) have shown a significant horizontal variablity in the SSTs. Therefore, we agree with Moncrieff et al. (1997) when they suggest that two-way coupling of CRMs to upper-ocean models is needed. Since perturbations in the ocean are often long-lived, they can persistently drive the atmospheric convective processes; therefore one should expect that the collective convective fluxes could be influenced by the evolution of the upper-ocean inhomogeneities.

Chapter 3

OBSERVATIONS

Tudo o que existe é de uma grande exatidão.
Pena é que a maior parte do que existe
com essa exatidão
nos é tecnicamente invisível.

Everything that exists has great accuracy.
Shame that most of what exists
With such accuracy
Is technically invisible to us.

(Clarice Lispector, Brazilian Poetess)

In this chapter observations from TOGA-COARE are presented. The first section contains an overview of COARE, focusing primarily on the flow characteristics over COARE intensive flux array (IFA) during the intensive observing period (IOP). Following that, observations of three cases are shown. The first two correspond to periods of ten days, during which convective was active (Cases 1 and 2). The third "case" is actually a 70-day period containing two convectively active phases of the intraseasonal oscillation, and includes the ten days corresponding to Case 2.

3.1 – COARE IOP

During TOGA-COARE, an intensive observing period (IOP) took place from November 1992 through February 1993, in which enhanced meteorological and oceanographic monitoring was carried out. In order to achieve its goals the COARE-IOP comprised an elaborate assemblage of observations from a variety of platforms in the ocean and the atmosphere (Webster and Lukas 1992). Figure 3.1 depicts the COARE sounding network, comprising a large-scale array (LSA), an outer sounding array (OSA) and the intensive flux array (IFA). The set of nested arrays was designed to provide a bridge from the large scales down to the IFA scale (Lukas et al., 1995). A significant part of the effort carried out during the COARE IOP was concentrated in the IFA area, including sounding sites, radar sites, research vessels, etc.

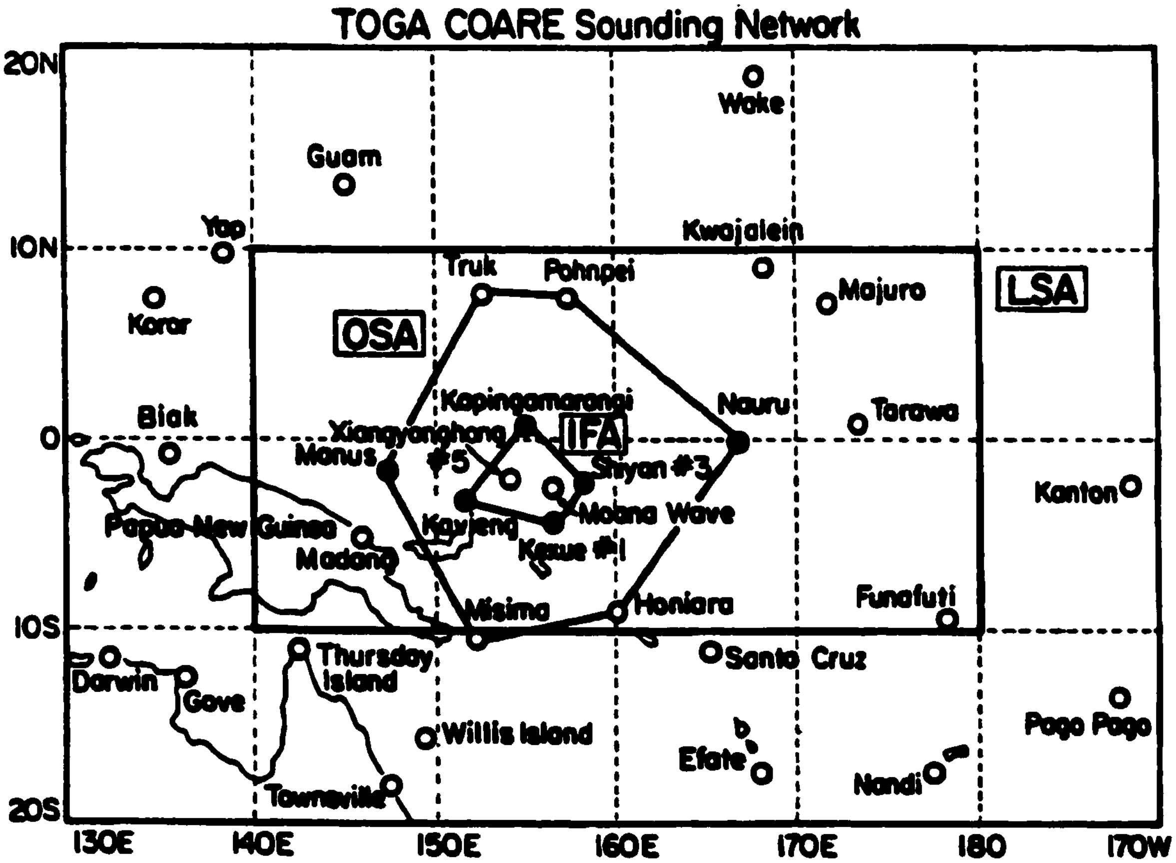

Figure 3.1 – The TOGA COARE sounding network (from Lin and Johnson, 1996a)

According to Ding and Sumi (1995), atmospheric conditions during the TOGA-COARE IOP were similar to those of a developing warm episode over the eastern Pacific, including the frequent occurrence of westerlies in the lower troposphere, accompanied by upper-tropospheric easterlies. Lukas et al. (1995), however, pointed out that the TOGA-COARE IOP took place after an unusual evolution of the 1991/1992 warm event. In the last half of 1992, warm anomalies in the cold tongue to the east turned to cold, although very warm SSTs (warmer than 30°C) remained displaced eastward, increasing the Southern Oscillation Index (SOI). However, although the SOI relaxed to zero preceding the COARE IOP, it decreased during the experiment.

The COARE IOP was characterized by the occurrence of westerly wind bursts (WWBs) and the sea level pressure changes were associated with the strong westerly wind activity and corresponded to the re-intensification of the warm episode (Lukas et al., 1995). In fact, three prominent WWBs occurred over the COARE IFA during the IOP. Analyses of the flow over the IFA by Lin and Johnson (1996a) contributed important findings for the understanding of the ISO structure over the WPWP.

The conceptual model of a westerly wind burst proposed by Lin and Johnson is depicted in Figure 3.2. Approximately 5 weeks before the maximum westerlies, weak winds dominated, SSTs were maximum, surface fluxes were small, and convection was suppressed. Upward motion preceded the peak low-tropospheric westerlies by 1 to 3 weeks. During that period, the vertical wind shear increased, the zonal wind component at low levels became increasingly westerly and the average surface wind speed increased. The SSTs decreased due to the combined effect of enhanced evaporation, blocking of solar radiation by the cloud systems and ocean mixing. At the time of the maximum WWB, subsidence prevailed and the SSTs continued to drop. About 1-2 weeks later, surface wind speeds relaxed and the SST progressively increased.

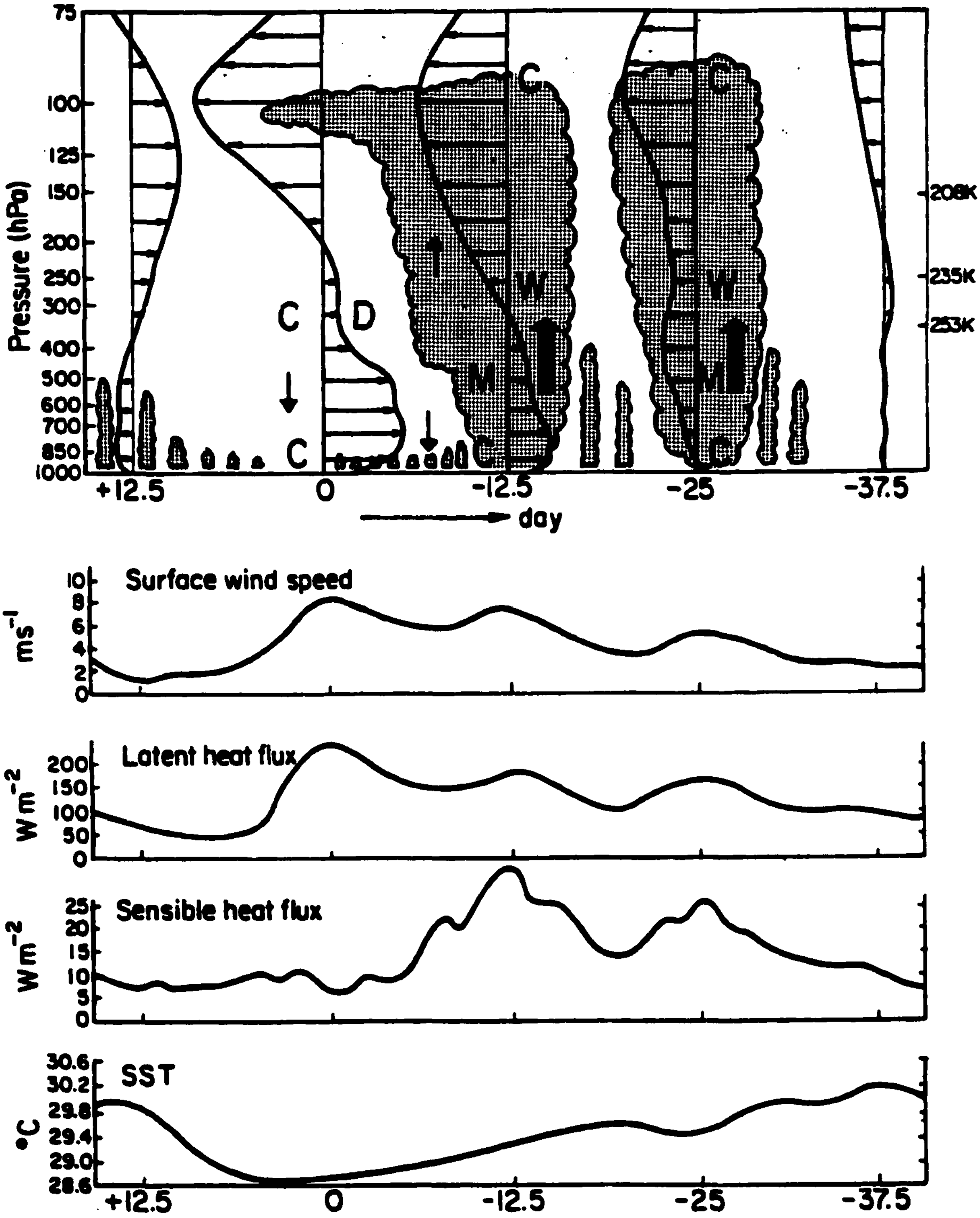

Figure 3.2 – Conceptual model of the kinematic, thermodynamic and surface properties of the December to January WWB over the COARE IFA. Letters correspond to warm (W), cool (C), moist (M), and dry (D) anomalies. Heavy (light) arrows indicate strong (weak) vertical motion. Maximum low-level westerlies are indicated by day 0, and early dates by negative days. From Lin and Johnson (1996a).

The enhanced network of rawinsonde stations over the COARE area allowed the calculations of heat and moisture budgets. Computations of rainfall, surface heat, and moisture fluxes by Frank et al. (1996) showed that convection preceded or coincided with increased surface fluxes in the more active regions. Lin and Johnson (1996b) examined the behavior of the atmosphere and ocean surface before, during and after the passages of WWBs in greater detail. They showed that low frequency oscillations associated with the intraseasonal oscillations strongly modulated convective heating and moistening, as well as vertical wind shear. The picture that emerged from Lin and Johnson's analysis is very different from the theory proposed by Neelin et al. (1987) and Emanuel (1987) to explain the occurrence of the MJO. In agreement with the strong ascending motion found by Lin and Johnson (1996a), heavy precipitation was found preceding the peak WWB by 1 to 3 weeks. Maximum SSTs were achieved during undisturbed periods. SSTs decreased as convection became active, with minimum values achieved during the periods of maximum westerly winds, when convection was mostly suppressed. Evaporation showed a high correlation with the wind speed and often peaked during strong WWBs. Therefore, enhanced evaporation was found to follow deep convection in time, instead of preceding it and setting up conditions for convective activity. Sensible heat fluxes reached their maximum during the convectively-active periods.

It is clear, from the data presented in this section, that deep convection often occurs in association with WWBs, with a phase lag of the order of a couple weeks between the peak convective activity and the peak near-surface winds (Lin and Johnson, 1996a). However, as can be shown from those TOGA-COARE observations, deep convection over the WPWP can also develop under conditions other than moderate westerlies associated with WWBs.

Figure 3.3 is a scatter plot showing the occurrence of values of the zonal wind, for events in which the minimum omega (vertical velocity in pressure coordinates) was less than -10 mb·day^{-1}. Each diamond corresponds to one observation (observations were taken each 6 hours). Although three of the five events occurred under moderate westerlies (11 November, 22 December and 24 December 1992), related to developing WWBs, deep convection was also observed under moderate easterlies (19 January 1993) and under weak easterlies in transition to westerlies, about three weeks before the peak WWB (11 December 1992).

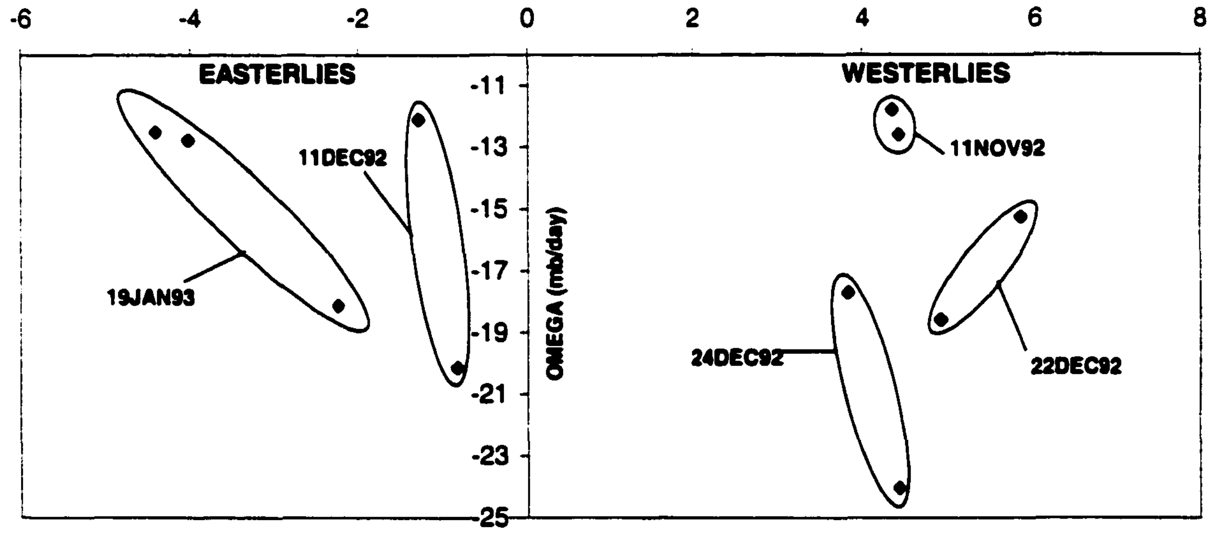

Figure 3.3 - Scatter plot of the vertical velocity in pressure coordinates against the near surface zonal wind, showing cases with large-scale ascending motion stronger than -10mb/day. Favorable conditions for deep convection during the COARE IOP are shown to have occurred not only under moderate westerlies (as the ones preceding the maximum in a westerly wind burst), but also under easterlies and under weak westerlies.

Different convective regimes can possibly be associated with different oceanic responses to the atmospheric forcing. For instance, one must expect distinct ocean mixed-layer responses in the presence of well-organized convective systems formed under moderate low-level westerlies and strong vertical wind shear and less-organized convection formed under weak low-level winds in a somewhat weakly-sheared environment.

3.2 – Case 1 – Convection under weak winds

Case 1 corresponds to the occurrence of deep convection under weak large-scale winds between 07 December and 17 December. Figure 3.4 depicts the time evolution of the COARE IFA average zonal wind (3.4a), vertical velocity in pressure coordinates (3.4b) and the advective tendencies of potential temperature (3.4c) and moisture (multiplied by L/c_p, 3.4d) for the period between 00UTC 07 December 1992 and 00UTC 17 December 1992. That period was characterized by weak low-level westerlies, with an increasing eastward trend starting on 12 December (Figure 3.4a). The large-scale surface winds are below 2.5 ms^{-1} until that date. The 10-day period is characterized by ascending motion, as indicated in Figure 3.4b, with very significant large-scale ascent on 11 December, as also shown in Figure 3.3. Accompanying the rising motion, significant large-scale cooling (Figure 3.4c) and moistening (Figure 3.4d) are present, particularly on 11 December.

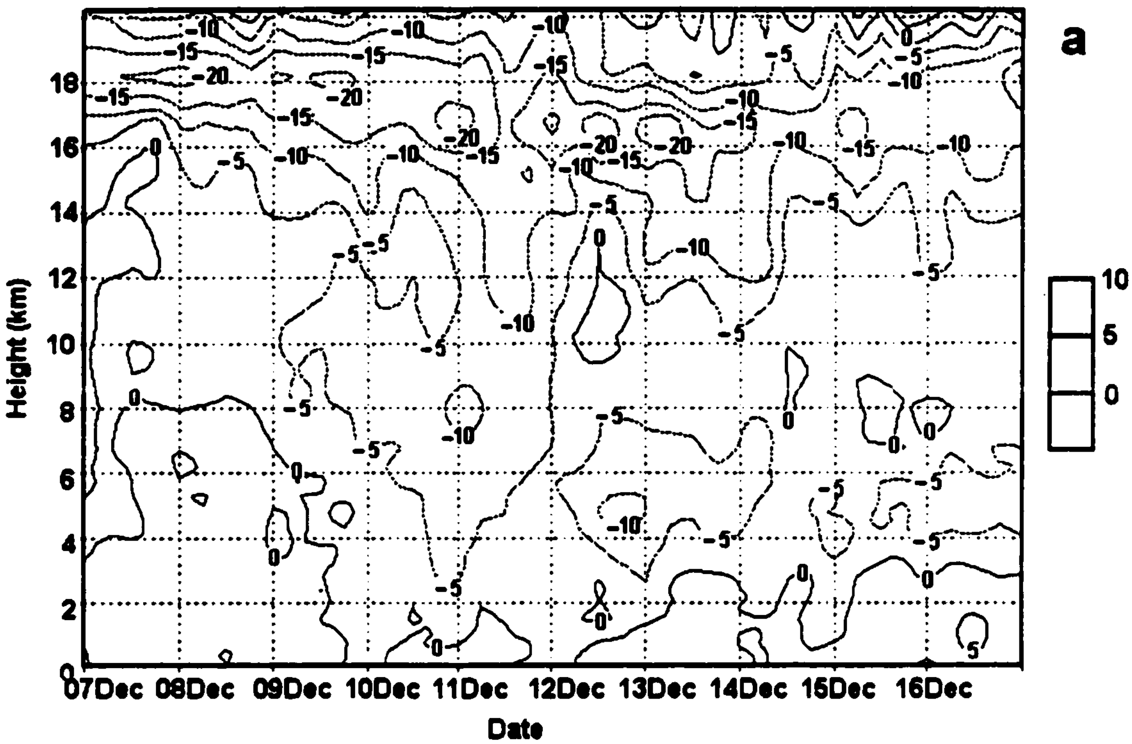

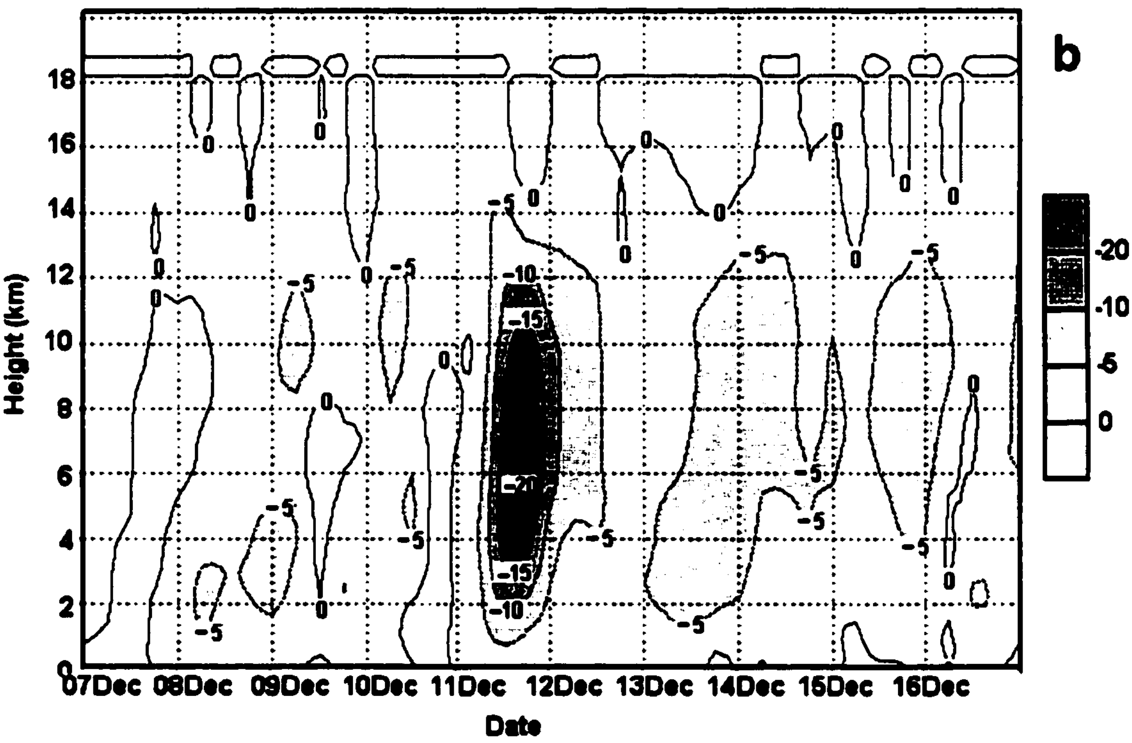

Figure 3.4 - (a) Observed zonal wind, in m.s^{-1}; (b) omega, in mb.h^{-1}; (c) temperature advection, in K.day^{-1}; and (d) water vapor mixing ratio advection, multiplied by L/c_p in K.day^{-1}. Westerlies (panel a), ascending motion (b), cooling (c) and moistening (d) are in gray-scale. All fields are averages over COARE IFA between 07 and 17 December 1992.

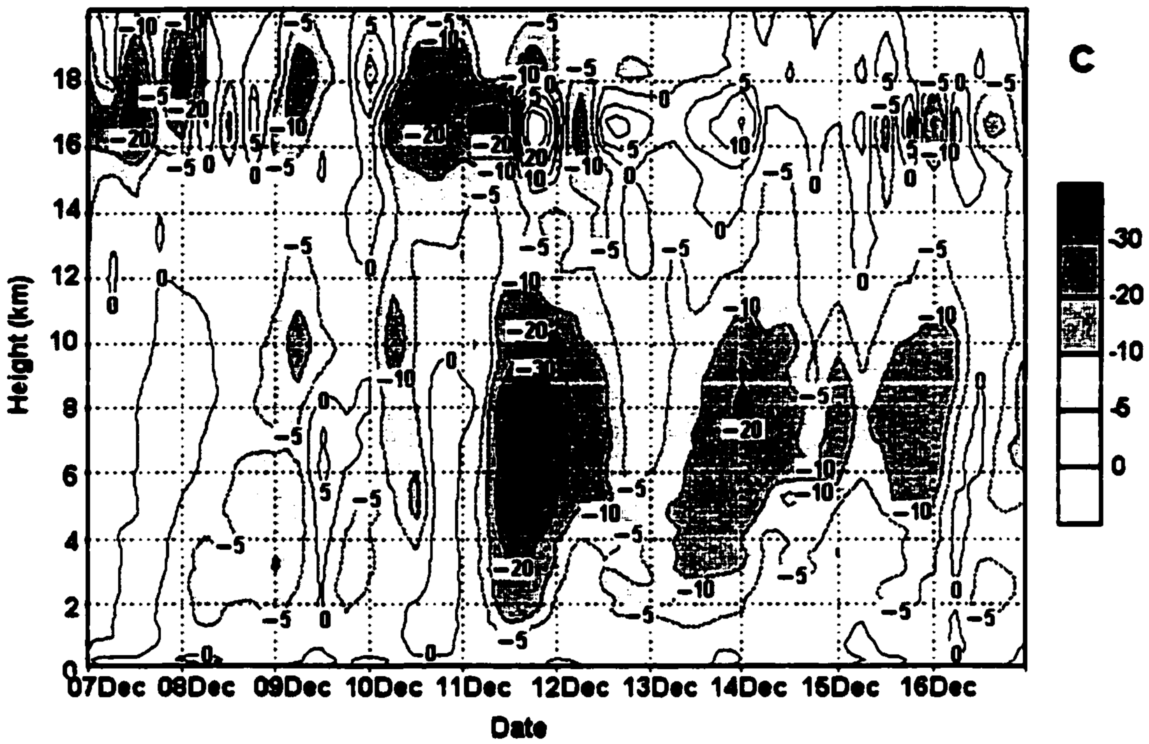

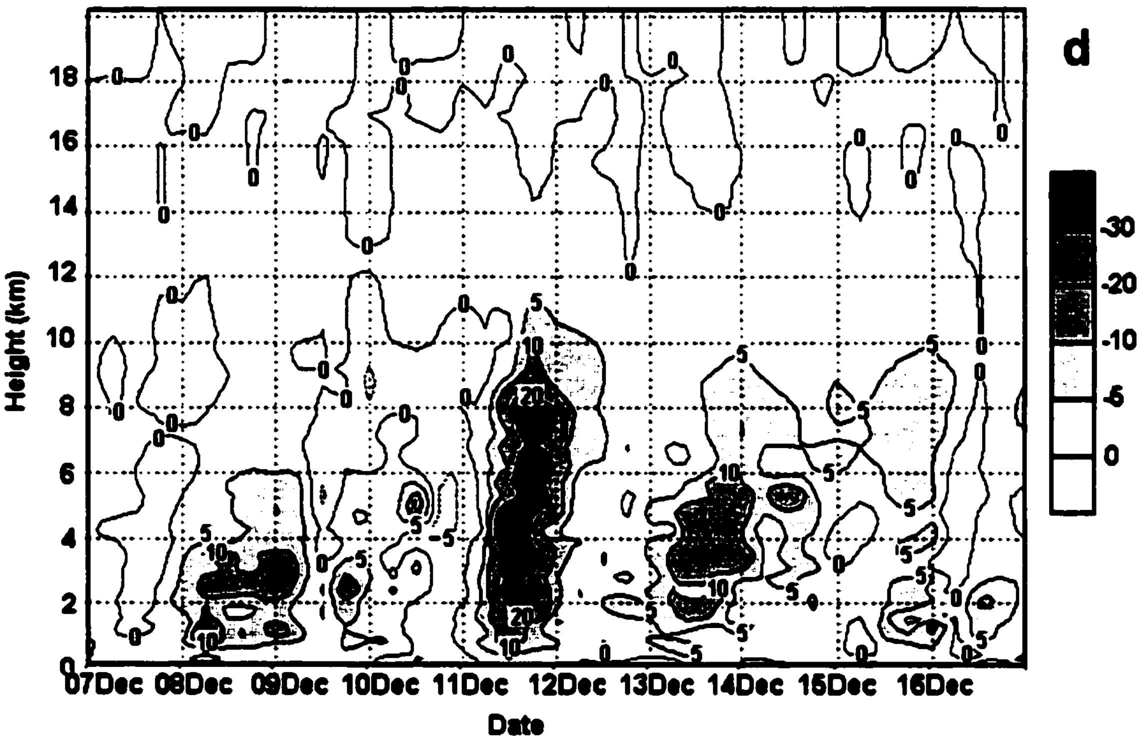

Figure 3.4 (continuation)

3.3 – Case 2 – The GCSS WG4 Case 2

The case studied in this section is the evolution of the cloud systems between 19 and 26 December 1992 during a WWB event (Case 2 of the GCSS Working Group 4, Moncrieff et al., 1997). The large-scale forcing for that period was constructed from the analyzed TOGA-COARE data (Lin and Johnson, 1996), obtained from soundings over the COARE intensive flux array (IFA). Figure 3.5 shows the evolution of the zonal wind (a), the vertical velocity in pressure coordinates (b), and the large-scale advective tendencies of temperature (c) and moisture (d), for that period.

As can be seen in Figure 3.5a, near-surface westerlies peak on 22 December. Large-scale rising motion prevails during most of the 7-day period, with the exception of 23 and 25 December.

Peaks of large-scale advective cooling and moistening occurred at altitudes about 6 to 7km, on 20, 21, 22, and 24 December. As a result, significant convective activity, generating warming and drying (Q1 and Q2, not shown) occurred during most of the period, again with the exception of 23 and 25 December.

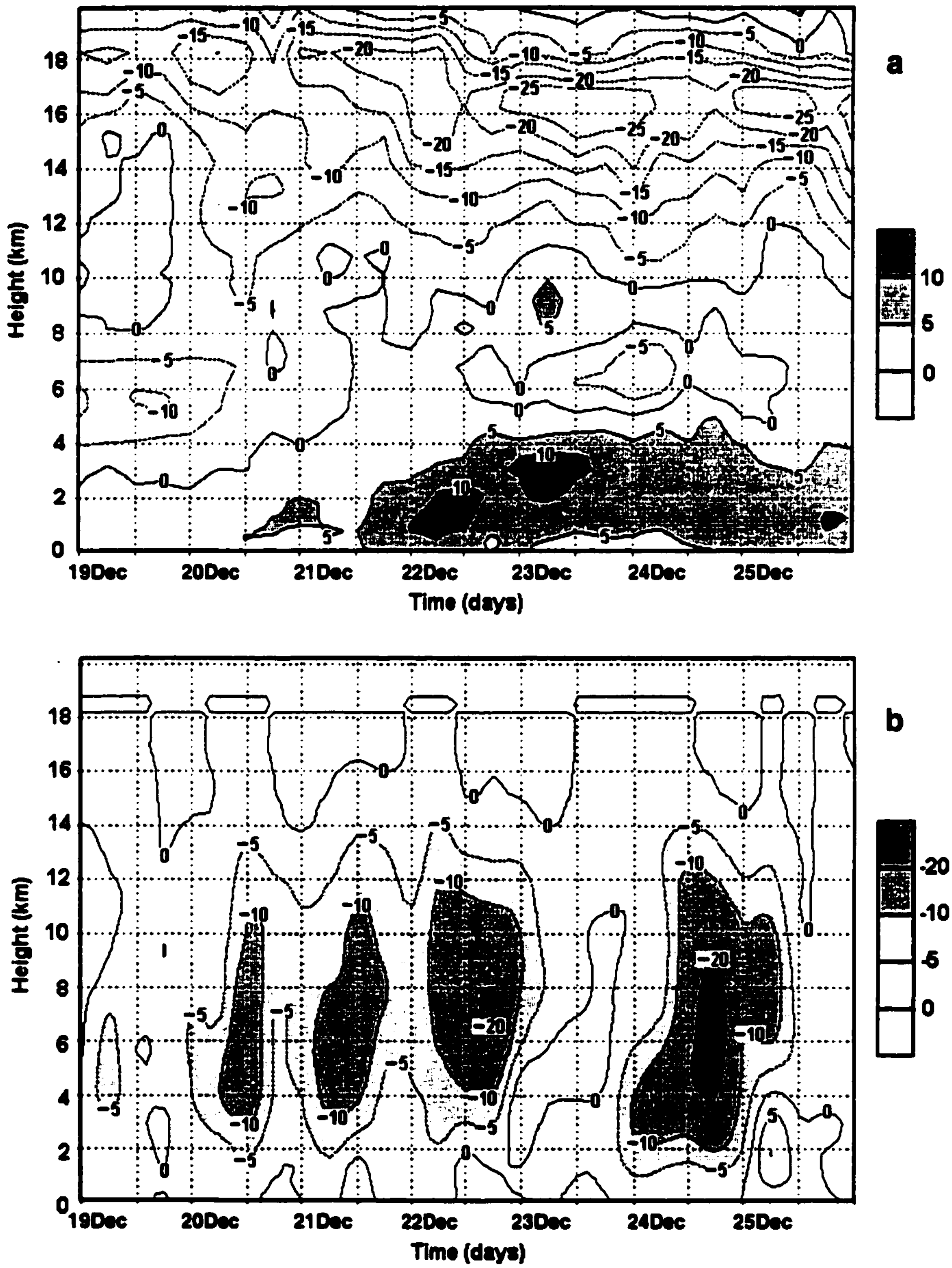

Figure 3.5 - (a) Observed zonal wind, in m.s^{-1}; (b) omega, in mb.h^{-1}; (c) temperature advection, in K.day^{-1}; and (d) water vapor mixing ratio advection, multiplied by L/c_p in K.day^{-1}. Westerlies (panel a), ascending motion (b), cooling (c) and moistening (d) are in gray-scale. All fields are averages over COARE IFA between 19 and 26 December 1992.

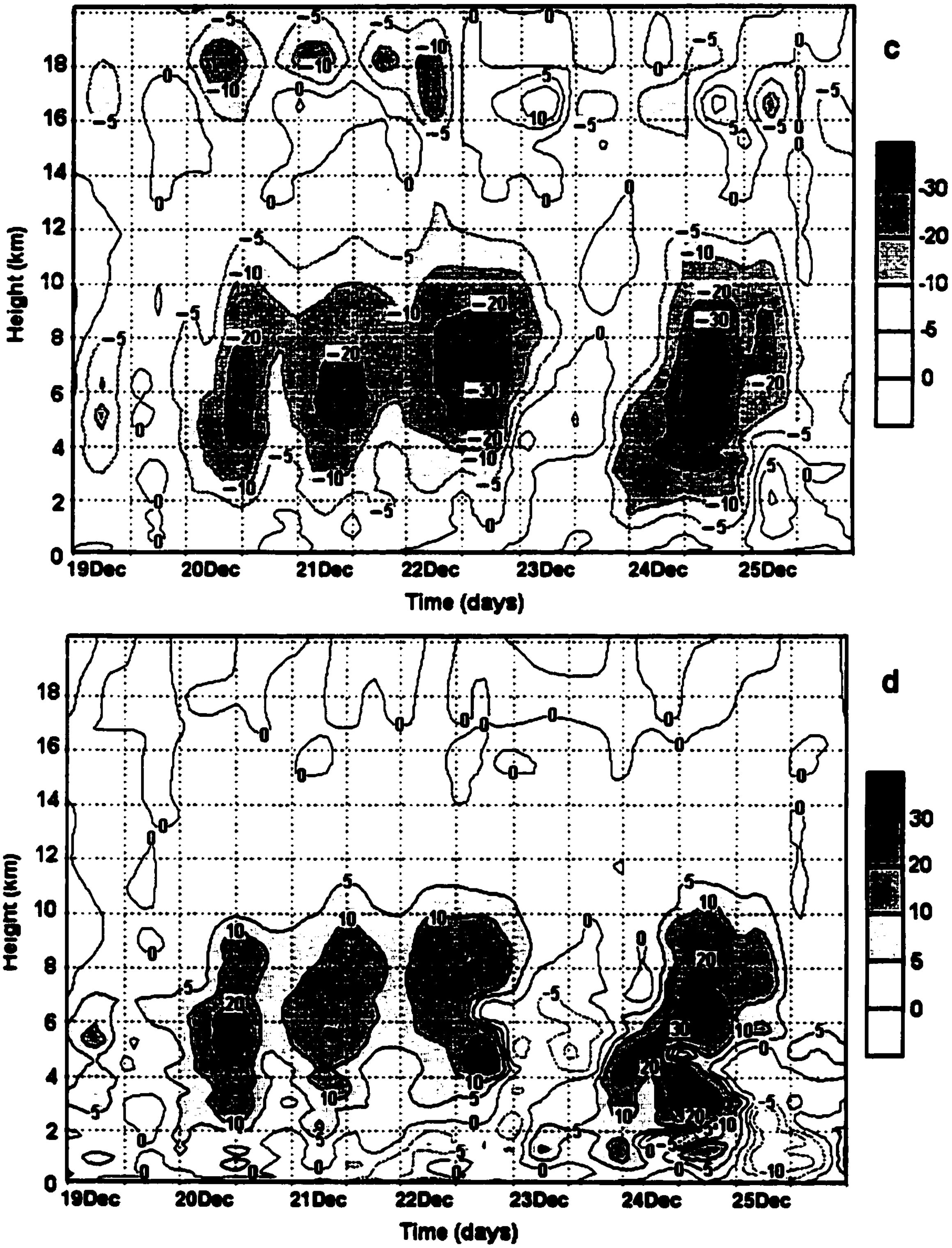

Figure 3.5 (continuation)

Between 19 and 26 December 1992, the SSTs experienced a general cooling trend, due to the strong surface fluxes associated with the WWB. The evolution of the average SST over the IFA during such a period is depicted in Figure 3.6.

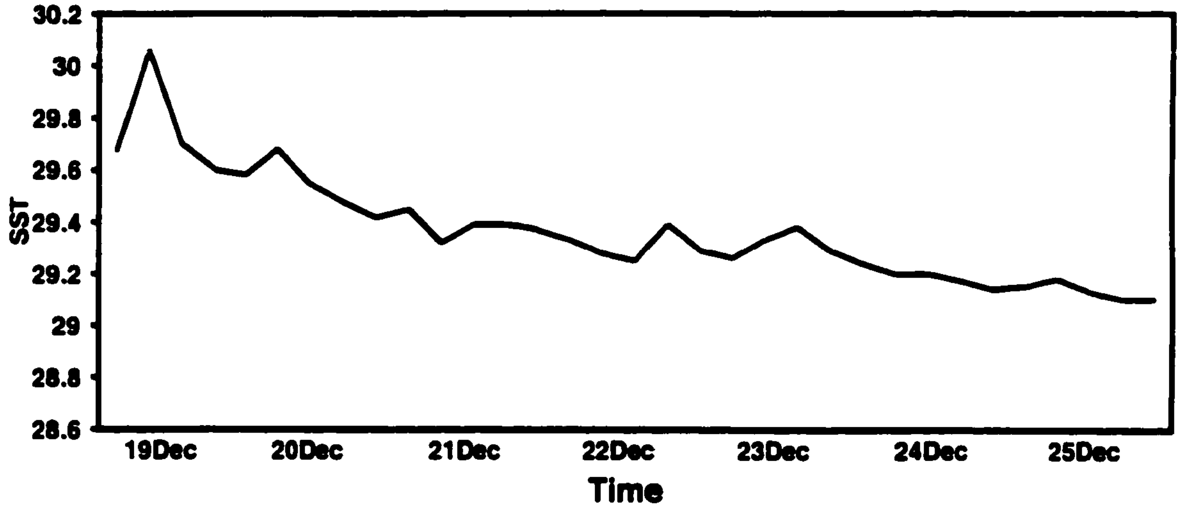

Figure 3.6 - Observed COARE IFA average SST, in °C, between 19 and 26 December 1992

In the simulations described in Chapter 7 (in which the coupled model is used) the period of simulation for Case 2 is extended for three more days (from 19 to 29 December 1992).

3.4 – Case 3 – Beyond a complete MJO cycle

In order to understand the role of the coupling of the atmosphere to the ocean surface during different phases of the MJO, one needs to investigate air-sea interactions on a timescale of at least several weeks, including different regimes of deep convection, and the opposite "trade-wind" phases related to the maximum WWBs and calm winds (Johnson and Lin, 1997).

Case 3 corresponds to the 70-day period between 19 December 1992 and 27 February 1993. Some of the characteristics of the flow over the COARE IFA are depicted in Figures 3.7-3.11 that shows time-height plots of the zonal wind, apparent heat source and apparent moisture sink, and the time evolution of the near-surface winds.

In Figure 3.7, two different flow regimes can be clearly identified. First, it shows the convectively active period between 19 December and 26 December, corresponding to the Case 2, described before. As shown previously, during that time interval, the layer of westerly winds in the lower tropospheric deepened and intensified, as the flow aloft turned increasingly easterly, intensifying the vertical wind shear (Figure 3.7a). The near-surface wind speed showed a generally increasing trend (Figure 3.7b) and strong convective warming (Figure 3.7c) and drying (Figure 3.7d) dominated. Following the series of convective episodes, between 26 December 1992 and roughly 03 January 1993, very strong shear was established throughout the troposphere over the COARE IFA. Westerly winds extended up to 8-10 km during that period, with zonal wind values greater than 15 ms^{-1} occupying most of the layer between 2 and 6km between 30 December 1992 and 02 January 1993 (Figure 3.7a). Concurrently, significant average wind speeds were found close to the surface, with values ranging from 6 to 8 ms^{-1} observed from 30 December 1992 and 02 January 1993 (Figure 3.7b). The peak WWB was often characterized by weak convective warming (Figure 3.7c) and weak, shallow moistening (Figure 3.7d), as convection was mostly suppressed over the COARE IFA.

Figure 3.8 represents the 14-day period following the peak WWB. After 02 January 1993, westerly winds relaxed, and shear decreased (Figure 3.8a). From that date until 08 January, the surface wind speed decreased (Figure 3.8b). After 06 January, the pattern of small positive values of Q_1 and Q_2 found in Figures 3.7c and 3.7d was also present between 02 and 06 January (Figures 3.8c and 3.8d). Following the WWB decay, the troposphere became mostly filled with easterlies, and the vertical wind shear decreased gradually, reaching particularly small values between 10 and 12 January (Figure 3.8a). Very weak near-surface winds prevailed from 08 to 15 January (Figure 3.8b). Q_1 and Q_2 were generally very small between 08 and 15 January, tending to negative values (Figures 3.8c and 3.8d). After 15 January, the environmental shear (Figure 3.8a) and the near-surface wind speed (Figure 3.8b) started to increase. Positive values of Q_1 and Q_2 indicate the re-establishment of convective activity.

In Figure 3.9, flow characteristics are depicted for the period between 16 and 30 January 1993. Between 15 and 20 January, the troposphere exhibited a moderate vertical shear (Figure 3.9a), and large-scale wind speeds of about $3ms^{-1}$ close to the surface (Figure 3.9b). The large positive values of the apparent heat source and apparent moisture sink indicate the presence of intense convective activity over the COARE IFA during that period, particularly on 18 and 19 January (Figures 3.9c and 3.9d). That brief period of convective activity under low-level easterlies was followed by an approximately 6-day period of mostly suppressed convection. Between 20 and 25 January, the low-level flow remained easterly; the middle and upper troposphere was mostly filled by weak westerlies (the layer of westerlies deepened throughout that period) with easterlies on top, close to the tropopause (Figure 3.9a). Q_1 and Q_2 were often small (Figures 3.9c and 3.9d).

Between 25 and 29 January, the low-level flow turned to westerly, with easterly winds aloft (Figure 3.9a). Near-surface winds showed an increasing trend (Figure 3.9b). Positive values of Q_1 and Q_2 suggest the presence of convection (Figures 3.9c and 3.9d).

The zonal wind, near-surface large-scale wind speed, Q_1 and Q_2 from 30 January to 13 February are shown in Figure 3.10. Between 30 January and 02 February, a layer of low-level westerlies deepened from a height of about 3km to 7km, with a significant easterly flow aloft, producing relatively large vertical wind shear (Figure 3.10a). Near-surface wind speeds peaked late on 30 January, reaching about 9 ms^{-1} (Figure 3.10b). Significant convective warming and drying occurred until 31 January. This episode was followed by a suppressed period, between 01 and 09 February, characterized by the presence of low-level westerlies (Figure 3.10a), wind speeds on the order of 4-5 ms^{-1} close to the surface (Figure 3.10b), and small values of Q_1 (Figure 3.10c) and Q_2 (Figure 3.10d). After 09 January, the flow over the COARE IFA showed the characteristics of convection preceding maximum low-level westerly flow.

Figure 3.11 depicts the zonal wind, near-surface large-scale wind speed, Q_1 and Q_2 from 13 February to 27 February. The evolution of the conditions over the COARE IFA during February 1993 did not follow Lin and Johnson's conceptual view of an ISO, depicted in Figure 3.2. However, late during that period, typical conditions of the active phase of the MJO occurred, such as increasing westerlies (Figure 3.11a), increasing near-surface winds (Figure 3.11b), and strong convective warming (Figure 3.11c) and drying (Figure 3.11d).

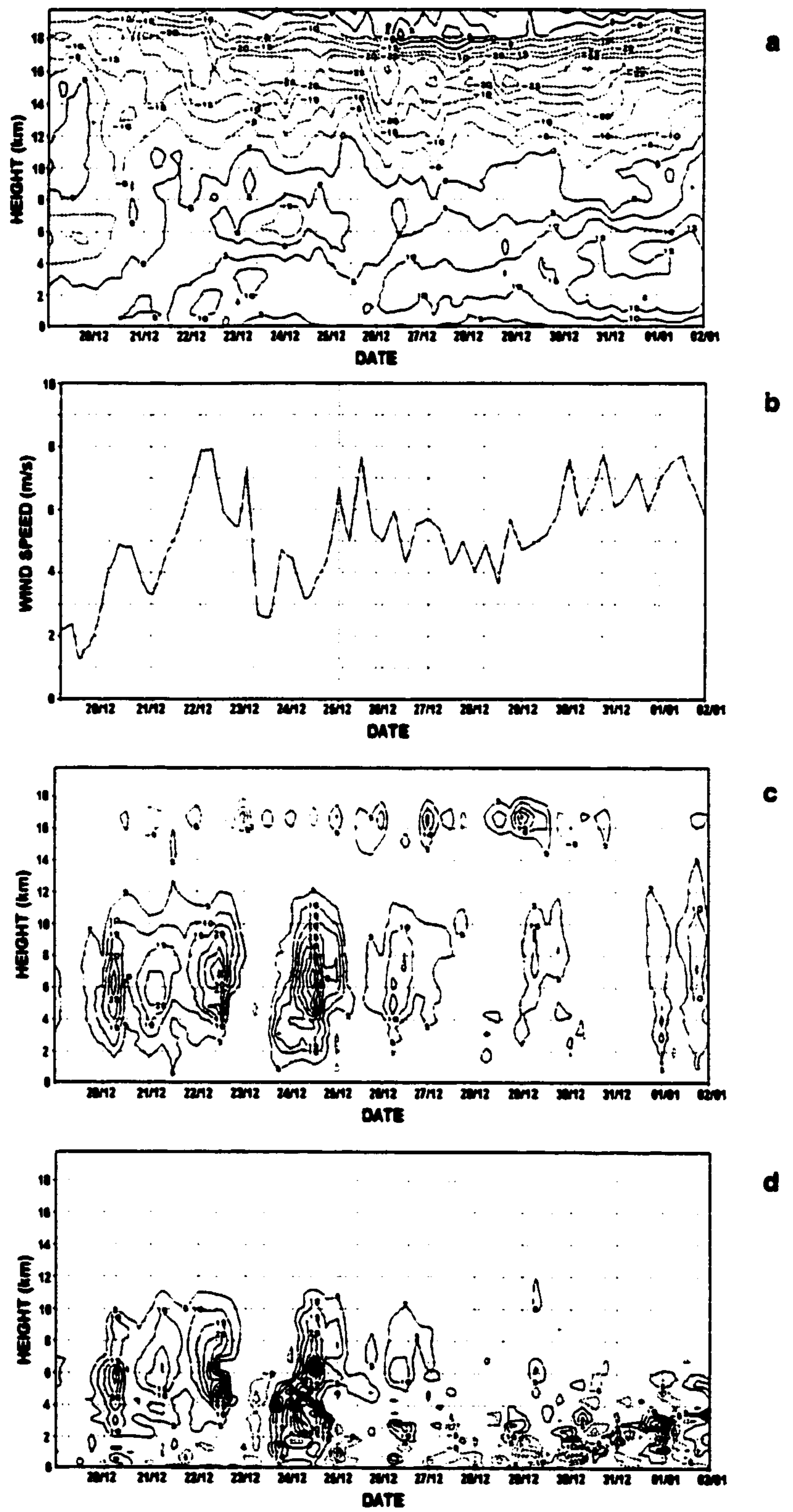

Figure 3.7 – Observed (a) zonal wind in ms^{-1}, (b) near-surface wind speed in ms^{-1}, (c) apparent heat source in $Kday^{-1}$, and (d) apparent moisture sink in $Kday^{-1}$ over the COARE IFA between 00UTC 19 December 1992 and 00UTC 02 January 1993.

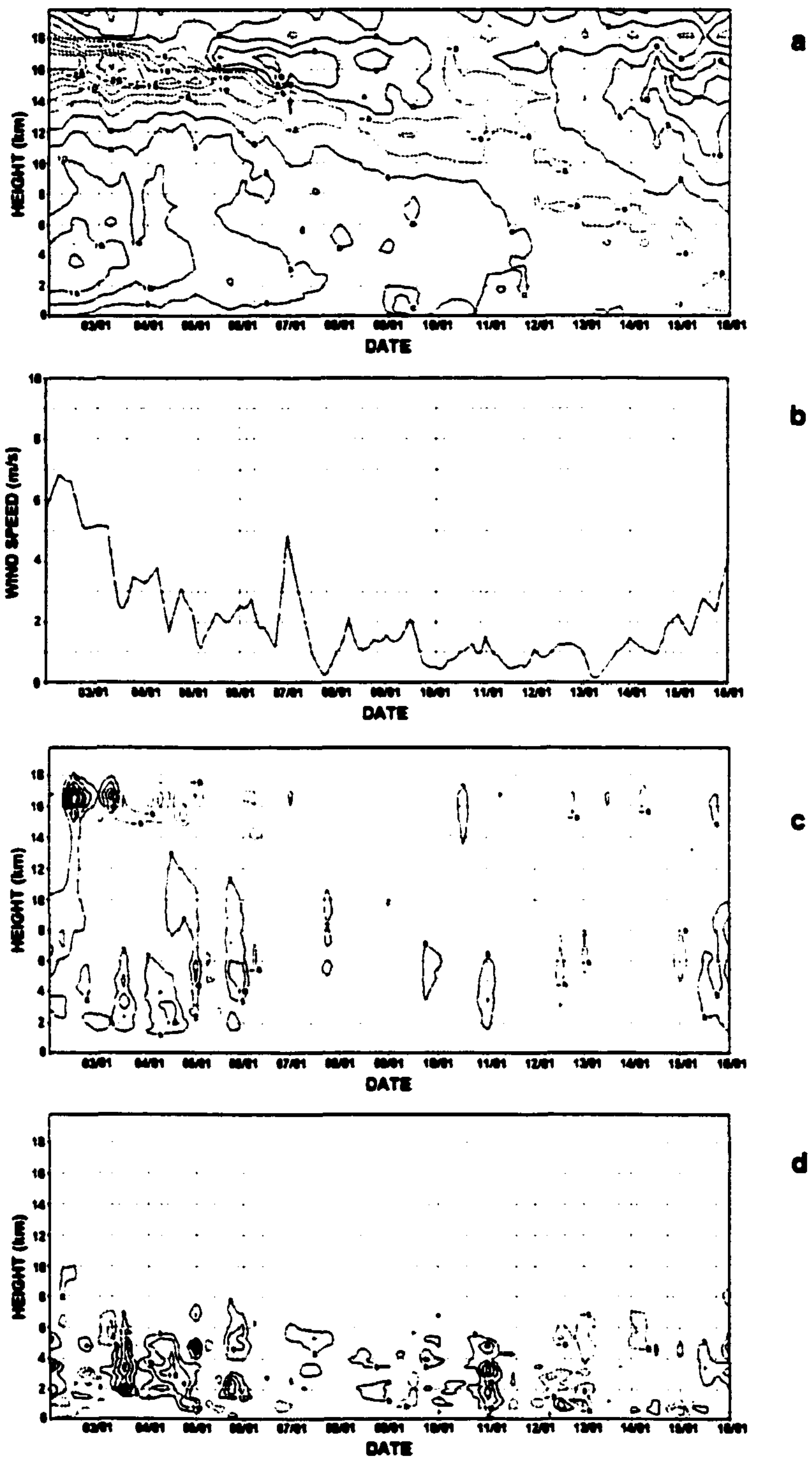

Figure 3.8 – Same as Fig. 3.7, except between 00UTC 02 January 1993 and 00UTC 16 January 1993.

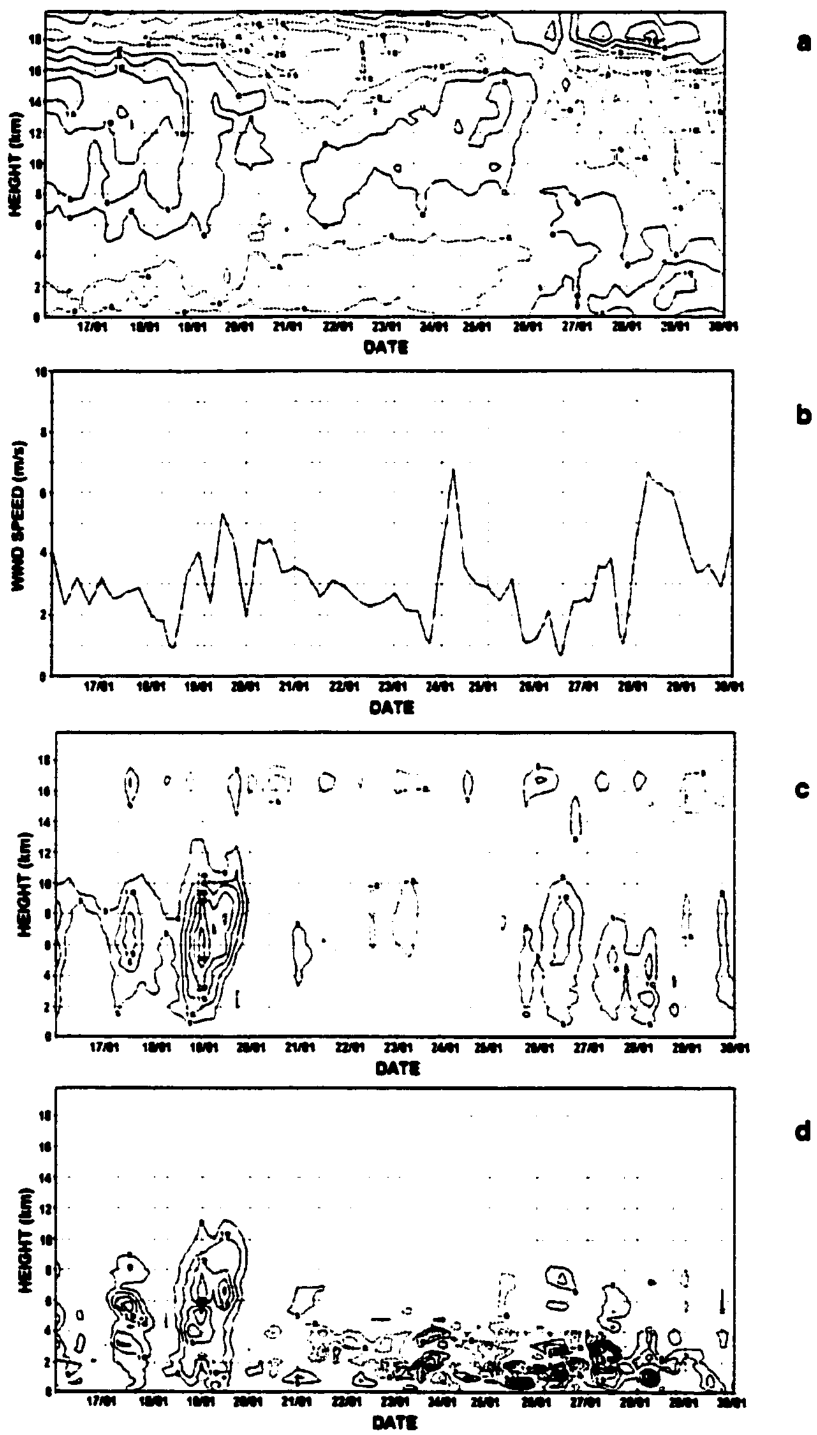

Figure 3.9 – Same as Fig. 3.7, except between 00UTC 16 January 1993 and 00UTC 30 January 1993.

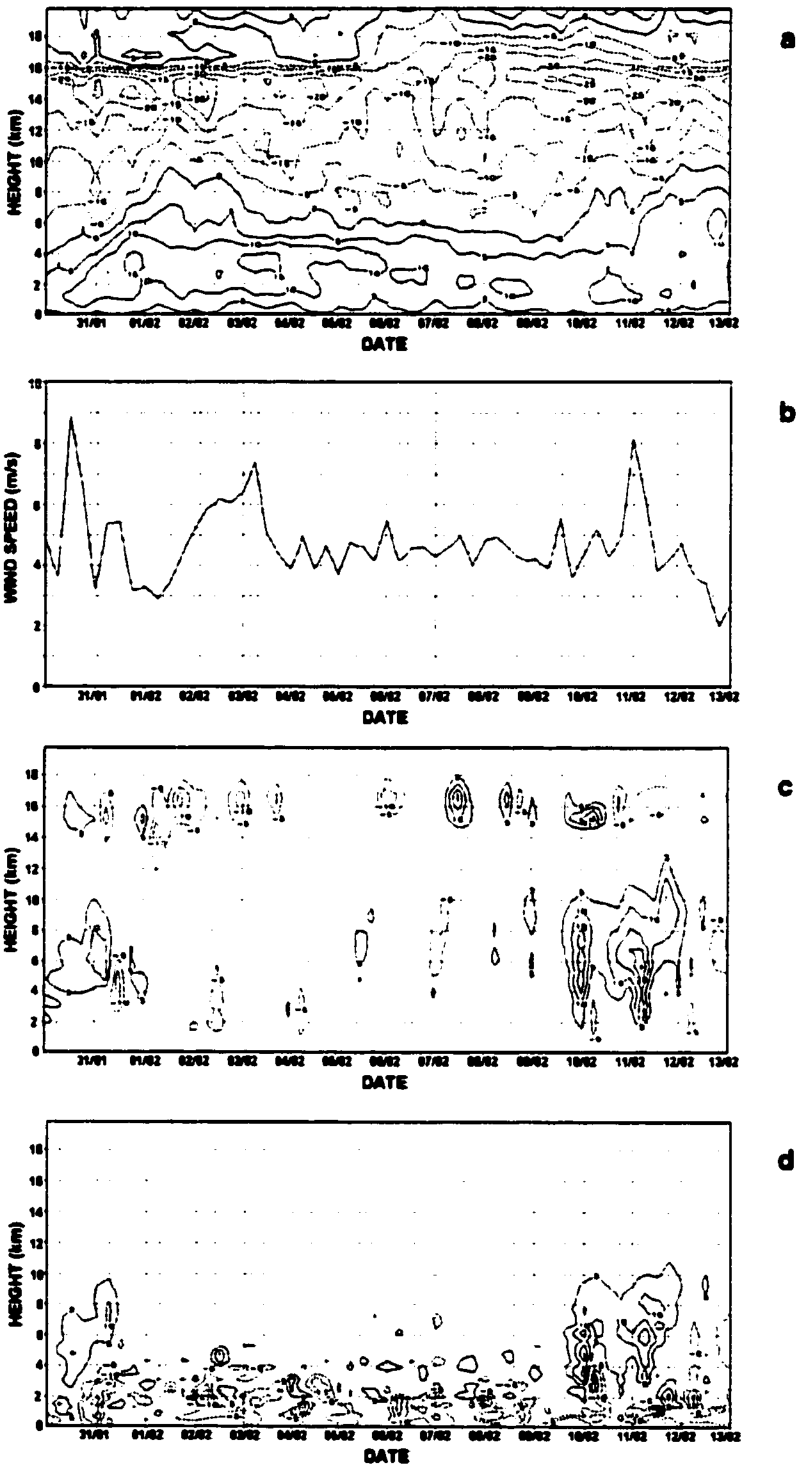

Figure 3.10 – Same as Fig. 3.7, except between 00UTC 30 January 1993 and 00UTC 13 February 1993.

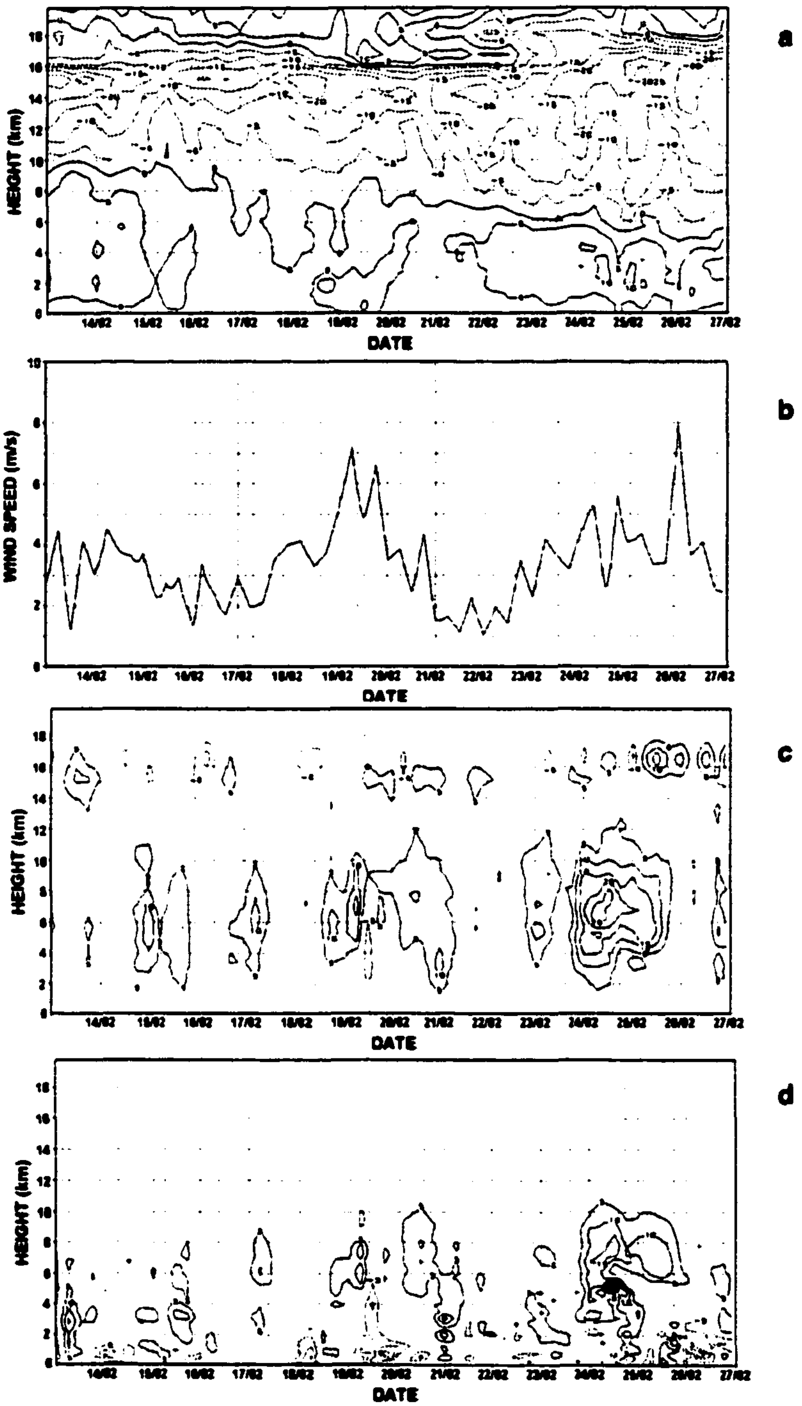

Figure 3.11 – Same as Fig. 3.7, except between 00UTC 13 February 1993 and 00UTC 27 February 1993.

Figure 3.12 depicts the time evolution of the average SST over the IFA during the 70-day period between 19 December 1992 and 27 February 1993. A strong relationship can be found between the behavior of the SST and the characteristics of the atmospheric flow. During the first week, the SST field was characterized by a significant decreasing trend, and small diurnal variation, in association with strong convective activity. The SST continued to drop, due to the presence of strong westerly winds, until 06 January, eventually showing diurnal oscillations. Between 07 and 14 January, increasing SSTs and a pronounced diurnal signal accompanied the suppressed convection and light winds. As the winds became stronger, preceding the convective event on 19 January, the SST decreased. The diurnal heating was still significant, however, with the exception of 19 January, when clouds associated with strong convective activity blocked a significant part of the incoming solar radiation. After that episode of deep convection, calm winds prevailed until 27 January, and the ocean temperatures increased once again. Low-level moderate winds, along with episodic convective events, helped to regulate the SSTs during most of the month of February, when high-frequency variations such as the diurnal cycle dominated. During that period (about three weeks), the minimum (nighttime) average SST ranged in a narrow interval, between 28.9 and 29.1 degrees Celsius. A cooling trend and a suppressed diurnal cycle in the SST were observed during the late February convective event.

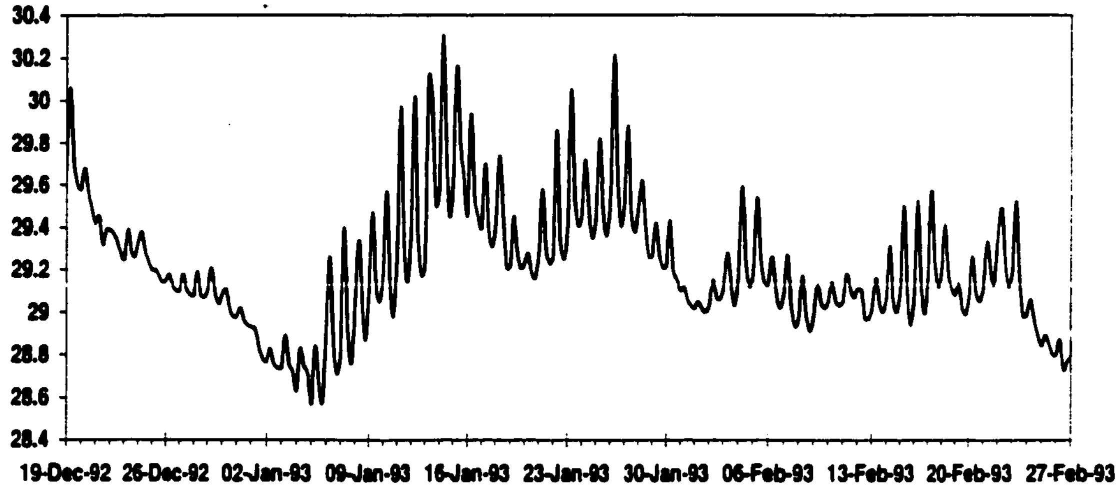

Figure 3.12 – Time evolution of the COARE IFA average SST between 19 December 1992 and 27 February 1993.

Chapter 4

THE ATMOSPHERIC MODEL

"Eu, ególatra céptico, cismava	"I, selfish skeptical, thought over
Em meu destino!... O vento estava forte	My destiny! ... The wind was strong
E aquela matemática da Morte	And that mathematics of Death
Com os seus números negros me assombrava!"	With its black numbers frightened me!"

(Augusto dos Anjos, Brazilian poet)

The atmospheric model used for this study is the *Regional Atmospheric Modeling System* (RAMS), developed at Colorado State University. As discussed by Pielke et al. (1992), RAMS has multiple options of numerical schemes and parameterizations and can be used in a wide spectrum of applications. In particular, RAMS have been successfully used in simulation of both mid-latitude and tropical convection (e.g., Alexander and Cotton, 1998; Ziegler et al., 1997; Olsson and Cotton, 1997; Nair et al., 1997; etc.).

4.1. Numerical schemes and parameterizations

RAMS is a primitive equation numerical model solved on a Eulerian grid. The basic model equations are written in a non-hydrostatic, compressible form (e.g., Tripoli and Cotton, 1986). For the simulations performed here, a hybrid time-integration scheme was used, in which scalar fields were integrated using a forward-in-time scheme, and momentum fields were integrated using a centered-in-time (leapfrog) scheme. Second-order space differencing was used to represent advection.

The one-moment bulk microphysics includes seven categories of hydrometeors: cloud water, rainwater, pristine ice, snow, aggregates, graupel and hail or frozen raindrops (Walko et al., 1995). The microphysical settings used in our simulations are described in Table 4.1.

Category	**Concentration scheme**	**Specified concentration**	**Specified mean diameter**	**Specified width parameter**
Cloud water	Specified concentration	100 cm^{-3}	-	2
Rainwater	Specified mean diameter	-	1 mm	2
Pristine Ice	Prognostic concentration	-	-	2
Snow	Specified mean diameter	-	1 mm	2
Aggregates	Specified mean diameter	-	1 mm	2
Graupel	Specified mean diameter	-	1 mm	2
Hail	Specified mean diameter	-	3 mm	2

Table 4.1 - Microphysical settings. For a given hydrometeor category, the number concentration can be user-specified, predicted, or diagnosed from the predicted mixing ratio and a user-specified mean diameter. A width parameter for the generalized gamma distribution is also specified (see Walko et al., 1995).

A two-stream radiative scheme, coupled to the microphysics, and comprising three bands of short-wave and five bands of long-wave radiation (Harrington, 1997;

Olsson et al., 1998) is used. Longitudinal variations of the incoming short-wave radiation are not considered. In order to save computer time, the tendencies to the thermodynamic equation due to radiative processes were updated every 10 minutes in our simulations.

The surface parameterization is the one by Louis et al. (1981), in which the fluxes are computed as a function of the roughness length, the Richardson number, the wind speed, and the differences of temperature and moisture between the air and the surface.

A simple deformation-K closure (Smagorinsky, 1963), in which the influences of the Richardson number (Lilly, 1962) and the Brunt-Vaisala frequency (Hill, 1974) are considered, was used to represent sub-grid scale turbulence.

4.2. Experimental Set-up

A two-dimensional, cloud-resolving model of RAMS was used in all simulations, with slightly different set-ups depending on the total simulation time.

Two-dimensional cloud-resolving simulations of convection have shortcomings (the three-dimensional structure of cloud systems cannot be represented and downdrafts tend to be exaggerated because of the lack of a degree of freedom). However, it has been shown that their statistics (time and domain averages of several cloud-related quantities) are very close to those produced by full three-dimensional models. Tao et al. (1987) and Grabowski et al. (1998) showed that the mean dynamic, thermodynamic and cloud fields were very similar in their 2-D and 3-D simulations. Also, the model intercomparison performed by the GCSS Working Group #4 showed that the several 2-D CRMs and the only 3-D CRM exhibited similar behaviors (Krueger and Lazarus, 1999). Hence, despite the obvious limitations, two-dimensional simulations are valid tools to investigate sensitivities of cloud-resolving simulations of convection to interactions with the upper ocean.

For the 7 to 10 day-long (short term) simulations, the model set-up followed much of the recommendations for the Case 2 of the GEWEX cloud systems study (GCSS) Working Group #4 (Moncrieff et al., 1997). In the short-term runs, the horizontal grid contained 512 points in the horizontal, with a grid spacing of 1km and the vertical grid comprised of 50 points with variable resolution (100m to 500m grid spacing). A timestep of 10s and periodic lateral boundary conditions were used.

For the long-term runs (about 2 month-long), a slightly different model set-up was adopted. The vertical grid from the short-term simulations was maintained, however the horizontal grid was modified. The number of horizontal grid points was reduced to 400 and the grid spacing was increased to 2km. A timestep of 12s was used in the long-term runs. As in the previous case, the lateral model boundaries were cyclic.

4.3. Initialization and Forcing

In all simulations, the atmospheric model was initialized from a horizontally homogeneous sounding, obtained by interpolating the values from the Colorado State University TOGA-COARE sounding archive (CSU-TCSA) into the model levels. Small random perturbations in the thermodynamic fields were introduced in the beginning of the simulations, in order to allow convection to develop.

Forcing terms were added to certain prognostic equations to represent the large-scale tendencies of momentum, temperature and moisture.

In the short-term simulations, the large-scale forcing was applied as in Grabowski et al. (1996). The contribution of the large-scale to the horizontal velocity is calculated using a relaxation technique, in which the nudging terms are calculated from the averaged velocity components and are uniform through the model domain. Equations (4.1) and (4.2), which are identical to Grabowski et al.'s (1996) equations (8a) and (8b), give the large-scale forcing for the momentum equations:

$$\left.\frac{\partial u}{\partial t}\right|_{LSF} = -\frac{\bar{u} - u_0}{\tau_m} \tag{4.1}$$

$$\left.\frac{\partial v}{\partial t}\right|_{LSF} = -\frac{\bar{v} - v_0}{\tau_m}, \tag{4.2}$$

where the subscript LSF refers to the large-scale forcing, u and v are the model-predicted zonal and meridional winds, u_0 and v_0 are the large-scale horizontal winds, τ_m is the relaxation timescale for momentum, and the bars denote horizontal averages over the model domain. In our simulations, a value of 3600s was used for τ_m.

This approach is different from the traditional nudging technique, in which the relaxation terms are calculated from the model-predicted variable in each grid point. While the relaxation is not constant across the horizontal domain in the traditional ("local") nudging technique, the forcing becomes horizontally uniform in the "non-local" approach. The local nudging relaxes the variable in each point towards the imposed value, which, in our case, would smooth out the small-scale variability inside the model domain. Conversely, the non-local nudging acts essentially on the horizontally averaged fields, allowing the smaller-scale features to develop within the model domain.

For the temperature and moisture fields, forcing terms representing the contribution from both large-scale horizontal and vertical advection were summed to the tendencies in the ice-liquid potential temperature and total water mixing ratio (prognostic variables in RAMS). The CSU-TCSA contains advective tendencies of temperature and water vapor. Therefore, the large-scale forcing for the ice-liquid potential temperature and total water mixing ratio has to be derived from them.

Let the ice-liquid potential temperature

$$\theta_{il} = \theta \exp\left[-\left(\frac{Lq_l}{c_p T} + \frac{L_i q_i}{c_p T}\right)\right], \tag{4.3}$$

where θ is the potential temperature, T is the temperature, q_l and q_i are the mixing ratios of liquid water and ice, L and L_i are the latent heat of liquid-to-vapor and ice-to-vapor phase changes and c_p is the heat capacity of dry air.

The approximation by Tripoli and Cotton (1981) results in:

$$\theta_{il} \cong \theta\left(1 - \frac{Lq_l}{c_p T} - \frac{L_i q_i}{c_p T}\right). \tag{4.4}$$

From equation (4.4), the large-scale forcing for θ_{il} can be written in terms of the advective tendencies of the potential temperature and the ice and liquid water mixing ratios:

$$\left.\frac{\partial\theta_{il}}{\partial t}\right|_{LSF} = \underbrace{\left.\frac{\partial\theta}{\partial t}\right|_{LSF}}_{1} \underbrace{-\left.\frac{L\theta}{c_p T}\frac{\partial q_l}{\partial t}\right|_{LSF}}_{2} \underbrace{-\left.\frac{L_i\theta}{c_p T}\frac{\partial q_i}{\partial t}\right|_{LSF}}_{3}$$
$$\underbrace{-\frac{Lq_l}{c_p}\frac{\partial}{\partial t}\left.\left(\frac{\theta}{T}\right)\right|_{LSF}}_{4} \underbrace{-\frac{L_i q_i}{c_p}\frac{\partial}{\partial t}\left.\left(\frac{\theta}{T}\right)\right|_{LSF}}_{5} . \tag{4.5}$$

Because $\frac{\theta}{T} = \left(\frac{p_0}{p}\right)^{R/c_p}$, where R is the gas constant for dry air, $\frac{\partial}{\partial t}\left(\frac{\theta}{T}\right)$ is equal to zero in pressure coordinates (even in Cartesian coordinates it can be neglected) and terms 4 and 5 vanish and Equation (4.5) can be written as follows:

$$\left.\frac{\partial\theta_{il}}{\partial t}\right|_{LSF} = \left.\frac{\partial\theta}{\partial t}\right|_{LSF} - \left.\frac{L\theta}{c_p T}\frac{\partial q_l}{\partial t}\right|_{LSF} - \left.\frac{L_i\theta}{c_p T}\frac{\partial q_i}{\partial t}\right|_{LSF} . \tag{4.6}$$

The total water mixing ratio is simply the sum of the vapor, liquid and ice mixing ratios, therefore its large-scale advective tendencies are given by:

$$\left.\frac{\partial q_t}{\partial t}\right|_{LSF} = \left.\frac{\partial q_v}{\partial t}\right|_{LSF} + \left.\frac{\partial q_l}{\partial t}\right|_{LSF} + \left.\frac{\partial q_i}{\partial t}\right|_{LSF} , \tag{4.7}$$

where q_t and q_v represent the total water and water vapor mixing ratios, respectively.

There are no observed data concerning the large-scale advective tendencies of condensate. However, two procedures can be used to overcome this problem. The first alternative is to neglect the large-scale horizontal advection of hydrometeors and to approximate the large-scale vertical advection using the condensate field calculate by the cloud-resolving model itself. The second is to simply assume that the large-scale forcing of the condensate field can be neglected.

In the first case, after substituting the proper advective terms, Equations (4.6) and (4.7) become:

$$\left.\frac{\partial \theta_{il}}{\partial t}\right|_{LSF} = -u_0 \frac{\partial \theta_0}{\partial x} - v_0 \frac{\partial \theta_0}{\partial y} - \omega_0 \frac{\partial}{\partial p}\left(\theta_0 - \frac{L\theta_0}{c_p T_0}\overline{q_l} - \frac{L_i \theta_0}{c_p T_0}\overline{q_i} \right) \tag{4.8}$$

and

$$\left.\frac{\partial q_t}{\partial t}\right|_{LSF} = -u_0 \frac{\partial q_{v,0}}{\partial x} - v_0 \frac{\partial q_{v,0}}{\partial y} - \omega_0 \frac{\partial}{\partial p}\left(q_{v,0} + \overline{q_l} + \overline{q_i} \right), \tag{4.9}$$

where ω_0 is the observed large-scale vertical velocity in pressure coordinates. As in previous equations, the bars indicate domain-averages over modeled fields and the zero subscripts refer to observed values.

In the second case, the ice-liquid potential temperature and total water mixing ratio forcing terms are approximated by the advective tendencies of the potential temperature and water vapor mixing ratio, as shown in Equations (4.10) and (4.11):

$$\left.\frac{\partial \theta_{il}}{\partial t}\right|_{LSF} = -u_0 \frac{\partial \theta_0}{\partial x} - v_0 \frac{\partial \theta_0}{\partial y} - \omega_0 \frac{\partial \theta_0}{\partial p} = \left.\frac{\partial \theta}{\partial t}\right|_{LSF}, \tag{4.10}$$

$$\left.\frac{\partial q_t}{\partial t}\right|_{LSF} = -u_0 \frac{\partial q_{v,0}}{\partial x} - v_0 \frac{\partial q_{v,0}}{\partial y} - \omega \frac{\partial q_{v,0}}{\partial p} = \left.\frac{\partial q_v}{\partial t}\right|_{LSF} . \tag{4.11}$$

Along with simplicity, the later approach has the advantage that all the forcing relies only in the observations. In all short-term simulations, Equations (4.10) and (4.11) were used to force the cloud-resolving model.

In the long term simulations, extra terms were added to the thermodynamic and moisture equations. As discussed by Wu et al. (1998), eventual errors in the TOGA COARE sounding data, particularly in the water vapor field, can lead to significant moisture and, as a consequence, temperature biases in cloud-resolving simulations. In order to reduce the biases in their modeling study, Wu et al. (1998) introduced a relaxation term to the water vapor equation. The result was a significant improvement of the agreement between the model results and the observations in the moisture field, but also in the temperature field, at least below 16km. By the tropopause, however, significant temperature biases were still present, as in all simulations submitted to the intercomparison study performed by Krueger and Lazarus (1999). Those errors could be related to the assumption that the vertical velocity always vanishes at 75mb, used in the calculations performed to prepare the CSU-TCSA. Since the vertical derivative of the potential temperature increases dramatically in that region, even small errors in the vertical velocity diagnostics can lead to large errors in the calculated thermal tendency due to vertical advection. Hence, in the long-term simulations presented in this work, as in the prognostic equation for the total water mixing ratio, a relaxation term was also summed to the thermodynamic equation to reduce the model biases. This formulation is shown in Equations (4.12) and (4.13):

$$\left.\frac{\partial \theta_{il}}{\partial t}\right|_{LSF} = -u_0 \frac{\partial \theta_0}{\partial x} - v_0 \frac{\partial \theta_0}{\partial y} - \omega_0 \frac{\partial \theta_0}{\partial p} - \frac{\bar{\theta} - \theta_0}{\tau_\theta}, \tag{4.12}$$

$$\left.\frac{\partial q_t}{\partial t}\right|_{LSF} = -u_0 \frac{\partial q_{v,0}}{\partial x} - v_0 \frac{\partial q_{v,0}}{\partial y} - \omega \frac{\partial q_{v,0}}{\partial p} - \frac{\overline{q_v} - q_{v,0}}{\tau_q}, \tag{4.13}$$

where τ_θ and τ_q are the relaxation timescales for temperature and moisture, respectively. In the simulations described in Chapter 10, a value of 1 day was used for both parameters.

Chapter 5

UNCOUPLED SIMULATIONS

A descriver lor forme più non spargo	Reader! to trace their forms no more I waste
rime, lettor; ch'altra spesa mi strigne,	My rhymes; for other spendings press me so,
tanto ch'a questa non posso esser largo;	That I in this cannot be prodigal.
ma leggi Ezechiel, che li dipigne	But read Ezekiel, who depicteth them
come li vide da la fredda parte	As he beheld them from the region cold
venir con vento e con nube e con igne;...	Coming with cloud, with whirlwind, and with fire;...

(Dante Alighieri, translation by H. W. Longfellow)

In order to verify the capability of the atmospheric model described in the previous Chapter in simulating ensembles of deep convective clouds over the Western Pacific, a control experiment was performed, focusing on the multiple events of convection that occurred between 19 and 26 December 1992, over the TOGA-COARE IFA. In order to assess the statistical significance of the simulation of this convective period, 4 other realizations were performed, with slight differences in the temperatures perturbations imposed to the basic state. Sensitivity experiments were carried out, in which the sea surface temperature was increased or decreased by one degree Celsius and the same evolving large-scale forcing used in the control simulation. Also, in order to investigate the influence of inhomogeneous surface forcing, sinusoidal SST perturbations of different wavelengths were superimposed onto the observations in three sensitivity runs. The results of those ten numerical experiments are reported in this Chapter.

5.1 - Case 2 - control simulation

In the control simulation, hereafter referred to only as CONTROL, the cloud-resolving model was forced by the actual observed SST (average over COARE IFA), depicted in Figure 3.6. In order to create inhomogeneities in the model atmospheric variables, a random perturbation with a 1K amplitude was applied to the air temperature field, during the first hour of simulation.

5.1.1 - Comparison with the observations

In general, the cloud-resolving model was able to reproduce the observed fields, shown in the previous Section. Since the model winds are systematically nudged toward the observed values, very good agreement was obtained between both zonal and meridional simulated wind components and the corresponding observations.

Departures from the modeled temperature and moisture fields from the observations demonstrate one of the weaknesses of the present approach. A dry, cold bias developed in most of the troposphere, as in the model intercomparison performed by the GCSS Working Group #4 on the same TOGA-COARE case (Krueger, 1997; Krueger and Lazarus, 1999). The differences between the modeled and observed temperature and water vapor mixing ratio at the end of the 7-day simulation are shown in Figure 5.1. A comparable drift toward a colder troposphere was found by other authors that performed similar simulations (Krueger and Lazarus 1999; Su et al. 1999). Temperature and moisture biases were also reported in cloud-ensemble simulations of different cases, as shown in the works by Grabowski et al. (1996) and Wu et al. (1998). Grabowski et al. (1996) propose that biases can develop in association with the lack of a prescribed large-scale advective forcing of hydrometeors. Also, imperfections in the large-scale forcing can generate departures from the observations, as discussed by Su et al. (1999) regarding the GCSS Working Group #4 case 2.

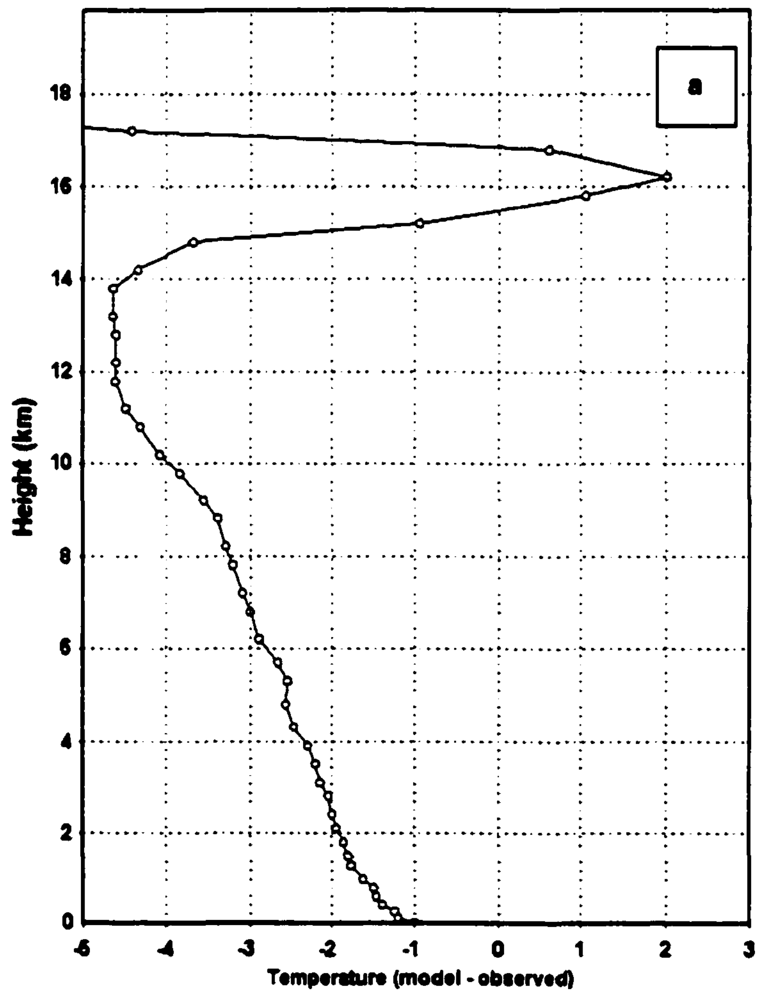

Figure 5.1 - Differences between the modeled and observed temperature, in °C (a) and water vapor mixing ratio, in gkg^{-1} (b) at the end of the CONTROL simulation.

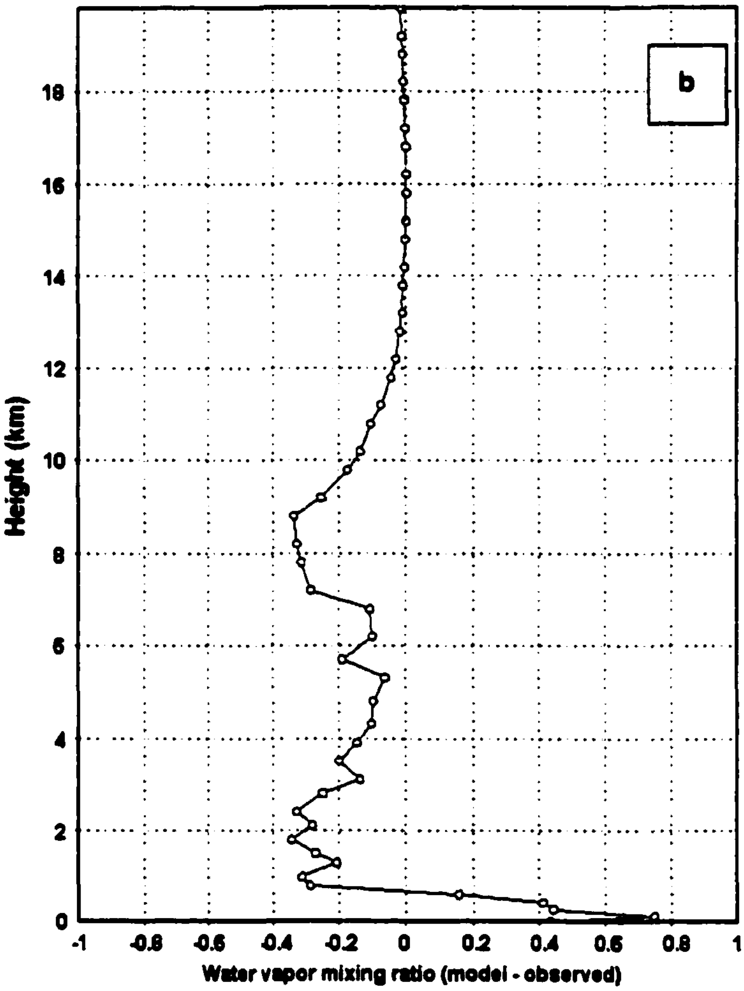

Figure 5.1 (continuation).

As discussed in Chapter 4, Wu et al. (1998) showed that if a relaxation term is added to the moisture (and possibly to the temperature) forcing there is an improvement in the agreement between modeled and observed fields, no matter what the actual cause of the biases is. Such a nudging term was not introduced in the simulations described in this Chapter, though. The major goal of this study was not to reproduce the observed fields using the CRM, but to explore sensitivities. Hence, in order to maintain simplicity, as well as to reduce the constraints that could limit the degrees of freedom in the model and might obscure the model sensitivities, no nudging was applied to the temperature and moisture fields.

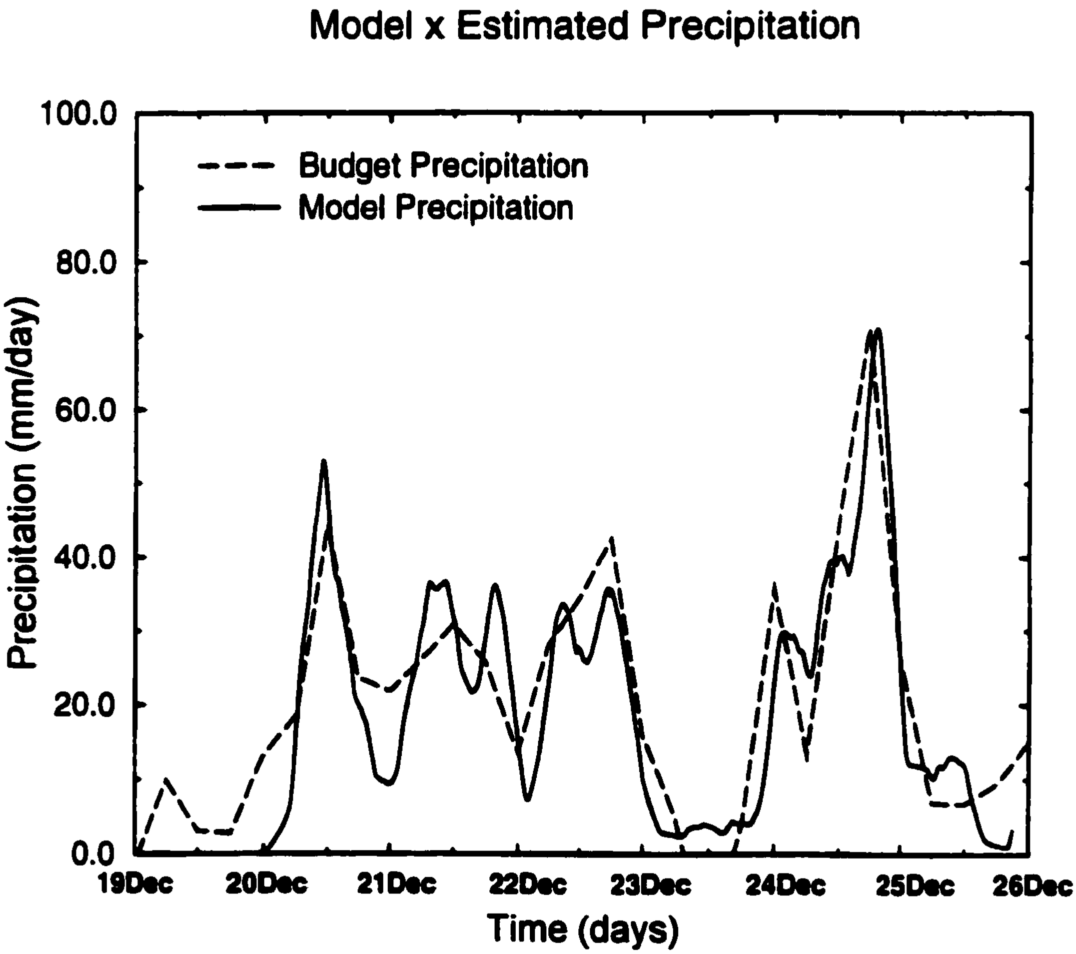

Figure 5.2 – Model (from CONTROL) versus "observed" (estimated from COARE IFA moisture budgets) precipitation, in mmh^{-1}.

The key trends in the surface precipitation were well reproduced, and the quantitative agreement between the observations and the modeled rainfall was good, as can be seen in Figure 5.2, which compares the modeled rainfall with the one estimated from the COARE IFA budget. Of course, such agreement is expected, based on the fact that the IFA precipitation was estimated using the same large-scale fields that drive the CRM. The average budget precipitation for the 6-day period between 20 and 26 December was 21.9 mm day^{-1}, while the corresponding average modeled precipitation was 21.2 mm day^{-1}. 19 December was excluded from the calculation of the averaged cloud and precipitation fields, because the model requires about 23h to produce clouds (in the form of a mid-level stratiform deck) and about 26h to generate significant precipitation at the surface.

The surface heat fluxes were, in general, accurately simulated by the CRM (see Figure 5.3). The 7-day averaged model fluxes were 18.6 Wm^{-2} (sensible) and 132.8 Wm^{-2} (latent), while the corresponding observed values were 16.0 Wm^{-2} (sensible) and 137.8 Wm^{-2} (latent). All major trends were captured, especially at the end of the simulation. Despite the limitations of a 2D CRM, our results concerning the surface precipitation and the surface heat fluxes are actually in better agreement with the observations than the ones obtained by Su et al. (1999) using a 3D CRM. This shows the importance of a good surface flux parameterization to generate realistic results concerning the heat transport at the air-sea interface. Of course, this issue can be even more critical as one performs numerical simulations using coupled models.

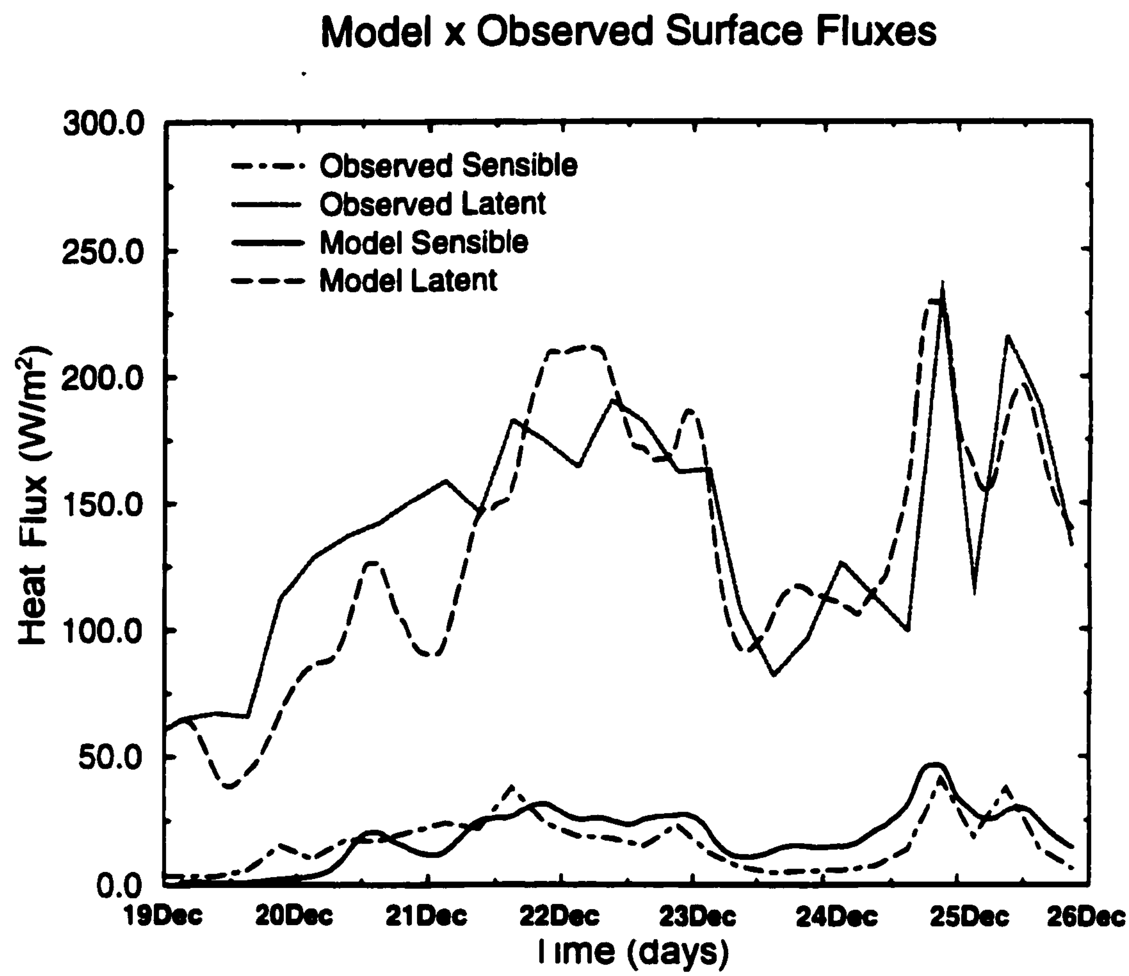

Figure 5.3 - Model (from CONTROL) versus observed surface heat fluxes, in Wm^{-2}.

5.1.2 – Condensate fields, cloud coverage

According to observations (see for instance Wu et al., 1998), the region of COARE IFA was mostly covered by clouds between 20 and 25 December 1992, with particularly low values of the cloud-top temperature on the days 20-22 and 24.

Figure 5.4 shows the temporal evolution of the domain-averaged total condensate mixing ratio for the simulation period and Figure 5.5 represents the 6-day averages of the total condensate, cloud water, rainwater, low-density ice and high-density ice mixing ratios.

Figure 5.4 - Model total condensate mixing ratio, 3h-running domain-average (CONTROL), in gkg^{-1}

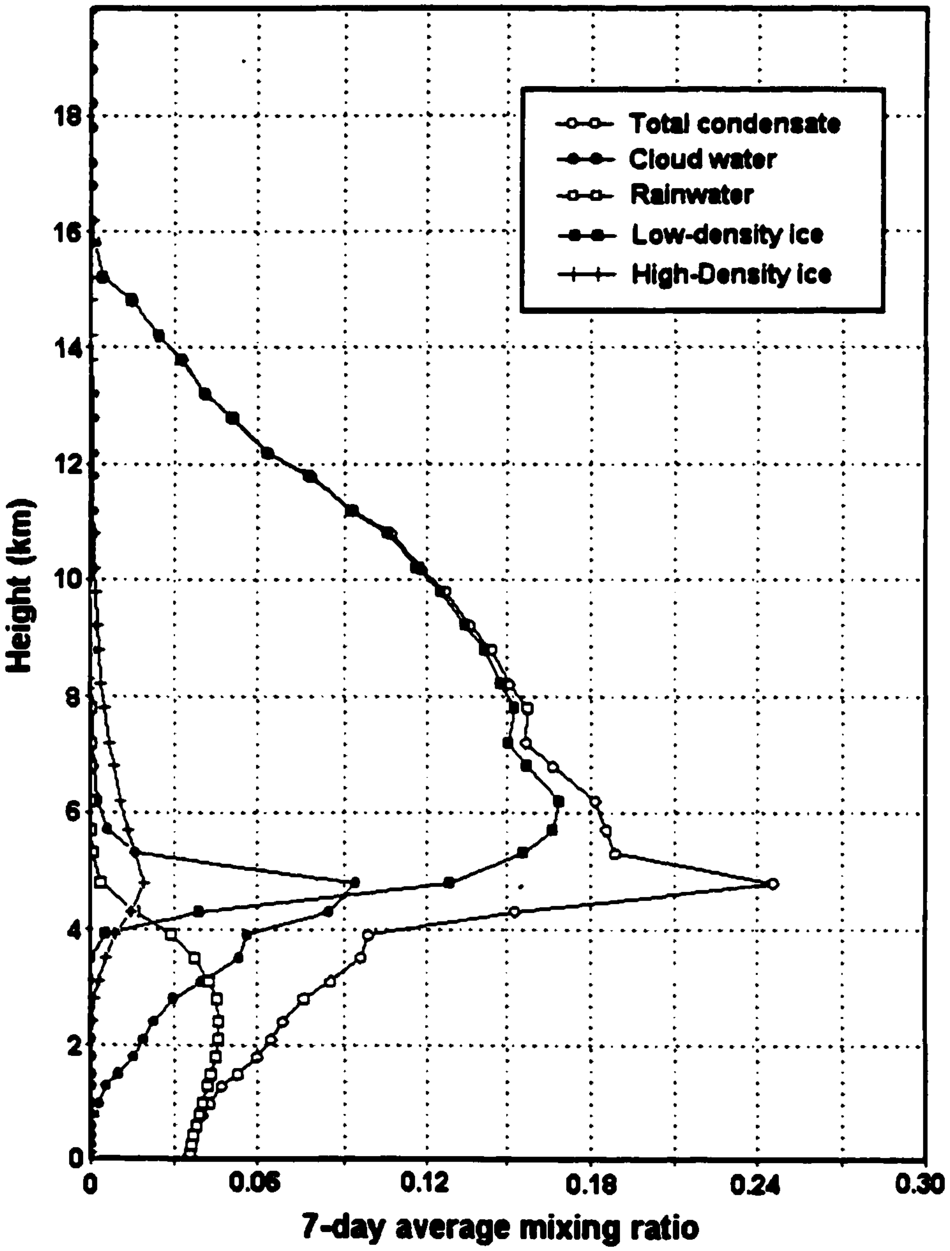

Figure 5.5 - 6-day (between 20 and 26 December) averaged mixing ratios (CONTROL) in gkg^{-1}

In Figure 5.4, convection develops on the second day of simulation, and deep clouds last until the end of the fourth day. At that time, deep convection produced a deck of cirrus clouds, and only shallow convective clouds are produced. Deep convection returns on the sixth day, lasting until close to the end of the simulation. In general, the present results agree with other modeling studies of the same case (e.g., Su et al., 1999). In contrast with the total condensate, which is constrained by the imposed large-scale forcing, the distribution of the water substance among different categories (cloud water, rainwater and ice species) depends on the microphysical parameterization and the microphysical setting. For instance, our results have significant departures from Su et al. (1999) that used a microphysical parameterization in which graupel was not included. For the current microphysical settings, low-density ice (pristine ice, snow and aggregates) dominates the condensate field in our simulations. At least for the particular choice of microphysical parameters shown in Table 4.1, the presence of graupel and hail is small during the entire period.

Figure 5.6 shows the 6-day average of the domain-averaged cloud fractional area (a cloudy grid box is defined as the one containing at least $0.01 gkg^{-1}$ of cloud water plus cloud ice). As in the GATE simulations by Grabowski et al (1998), a bimodal distribution of cloud coverage occurs in CONTROL, with a primary peak of cloudiness at high levels, and a secondary peak near the melting level. However, for the present simulated TOGA-COARE case, both peaks were more intense, and the high-level peak is located at a more elevated altitude than in the GATE simulations referred to above.

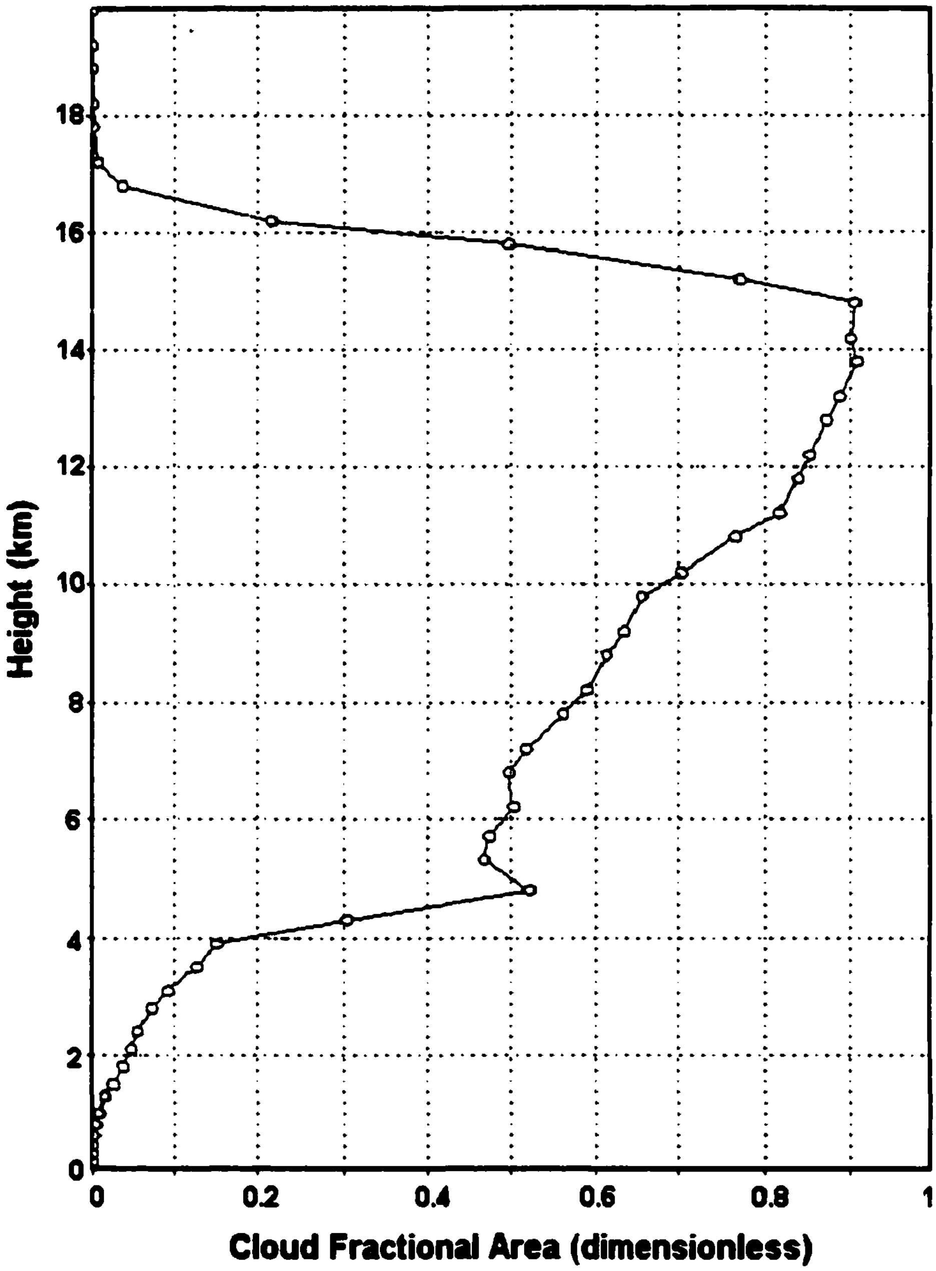

Figure 5.6 - 6-day (between 20 and 26 December) averaged cloud fractional area (CONTROL)

5.1.3 – Convective-stratiform partition, cloud mass flux

One important issue for the development of parameterizations for GCMs is the separation between the convective and the stratiform parts of cloud systems. In cloud-resolving simulations such a partition can be assessed explicitly (see Xu 1995 and Alexander and Cotton, 1998).

Figure 5.7 shows the temporal evolution of the convective and stratiform precipitation in CONTROL. Table 5.1 shows the 7-day averaged model convective and stratiform precipitation and convective and stratiform fractional area. Although "convective columns" cover less area than "stratiform columns" (as expected), the larger contribution to the total precipitation came from the convective elements of the cloud systems, due to the heavy rainfall produced by them. Stratiform precipitation and convective precipitation are out of phase, with stratiform rain generally following the occurrence of convective events. The obvious exception in Figure 5.7 is the first occurrence of stratiform precipitation, associated with the model spin-up.

Figure 5.8 represents the 7-day average of the total, updraft, saturated downdraft and unsaturated downdraft cloud mass flux in CONTROL. In the computation of the total cloud mass flux, the contribution of unsaturated downdrafts, which occur mostly in association with rainfall, was incorporated. Such a component is the major contributor to the downdraft cloud mass flux, especially below cloud base. It produces negative values of the total cloud mass flux at low levels, which are quite evident in Figure 5.8.

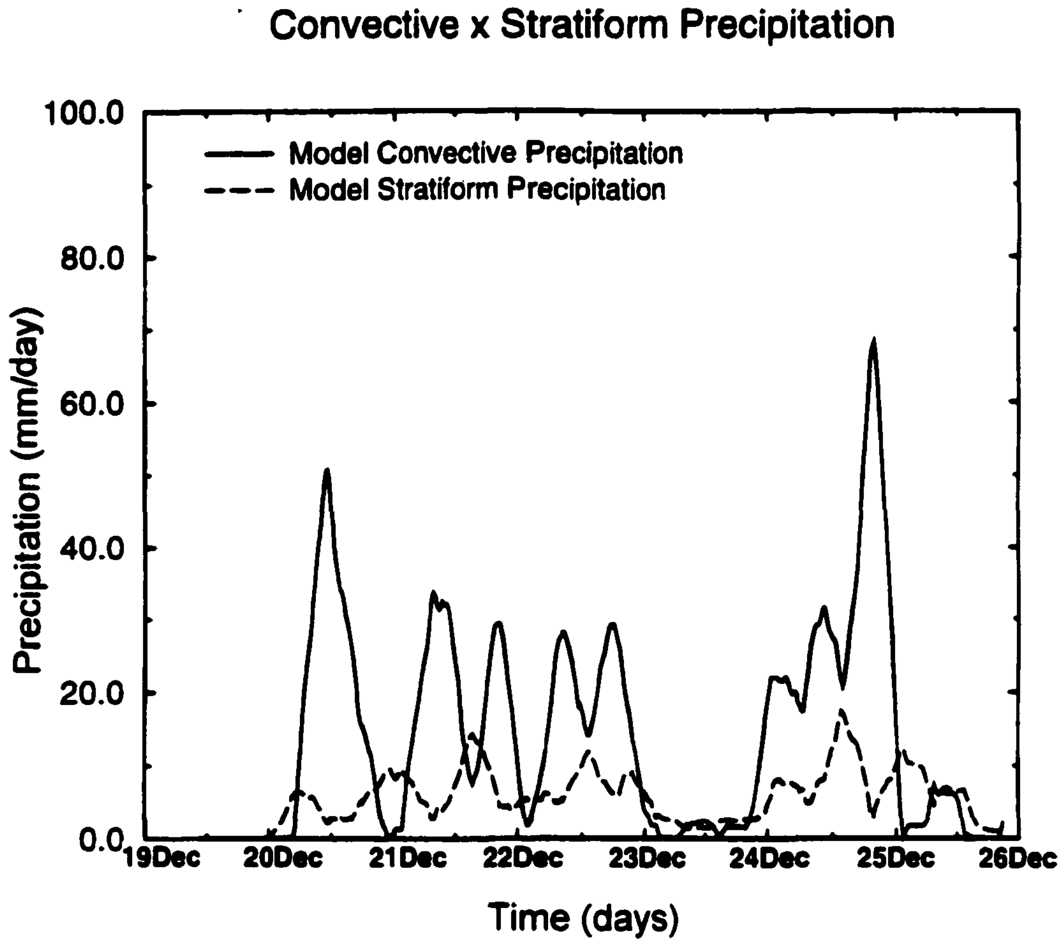

Figure 5.7 - Convective and stratiform precipitation, 3h-running domain-average (CONTROL), in mm day^{-1}

Convective precipitation	15.3 mmday^{-1} (72.2% of the total)
Stratiform precipitation	5.9 mmday^{-1} (27.8% of the total)
Total precipitation	21.2 mmday^{-1}
Convective fractional area	0.3103
Stratiform fractional area	0.4234
Total rainy fractional area	0.7337

Table 5.1 - 6-day averages of the convective and stratiform precipitation, convective and stratiform fractional area in CONTROL.

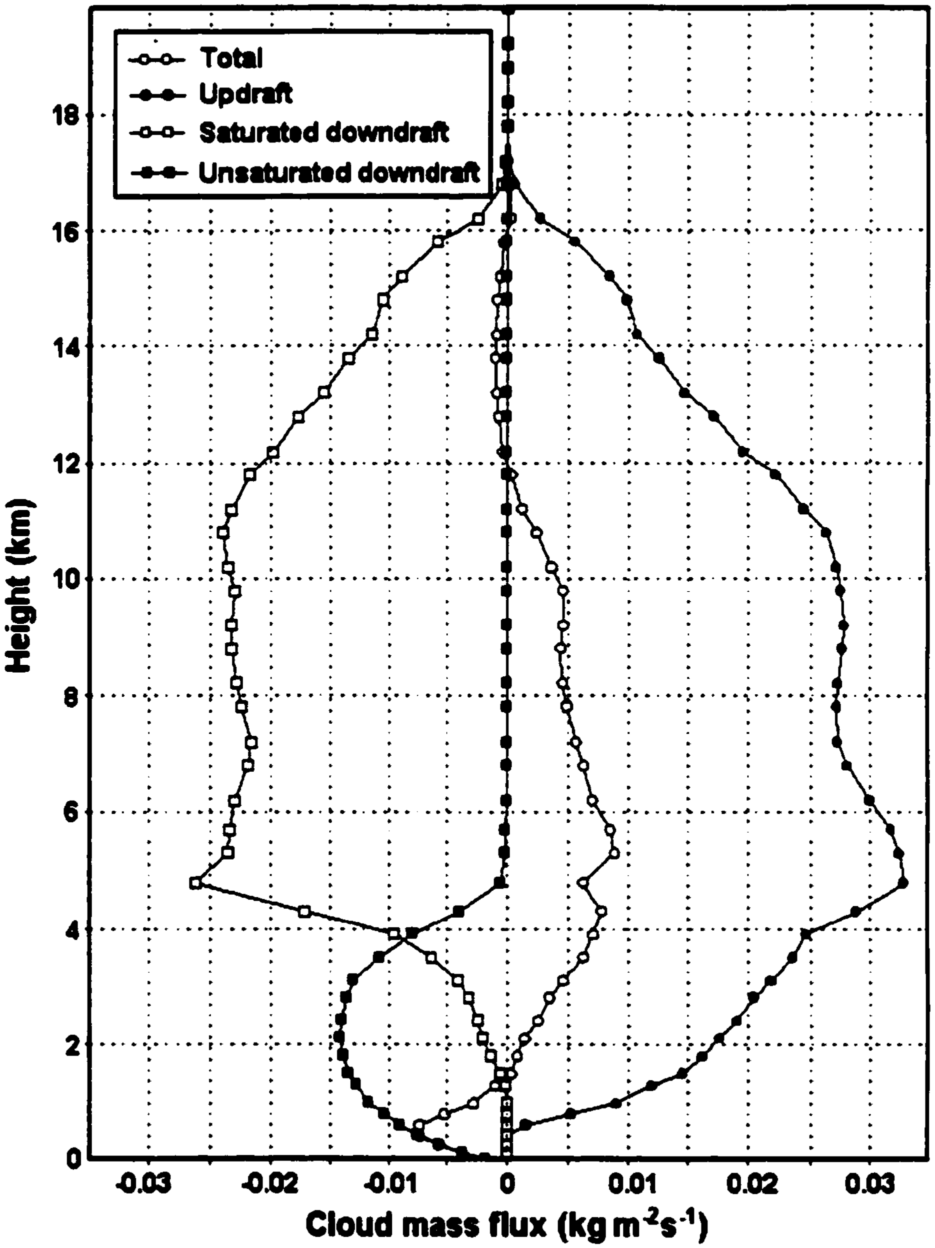

Figure 5.8 - 6-day (between 20 and 26 December) averaged cloud mass fluxes (CONTROL) in kgm^{-2}s^{-1}

5.2 – Statistical significance

In order to verify the statistical significance of CONTROL a small ensemble of similar runs was constructed. The difference among CONTROL and those four runs (hereafter referred to as ENS1, ENS2, ENS3 and ENS4) resides in the random temperature perturbations imposed to the temperature field. As will be demonstrated in this Section, despite the differences in the individual evolution of each one of those simulations, their statistics are strikingly similar.

As to illustrate the diversity of the individual unfolding of convection in each of the ENSn, Figures 5.9 to 5.12 depicts the total condensate mixing ratio produced by each of them, in particular times (00UTC, on 20 to 25 December 1992). The contour interval in those Figures is 0.5 g kg^{-1}, and mixing ratios greater than 1.0 g kg^{-1} are represented by shading. As shown in the first panel in Figures 5.9 to 5.12, the evolution of the cloud systems is similar in all realizations within the ensemble, with convective clouds emerging from a deck of transient stratiform clouds after the first 24 hours of simulation. The following snapshots show, at times, the development of more organized convection. Eventually, they also show growing or decaying convective clouds.

In general, however, the evolution of the domain-averaged quantities was very similar. This is expected, due to the fact that the tropical atmosphere tends to adjust itself to a profile close to the moist adiabatic. Hence, the statistical properties of convection (which accounts for the consumption of CAPE and the consequent "quasi-moist adiabatic

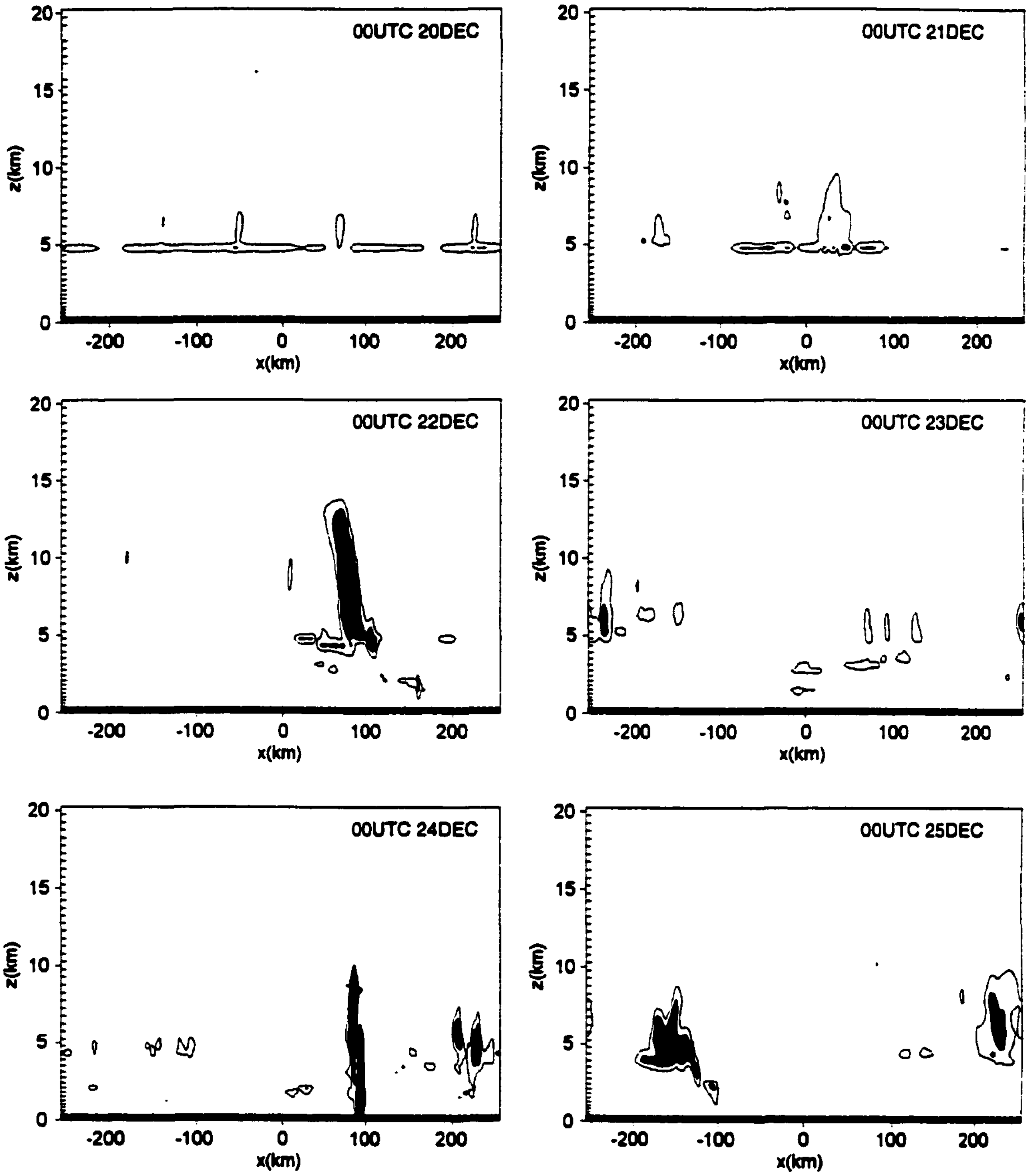

Figure 5.9 – Total condensate mixing ratio (in g kg^{-1}) for ENS1, on 00UTC 20 to 25 December 1992. Contour interval is 0.5 g kg^{-1}. Mixing ratios greater than 1.0 g kg^{-1} are shaded.

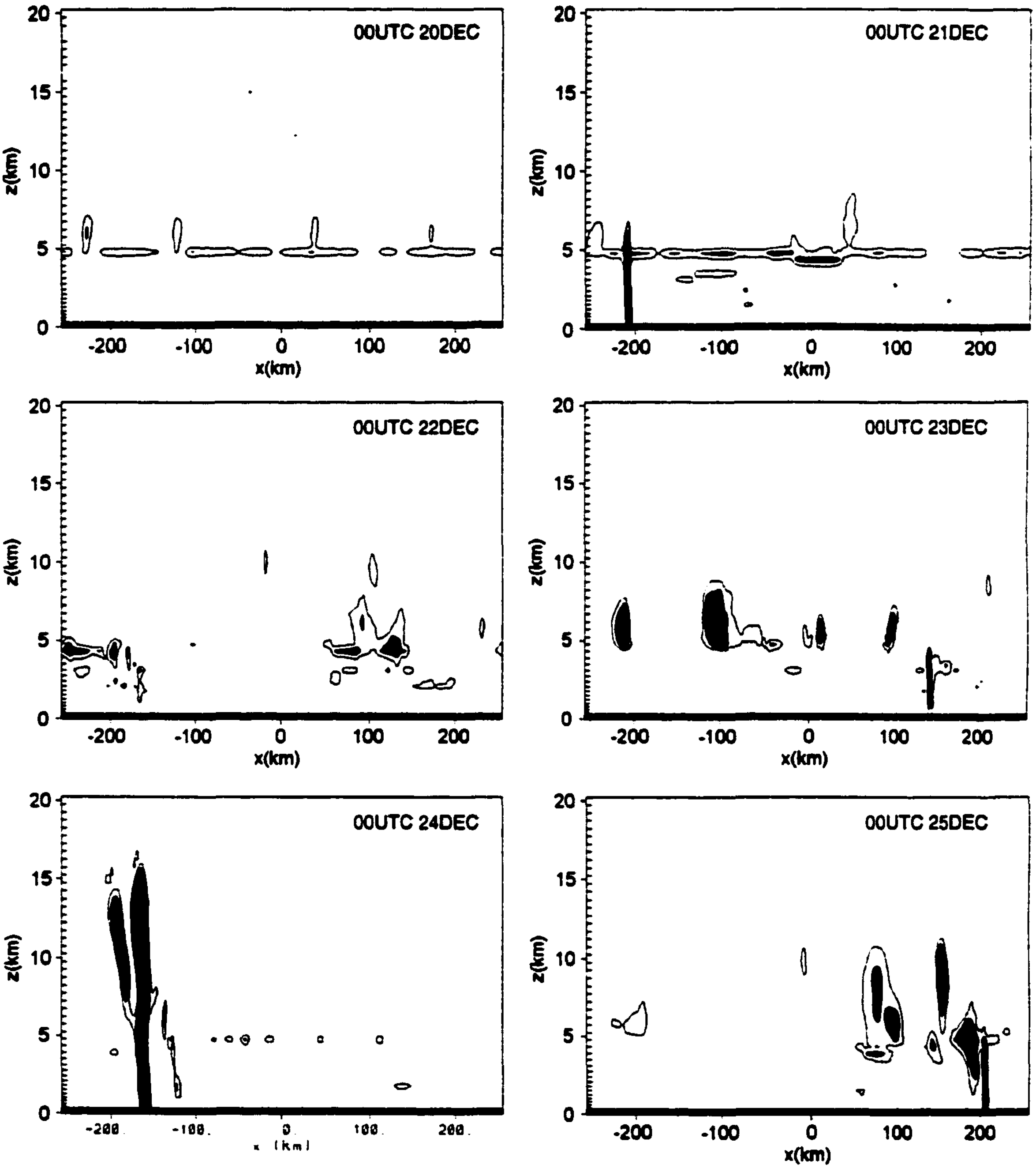

Figure 5.10 – Same as Figure 5.9, except for ENS2

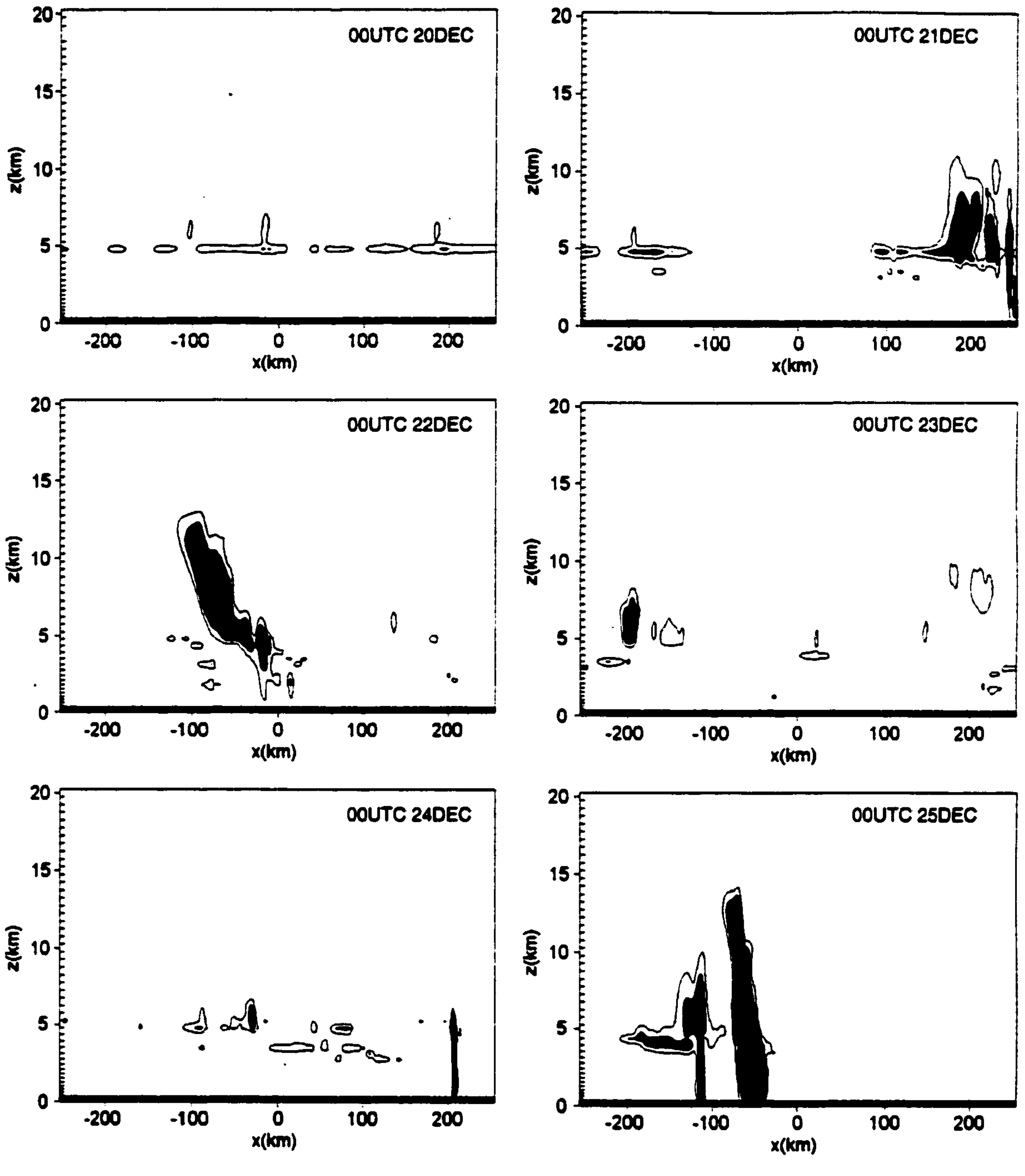

Figure 5.11 – Same as Figure 5.9, except for ENS3

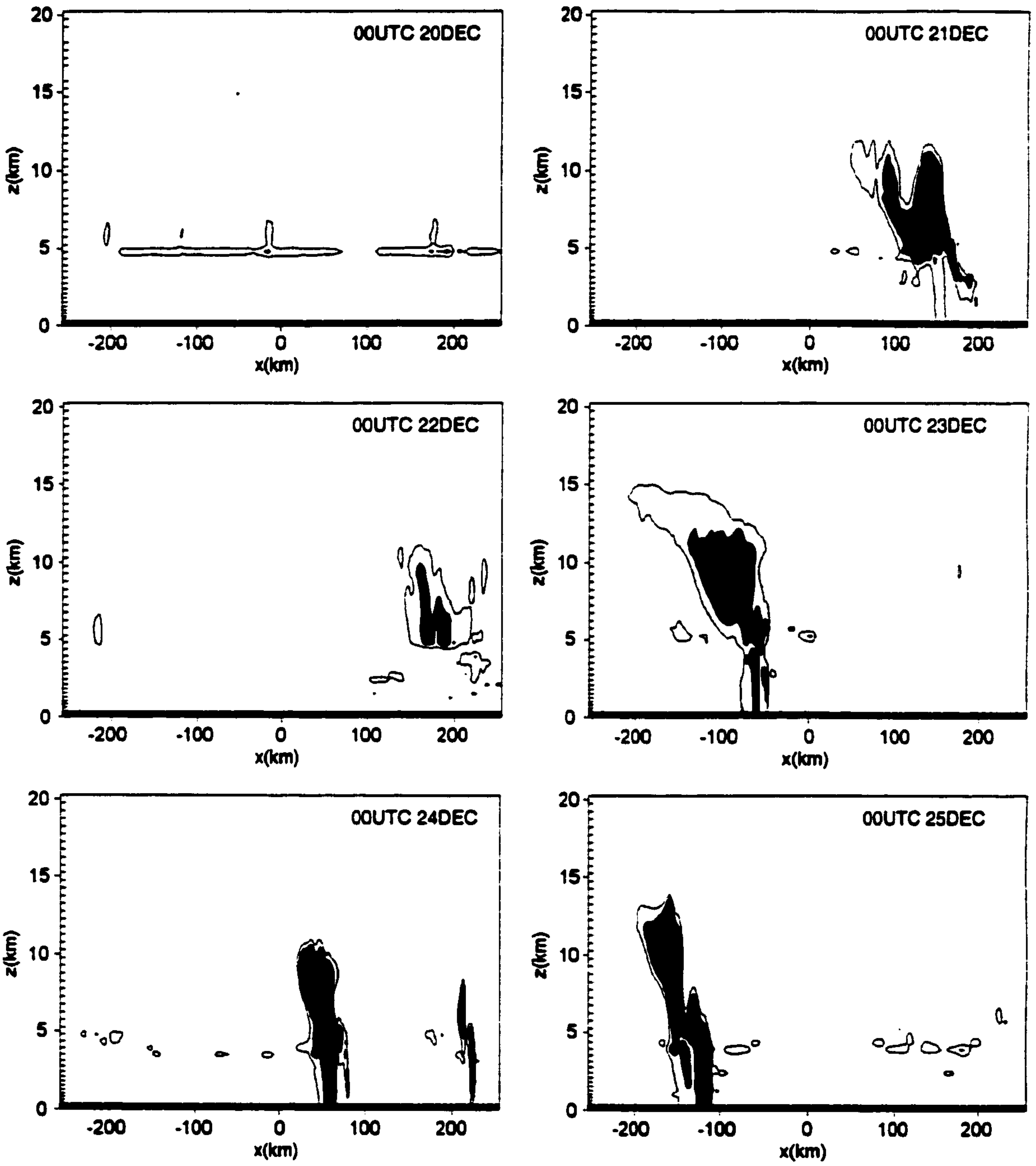

Figure 5.12 – Same as Figure 5.9, except for ENS4

adjustment") must obey the imposed large-scale forcing, regardless of the actual evolution of the convective systems. Particularly in a case of strong forcing on the large scale, multi-day CRM simulations are expected to be robust in terms of their statistics.

The evolution of the domain-averaged total surface precipitation in ENS1 to ENS4 is shown in Figure 5.13. The strong temporal variability shown in Figure 5.13 (contrasting with the much smoother 6h moving average of the precipitation in CONTROL shown in Figure 5.2) is a well-known characteristic of two-dimensional CRM simulations of convection (e.g., Grabowski et al., 1998). The same sort of variability appears in other variables, such as convective and stratiform precipitation, latent and sensible heat fluxes, radiative fluxes, etc. In an average sense, however, those variables exhibited very close values in ENS1 to ENS4, as well as in CONTROL, as shown in Table 5.2.

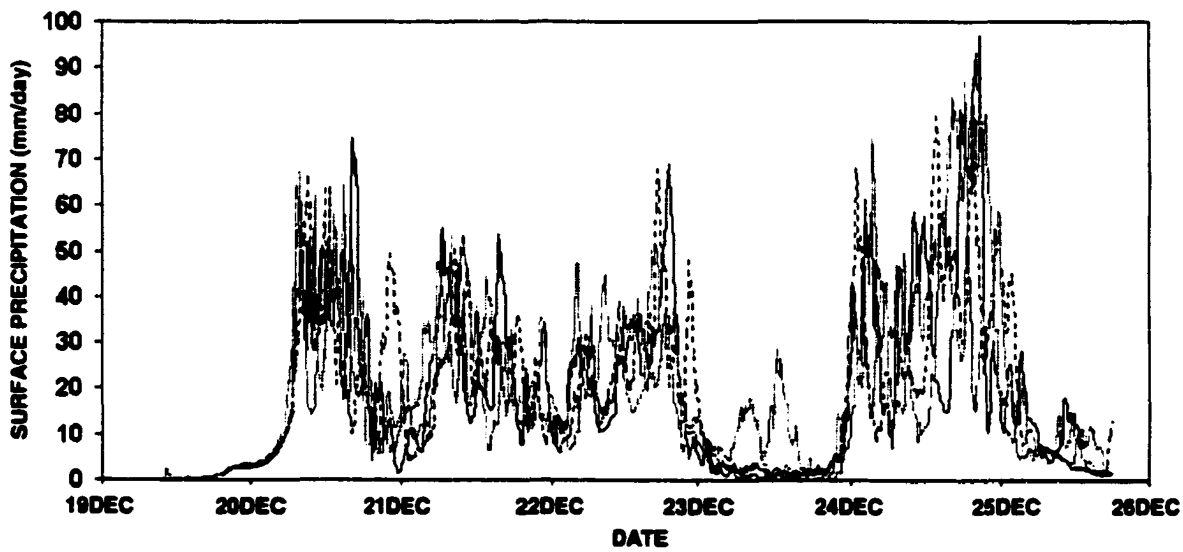

Figure 5.13 – Time evolution of the domain-averaged surface precipitation, in mm day^{-1}, between 19 and 26 December 1992, for the simulations ENS1 (black line), ENS2 (dotted line), ENS3 (dashed line) and ENS4 (gray line)

Variable	CONTROL	ENS1	ENS2	ENS3	ENS4	Standard deviation
Total precipitation (mm/day)	21.19	21.22	21.02	20.94	21.01	0.11 (0.5%)
Convective precipitation (mm/day)	15.25	15.01	15.16	14.77	15.03	0.16 (1.1%)
Stratiform precipitation (mm/day)	5.94	6.21	5.86	6.17	5.98	0.14 (2.2%)
Latent heat flux (Wm^{-2})	132.81	134.87	133.25	132.31	133.51	0.74 (0.6%)
Sensible heat flux (Wm^{-2})	18.63	18.57	18.73	18.49	18.47	0.10 (0.5%)
Downward solar radiation (Wm^{-2})	122.62	118.44	125.81	136.19	132.20	3.45 (2.7%)
Downward IR radiation (Wm^{-2})	412.00	412.87	413.66	414.05	412.52	0.75 (0.2%)
Upward solar radiation (Wm^{-2})	7.36	7.11	7.55	8.17	7.93	0.21(2.7%)
Upward IR radiation (Wm^{-2})	469.45	469.45	469.45	469.45	469.45	0.00 (0.0%)

Table 5.2 – Time average of some domain-averaged quantities for simulations CONTROL and ENS1 to ENS4. Precipitation-related variables were averaged between 20 and 26 December. Other variables were averaged in the entire 7-day simulation period. The value in parenthesis shown in the last column is the percentage of the standard deviation with respect to the average for the five simulations.

The greatest variability found in Table 2 was found in the shortwave radiation. The 7-day average incoming solar radiation depends mostly on how the clouds are distributed during the three to four hours around the time of maximum insolation. In contrast, the average of the other fields reflects the behavior of the cloud systems during the whole period of simulation. In general, the results from this collection of simulations suggest that any single realization within the ensemble can be used as a benchmark.

5.3 - Role of the SST magnitude

Two sensitivity experiments were performed in which the SST trend shown in Figure 3.6 was maintained, but the actual SST value was reduced (SST- simulation) or increased (SST+ simulation) by 1°C. In both simulations, as in CONTROL, the sea surface temperature was spatially homogeneous.

The evolving atmospheric large-scale forcing in SST- and SST+ was the same used to drive the CRM in CONTROL. Of course, from the point of view of the large-scale circulation, one expects that such a forcing will depend, in fact, on the SST field. For instance, contrary to common sense, Betts and Ridgway (1989) and Betts (1998) point out that the mass circulation in the tropics would decrease for warmer SSTs. As shown by Wu and Moncrieff (1999), there was no simple relation between the evolution of the SST and the thermal large-scale forcing over the TOGA-COARE IFA. However, the utilization of the same large-scale to drive all simulations, although not completely realistic, is useful. It allows us to evaluate the sensitivity of the organization of cloud systems with respect to SST only at the time and spatial scale of the convective systems themselves. Indeed, the use of the same large-scale forcing compelled the cloud systems in both SST- and SST+ to behave close to the ones in CONTROL.

5.3.1 – SST- simulation

The cold, dry bias described in Section 5.1 was exacerbated in this simulation - a consequence of reduced surface heating and moistening. Figure 5.14 shows the difference between the model temperature (panel a) and water vapor mixing ratio (panel b) in simulations SST- and CONTROL. Temperature differences larger than 1 degree and mixing ratio differences close to $1gkg^{-1}$ were observed.

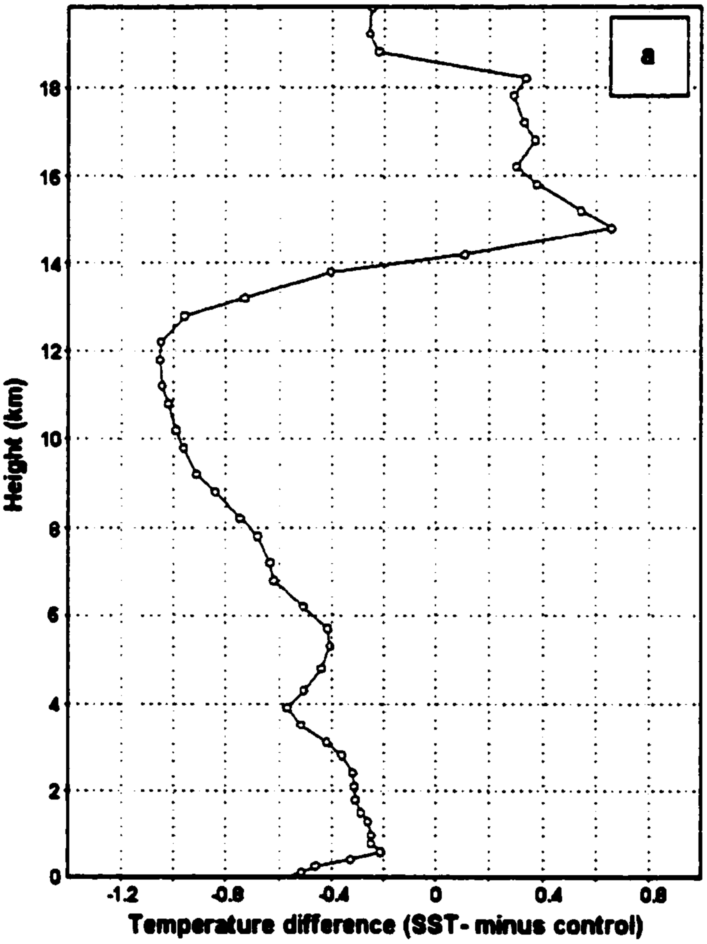

Figure 5.14 - Difference between SST- and CONTROL: (a) temperature, in °C and (b) water vapor mixing ratio, in gkg^{-1}

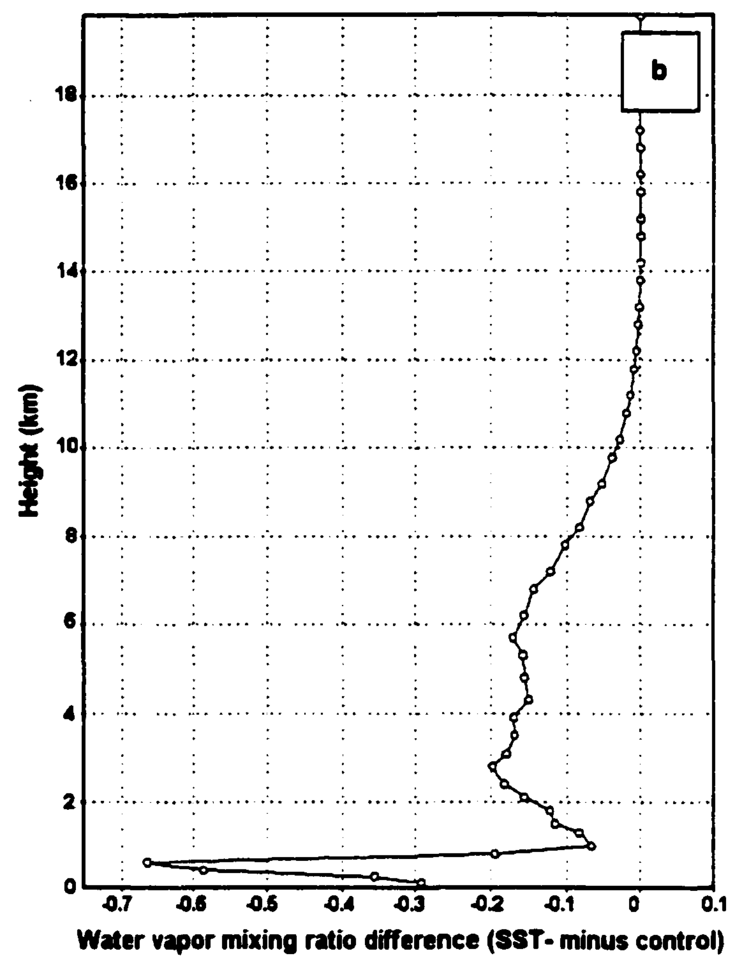

Figure 5.14 - continuation

The evolution of the domain-averaged total condensate field is quite similar to that in CONTROL, which suggests that the large-scale forcing plays a major role in determining the characteristics of tropical cloud systems. Some differences between the cloud systems in SST- and CONTROL were observed, though. The maximum in the total cloud mass flux is smaller by about 3% in SST-. Cloud water maxima are more persistent, rainwater peaks are slightly less pronounced, and the amount of ice is smaller in SST- than in CONTROL (Figure not shown). The 6-day averaged total condensate field and cloud fractional area in SST- exhibit some important departures from what was observed in CONTROL. There was an excess of condensate in SST-, in the form of cloud water, from above the boundary-layer up to the melting level, that is, on average, as high as 0.044 gkg^{-1}, which is very significant in terms of a domain average. Oppositely, in upper-levels, SST- exhibited a deficit of low-density ice, of the order of 0.026 gkg^{-1} at 13 km (Figure 5.15).

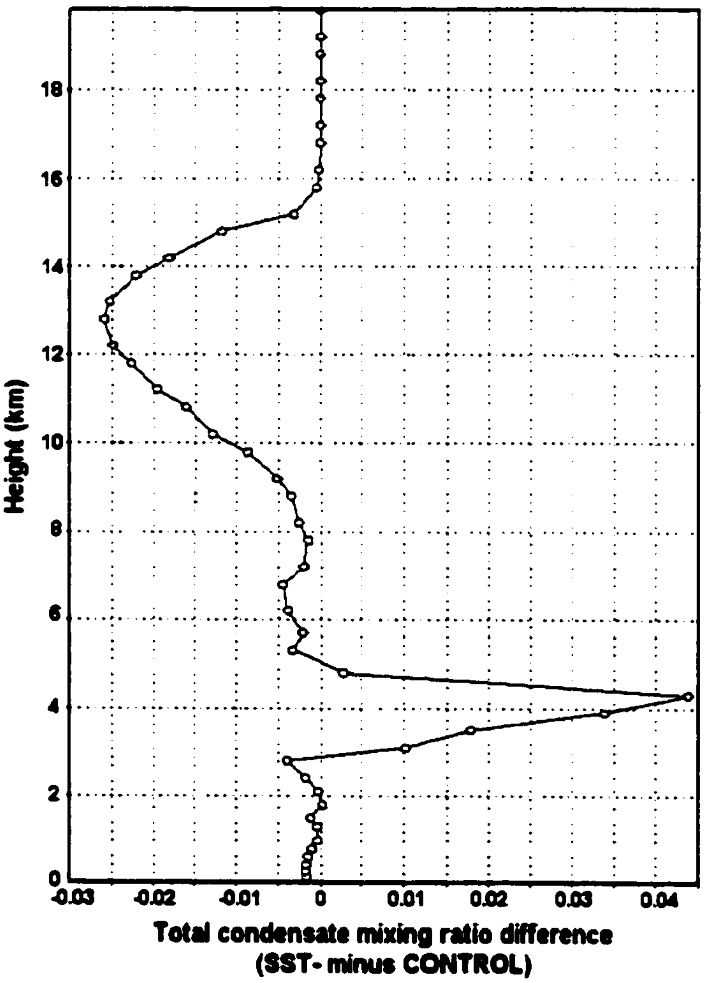

Figure 5.15 - Difference between SST- and CONTROL total condensate mixing ratio, in gkg^{-1}

In terms of cloud coverage, at most levels there were more clouds in SST- than in CONTROL. Below the melting level, at approximately 4.5 km height, the cloud fraction in SST- surpassed the one in CONTROL by as much as 10%. In contrast, at high-levels, due to the weakened convective transport, less ice was detrained from the top of the cloud systems, and the cloud fractional area associated with anvil clouds was reduced by more than 4% (Figure 5.16).

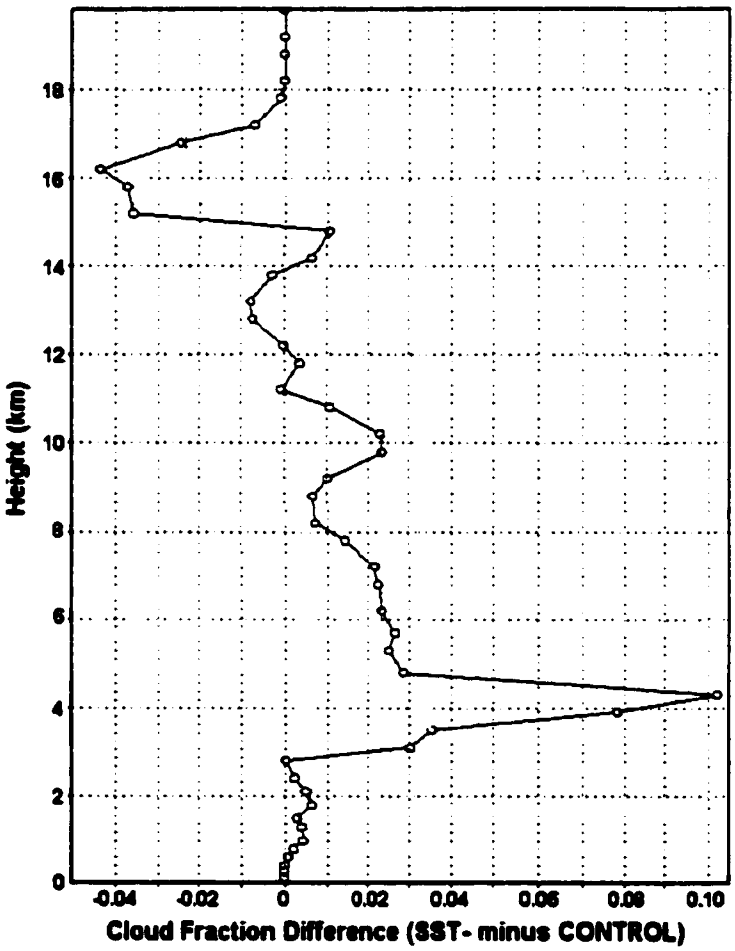

Figure 5.16 - Difference between SST- and CONTROL cloud fractional area, dimensionless

5.3.2 – SST+ simulation

Most of the differences between SST- and CONTROL also occurred between SST+ and CONTROL, with an opposite sign. The cold, dry bias was reduced in SST+ (Figure 5.17).

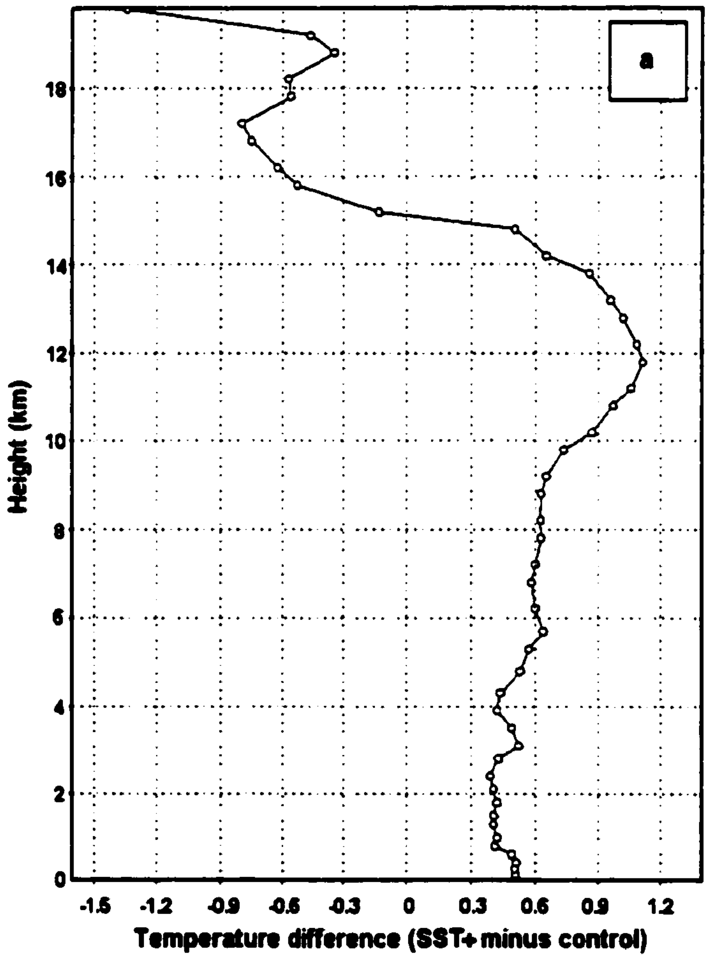

Figure 5.17 - Difference between SST- and CONTROL: (a) temperature, in °C and (b) water vapor mixing ratio, in gkg^{-1}

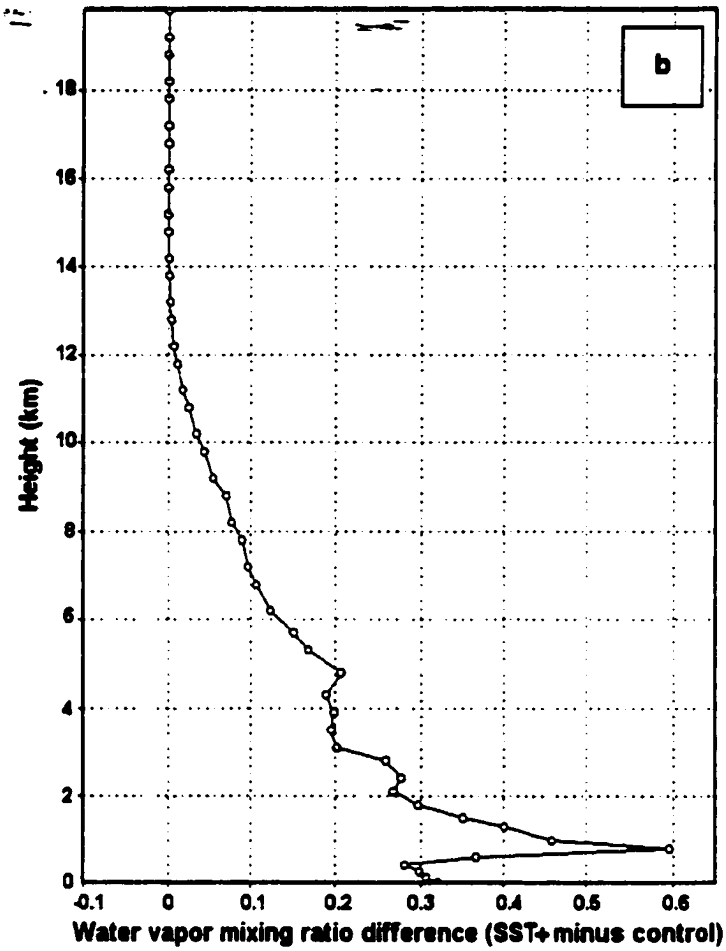

Figure 5.17 - continuation

Cloud water maxima were less steady and rainwater maxima were sharper. On average, the high-density ice mixing ratio, although still small, was greater in SST+ than in SST- and CONTROL. Aspects of the average behavior of the cloud systems in SST+ are depicted in Figures 5.18 and 5.19. The 7-day averaged total condensate mixing ratio was higher than in CONTROL through all the middle and upper troposphere, with an average excess of $0.008gkg^{-1}$. In contrast, at low levels, SST+ produced less condensate than CONTROL (maximum deficits of about $0.007gkg^{-1}$). SST+ presented about the same cloud coverage as CONTROL in most of the troposphere, with few exceptions. Above the boundary-layer and below the melting level there was a modest deficit in the cloud coverage (of the order of 2%), in opposition to the cloud fractional area excess observed in SST-. Conversely, more cloud coverage was found in the upper troposphere in association with more vigorous ice detrainment through anvil clouds. The average excess in the cloud fractional area aloft was as high as 18%, in contrast with the high-level cloud coverage deficit that occurred in SST-.

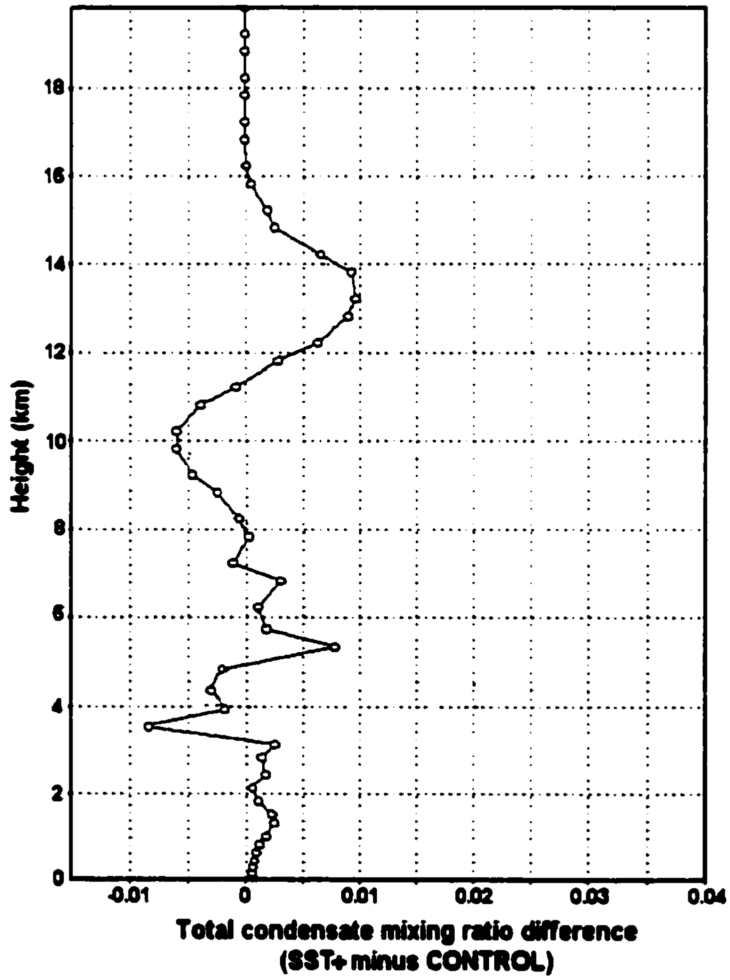

Figure 5.18 - Difference between SST+ and CONTROL total condensate mixing ratio, in gkg^{-1}

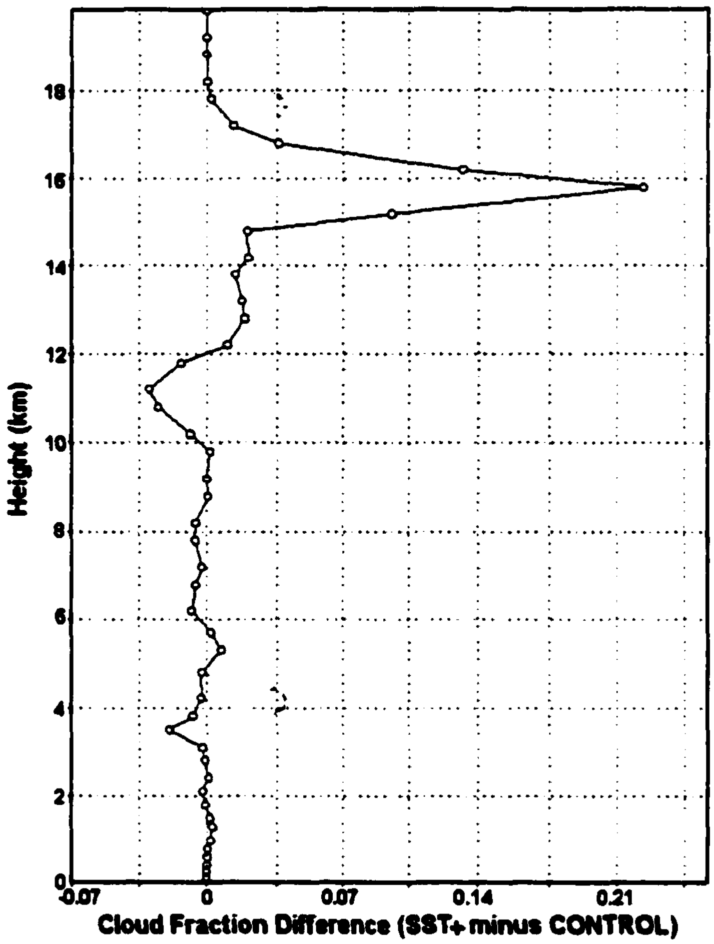

Figure 5.19 - Difference between SST+ and CONTROL cloud fractional area, dimensionless

5.3.3 – Heat fluxes, convective-stratiform partition

As expected, on average both sensible and latent heat fluxes increased as the sea surface temperature increased, i.e., SST+ showed the greatest fluxes, followed by CONTROL and SST- (Figure 5.20). In percentage terms, such hierarchy was more obvious at the beginning of the simulated period. However, as the simulations progressed, the CRM acted to reduce the relative differences in the heat fluxes. This might suggest that the model attempted to adjust the surface fluxes to the imposed large-scale forcing when convection occurs.

One could expect that the enhancement of the surface fluxes should increase the speed of the "precipitation engine", but the contribution from the increased or reduced evaporation was small in our CRM simulations. In fact, CONTROL, SST- and SST+ presented similar values of total precipitation, with the total precipitation in SST+ exceeding the one in SST- by less than 6%. Again, this reflects the strong control of the prescribed large-scale forcing on simulated precipitation. The results suggest that, at least for the simulated regime, there is only a weak direct relation between surface temperature and precipitation rates. Such a connection may be a multi-step process, involving surface parameters (as the SST), surface fluxes, large-scale circulation and precipitation. The present CRM results also suggest that, in fact, it is the large-scale circulation that determines the precipitation rate, although the large-scale forcing itself can be affected by the surface conditions over a greater scale. This is consistent with the premise behind many cumulus parameterizations such as the Arakawa-Schubert scheme (Arakawa and Schubert, 1974) and its cousins (Shrinivas and Suarez, 1992; Wang and Randall, 1996; Cheng and Arakawa, 1997; Pan and Randall, 1998; Ding and Randall, 1998).

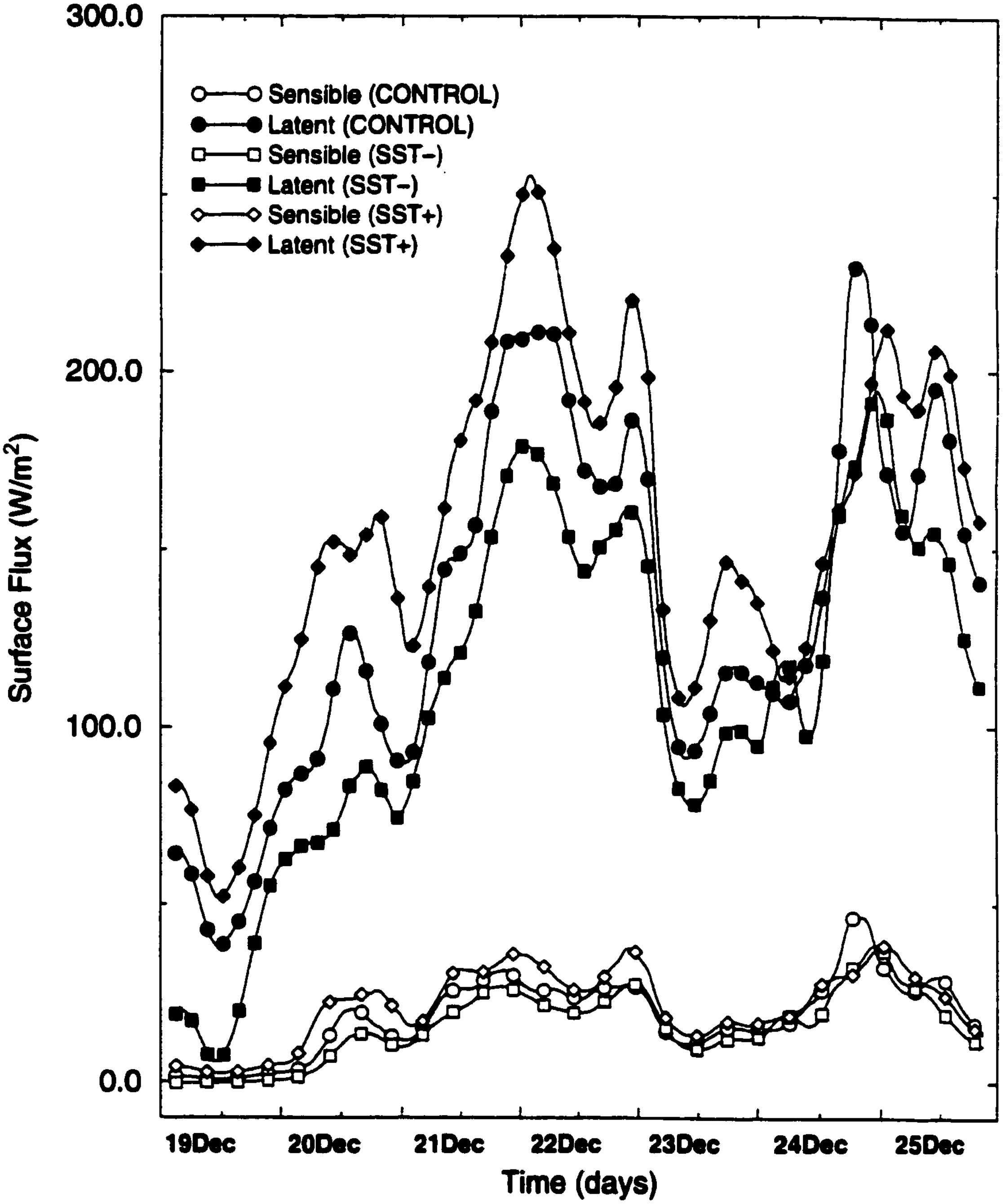

Figure 5.20 - Sensible and latent heat fluxes in CONTROL, SST- and SST+, in Wm^{-2}

If the sensitivity of the total precipitation to the SST changes was small, a more remarkable difference was observed on how the precipitation was produced in SST- and SST+. Table 5.3 shows the 6-day averaged model convective and stratiform precipitation and the convective and stratiform fractional area for those two simulations. It was observed that a significant growth in the convective component of the precipitating systems occurred as the SST increased. One possible explanation is that the enhanced (suppressed) surface fluxes, associated with warmer (cooler) SSTs, can generate more (less) vigorous thermals in the boundary-layer that can eventually generate more (less) deep convective elements. The more (less) pronounced subsidence related to more (less) vigorous convection and associated cloud mass fluxes account for the reduction (increase) in low-level cloud coverage in SST+ (SST-). Despite the obvious differences, such a mechanism is, in essence, similar to that observed by Krueger et al. (1995) and Wyant et al. (1997) in their simulations of marine stratocumulus, in which higher SSTs favored cumulus convection and inhibited the development of stratiform clouds.

Variable	**SST-**	**SST+**
Convective precipitation	14.1 mmday^{-1} (69.1% of the total)	16.6 mmday^{-1} (76.4% of the total)
Stratiform precipitation	6.3 mmday^{-1} (30.9% of the total)	5.1 mmday^{-1} (23.6% of the total)
Total precipitation	20.4 mmday^{-1}	21.7 mmday^{-1}
Convective fractional area	0.2860	0.3350
Stratiform fractional area	0.4574	0.4017
Total rainy fractional area	0.7434	0.7367

Table 5.3 - 6-day averages of the convective and stratiform precipitation, convective and stratiform fractional area in CONTROL, SST- and SST+.

In order to illustrate the differences in the updrafts and downdrafts in CONTROL, SST- and SST+, it is appropriate to use the definition of the "core updraft" and "core downdraft" velocities. In our simulations, a "core" is defined as a contiguous set of model points in which the absolute value of the vertical velocity exceeds $1ms^{-1}$. The domain-averaged updraft velocity at a certain time is simply the vertical velocity averaged over the points in which it exceeds $1ms^{-1}$. If, at a given time, the vertical velocity is smaller than this value everywhere in the domain, the domain-averaged updraft velocity is set to zero. The domain-averaged downdraft velocity follows a similar definition. Figure 5.21 depicts the 6-day mean of the domain-averaged updraft and downdraft velocities. It is clear that more vigorous updrafts, as well as a stronger compensating subsidence, occurs in association with higher SSTs. This is consistent with a greater 7-day averaged CAPE in SST+ (1129 Jkg^{-1}) and a smaller CAPE in SST- (966 Jkg^{-1}), with an intermediate value found in CONTROL (1039 Jkg^{-1}).

5.3.4 - Radiative fluxes

Ramanathan and Collins (1991) proposed that there exists a negative feedback between deep convection and SST: convection developing over warm SSTs would produce cirrus clouds that would block the solar radiation, leading to a cooling of the ocean surface. In opposition, several authors contested this "cirrus-thermostat hypothesis" (for instance, Fu et al., 1992 and Wu and Moncrieff, 1999). Controversy still persists on this subject.

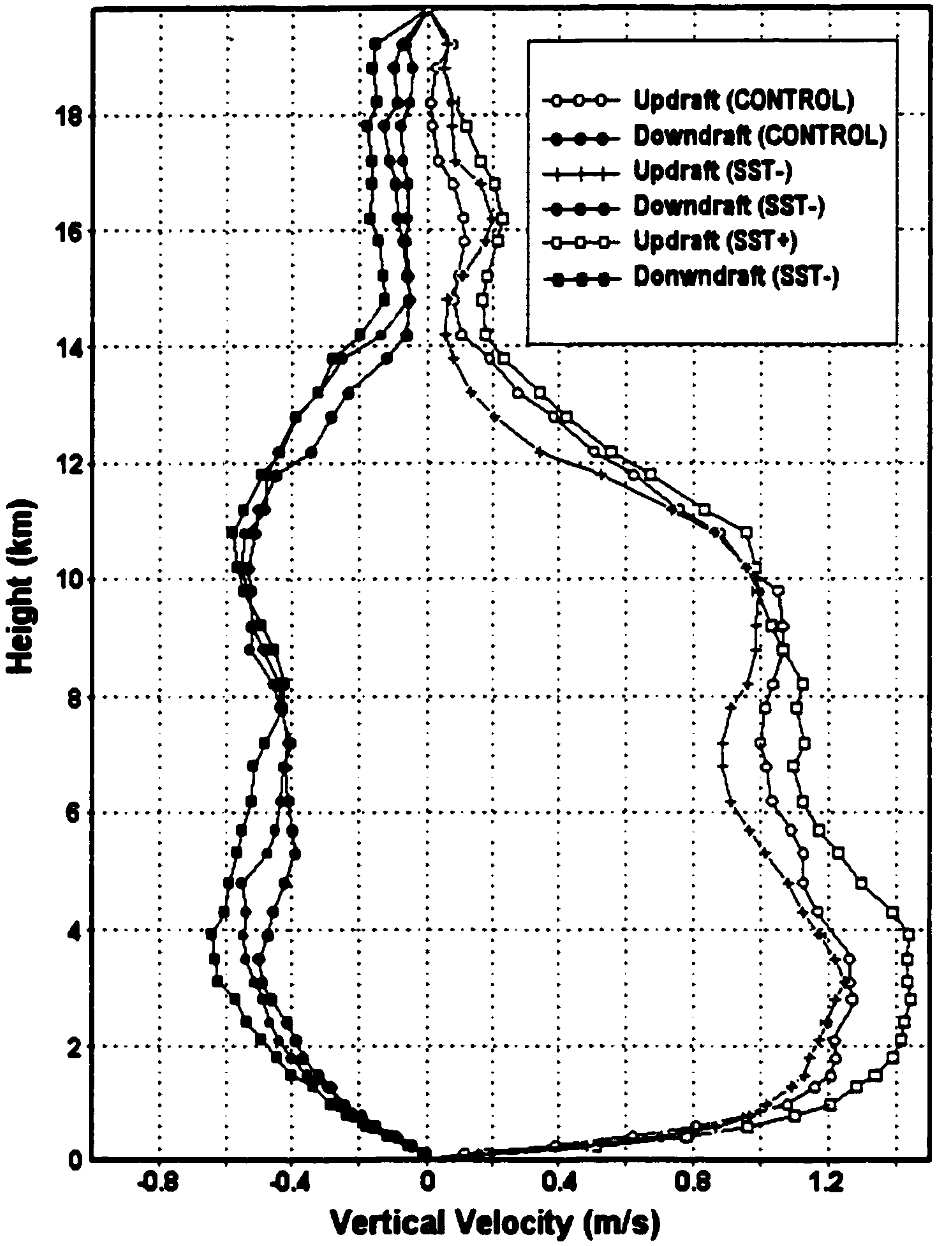

Figure 5.21 - 6-day (between 20 and 26 December) averaged core updraft and core downdraft velocities (CONTROL, SST- and SST+). See text for details.

In the present simulations, the influence of the organization of the cloud systems on the radiative budget was small (Table 5.4). Both the variations in the net radiative surface flux and the surface downward shortwave radiation were small compared to the changes in the surface latent heat flux. Therefore, this indicates that the extraction of heat from the surface by the turbulence fluxes can be an effective regulator of the SSTs in the tropics. Although, in our simulations, more high-level clouds were produced as the SST increased, the results in Table 5.4 suggest that the "cirrus-thermostat" account for a very small part of the regulation of the SSTs in the tropics, if any. In fact, the reduction in the downward shortwave radiation reaching the surface in SST+ is virtually balanced by an increase in the net longwave flux. Also, the structure of the cloud coverage in SST+ and SST- indicates the existence of a mechanism in opposition to the cirrus-thermostat. This mechanism is probably a positive boundary-layer cloud feedback similar to the one found in the stratocumulus-to-cumulus transition regime, i.e., more (less) boundary-layer cloud coverage is produced over colder (warmer) SSTs.

Numerical experiment	7-day averaged net surface radiative flux (Wm^{-2})	7-day averaged downward shortwave radiative flux (Wm^{-2})	7-day averaged surface latent heat flux (Wm^{-2})
CONTROL	66.8	132.2	132.9
SST-	73.4	135.2	109.2
SST+	62.6	128.0	154.7

Table 5.4 - 6-day averages of the net surface radiative flux and the surface downward shortwave radiative flux. Positive values indicate downward flux.

According to the present results, other factors than the blocking of solar radiation by cirrus clouds can play a more significant role to limit the values of the tropical ocean surface temperatures. Among those factors are the longwave radiation and, more important, the cooling associated with the turbulent fluxes. Considering the contribution from other mechanisms ("dynamic thermostat", e.g., Clement et al., 1996), the picture that emerges is one of a very complex regulation mechanism for the tropical SSTs. CRM simulations coupled to an ocean model, so the surface temperature would be allowed to evolve, can provide useful information on that subject. It is clear that the construction of a comprehensive conceptual model for the SST regulation is still incomplete and will require further investigation.

5.4 - Role of SST inhomogeneities

Three sensitivity experiments were performed in which the mean SST was the same as in CONTROL (Figure 3.6), with a superimposed sinusoidal SST perturbation with a one-degree amplitude. Three different perturbations were tested, corresponding to "large" (256km, LARGE simulation), "medium-sized" (64km, MEDIUM simulation) and "small" (16km, SMALL simulation) wavelengths.

As in the previous set of simulations, most of the collective characteristics of the modeled convective systems were determined by the imposed large-scale forcing. Since, on average, the input of heat and moisture from the surface in LARGE, MEDIUM and SMALL were very similar to the ones in CONTROL, the differences in the domain-averaged temperature and moisture fields were even less than in SST+ and SST-. This is no surprise, since a sinusoidal perturbation integrates to zero for an integer number of wavelengths.

The vertical structure of the 6-day mean of the domain-averaged cloud fields (various species of condensate, cloud fractional area, total cloud mass flux) was also very similar, and no significant sensitivity was observed.

Table 5.5 indicates the total, convective and stratiform precipitation in LARGE, MEDIUM and SMALL, as well as their respective rainy, convective and stratiform fractional areas. In all the simulations with heterogeneous SSTs, less precipitation was produced than in CONTROL. The relative contributions of convective and stratiform columns to the precipitation were also influenced by the horizontal dimension of the SST inhomogeneities, although the differences were only slightly bigger than the variability found in the ensemble of multiple realizations of the CONTROL simulation, described previously. In particular, LARGE exhibited more stratiform precipitation, while MEDIUM shows more convective rainfall.

Variable	LARGE	MEDIUM	SMALL
Convective precipitation	14.2 mmday^{-1} (70.0% of the total)	14.8 mmday^{-1} (73.6% of the total)	14.7 mmday^{-1} (71.7% of the total)
Stratiform precipitation	6.1 mmday^{-1} (30.0% of the total)	5.3 mmday^{-1} (26.4% of the total)	5.8 mmday^{-1} (28.3% of the total)
Total precipitation	20.3 mmday^{-1}	20.1 mmday^{-1}	20.5 mmday^{-1}
Convective fractional area	0.2765	0.2773	0.3002
Stratiform fractional area	0.4300	0.4447	0.4256
Total rainy fractional area	0.7065	0.7220	0.7258

Table 5.5 - 6-day averages of the convective and stratiform precipitation, convective and stratiform fractional area in LARGE, MEDIUM and SMALL.

Despite the similarities in most of the global characteristics of the cloud systems (constrained by the imposed large-scale forcing), including the total rainfall, there were noticeable differences in LARGE, MEDIUM and SMALL, related to the organization of the precipitation on the mesoscale in both time and space. That can explain most of the differences reported in Table 5.5. Figure 5.22 represents Hovmuller diagrams of the surface precipitation rate for the three simulations with inhomogeneous SSTs. The panel corresponding to MEDIUM (5.22b) has, in general, more small-scale structure, while in panel 5.22a, which shows the precipitation evolution in LARGE, coarse modes of the precipitation organization dominate. Apparently, SMALL does not show as many small-scale features as MEDIUM. All diagrams show two dominant modes of convection organization: one is the "convective mode", corresponding to individual convective cells propagating eastward; the other is the "mesoscale mode", corresponding to westward-propagating collectives of convective disturbances, which have stratiform precipitation from anvil clouds as their footprint. As seen in Figure 5.22, the mesoscale mode is inhibited in MEDIUM as compared to LARGE and SMALL. In particular, the systems formed after 3.5 and before 4.5 days of simulation look as if more westward-moving stratiform precipitation is present in LARGE and SMALL than in MEDIUM.

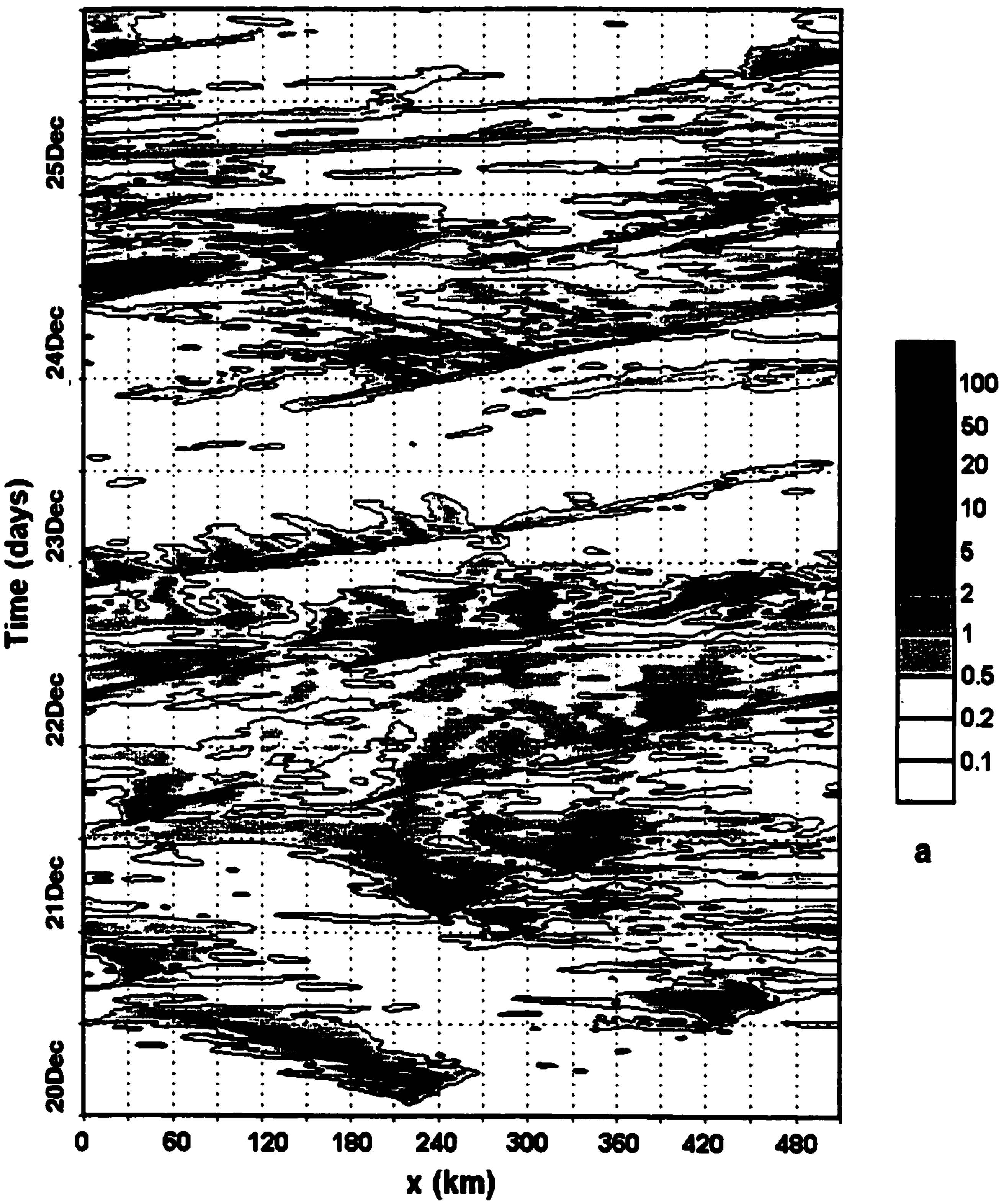

Figure 5.22 - Hovmüller diagrams of the surface precipitation: (a) LARGE, (b) MEDIUM and (c) SMALL. Gray levels represent different precipitation rates. The contour line represents $0.1 mmh^{-1}$

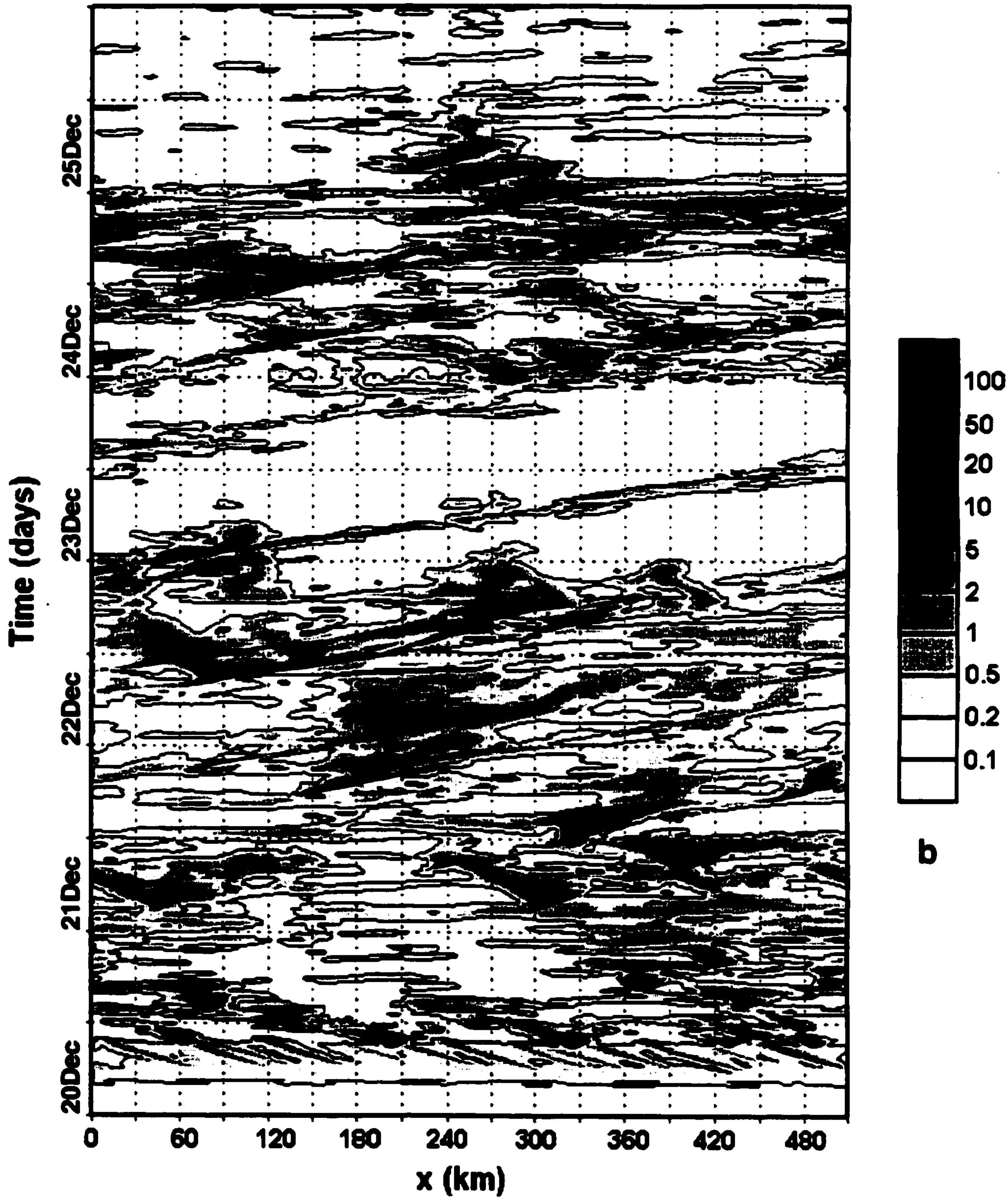

Figure 5.22 - continuation

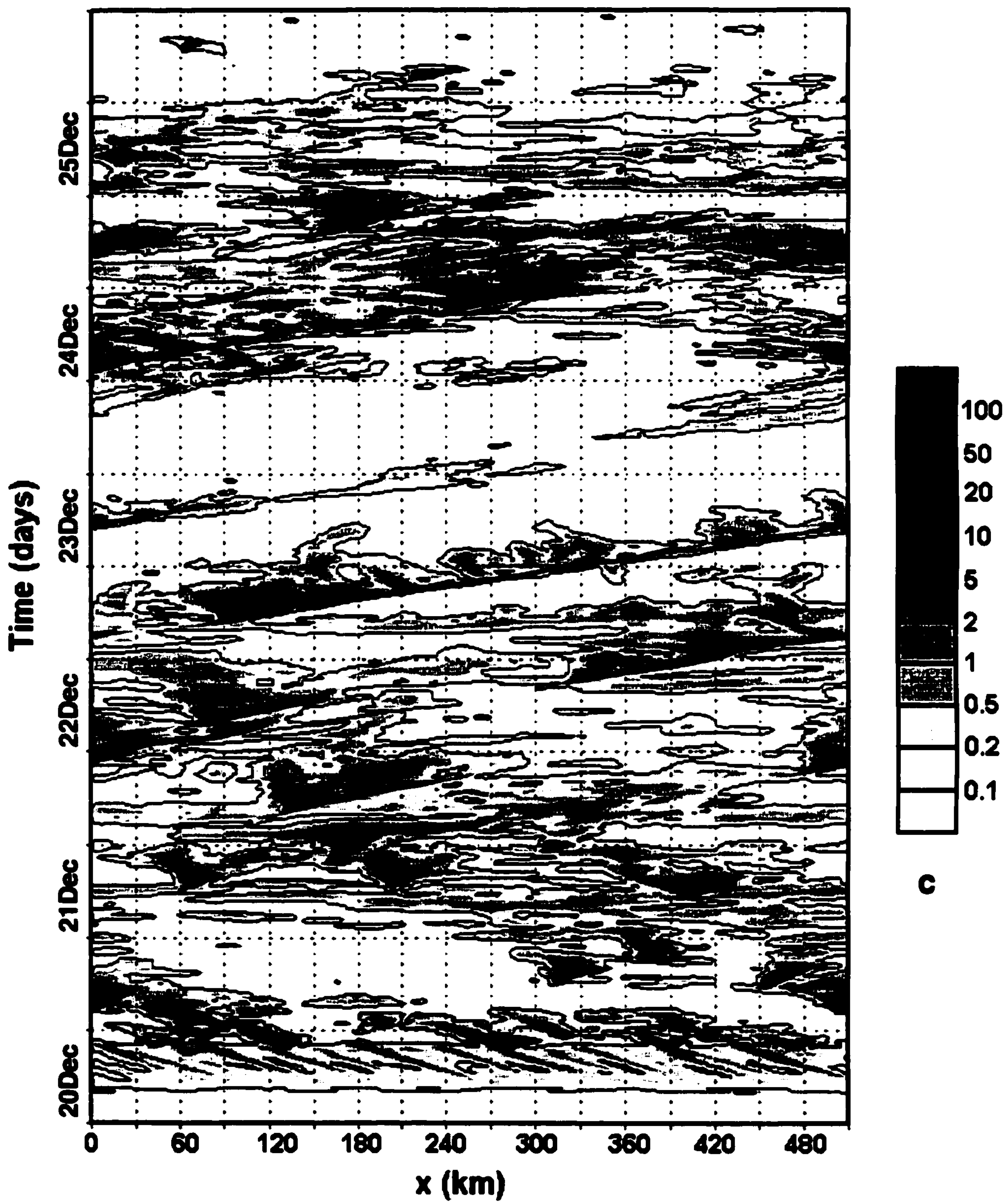

Figure 5.22 - continuation

Such differences become more evident in the spectral analysis of the precipitation patterns. The next set of plots represents two-dimensional spectral decompositions of precipitation fields in space and time. Figure 5.23 depicts the amplitude of the two-dimensional Fourier transform of the surface precipitation field for spatial scales between 2 and 500 km and temporal scales between 1 and 30h. The transform is given by:

$$\hat{P}(\kappa,\omega)=\alpha\iint P(x,t)e^{i(\kappa x-\omega t)}dxdt=\alpha\iint P(x,t)e^{i\left(\frac{2\pi x}{\lambda}-\frac{2\pi t}{T}\right)}dxdt \tag{5.1}$$

where P is the precipitation as a function of space and time, κ is the wavenumber, λ is the wavelength, ω is the frequency, T is the period and α is an arbitrary constant, set to $1.0\cdot10^{-4}(\mathrm{mm/day})^{-1}\mathrm{m}^{-1}\mathrm{s}^{-1}$, resulting in a non-dimensional $\hat{P}$.

The convective and mesoscale modes are not pure sinusoidal patterns. Hence, it is expected that all scales that fit into the model grid would appear in the transformation, in association with both of them (analogously, the transform of a square wave shows not only the contribution from its own wavelength, but also from the full range of smaller scales). The conclusion is that the direction of the mode propagation is a better criterion to separate the two modes. In Figure 5.23, westward-moving modes are represented by negative wavelengths, while positive wavelengths correspond to eastward propagation. The Fourier analysis shows that deep tropical convection has significant activity in a broad range of spatial scales between 10km (roughly the size of an individual cell) and the domain size, and timescales ranging on an order of an hour to greater than one day. This is obviously expected, since the actual organization of convection arises from the interaction between large, intermediate and small scales. It should be noted that there was an important contribution to the diurnal signal on the organization of convection in every case, with the possible exception of SMALL.

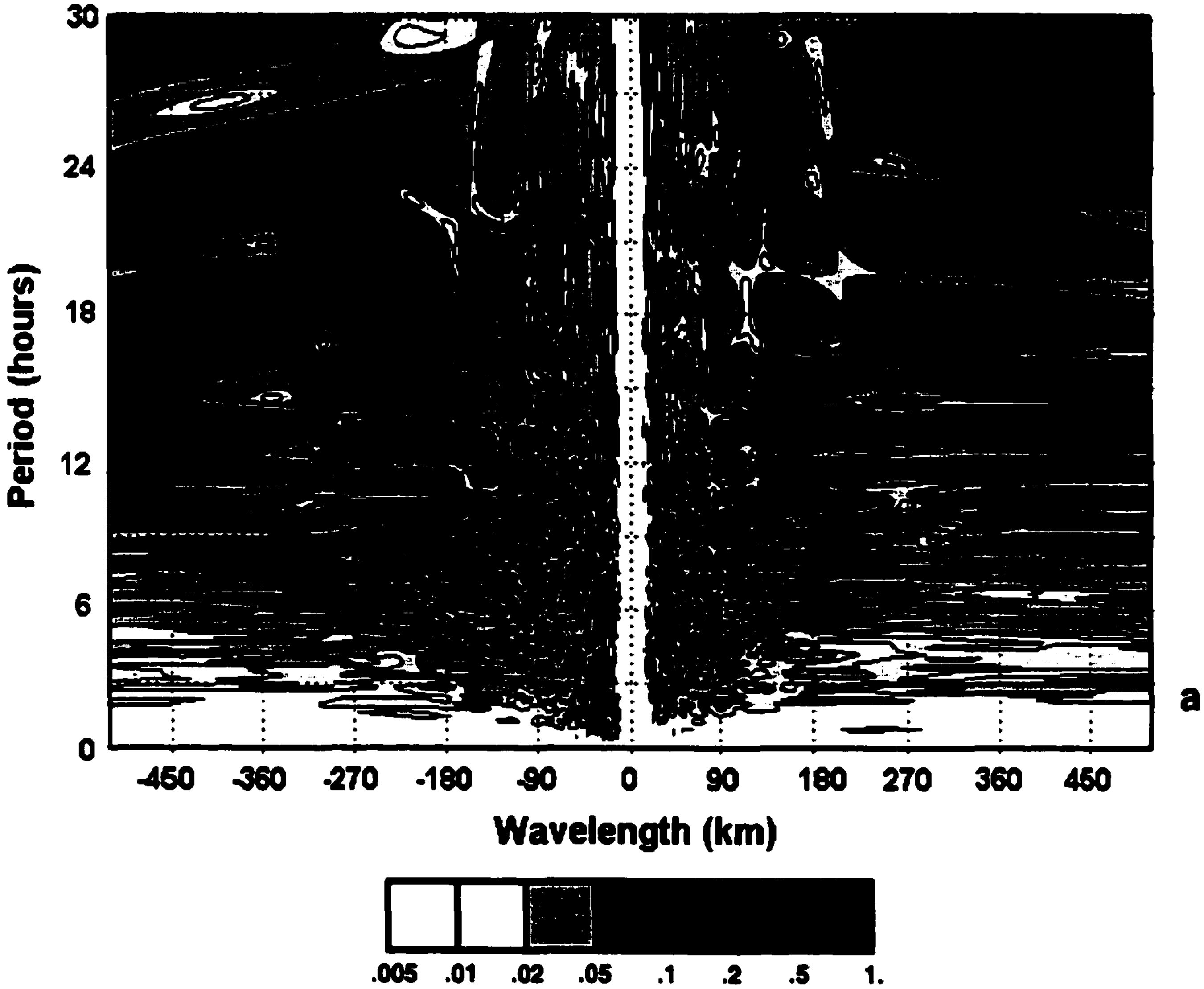

Figure 5.23 - Two-dimensional Fourier transformation of the surface precipitation: (a) LARGE, (b) MEDIUM and (c) SMALL.

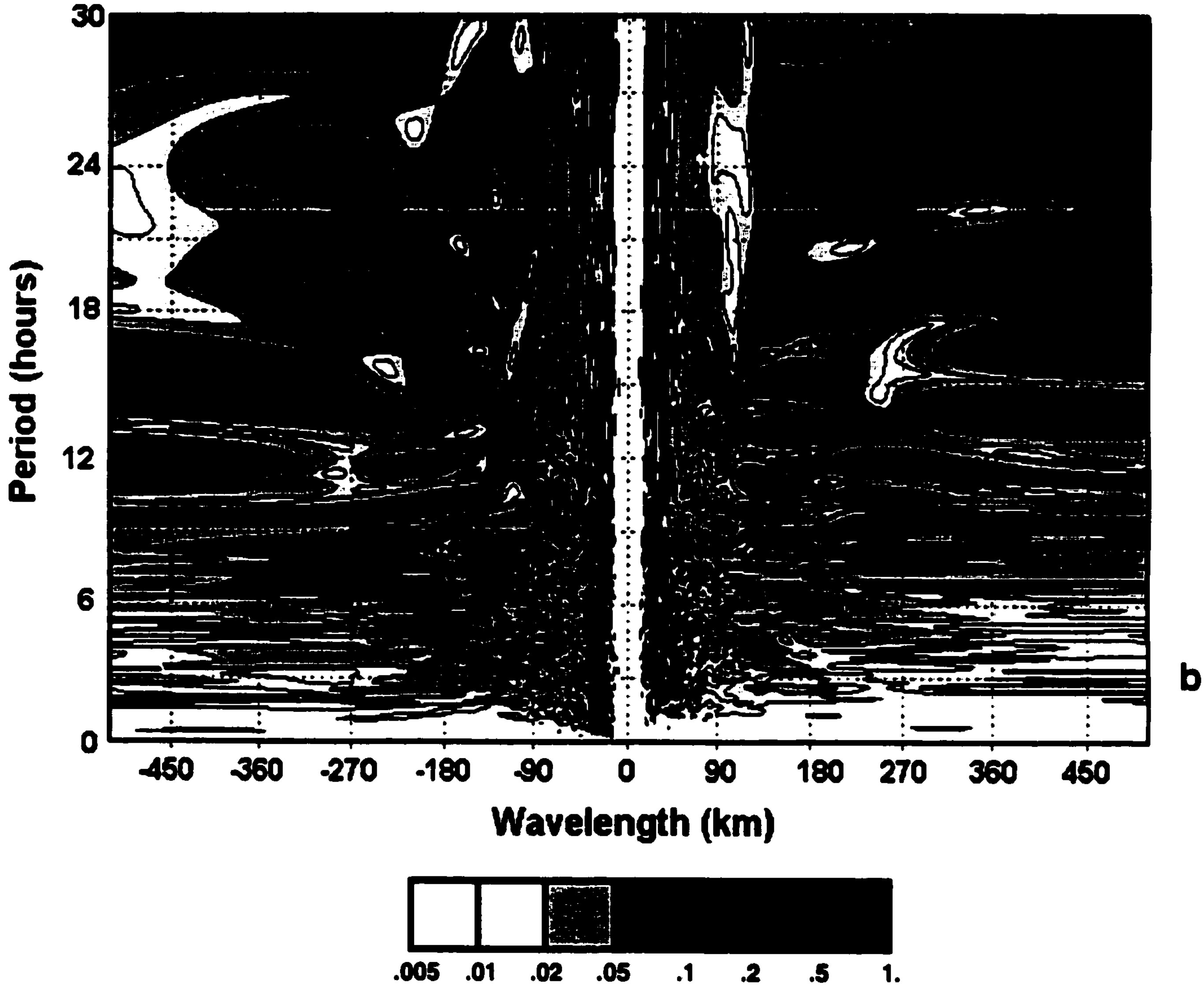

Figure 5.23 - continuation

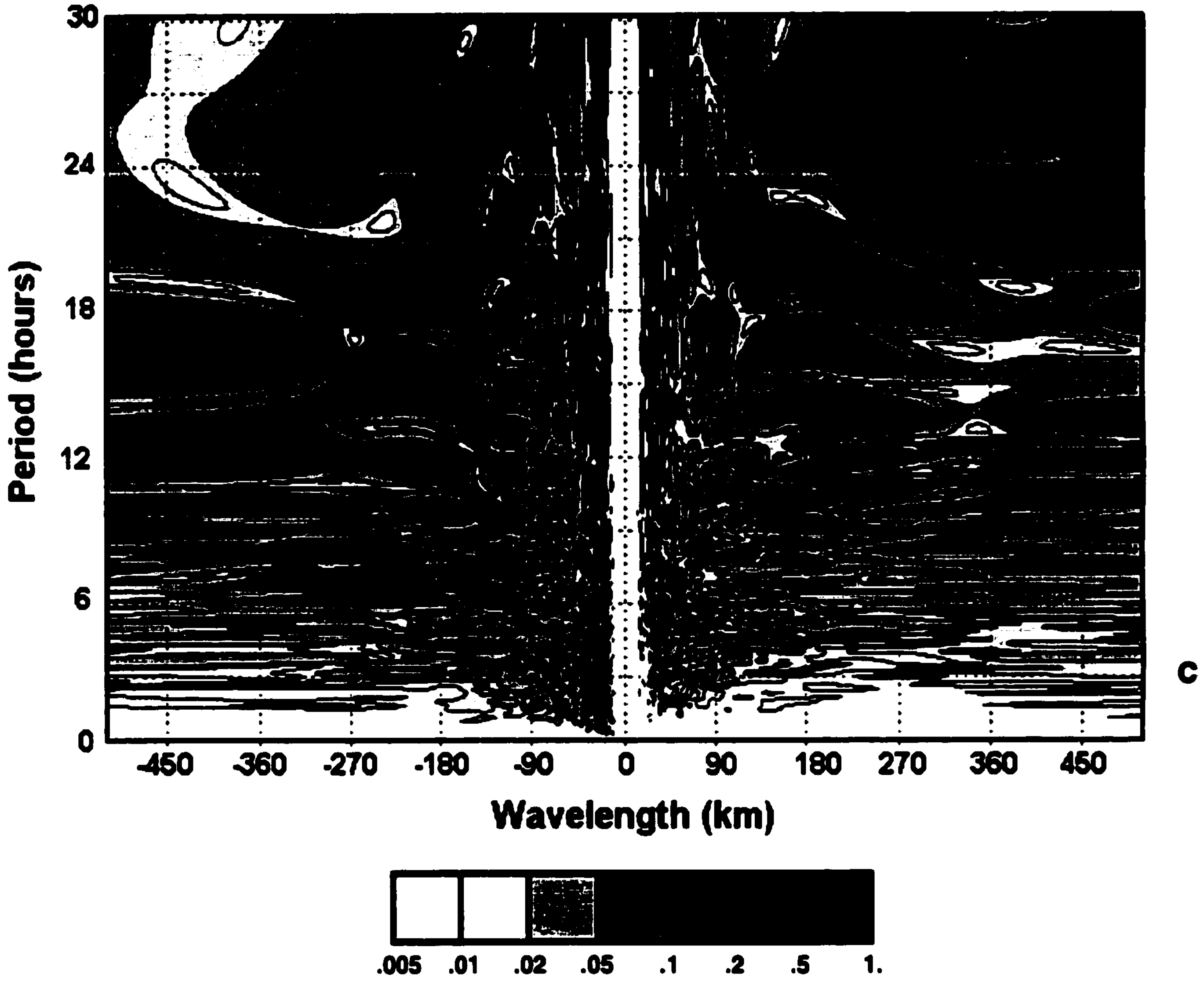

Figure 5.23 - continuation

LARGE (panel 5.23a) has a prominent maximum at the westward-propagating mesoscale mode with a time scale of the order of 17h and a broad range of spatial scales of the order of hundreds of kilometers. The structure of the convective mode is not as well defined, with elongated bands, corresponding to different timescales, all in association with a broad range of spatial scales. In MEDIUM (panel 5.23b), a similar westward-propagating maximum occurs, but its amplitude is reduced, and its average temporal scale goes down to about 15h. In opposition, the maxima at the convective mode were somewhat more intense than in LARGE.

Averaging over the spatial scales, and looking at individual timescales, MEDIUM has the most prominent activity on the shorter timescale. The existence of more convective action in short timescales in MEDIUM is illustrated in Figure 5.24, which depicts $\hat{P}$, averaged over timescales up to 512km, for the time interval between 30 minutes and 2 hours. Between 9-12h, convection in MEDIUM is reduced; while SMALL and LARGE have comparable activities, especially for periods between 10 and 12 hours (Figure 5.25). Finally, LARGE has most activity on timescales larger than 12h (Figure 5.26). The conclusion is that SST perturbations with large wavelengths favored the organization of convection on the mesoscale and the development of stratiform precipitation. Surprisingly, the medium-sized SST disturbances generated more small-scale precipitation patterns and more convective precipitation than their small counterparts. Although the present system is obviously highly non-linear, this behavior can be compared to the one of a simple harmonic oscillator forced by an external agent. The external forcing produces little response if its frequency is much larger or much smaller than the natural frequency of the oscillator, but if the two frequencies are similar, resonance emerges. In addition, the effect in the atmosphere at the spatial scale of the SSTs in SMALL might be also homogenized significantly due to horizontal turbulence and horizontal advection as concluded in an analytic study of horizontal scales of surface heating and their mesoscale response by Dalu et al. (1996).

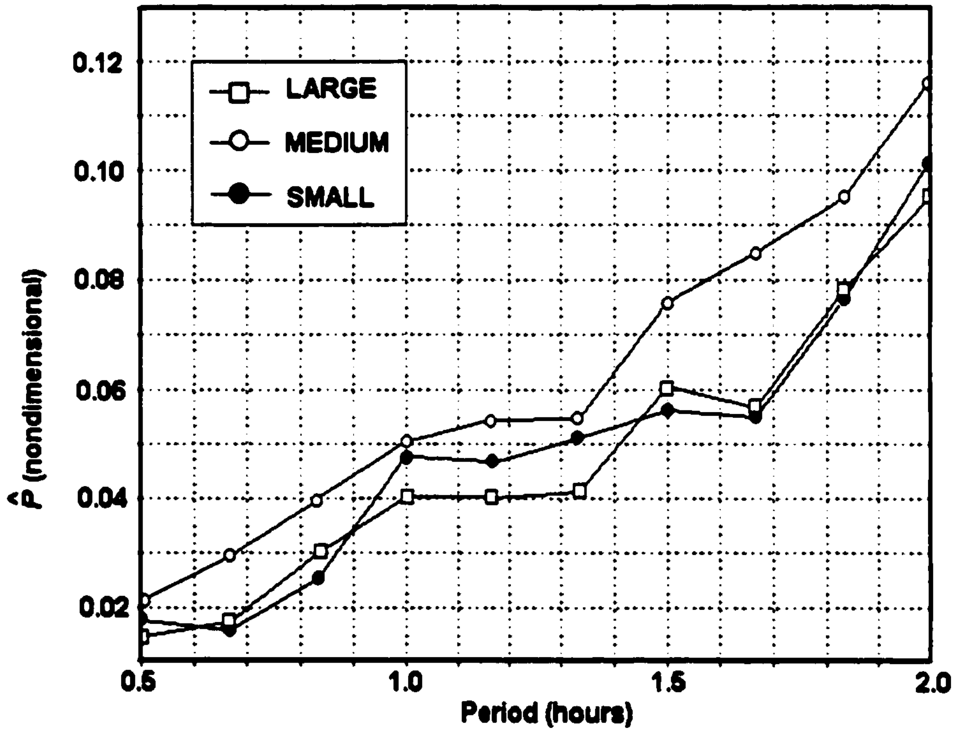

Figure 5.24 - Two-dimensional Fourier transformation of the surface precipitation, averaged over the spatial scales for timescales of less than 2h, in LARGE, MEDIUM and SMALL

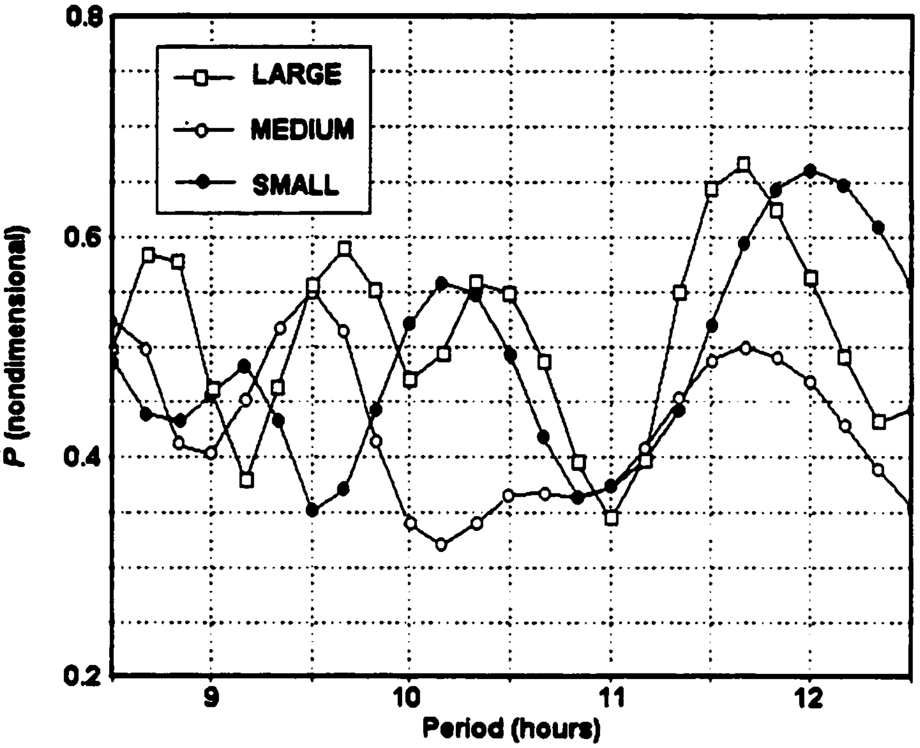

Figure 5.25 – Same as Figure 5.24, except for timescales between 8.5 and 12.5 hours.

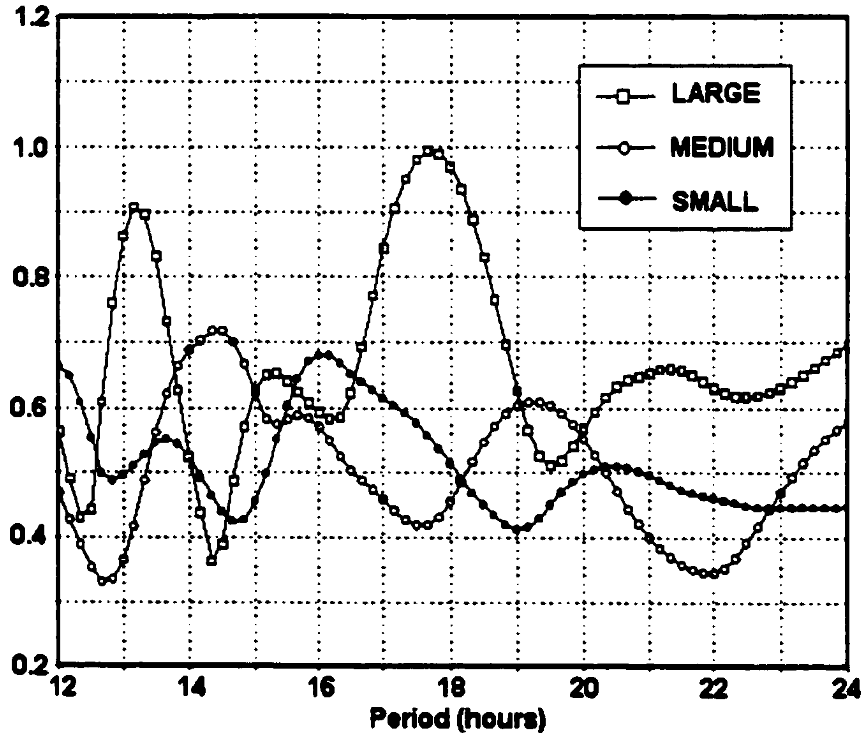

Figure 5.26 – Same as Figure 5.24, except for timescales between 12 and 24 hours.

Chapter 6

OCEAN MODEL AND COUPLING

"ADEUS! P'ra sempre adeus! A voz dos ventos	"GOOD-BYE! Good-bye forever! The voice of the winds
Chama por mim batendo contra as fragas.	Calls for me, hitting the ship.
Eu vou partir... em breve o oceano	I will leave... soon the ocean
Vai lançar entre nós milhões de vagas ..."	Will throw among us millions of waves..."

(Castro Alves, Brazilian poet)

The Princeton Ocean Model (POM) was used in all the coupled simulations, to predict the oceanic variables. A detailed description of the model is given by Blumberg and Mellor (1987).

6.1 - Ocean model features

The model contains prognostic equations for the zonal and meridional currents, potential temperature, salinity, turbulent kinetic energy (TKE) and turbulent length scale. A splitting procedure is used to resolve both the fast-varying external mode and the slow-varying internal mode.

The turbulence closure sub-model is the level-2.5 scheme in the hierarchy described by Mellor and Yamada (1974). Turbulent transport of heat and salinity are treated in the same way.

Long-wave radiative fluxes are evaluated at the boundary. Short-wave radiation is allowed to penetrate the ocean and is treated as a source term of heat in each level. The present radiation scheme is quite simple, as in Jerlov (1976). No spectral dependence is considered and a single exponential attenuation is calculated for the whole radiative flux. No large-scale forcing was imposed to the ocean model. It was assumed that the upper waters at the Western Pacific behave like the type IA in Jerlov's classification. In POM, IA-type waters are represented by a transmittance of 0.31 and an extinction coefficient of $0.042m^{-1}$.

6.2 - Experimental Set-up

POM was set-up in a two-dimensional framework, with a one-to-one correspondence between the atmospheric and oceanic model columns. As in the atmospheric model, 512 horizontal grid points and a horizontal grid spacing of 1km were used in the 10-day simulations, while in the long-term runs, the horizontal grid was arranged with 400 points and a 2km spacing. In all simulations, the ocean vertical grid contained 58 vertical levels with the grid-spacing varying from 2cm immediately below the surface, up to 5m at the model bottom (240m). The very fine resolution near the ocean surface is designed to resolve the shallow, diurnal oceanic warm-layer explicitly. The timestep for the internal mode was the same as for the atmospheric model (10s in the short-term, 12s in the long-term simulations). In all simulations a 1s timestep was used in the integration of the external mode. In all experiments cyclic lateral boundary conditions were adopted.

To simulate Case 1, the ocean model was initialized using data collected aboard the research vessel (R/V) Kexue No. 1, which was located at 3.963S, 156.053E at 0Z 07 December 1992. For the simulation of Case 2 and the long-term runs, the ocean model was initialized using current, temperature and salinity data collected aboard the R/V Moana Wave, which remained approximately stationary at 1.75S, 156E from 20 December 1992 to 11 January 1993.

In contrast to the atmospheric momentum, thermodynamic and moisture fields that were strongly constrained via relaxation and/or large-scale advection terms, no large-scale relaxation in the ocean currents nor large-scale advection of temperature and salinity were imposed to the oceanic variables. POM was forced only at the surface, by the coupling scheme.

6.3 - Coupling formulation

The coupling procedure used in this work is similar to the one described by Hodur (1997). The models interchange information at the boundary through momentum, heat and water substance fluxes. As in most atmosphere-ocean coupled models, a "salinity flux" is used to mimic the freshening or salting processes due to precipitation or evaporation respectively. Upward fluxes are assumed as positive.

The equations for the momentum fluxes are:

$$F_u = \langle u'w' \rangle = -\left(\frac{\rho_a}{\rho_o}\right) u_*^2 \frac{u}{|\mathbf{V}|} \tag{6.1}$$

$$F_v = \langle v'w' \rangle = -\left(\frac{\rho_a}{\rho_o}\right) u_*^2, \frac{v}{|\mathbf{V}|} \tag{6.2}$$

where u_* is the scale value for the velocity, computed following Louis et al. (1981); ρ_a and ρ_o are the densities of the atmosphere and the ocean at the air-sea interface; **V** is the wind vector with components u (zonal) and v (meridional); and the currents are assumed to be much smaller than the winds.

The boundary condition for heat comprises terms related to the sensible and latent heat fluxes, long-wave radiation and cooling by precipitation, as in Equation 6.3:

$$F_T = \langle w'T' \rangle = \left(\frac{\rho_a}{\rho_o}\right)\left(u_* T_* + \frac{L}{c_p} u_* q_*\right) + \frac{I\uparrow - I\downarrow}{\rho_o c_p} + P(SST - T_r), \tag{6.3}$$

where T_* and q_* are the scale values for temperature and water vapor mixing ratio (Louis et al., 1981), I represents the downward and upward longwave radiative fluxes, P is the precipitation rate, and T_r is the average temperature of the raindrops, calculated by the atmospheric model. Since the coupled model was designed to simulate convection over tropical oceans, it was assumed that there is no ice-phase or mixed-phase precipitation (for instance, hailstones). Short-wave radiation is absorbed below the surface, acting as a source term within each ocean model grid box. Therefore, the solar heating is not included in the boundary condition (6.3).

Finally, the salinity flux is given by:

$$F_s = \langle w'S' \rangle = -\left(\frac{\rho_a}{\rho_o}\right)(u_* q_* S - P) \tag{6.4}$$

where S is the salinity.

In the coupled model, the calculation of the fluxes is made at each timestep.

Chapter 7

COUPLED SIMULATIONS - CASES 1 AND 2

'Stamos em pleno mar... Dois infinitos
Ali se estreitam num abraço insano,
Azuis, dourados, plácidos, sublimes...
Qual dos dous é o céu? qual o oceano?...

We are on the high seas... Two infinites
Strain there in a mad embrace
Blue, golden, placid, sublime...
Which of the two is ocean? Which sky?...

(Castro Alves)

In this Chapter, results from 10-day simulations using the coupled CRM-UOM described previously are presented. First, a comparison is performed between some atmospheric and oceanic observations and the corresponding simulated fields. Then, the characteristics of simulated fresh anomalies (freshwater lenses) are discussed. Finally, the coupled simulations are compared with similar model runs, in which the atmospheric model was forced by a time-evolving, spatially-averaged SST, calculated from the coupled model results.

7.1 - Comparison with the observations

As many studies have already shown, cloud-resolving models constrained by a imposed forcing often produce results in good agreement with the observed fields (e.g., Grabowski et al., 1996, Su et al., 1999). As in the uncoupled simulations shown in Chapter 5, the atmospheric component of the coupled model produced results in very good agreement with several observed fields, such as the domain-averaged winds, the surface heat fluxes and the total precipitation. In contrast, because the ocean model was much less constrained than the atmospheric model, the agreement between observed and modeled oceanic fields was less than its atmospheric counterpart.

7.1.1 - Case 1

Most of the results from the atmospheric model are in good agreement with the observations. Figure 7.1 shows the difference between the modeled and the observed temperature and water vapor mixing ratio. After ten days of simulation, the model developed a cold bias, with a temperature deficit of the order of 1°C in the lower troposphere and about 4°C in the upper troposphere. At the end of the simulation period, the model also exhibited a moist bias with an excess of approximately $1 gkg^{-1}$ at low levels.

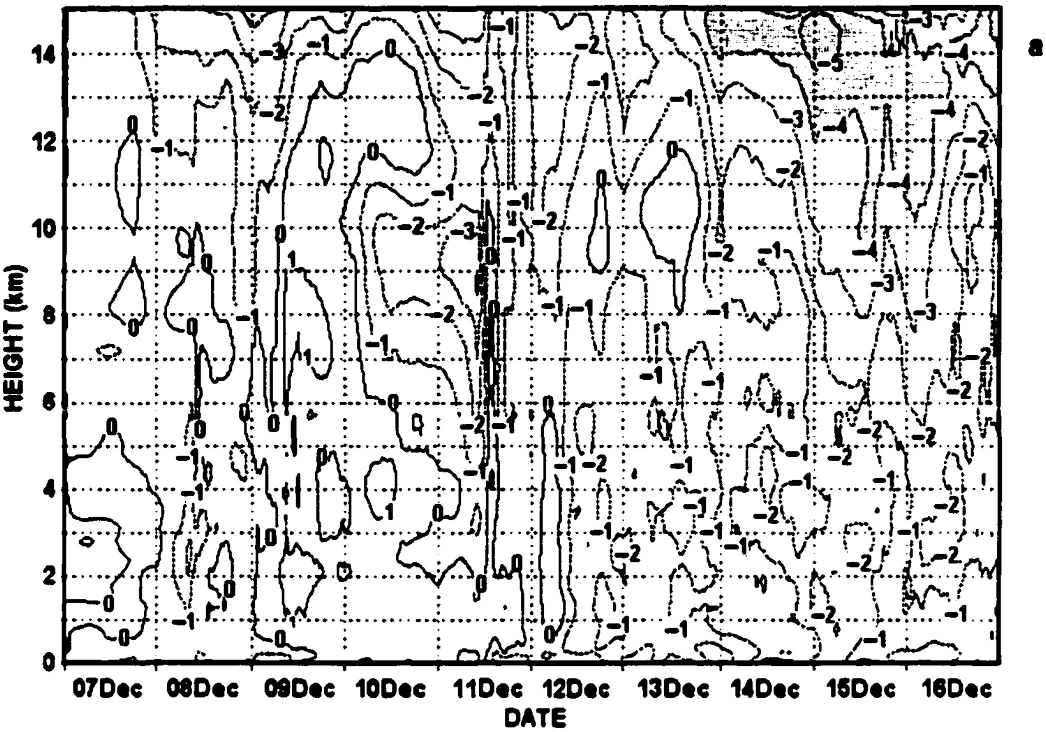

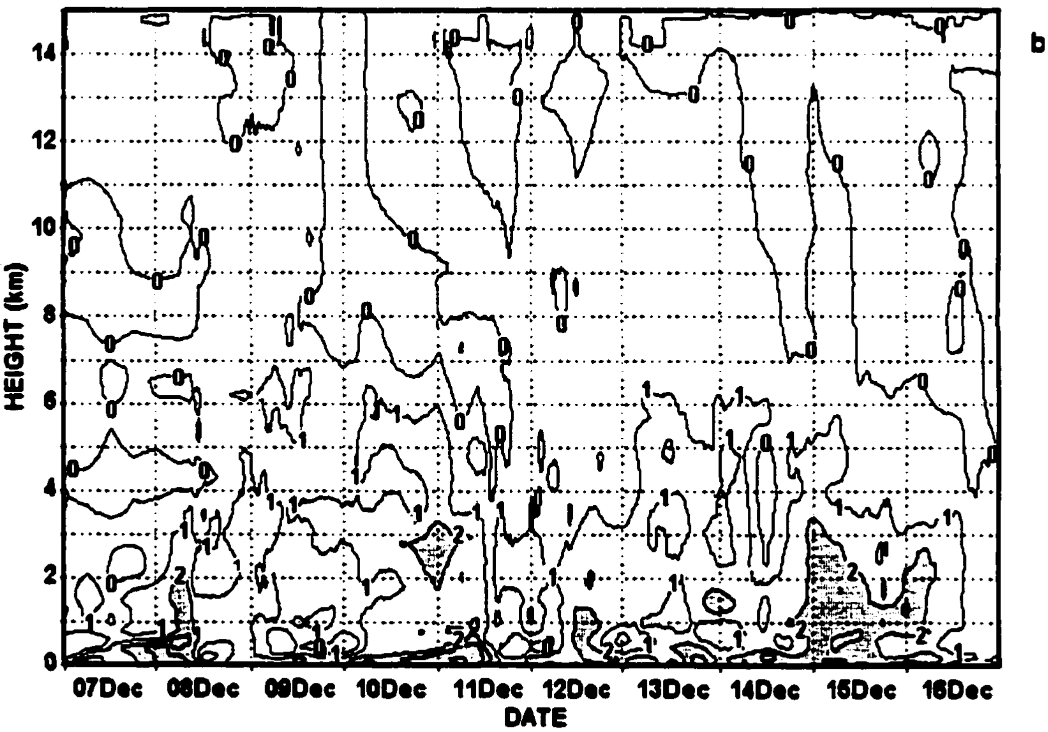

Figure 7.1 - Modeled minus observed (a) temperature and (b) water vapor mixing ratio, as a function of height and time, for Case 1. Temperature errors greater than 4K and mixing ratio errors greater than $2 g kg^{-1}$ are shaded.

The next plots depict the temporal evolution of the surface precipitation (7.2) and surface heat flux (7.3) as calculated from the observations (solid lines) and simulated by the coupled CRM (dashed lines). Qualitatively, the model represented well the evolution of all three fields. The agreement between the 9-day average modeled and observed fields for the period between 08 December and 16 December is also good, particularly for the sensible heat flux, as shown in Table 7.1. The moist bias probably contributed to the underestimation of the latent heat flux.

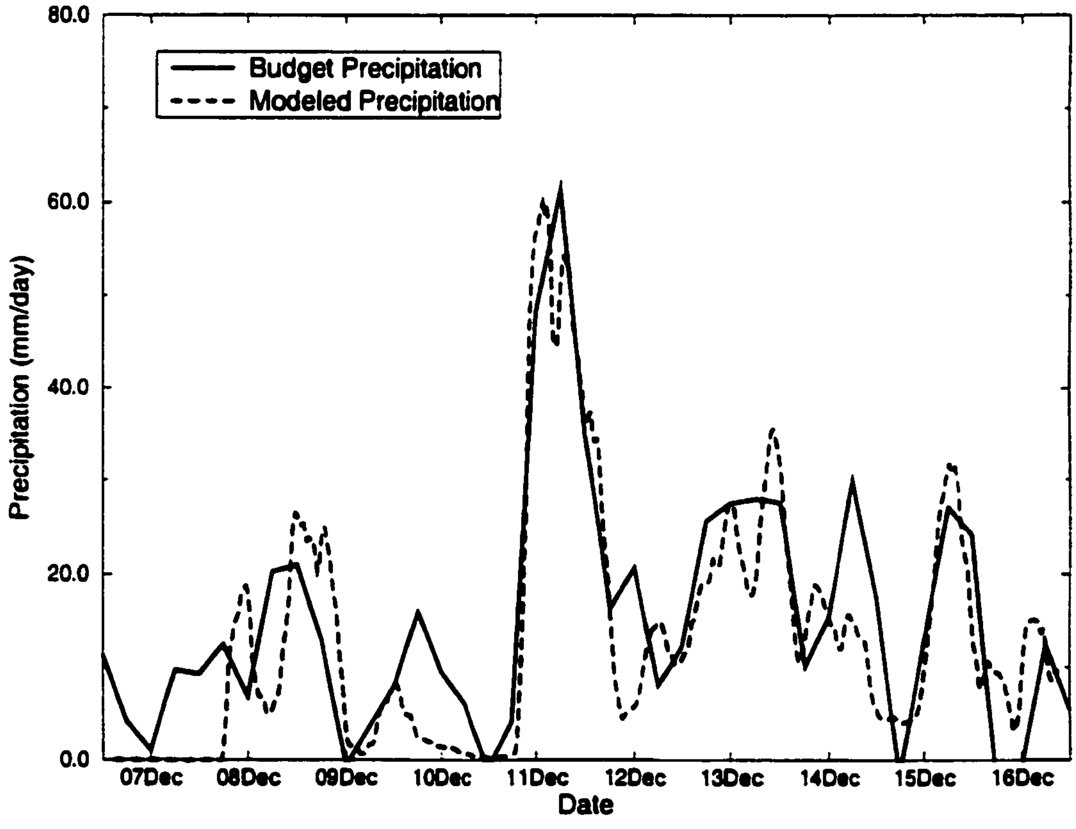

Figure 7.2 - Precipitation, in mm/day, as calculated from the observations and simulated by the coupled model for Case 1.

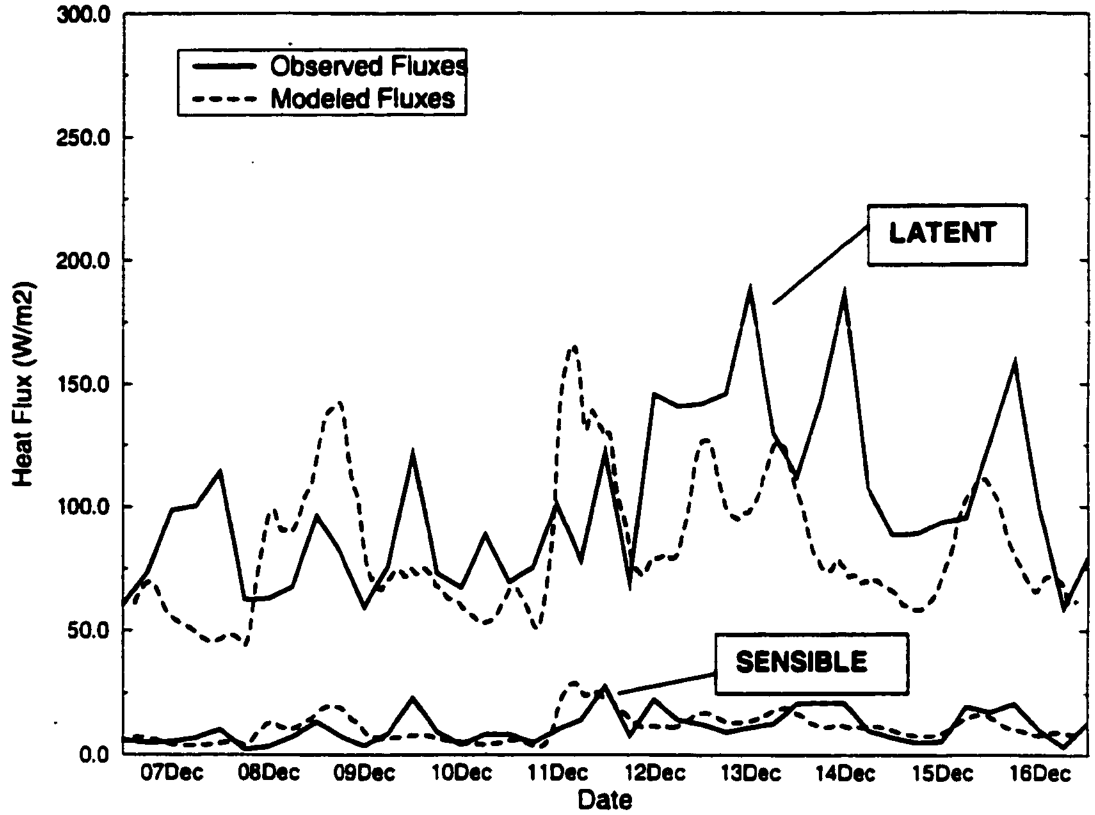

Figure 7.3 - Surface heat fluxes, in Wm^{-2}, as calculated from the observations and simulated by the coupled model for Case 1.

Variable	Calculated from the Observations	Modeled (and percentage difference from the observations)
Precipitation (mm day^{-1})	15.92	14.60 (-8.29%)
Sensible heat flux (Wm^{-2})	11.78	11.84 (+0.51%)
Latent heat flux (Wm^{-2})	102.25	86.49 (-15.41%)

Table 7.1 - 9-day averaged surface precipitation, sensible heat flux and latent heat flux, as calculated from the observations and simulated by the coupled model (Case 1). The first day of simulation was excluded from the averages due to the model spin-up process.

Unfortunately, there were no measurements of ocean fields from the R/V Kexue after 11 December, which prevents a proper validation of the ocean model data for most of the simulated period. Between 08 and 11 December, there is a reasonable agreement between the observed and modeled temperature at a depth of 2m, including an important diurnal variation and a general cooling trend (Figure 7.4). On the other hand, the agreement between the model domain-averaged 2m salinity and the observations from the research vessel is not good (Figure 7.5). Although the model was able to represent some aspects of the evolution of the salinity field (for instance, the significant freshening of the upper ocean from 08 to 09 December), the differences between the modeled and observed fields is large at certain times. In part, this is due to the crucial difference between an area-averaged model variable and a point observation. The sudden and large variations in the salinity field suggest that occasionally the vessel was sitting over fresh anomalies. Conversely, it might suggest that the surface forcing was not the only mechanism controlling the upper ocean budget, particularly concerning the salinity field.

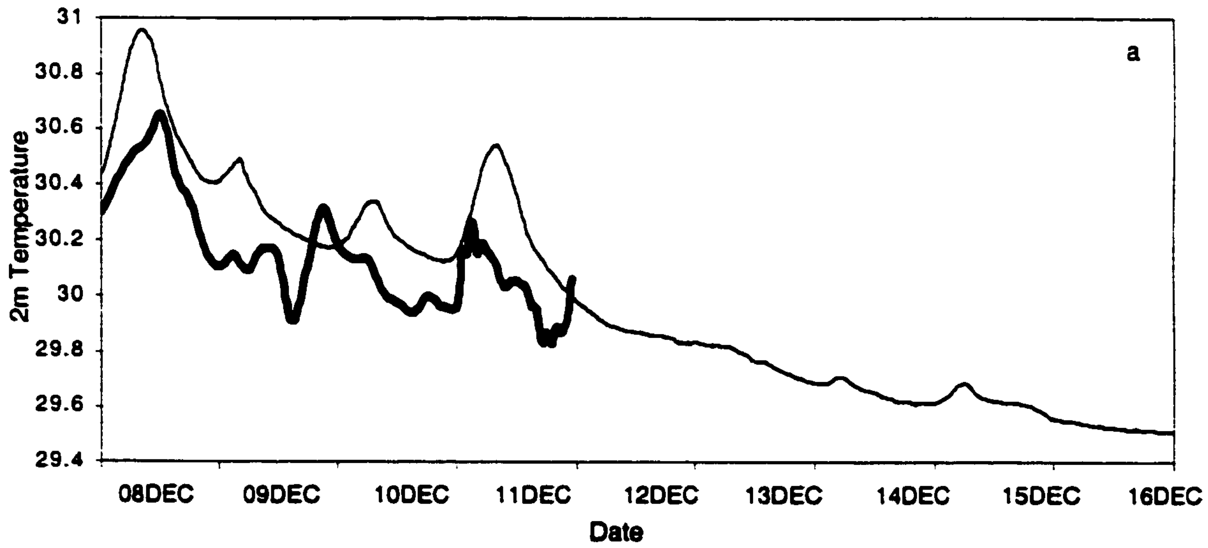

Figure 7.4 - Observed and modeled temperature at a depth of 2m for Case 1.

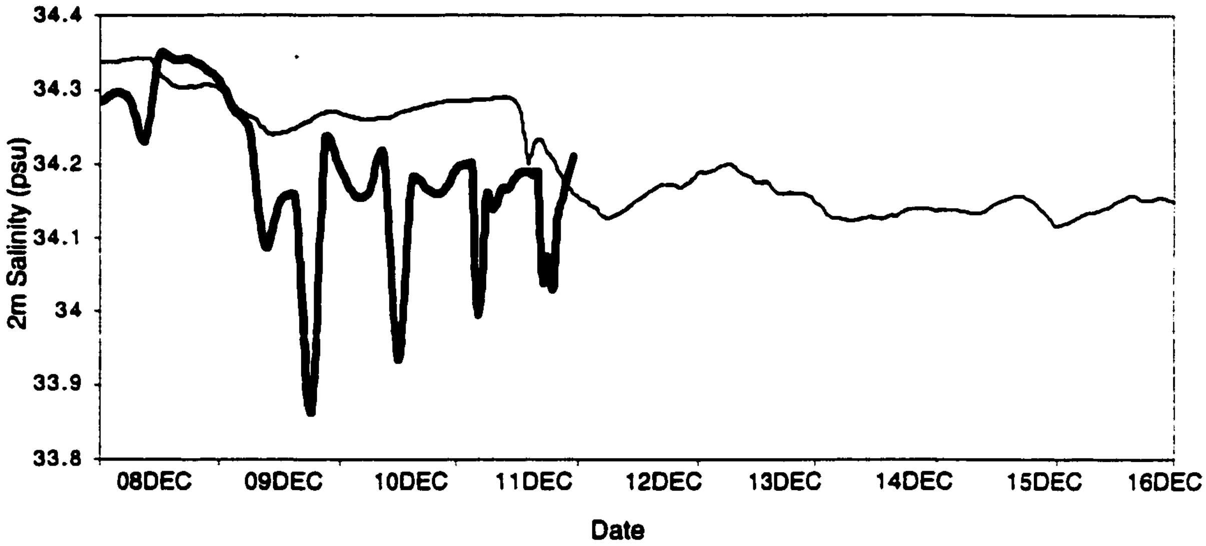

Figure 7.5 - Observed and modeled salinity at a depth of 2m for Case 1.

7.1.2 - Case 2

As in the previous case, the results from the atmospheric model were in good agreement with the observations, particularly the surface heat fluxes and the precipitation, which are important to force the ocean model. The comparison between those fields and their observed counterparts is depicted in Figures 7.6 (precipitation) and 7.7 (sensible and latent heat fluxes) and Table 7.2. The agreement between the model precipitation and surface latent heat flux (evaporation) and the observations was better in Case 2 than in Case 1. In contrast, the model overestimated the sensible heat flux. Concerning other atmospheric model fields, the results were akin to the ones obtained using the uncoupled CRM (Section 5), including the development of a cold, dry bias at most tropospheric levels, similar to the one shown in Figure 5.1. The atmospheric cold bias is a possible cause for the overestimation of the surface sensible heat flux.

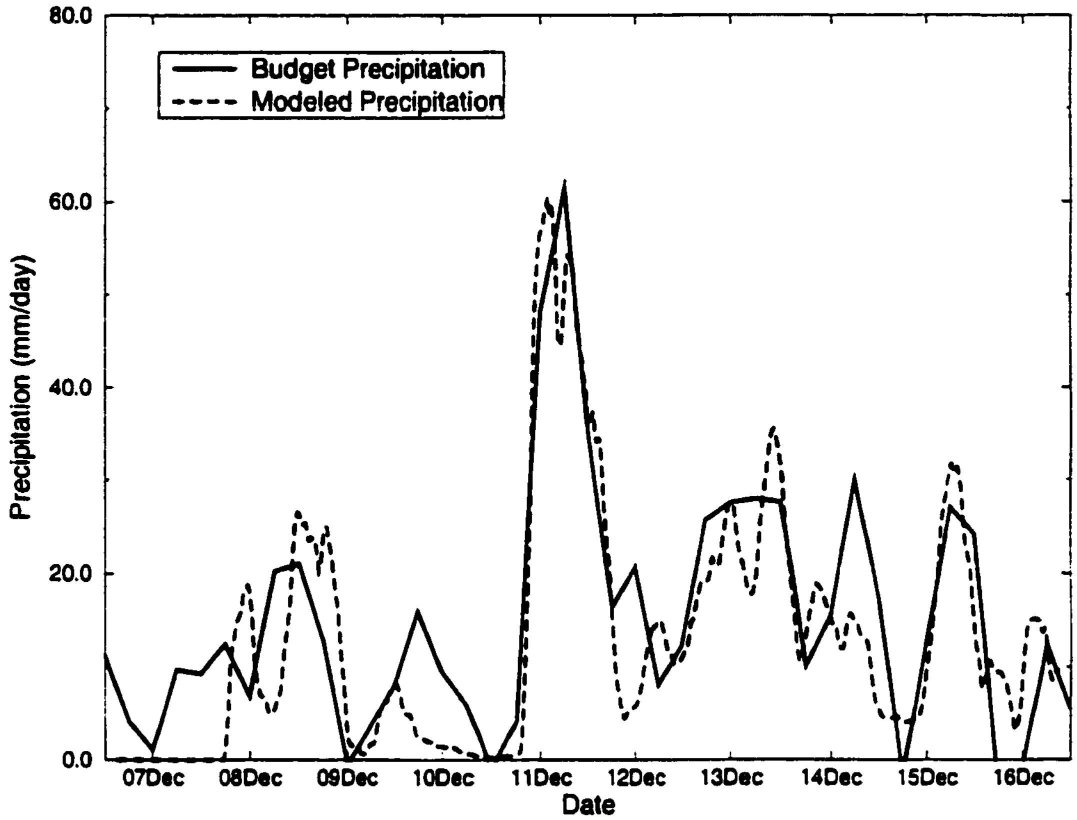

Figure 7.6 - Same as Figure 7.2, except for Case 2

Variable	Calculated from the Observations	Modeled (and percentage difference from the observations)
Precipitation (mm day^{-1})	17.96	17.63 (-1.84%)
Sensible heat flux (Wm^{-2})	13.87	18.65 (+34.46%)
Latent heat flux (Wm^{-2})	140.68	144.02 (+2.37%)

Table 7.2 - Same as Table 7.1, except for Case 2

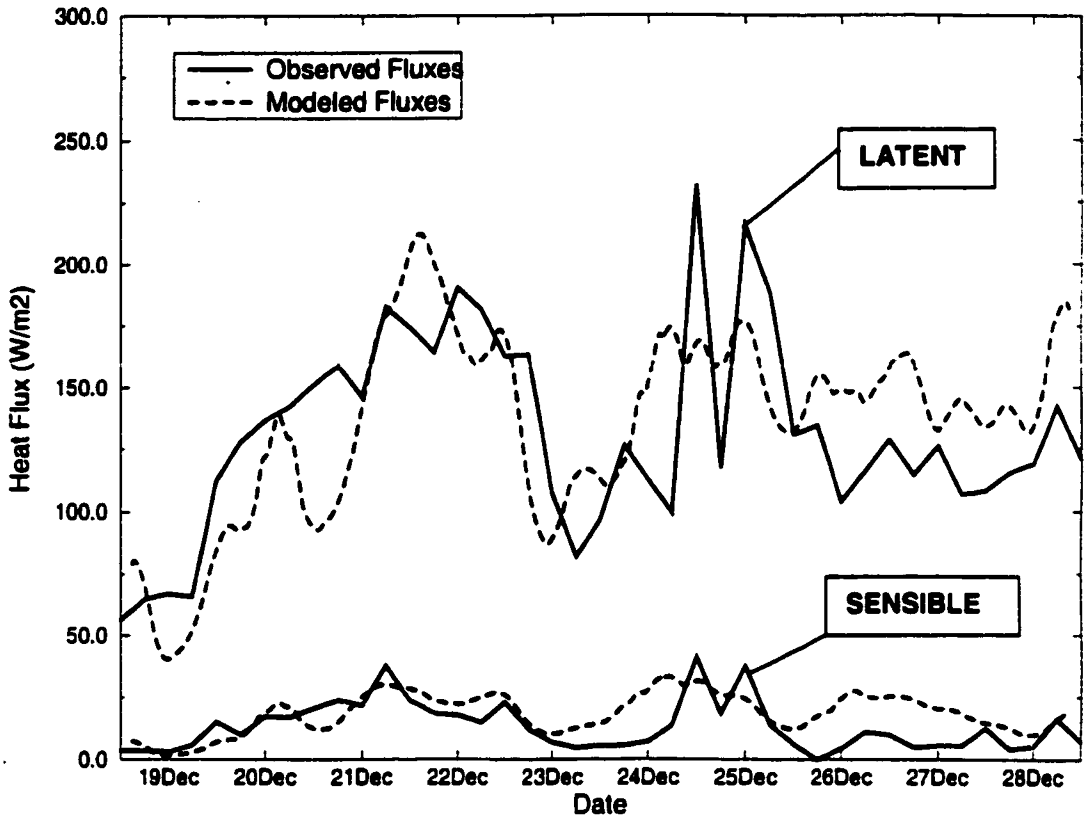

Figure 7.7 - Same as Figure 7.3, except for Case 2

Figure 7.8 depicts the time evolution of the observed 2m temperature (measured by the R/V Moana Wave) and the horizontally averaged 2m temperature predicted by the ocean model for Case 2.

Despite its limitations, the ocean model was able to reproduce important observed features of the 2m temperature (Figure 7.8). With the exception of the exaggerated diurnal warming on 20 December due to the overestimated downward solar radiation associated with the atmospheric model spin-up, the departure from the observed field is always smaller than 0.3°C (the difference at 0Z 29 December is 0.15 °C). The observed cooling trend between 20 and 28 December was well represented. The temperature drop observed by the vessel was 0.69 °C, compared with 0.59 °C predicted by the model. Although small, the warm ocean bias must have contributed to the overestimation of the surface sensible heat flux along with the cold bias in the air temperature.

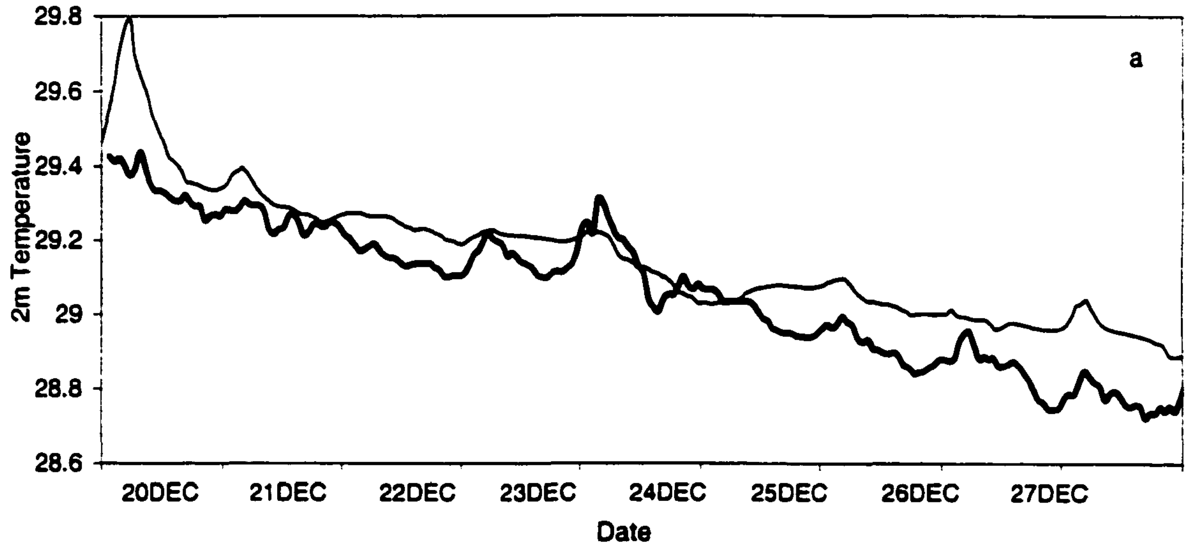

Figure 7.8 - Same as Figure 7.4, except for Case 2

Figure 7.9 depicts the time evolution of the salinity observed at a depth of 2m and the horizontal average of the temperature predicted by the ocean model at the same depth, for Case 2.

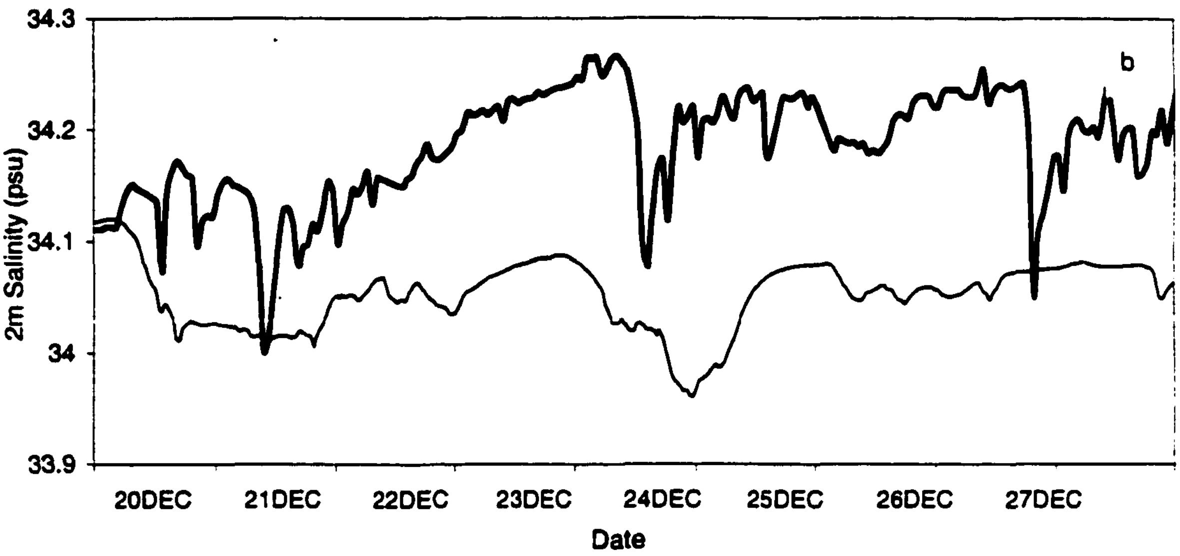

Figure 7.9 - Same as Figure 7.5, except for Case 2.

The agreement in the salinity field was not as good as its counterpart for the temperature, and the model showed a fresh bias of 0.17psu at the end of the simulated period. As seen in Figure 7.9, despite the large flux of freshwater associated with the heavy precipitation over the COARE IFA, the observed salinity field showed an increasing trend, which can be associated with other factors, such as horizontal advection of saltier water to the location of the vessel. Nevertheless, despite the amplitude difference (that can be attributed to the contrast between a point measurement and the model domain-average), the major freshening events were represented by the model. Overall, the agreement between the modeled oceanic fields and the observations is better in Case 2 than in Case 1. From an oceanic point of view, the surface forcing was stronger in Case 2, therefore atmospheric forcing can dominate the heat and freshwater budget of the upper ocean in this case. In contrast, in Case 1, for which the surface forcing was weaker, larger scale transport of heat and salt could play a more significant role.

7.2 - Characteristics of simulated freshwater anomalies

Tropical convection is often organized in mesoscale systems comprising multiple convective cells that produce heavy precipitation and a stratiform region that produces lighter precipitation. The complex structure of convection accounts for a large spatial variability in the surface precipitation fields. Freshwater anomalies are generated at the tropical ocean surface by rainfall (Paulson and Lagerloef 1993; Soloviev and Lukas 1997b; Wijekera et al. 1999), producing a correspondent variability in the sea surface salinity (SSS) field. The amplitude of the SSS perturbations is particularly large at newly formed freshwater anomalies, particularly the ones generated behind cores of intense convective precipitation. Since they are often formed from cooler rainwater, freshwater anomalies also correspond to cold anomalies in the SST field, at least in the early stages of their life cycles. Those anomalies are haline-stratified, and, since the salinity effect dominates the temperature effect, exhibit strong vertical stability and a significant inhibition to vertical mixing, which therefore modifies the transport processes near the ocean surface. As a consequence, the further evolution of the SST field is also influenced by the presence of freshwater anomalies.

To illustrate the formation of freshwater anomalies from precipitation and their influences on the SST field, Figures 7.10 and 7.11 show Hovmuller diagrams of the surface precipitation, the SSS and the SST for Case 1 and Case 2 respectively.

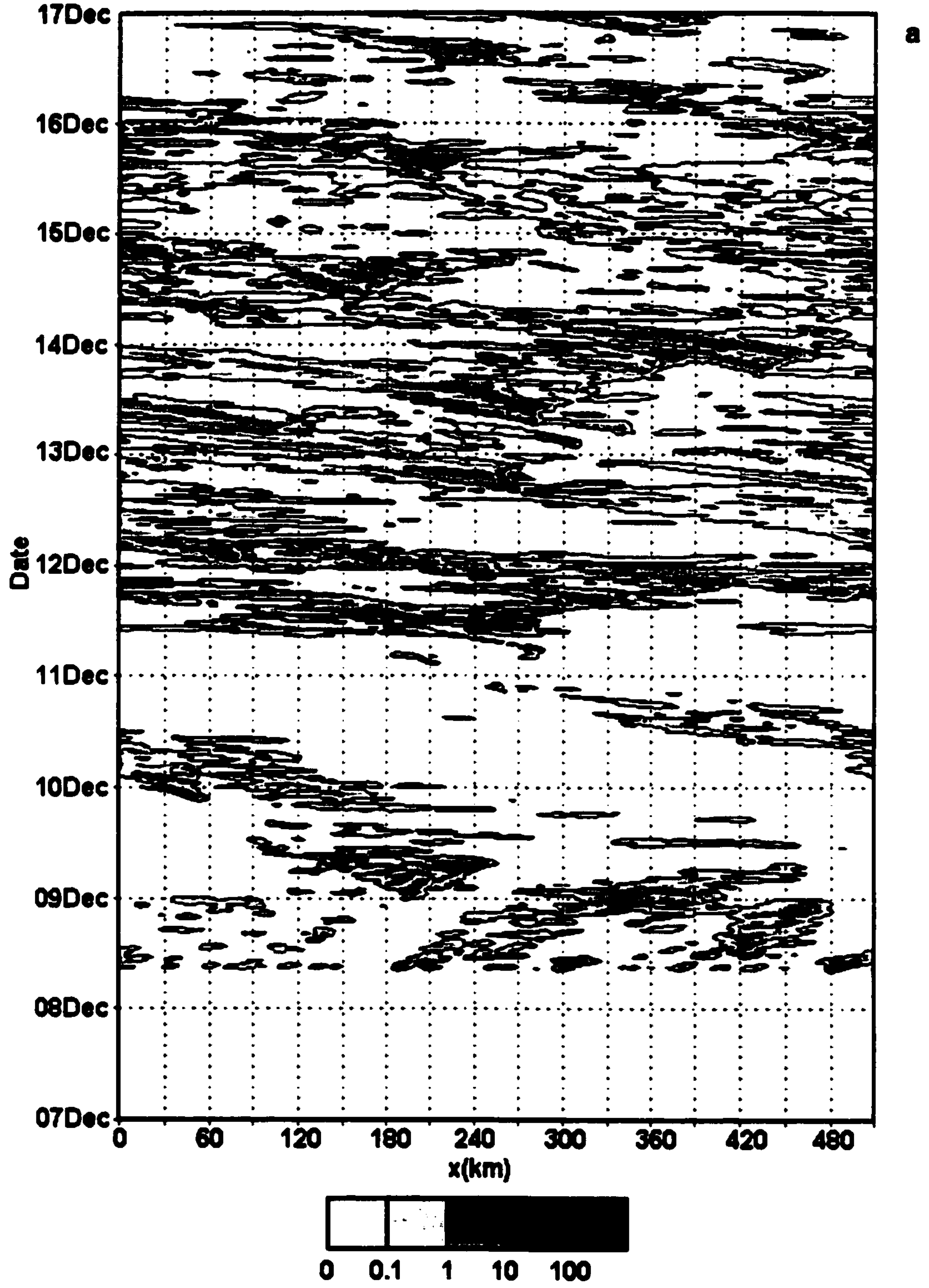

Figure 7.10 - Hovmuller diagrams of the (a) surface precipitation, in mm/h, (b) sea surface salinity, in psu and (c) sea surface temperature for Case 1. The contours at the first and second panels are the 0.1 mm/h and the 34.0 psu isolines, respectively.

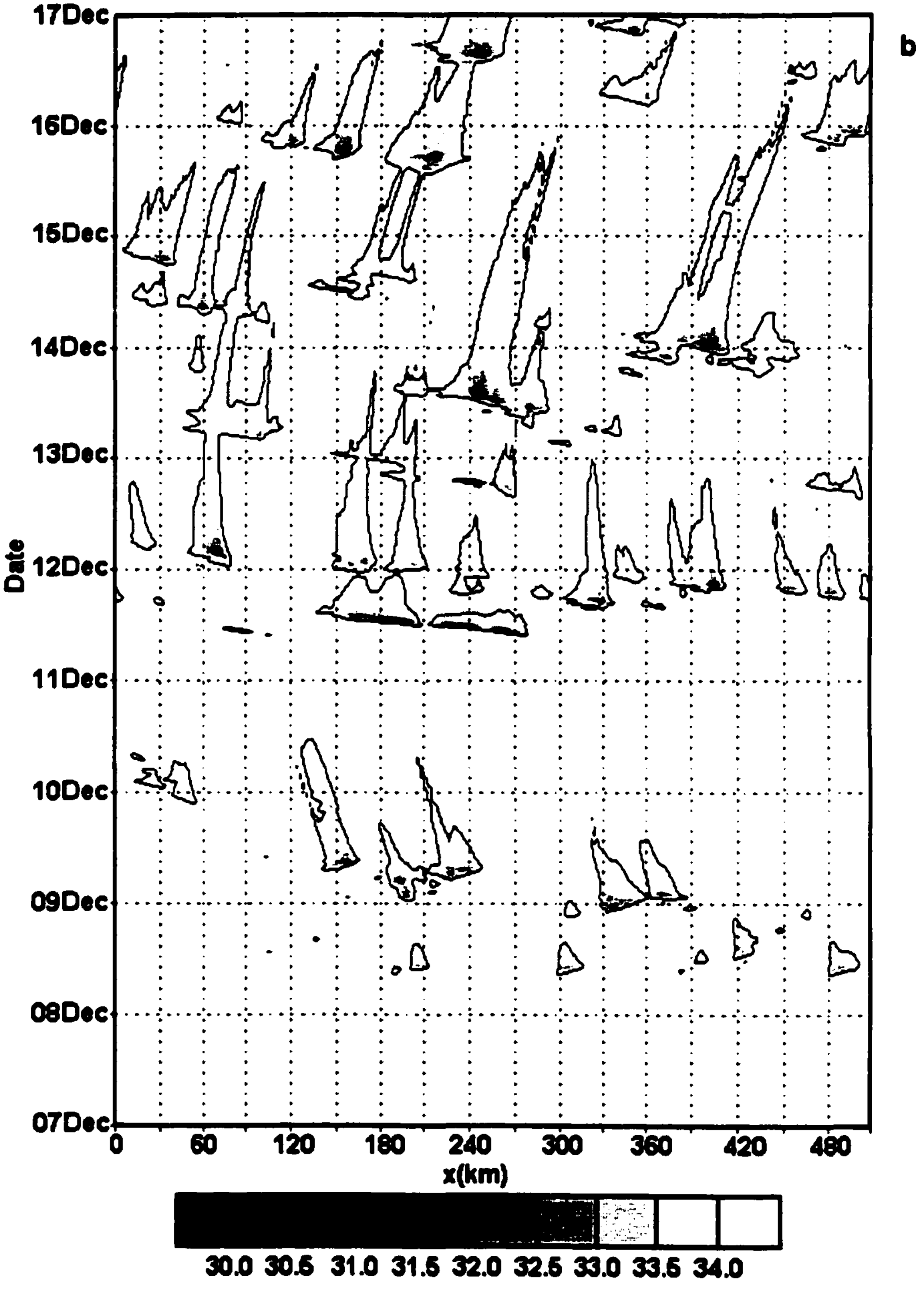

Figure 7.10 - continuation

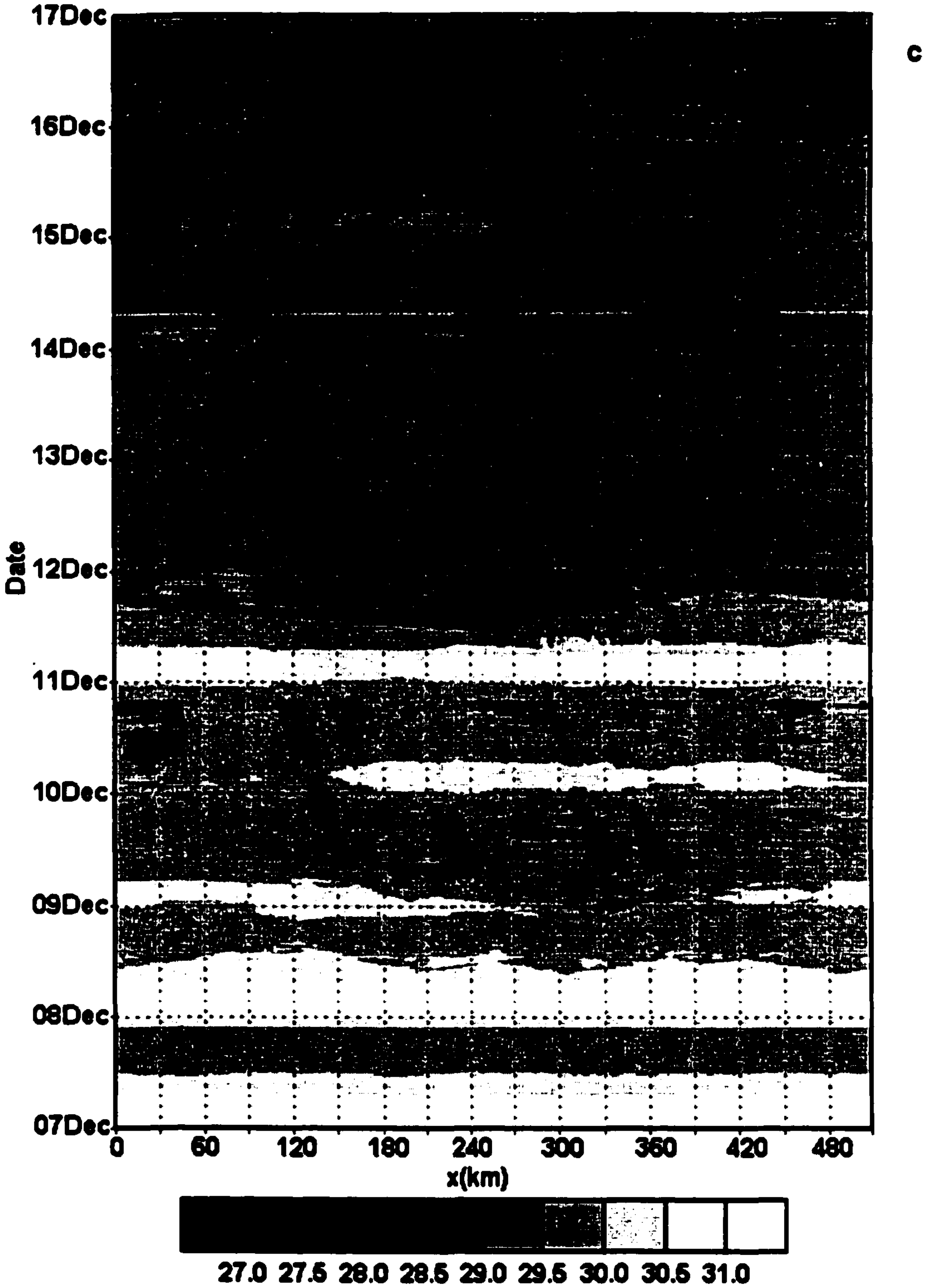

Figure 7.10 - continuation

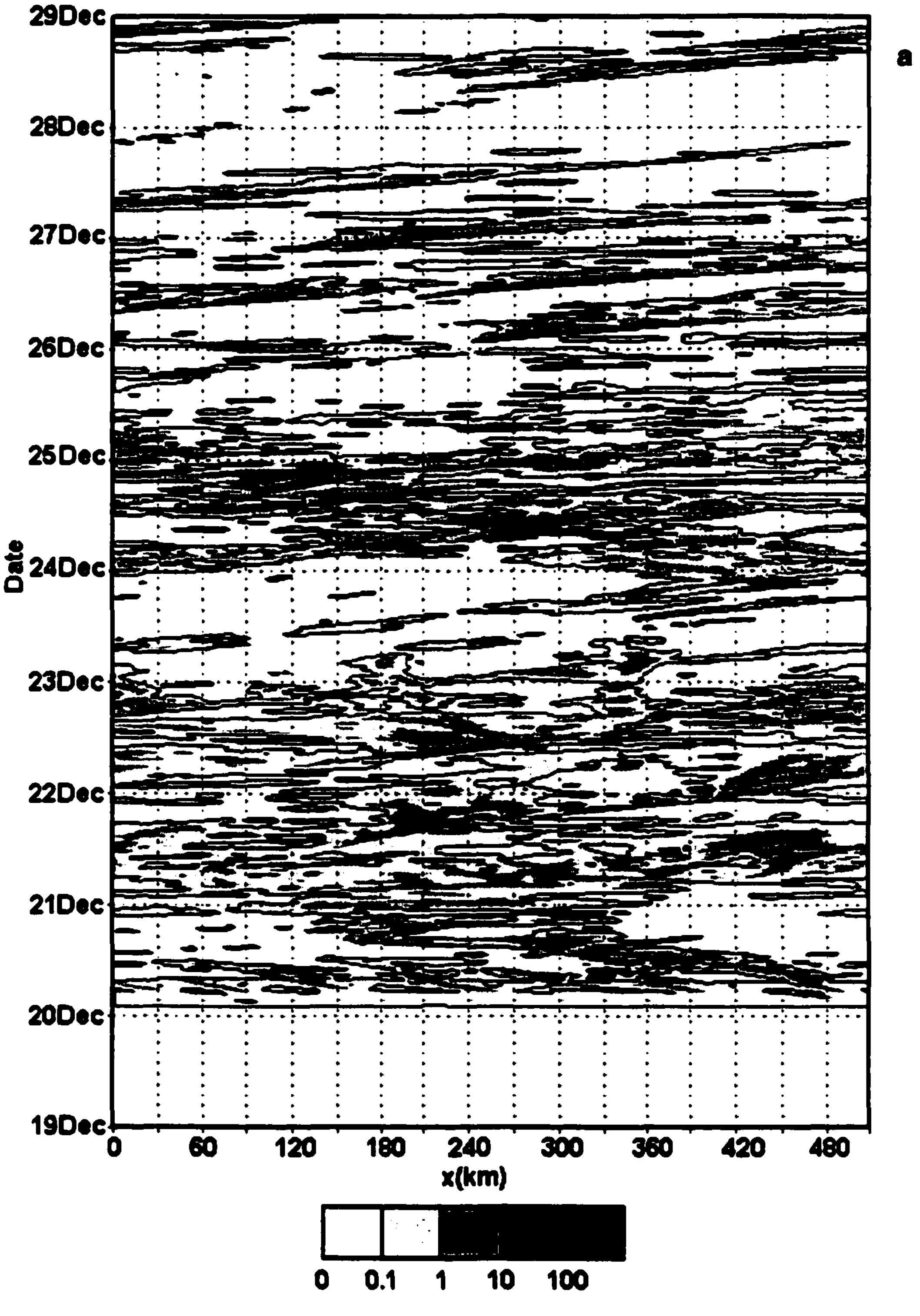

Figure 7.11 - Same as Figure 7.10, except for Case 2

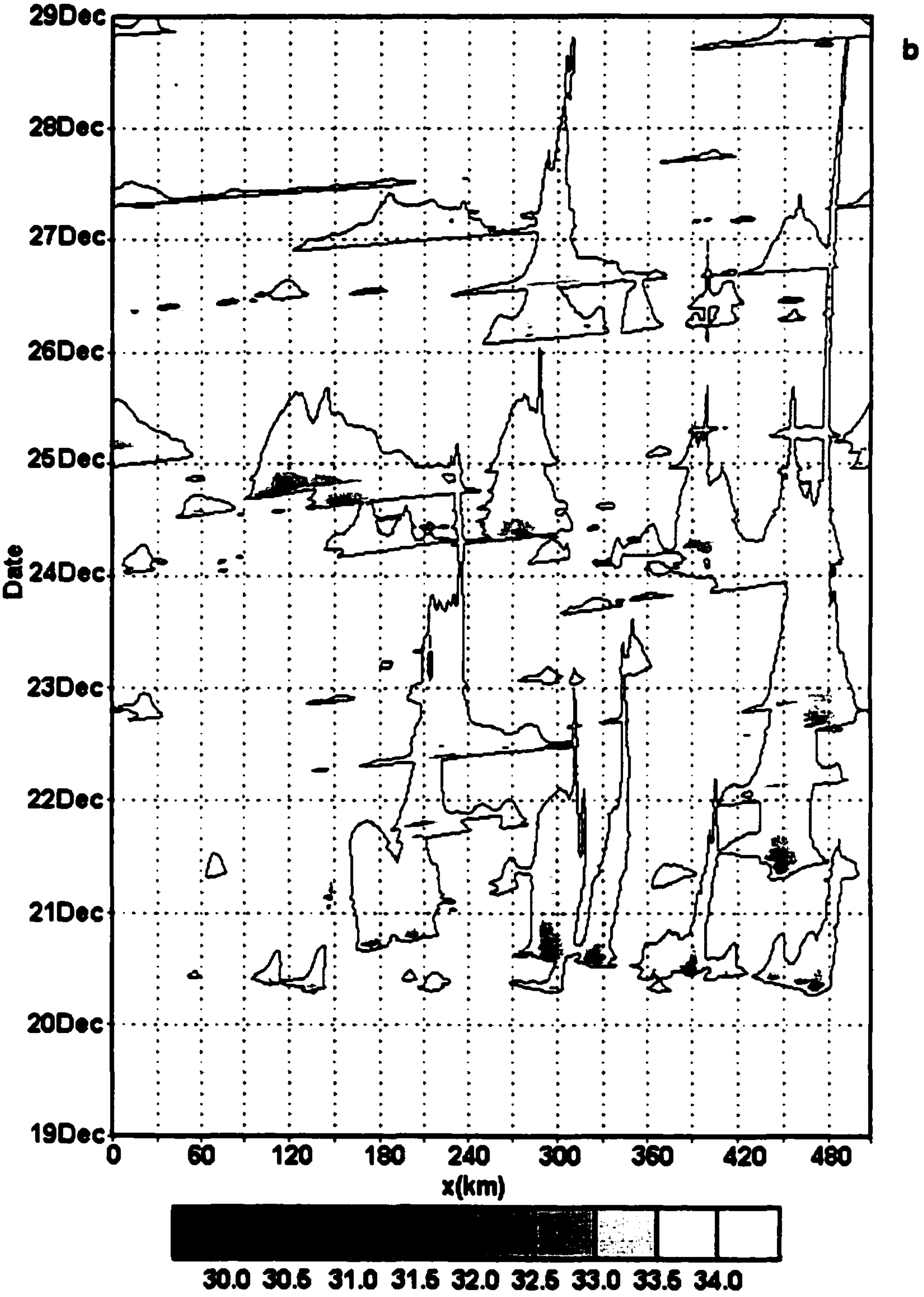

Figure 7.11 - continuation

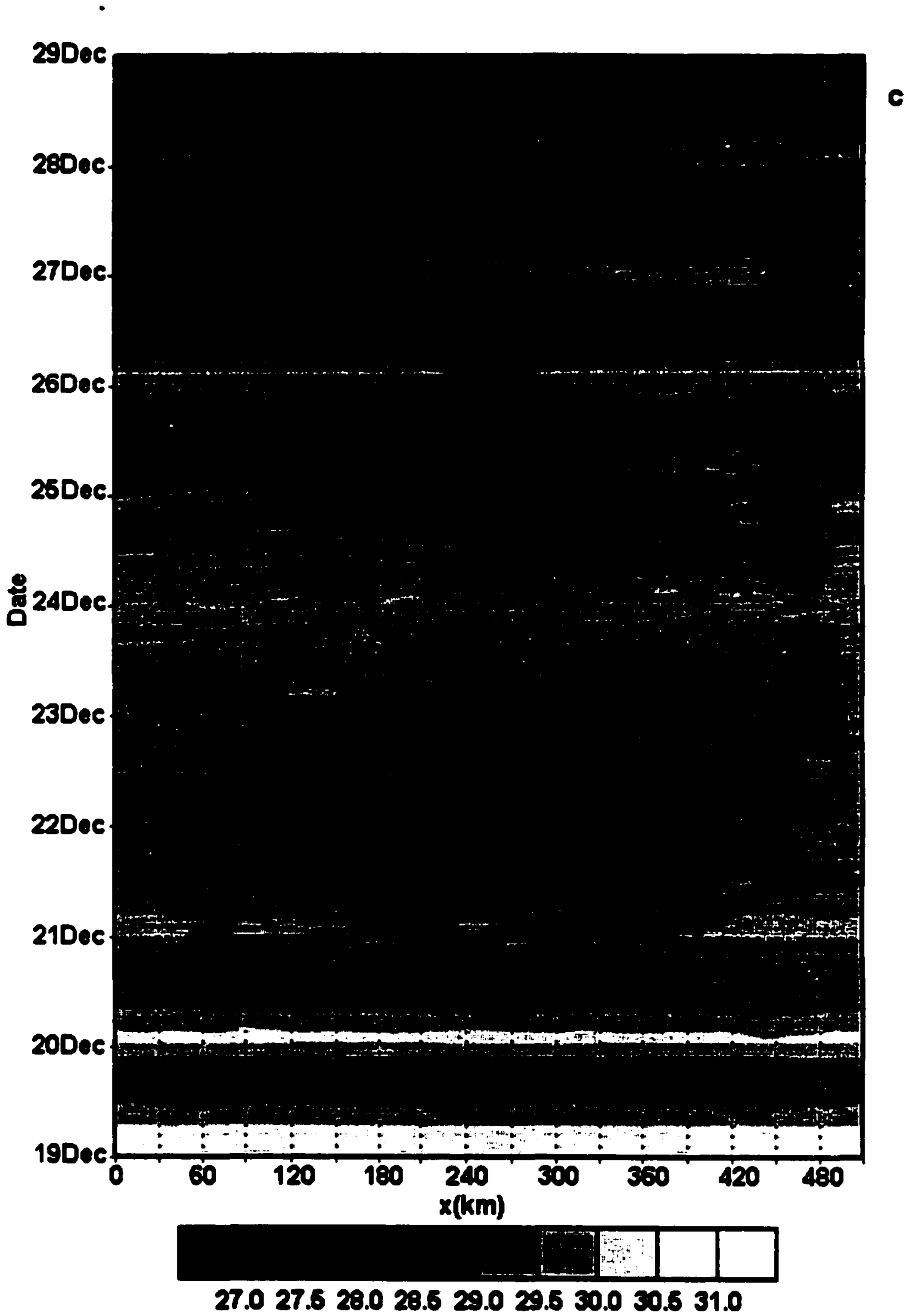

Figure 7.11 - continuation

In both cases, the complex structure of the precipitation fields produced a spectrum of freshwater anomalies with a variety of horizontal dimensions and lifetimes. It is apparent that nearly all freshwater anomalies correspond to cold SST anomalies during most of their life cycles.

The initial characteristics of a freshwater anomaly are strongly dictated by the behavior of its parent storm. The horizontal dimension of a newly formed freshwater anomaly depends on the propagation speed of the precipitating system. Fast-propagating systems generate widespread anomalies, while near-stationary storms tend to produce localized salinity disturbances. The lifetime of the freshwater anomalies depends strongly on the near-surface winds. Because strong winds induce vertical mixing in the ocean mixed layer, the duration of freshwater anomalies becomes shorter. On the other hand, calm winds favor long-lived upper-ocean salinity perturbations. Case 1 was generally characterized by slowly-propagating precipitating systems and weak large-scale winds that generate relatively narrow, long-lived freshwater anomalies. Simulated perturbations as large as 0.2 psu persisted for more than 48 hours. In contrast, Case 2 exhibited fast-moving precipitating systems and moderate large-scale winds, which produced wider salinity disturbances with shorter lifetimes.

Figures 7.12 shows two-dimensional distribution functions, in which the occurrence of freshwater anomalies is distributed among six categories of maximum horizontal extension and five categories of lifetime (only freshwater lenses with maximum salinity perturbations greater than 1.0 psu were considered). In both Case 1 and Case 2, the horizontal extension and the lens duration are correlated, with a larger horizontal extension favoring a longer life cycle. As discussed previously, there is a larger occurrence of lenses with a large horizontal extension in Case 2, when moderate near-surface winds were present, along with a greater organization of convection on the mesoscale.

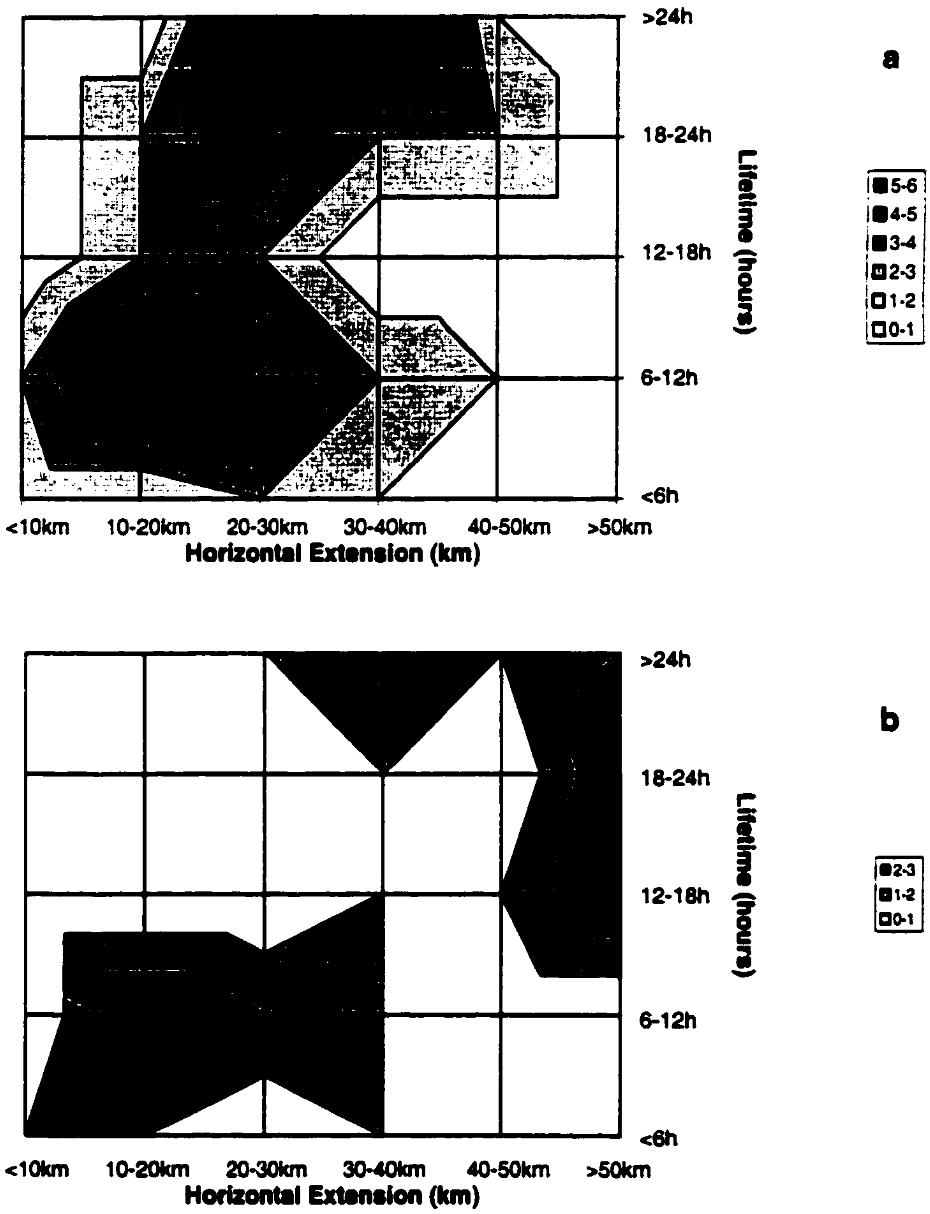

Figure 7.12 – Number of freshwater lenses by categories of maximum horizontal extension and lifetime, formed in the simulations of (a) Case 1 and (b) Case 2.

As discussed by Webster (1994), who analyzed data from the Western Equatorial Pacific Ocean Circulation Study (WEPOCS) experiment (Lukas and Lindstrom, 1991), three major physical processes account for the variability of the SST and the SSS over the WPWP: diurnal heating, precipitation and entrainment/evaporation (one could add the transport of heat and salt by the currents). The diurnal warming and cooling of the ocean surface layer is often more pronounced when convection is suppressed and the winds are light. When such a process dominates, the SST experiences a diurnal variation often greater than 1°C while the SSS remains almost constant, due to little evaporation (precipitation is usually near zero in those situations). During periods of active convection, the diurnal cycle is usually very small due to the blocking of solar radiation. However, the variability of both SSS and SST is often large, due to the presence of precipitation-formed disturbances, in which both the salinity and the temperature are reduced. Finally, strong westerly winds (often associated with suppressed convection) induce simultaneously surface evaporation and deep mixing. The later allows cooler, saltier water to penetrate the ocean mixed-layer from below. Both processes contribute to lower the SST and to increase the SSS. The two first processes differ from the third in the timescales in which they operate. Both the diurnal warming and the precipitation generate shallow layers, in which the stability is governed by thermal or haline stratification, respectively. In those two cases, the lifetime of the SST/SSS disturbances is of the order of one day or less. By contrast, the cooling and salting by evaporation and entrainment operate on a deeper vertical scale and a longer timescale.

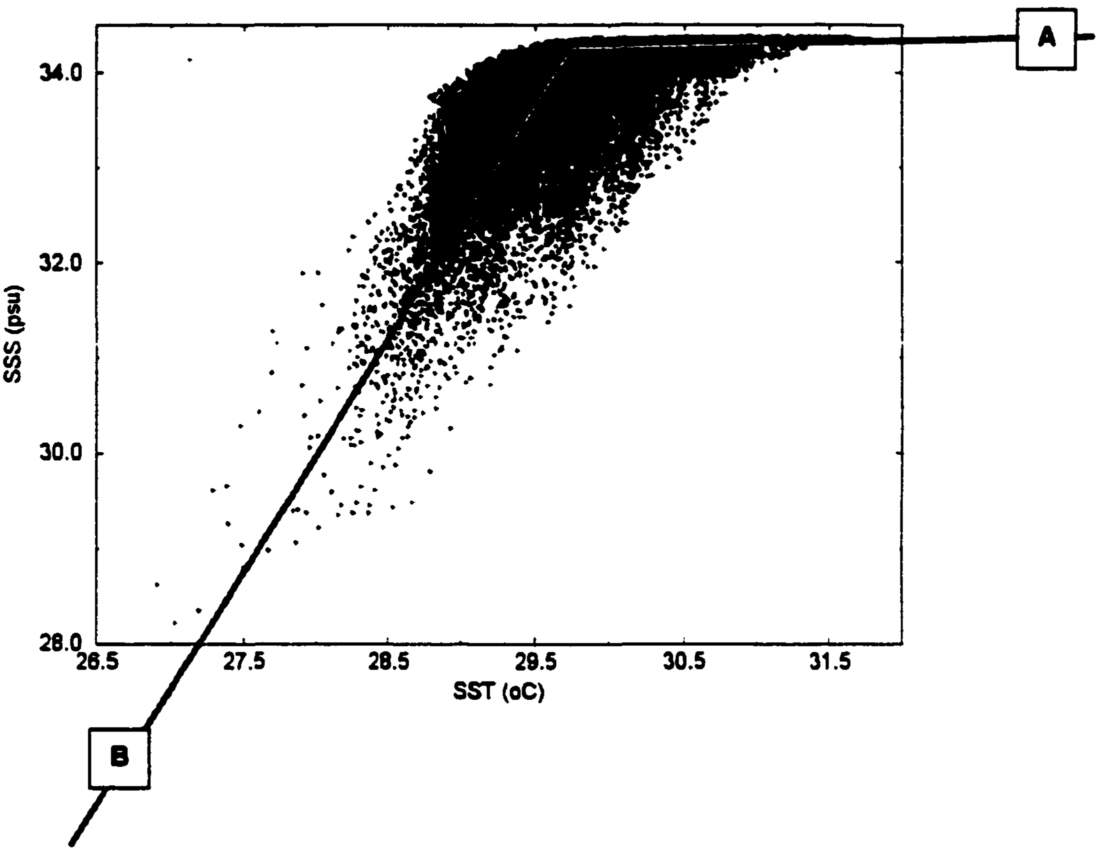

Figure 7.13 - Scatter plot of the simulated sea surface salinity against the sea surface temperature for Case 1. The gray lines represent idealizations of the diurnal heating and cooling (A) and the cooling and freshening associated with precipitation (B).

The crucial distinction between those two groups of processes was shown in our modeling study and illustrated in Figures 7.13 and 7.14, which represents scatter plots of SST and SSS for Cases 1 and 2, respectively. As in Webster's (1994) Figure 14, theoretical axes are superimposed on the scatter plots in our Figures, representing particular physical processes. The diurnal warming and cooling of the ocean surface is represented by the points lying on an almost horizontal line (axis A) at the top of both

Figure 7.13 and Figure 7.14. The points representing reduced SST and SSS in both panels are generally associated with precipitation (axis B). Webster's axis C is absent for two reasons: First, the regime in which evaporation and entrainment is the dominant process (trade-wind regime accompanying strong near-surface westerlies) was not simulated; Second, it requires a longer timescale to operate than the one associated with the other two processes.

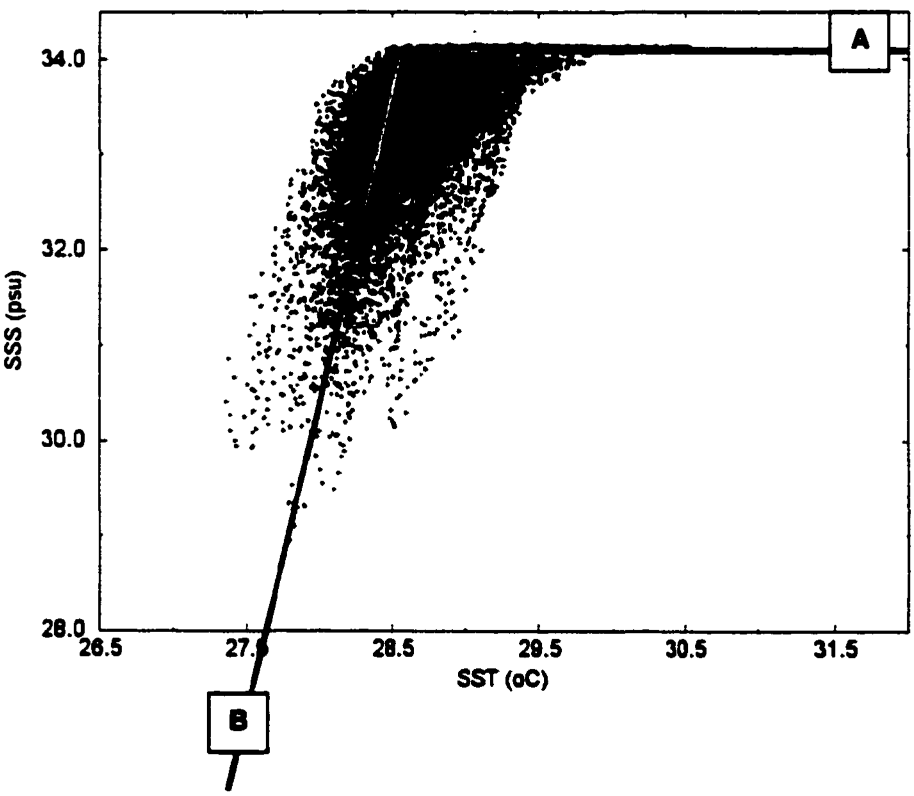

Figure 7.14 - Same as Figure 7.13, except for Case 2

The two scatter plots are similar, although Case 1 exhibited greatest maximum temperatures, and smaller minimum salinity and minimum temperature. This is obviously caused by the different surface-wind regime, with the stronger winds in Case 2 inducing more vertical mixing and avoiding extreme values of temperature and salinity at the ocean surface. It is also clear from Figures 7.13 and 7.14 that precipitation-produced freshwater anomalies are often cooler than its surroundings. In fact, as shown in Figures 7.15 and 7.16, the spatial correlation between SST and SSS tends to be close to one just after events of strong rainfall, as occurred between 11 and 14 December (Figure 7.15) and between 20 and 22 December and at 24 December (Figure 7.16). Especially under stronger near-surface winds, if precipitation is not present or is weak, the correlation between the SST and the SSS decreases rapidly with time. That occurred, for instance, late on 23 December, when convection was suppressed and the SST-SSS correlation decreased from 0.90 to 0.21 (minimum value, early on 24 December, Figure 7.16). A more dramatic example occurred early on 28 December, when the SST-SSS correlation changed signed, falling from 0.75 to -0.27 in 9h. During that period, the modeled precipitation was zero or almost zero (Figure 7.6), freshwater anomalies were mostly absent (Figure 7.11) and the evaporation was very significant, with a latent heat flux of more than 100 Wm^{-2} (Figure 7.7).

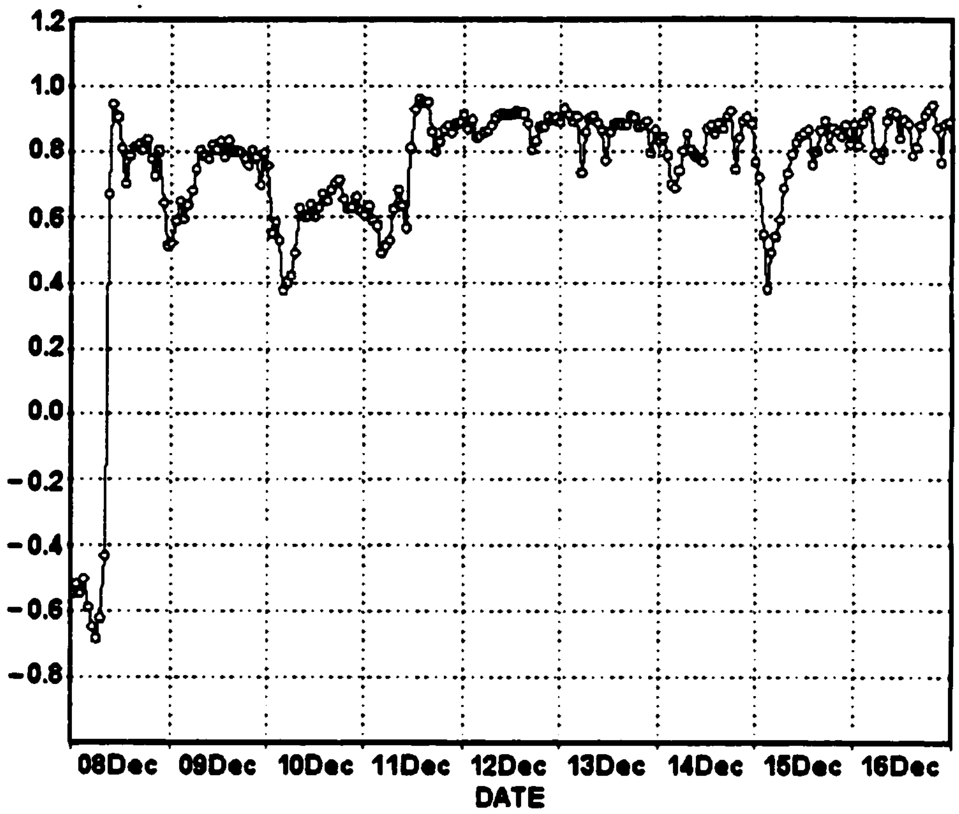

Figure 7.15 - Spatial correlation between the SST and the SSS, as a function of time, for Case 1

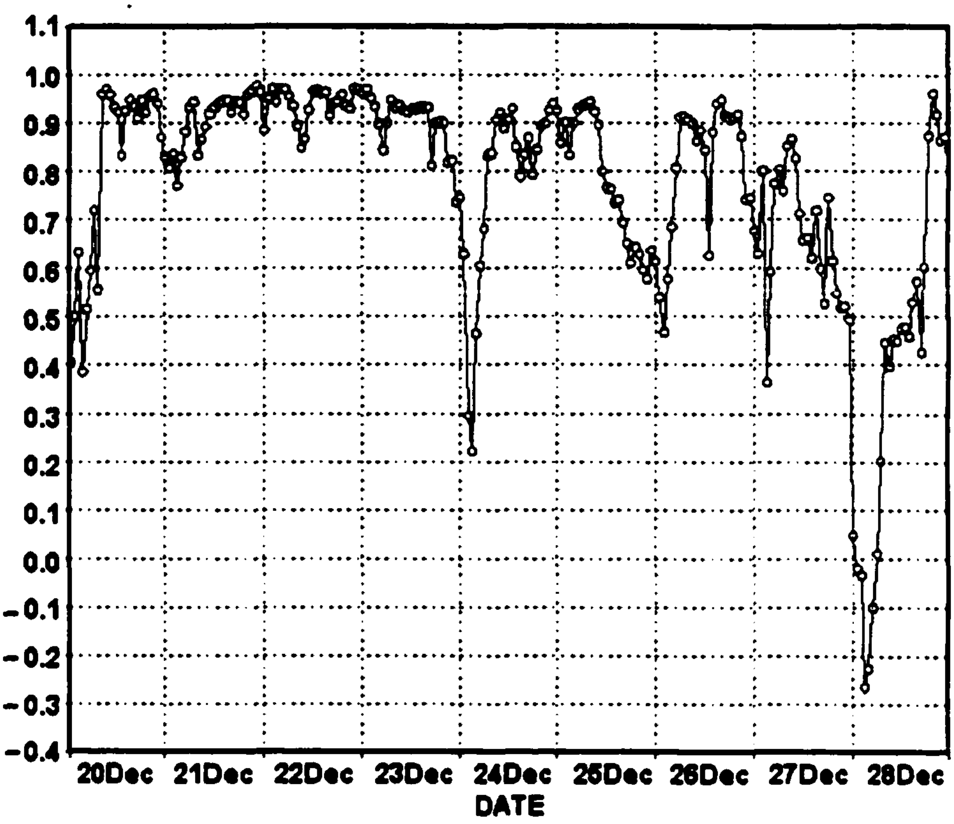

Figure 7.16 - Same as Figure 7.15, except for Case 2

Observations from TOGA-COARE, as described by Wijesekera et al. (1999), indicate that fresh anomalies have a complex structure of both their thermohaline and dynamic characteristics. The following are some of the features of a precipitation-produced freshwater disturbance described by Wijesekera et al. (1999):

1. The fresh anomaly, or freshwater lens, deepens with time, as a result of vertical transport;
2. Temperature and salinity are highly correlated within the lens, consistent with its formation by cool precipitation;
3. A jet (horizontal velocity anomaly) develops at the lens, in the direction of the wind, associated with the trapping of the momentum transferred from the atmosphere due to the haline stratification;
4. In relation to the jet, downwelling (upwelling) occurs at the downwind (upwind) edge of the lens.

Despite the limitations associated with the lack of the third dimension, the coupled model was able to simulate those characteristics. Figure 7.17 depicts a newly-formed fresh anomaly and its parent storm at 19Z 22 December, corresponding to two hours after the beginning of the precipitation event. The rainfall-generated freshwater lens is initially shallow. In Figure 7.17, salinity values of 34.0 psu, corresponding to a fresh anomaly of about 0.1psu are found to less than 6m of depth. The initial geometry of the lens is strongly dictated by the precipitation field.

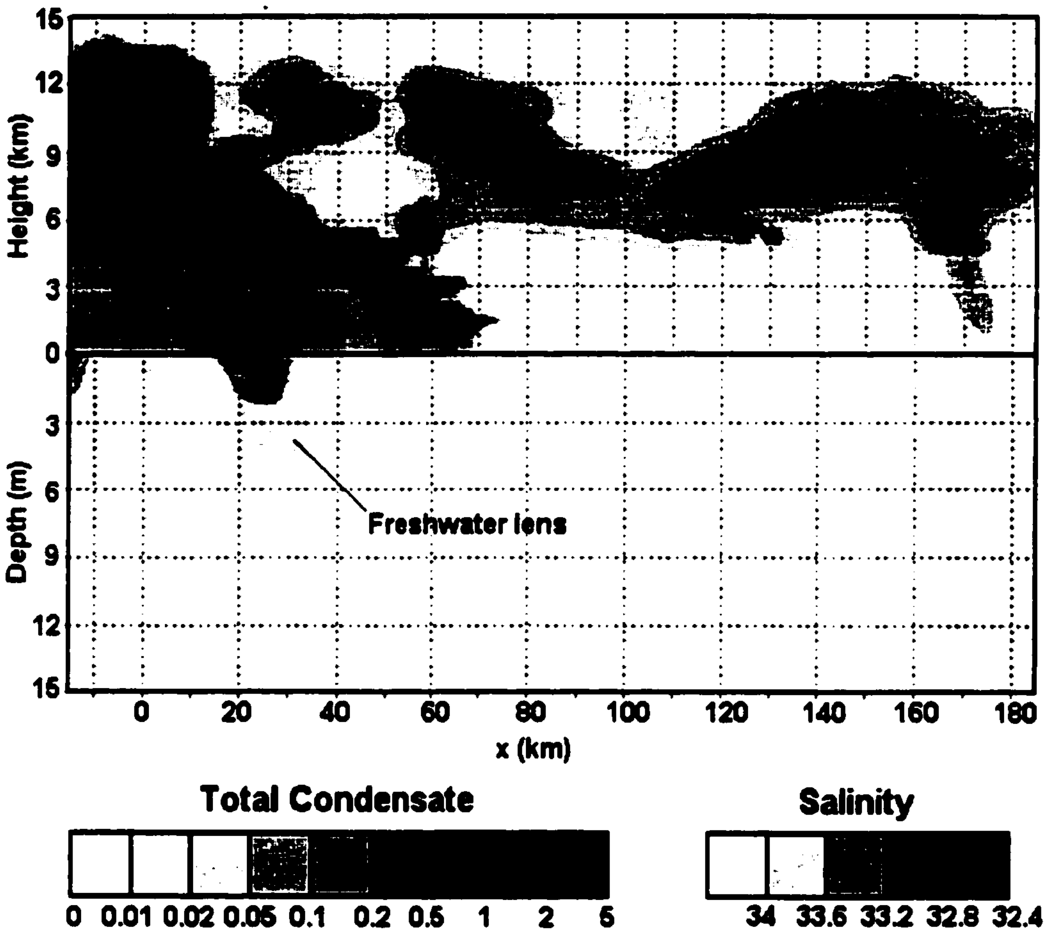

Figure 7.17 - A newly-formed freshwater lens and its parent storm at 19Z 22 December. The total condensate mixing ratio is shown in the upper panel (atmosphere) and the salinity field is depicted in the lower panel (ocean). The upper and lower panels have different vertical scales.

Some aspects of the time evolution of the same freshwater lens are shown in Figure 7.18. The two panels in Figure 7.18 are Hovmüller diagrams depicting the SSS and the vertical velocity at a depth of 22.5m (panel a), and the SST and the surface zonal current (panel b).

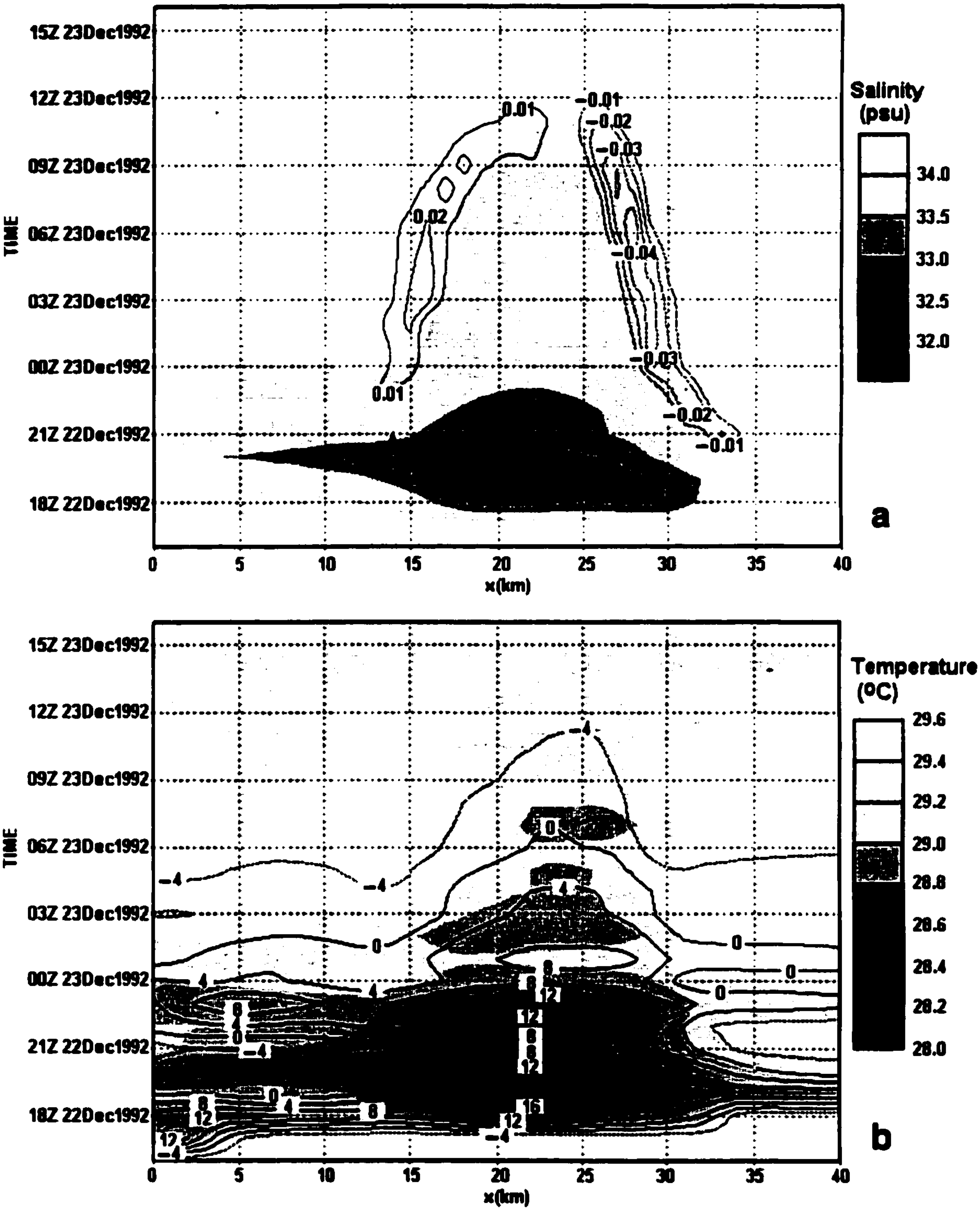

Figure 7.18 - Hovmuller diagrams of (a) SSS, in psu, and vertical velocity, in cm/s and (b) SST, in °C, and zonal current, in cm/s for a fresh anomaly. Only part of the model domain (0<x<40km) is shown.

As expected, after the end of the precipitation event, the amplitude of the fresh anomaly at the surface decreased with time, mostly due to vertical transport (Figure 7.18a). Concurrently, the lens contracted in the horizontal. During its whole life cycle, the freshwater lens was cooler than the environment (Figure 7.17b). The location and time of the SST and SSS minima coincided. A significant westerly anomaly developed in the surface zonal current, with a peak westward current of more than $0.16 ms^{-1}$ (Figure 7.18b). Such an anomaly was caused by the trapping of the westerly momentum transferred from the atmosphere in the shallow, salinity-stratified layer. In association with the anomaly in the horizontal current, downwelling developed at the downwind edge of the lens, while upwelling developed at the upwind edge. At a depth of 22.5m the downwelling was as strong as $4 \cdot 10^{-4}$ ms^{-1} (more than 30m/day), as shown in Figure 7.18a.

Some characteristics of the same simulated fresh anomaly in its mature stage are shown in Figure 7.19. This Figure depicts the salinity and vertical velocity (panel a) and the ocean temperature and zonal current (panel b) at 04Z 23 December (9 hours after its formation). The comparison between Figures 7.19a and 7.17 indicates the deepening of the fresh lens. In Figure 7.19a, the 34.0psu contour has deepened to a depth of about 16m (compared to less than 6m earlier). The base of the fresh anomaly is tilted, with a deeper fresh layer on its downwind (right) edge and a shallower layer on its upwind (left) edge. Due to the significant downwelling, fresh water is allowed to penetrate deep into the mixed-layer on the downwind side of the lens. As shown in Figure 7.19a, water with a salinity of less than 34.1psu was found down to a depth of about 40m. To the left of the lens, the increased SSS indicates the upwelling of deeper, saltier water. Figure 7.19b shows that the freshwater lens was significantly cooler than the environment, even several hours after its formation. Cool water is transported downward on the downwind side of the lens and warmer water is carried upward on the upwind side. As a consequence, the isotherms and the isohalines are tilted downward in the direction of the surface wind. The existence of a jet coinciding with the fresh, cool anomaly is evident in Figure 7.19b, with a positive (eastward) perturbation zonal current of about 7cm/s. Below the lens, the perturbation current changes sign, becoming negative (westward).

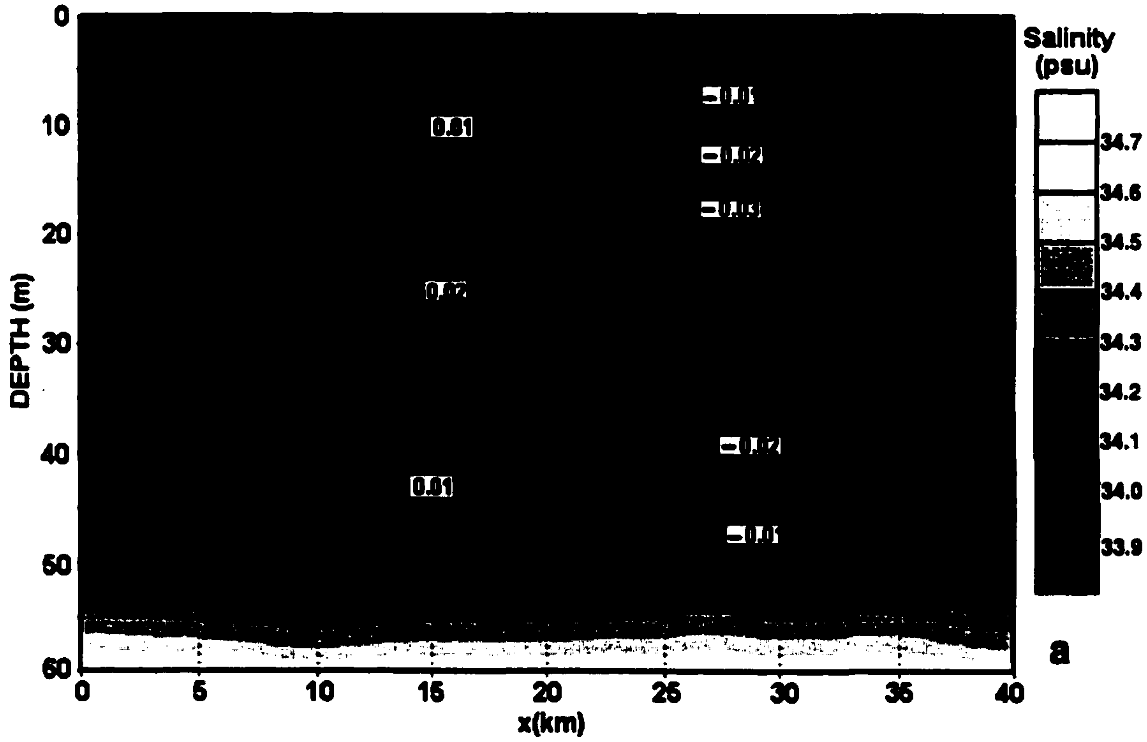

Figure 19 - Vertical cross section of the same fresh anomaly depicted in Figure 7.17, in a later time (04Z 23 December), showing (a) salinity, in psu, and vertical velocity, in cm/s, and (b) ocean temperature, in °C, and zonal current, in m/s.

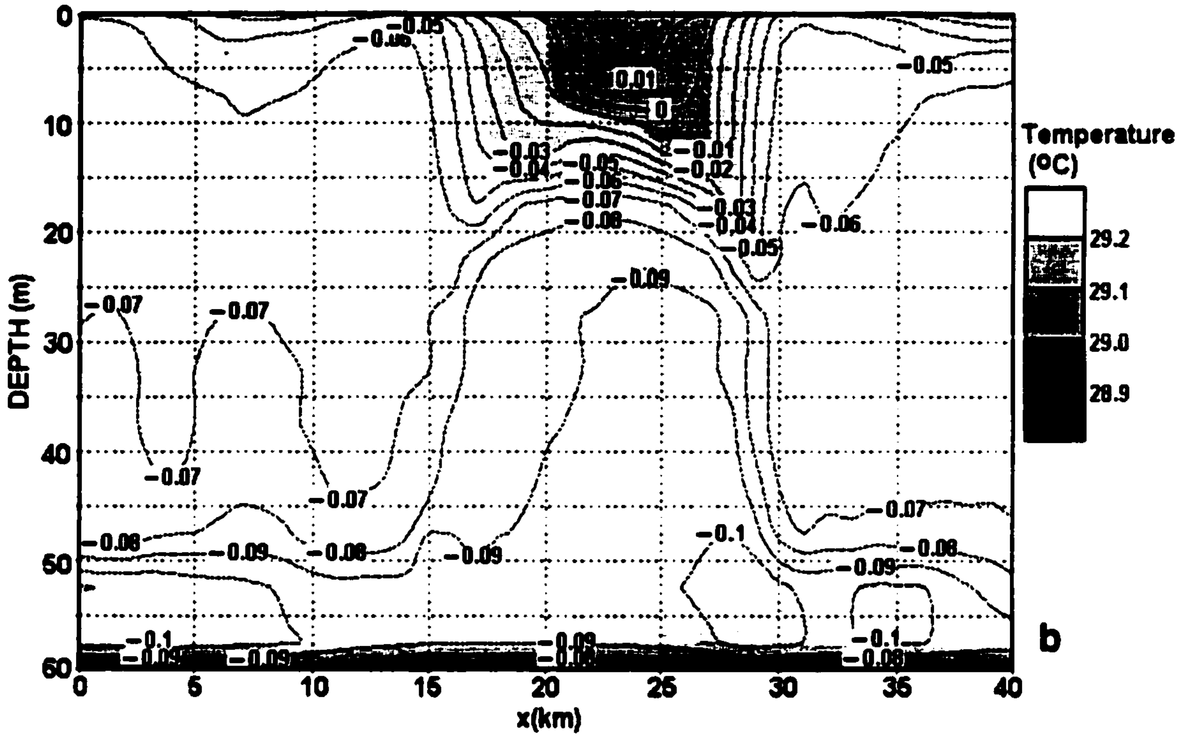

Figure 7.19 - continuation

7.3 - Comparison with uncoupled simulations

In order to assess the influence of the surface heterogeneous forcing on the CRM statistics, uncoupled simulations were performed, in which the atmospheric model was forced by a homogeneous SST equal to the time-evolving averaged surface temperature calculated by the ocean model in each of the two coupled simulations. This procedure assures that the influence of the magnitude of the SST is, at least on average, the same, and that the effect of the SST inhomogeneities can be isolated.

7.3.1 - Case 1

The prescribed SST used to force the uncoupled CRM in the simulation of Case 1, and derived from the date generated by the coupled model is shown in Figure 7.20. A comparison with the corresponding observed field (Figure 3.6) reveals a more pronounced diurnal cycle, particularly in the beginning of the simulation.

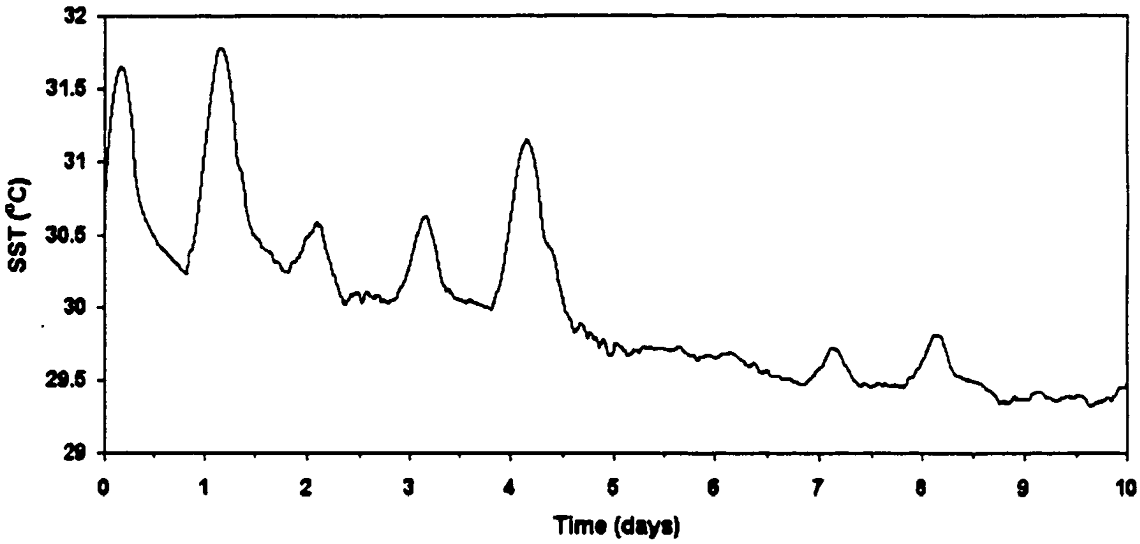

Figure 7.20 - Time evolution of the domain-averaged SST, Case 1.

As in the sensitivity studies in Chapter 5, the evolving advective tendencies had the greatest influence in determining the characteristics of the simulated cloud systems. As a consequence, both the coupled and uncoupled runs exhibited similar statistics. However, the inhomogeneous surface forcing, the temporal and spatial organization of the convective systems was modified in the coupled simulation.

A comparison is shown in Table 7.3 between several time- and space-averaged variables from the coupled run and their counterparts from the uncoupled simulation.

Variable	Coupled simulation	Uncoupled simulation
Total precipitation (mm/day)	13.15	12.92
Convective precipitation (mm/day)	10.72 (81.52% of the total)	10.27 (79.49% of the total)
Stratiform precipitation (mm/day)	2.43 (18.48% of the total)	2.65 (20.51% of the total)
Sensible heat flux (Wm^{-2})	11.18	11.42
Latent heat flux (Wm^{-2})	83.43	83.21

Table 7.3 - Averages (over the model domain and the simulated period) of the total, convective and stratiform precipitation and sensible and latent heat flux for the coupled and uncoupled simulations of Case 1.

The results above show that the surface parameters varied only slightly from one simulation to another. The total precipitation increased 1.8% from the uncoupled to the coupled run, suggesting that, at least under the type of conditions prevailing during Case 1, small-scale circulations induced by the SST variability are able to contribute to enhanced precipitation. The average total surface heat flux (sensible plus latent) was basically unaltered: 94.61 Wm^{-2} in the coupled simulation versus 94.63 Wm^{-2} in the uncoupled simulation, the sensible (latent) component was barely favored in the uncoupled (coupled) run. In terms of the convective-stratiform partition of the precipitation field, it was clear that all enhanced precipitation came from convective cores (the convective precipitation was 2.4% greater in the coupled run). This result agrees with what was expected, based on the numerical experiments described in Section 5.3.

The convective component was favored in this case, primarily due to the influence of SST inhomogeneities with intermediate spatial scales, as depicted in Figure

7.21. The two panels depict the time-average of the Fourier transformation of the SSS (panel a) and the SST (panel b), given by the equations:

$$\widehat{SSS}(t,\lambda) = \frac{1}{2\pi L}\int_0^L SSS(t,x)\exp\left(-i\frac{2\pi x}{\lambda}\right)dx \tag{7.1}$$

and

$$\widehat{SST}(t,\lambda) = \frac{1}{2\pi L}\int_0^L SST(t,x)\exp\left(-i\frac{2\pi x}{\lambda}\right)dx\,, \tag{7.2}$$

where λ is the wavelength, and L represents the model domain size (512km).

Both transformations are well correlated, and show significant influence of SST/SSS wavelengths on the order of 100km, a value close to the 64km wavelength used in the MEDIUM simulation, which results were reported in Chapter 5. This is possibly associated with the increase in the convective component of the total precipitation in the coupled simulation.

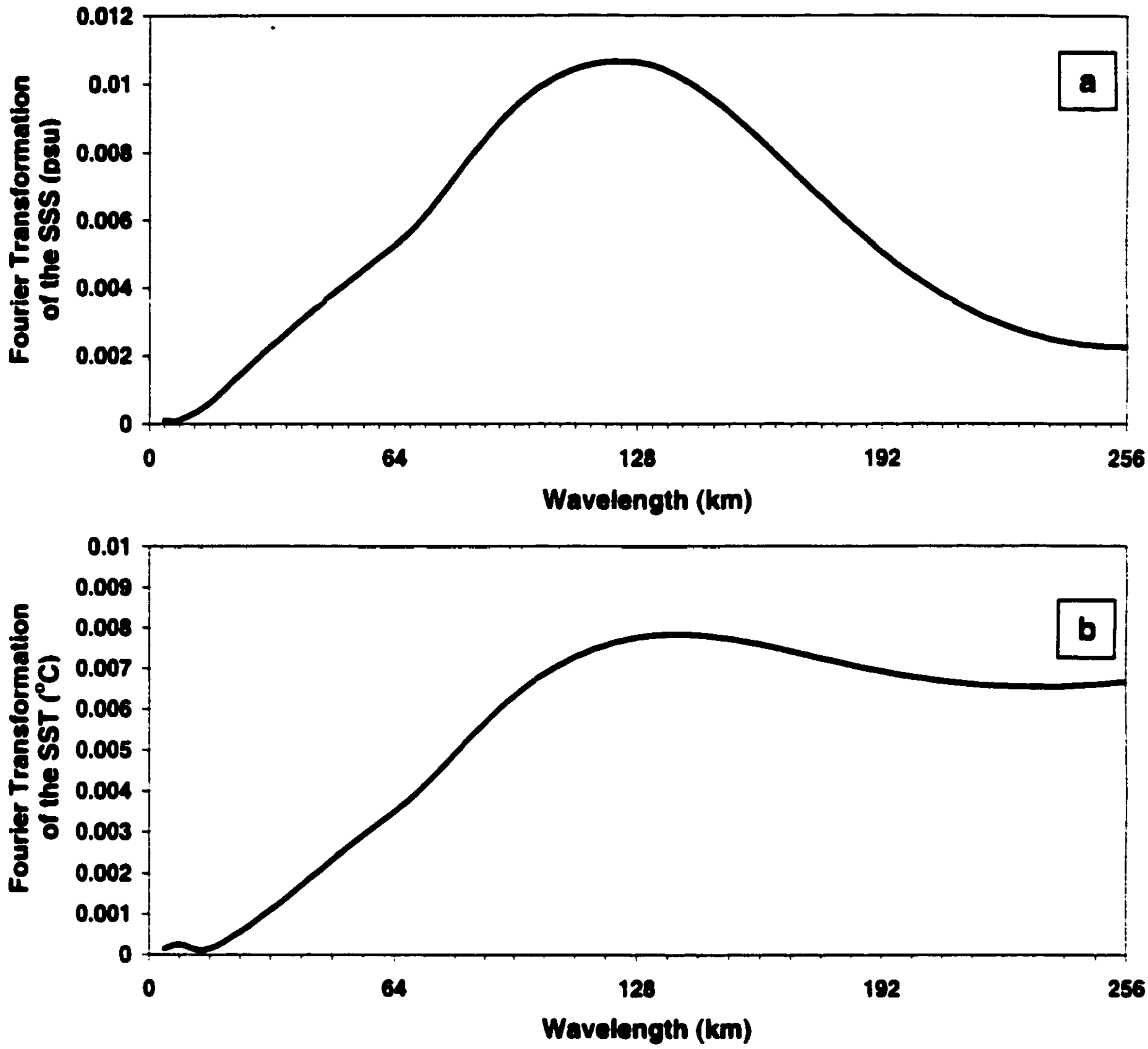

Figure 7.21 – Fourier transformation in space of the (a) SSS and (b) SST, averaged over the 10-day period, for the coupled simulation of Case 1.

7.3.2 - Case 2

A similar uncoupled simulation was performed focusing on the Case 2, and the time evolution of the homogeneous SST used to drive the uncoupled model is depicted in Figure 7.22.

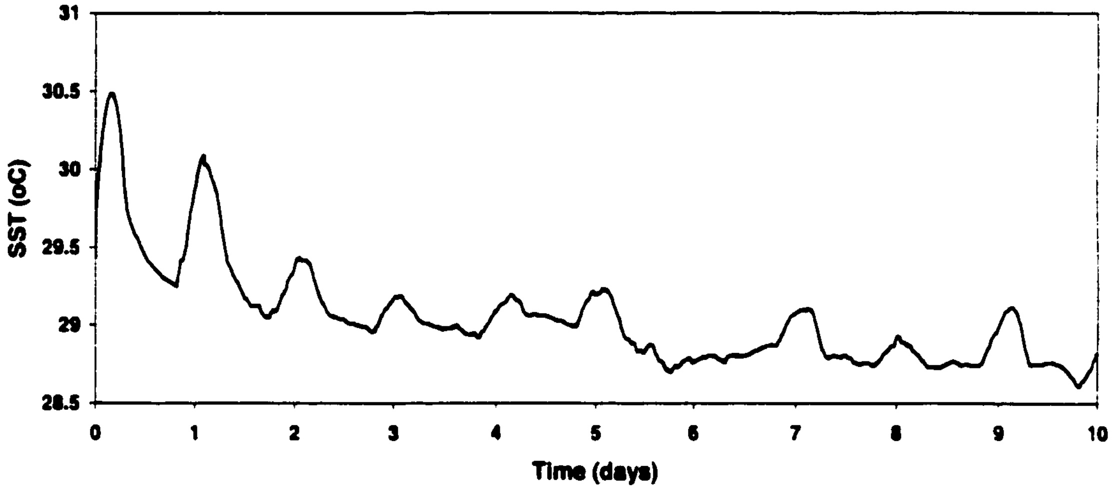

Figure 7.22 – Same as Figure 7.20, except for Case 2

Some of the averages over the model domain and the simulation period for the coupled and uncoupled simulation for Case 2 are presented in Table 7.4. The results were mostly in agreement with the findings for Case 1. For instance, as in the previous case, the coupled model produced a slightly larger total precipitation, although one cannot assure the statistical significance of such result. Again, the differences in the sensible and latent heat fluxes in the coupled and uncoupled runs were extremely small. Those similarities suggest that, at least regarding the influence of the ocean coupling on the total precipitation and surface heat fluxes, the model behavior is relatively insensitive to the type of deep convective regime (weakly sheared environment and weak near-surface winds, in Case 1, versus relatively large shear and moderate near-surface winds in Case 2).

Variable	Coupled simulation	Uncoupled simulation
Total precipitation (mm/day)	15.86	15.63
Convective precipitation (mm/day)	11.24 (70.87% of the total)	11.05 (70.70% of the total)
Stratiform precipitation (mm/day)	4.62 (29.13% of the total)	4.58 (29.30% of the total)
Sensible heat flux (Wm^{-2})	18.65	18.51
Latent heat flux (Wm^{-2})	135.61	135.21

Table 7.4 – Same as Table 7.3, except for Case 2.

On the other hand, the sensitivity regarding the convective-stratiform partition of the precipitation rate was smaller in Case 2. As shown in Table 4, the percentage of convective and stratiform precipitation is approximately the same in both simulations. Several factors can contribute to this model insensitivity. First, as discussed by Dalu et al. (1996), and briefly in Chapter 5 in reference to the uncoupled runs with imposed sinusoidal SST patterns, horizontal advection can diminish the effect of the inhomogeneous surface forcing in the coupled simulation. Second, convection in Case 2 is more organized and is probably less sensitive to the influence from the surface. Third, as discussed previously, SST inhomogeneities were often short-lived in Case 2, in comparison to their counterparts in Case 1. In fact, the plots of the spatial Fourier transforms of the SSS and SST for Case 2 (Figure 7.23), reveal a smaller amplitude of the signals in almost all wavelengths, as well as the dominance of larger modes (wavelengths greater than 200km). As discussed in Chapter 5, "long-wave" SST modes show little influence on the convection organization.

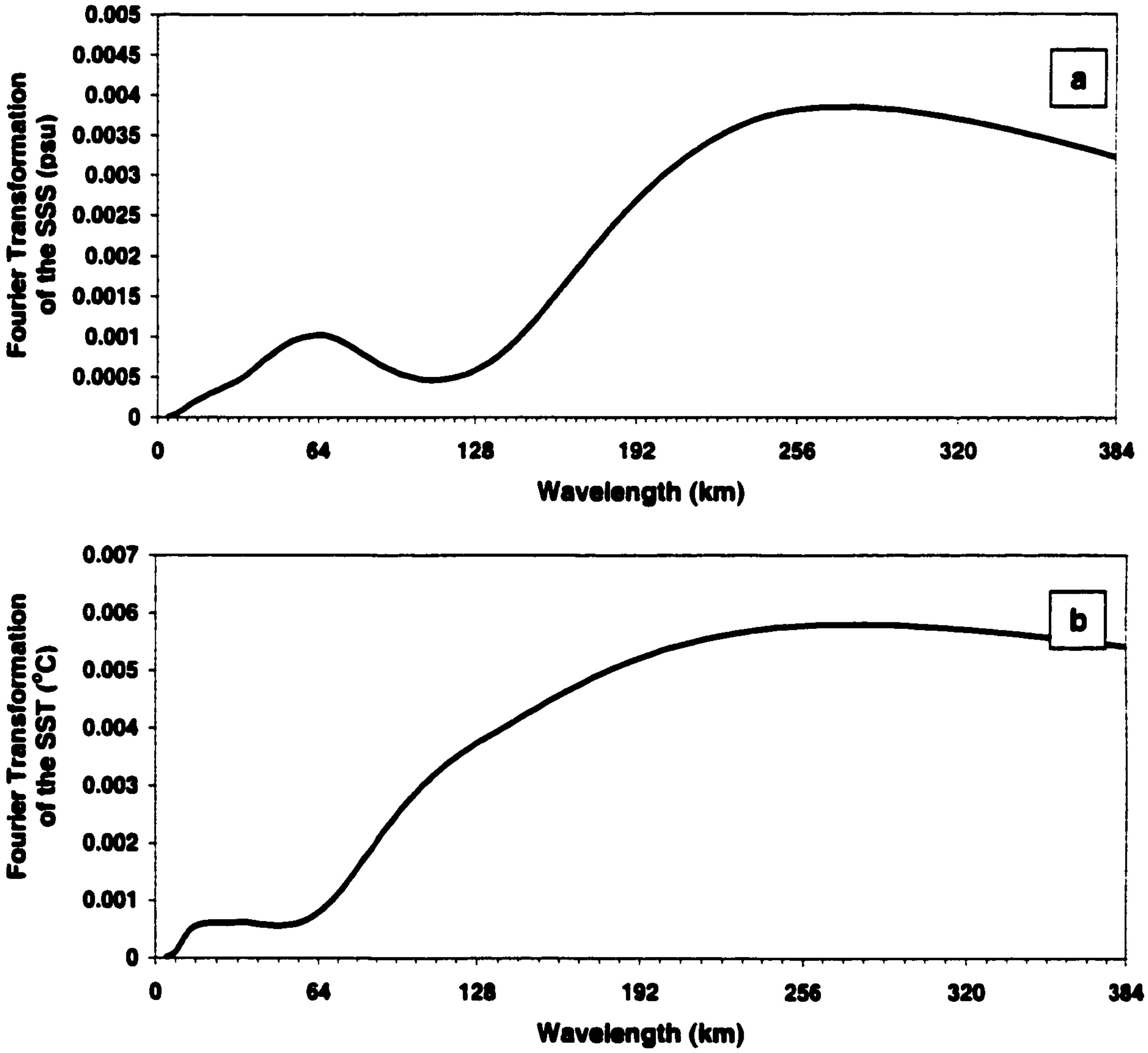

Figure 7.23 – Same as Figure 7.21, except for Case 2.

Chapter 8

SST INFLUENCES ON Q_1 AND Q_2

Passou a nuvem; o sol volta. *A alegria girassolou.* *Pendão latente de revolta,* *Que hora maligna te enrolou?*	The cloud passed; the sun returns. Happiness "sunflowered". Latent rebel flag, What evil hour did lower you?

(Fernando Pessoa, Portuguese poet)

Based on observations of both tropical and mid-latitude convective systems, several researchers have shown that the vertical profiles of both heating and drying rates are different in regions of convective and stratiform precipitation (e.g., Houze 1982; Johnson 1984; Cheng and Yanai 1989; Lin and Johnson 1994; Greco et al. 1994, etc.). Convective regions present warming and drying through most of the troposphere. In contrast, stratiform regions produce warming and drying at the upper troposphere only. At low levels (roughly below the melting level), regions of stratiform precipitation are often characterized by cooling and moistening.

In this chapter, observations of the apparent heat source (Q_1) and apparent moisture sink (Q_2) during TOGA-COARE are shown, along with a comparison between them and the CRM results for the simulations described in previous chapters. Following, the influences of the SSTs on the Q_1 and Q_2 profiles are examined. Finally, a simple analytical representation of those profiles is used to provide explanation for some of the results shown.

8.1 – Observed and Modeled Q_1 and Q_2

The apparent heat source (Q_1) and the apparent moisture sink (Q_2) are associated with the atmospheric response to large-scale advection (horizontal plus vertical) of temperature and moisture. Because the tropical atmosphere shows little deviation in its vertical profile (CAPE is consumed by convection to provide a quasi-moist adiabatic sounding), the time evolution of Q_1 and Q_2 tends to be similar to that of the large-scale advective tendencies of temperature and water vapor mixing ratio, respectively. Such similarity becomes obvious comparing, for instance, Figure 8.1, which depicts the time evolution of the Q_1 and Q_2 profiles for Case 2 and the panels c and d of Figure 3.5. The same behavior was found for Case 1 (Figure not shown).

In order to illustrate the model capabilities in simulating the observed profiles of warming and drying, Figure 8.2 depicts the time evolution of the modeled Q_1 and Q_2 profiles for Case 2 in the CONTROL simulation, described in Chapter 5, in which the uncoupled model was used. In addition, Figures 8.3 and 8.4 shows plots of the 7-day averaged Q_1 and Q_2 for Case 2, in the CONTROL simulation.

A comparison between Figures 8.2 and 8.3 shows that the model is able to simulate the evolution of the apparent heat source and apparent moisture sink, showing significant warming and drying on 20, 21, 22 and 24 December.

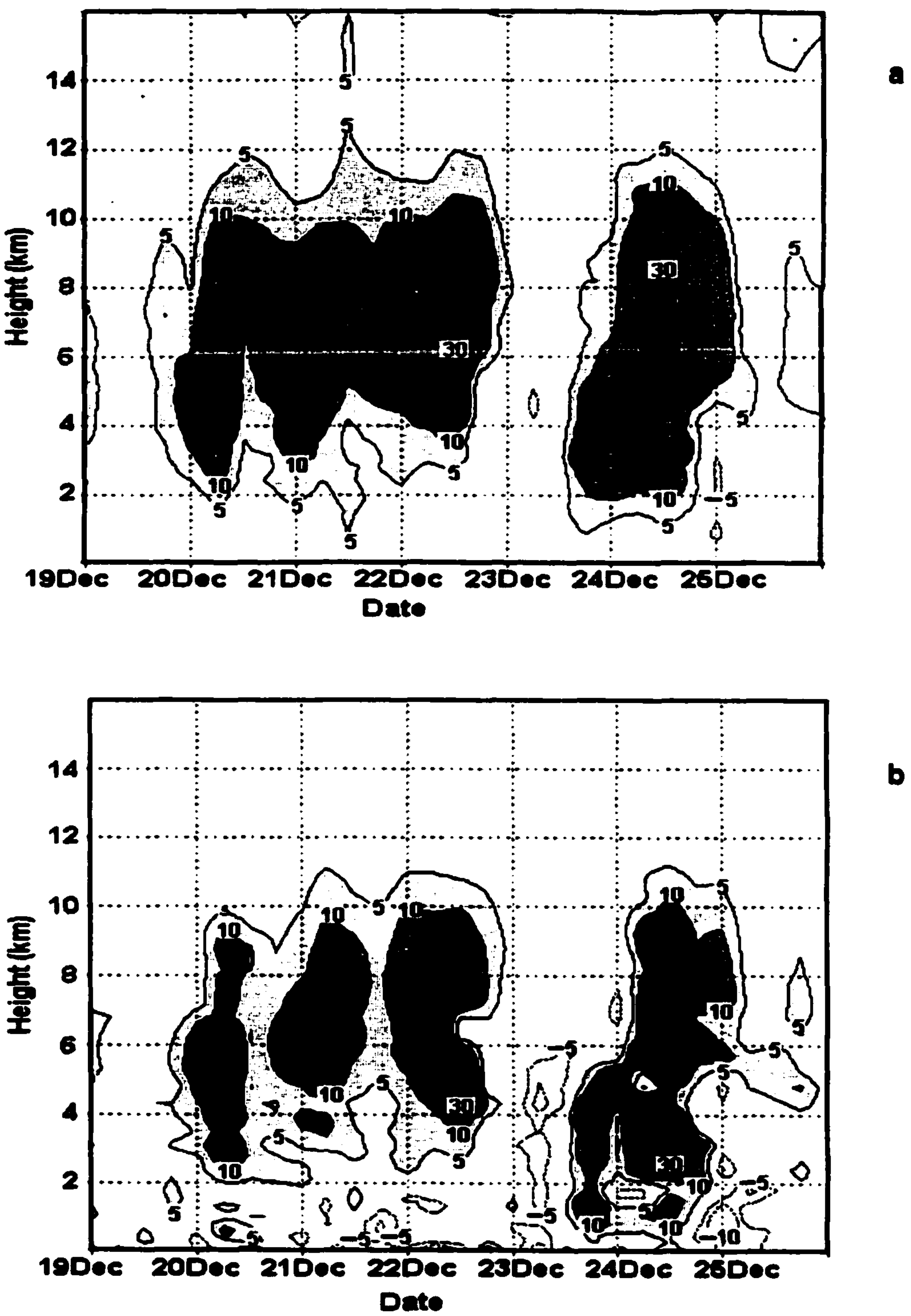

Figure 8.1 – (a) Apparent heat source and (b) apparent moisture sink, from budget calculations over the COARE IFA, between 19 and 26 December 1992 (Case 2). Values greater than 5K/day are shaded.

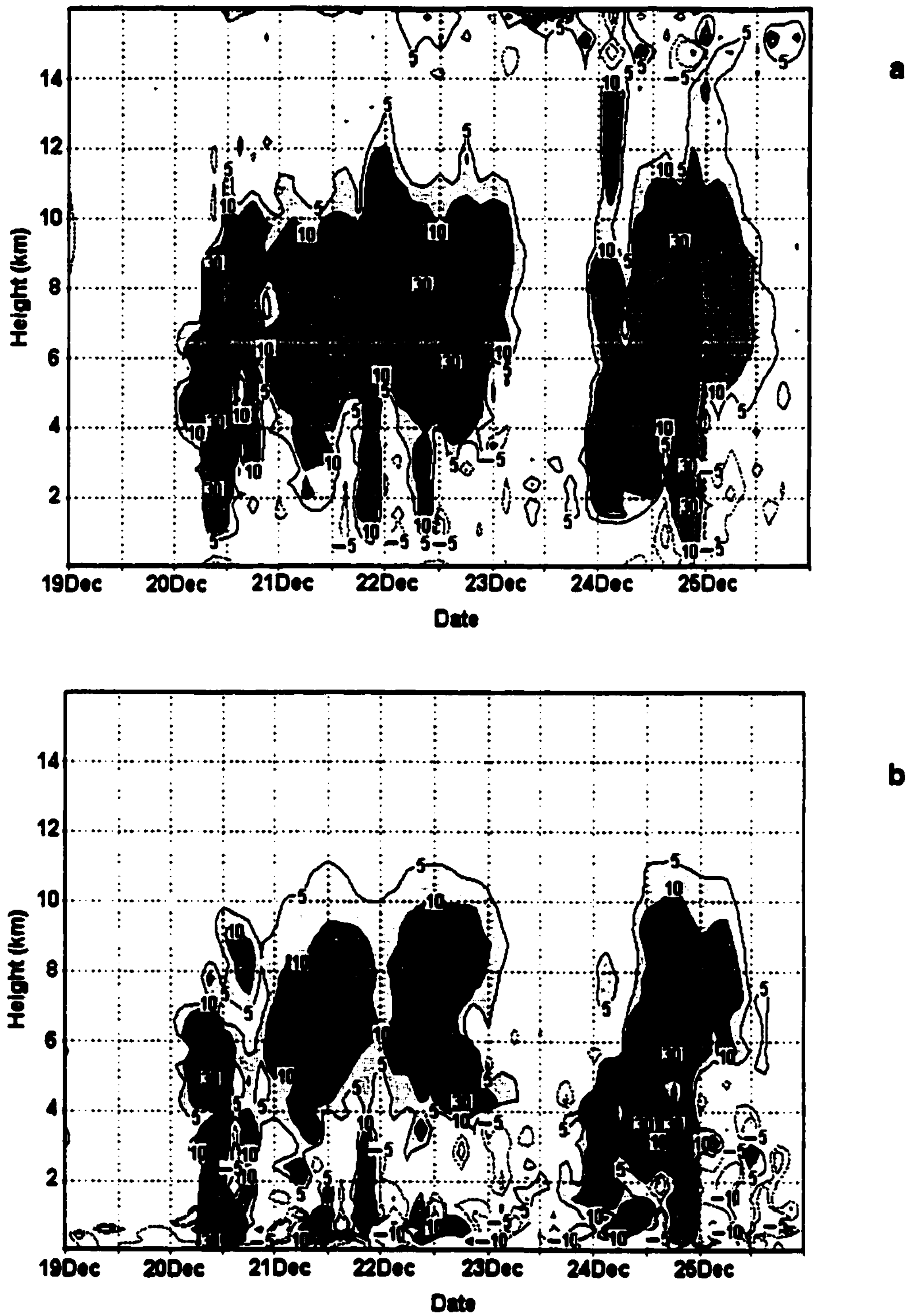

Figure 8.2 – (a) Apparent heat source and (b) apparent moisture sink, from the CONTROL simulation. Values greater than 5 K/day are shaded.

In addition, both average profiles in Figure 8.3 and 8.4 show, in general, only small departures between them. Similarly, the coupled model provided average Q_1 and Q_2 profiles in good agreement with the observations in both Case 1 and Case 2.

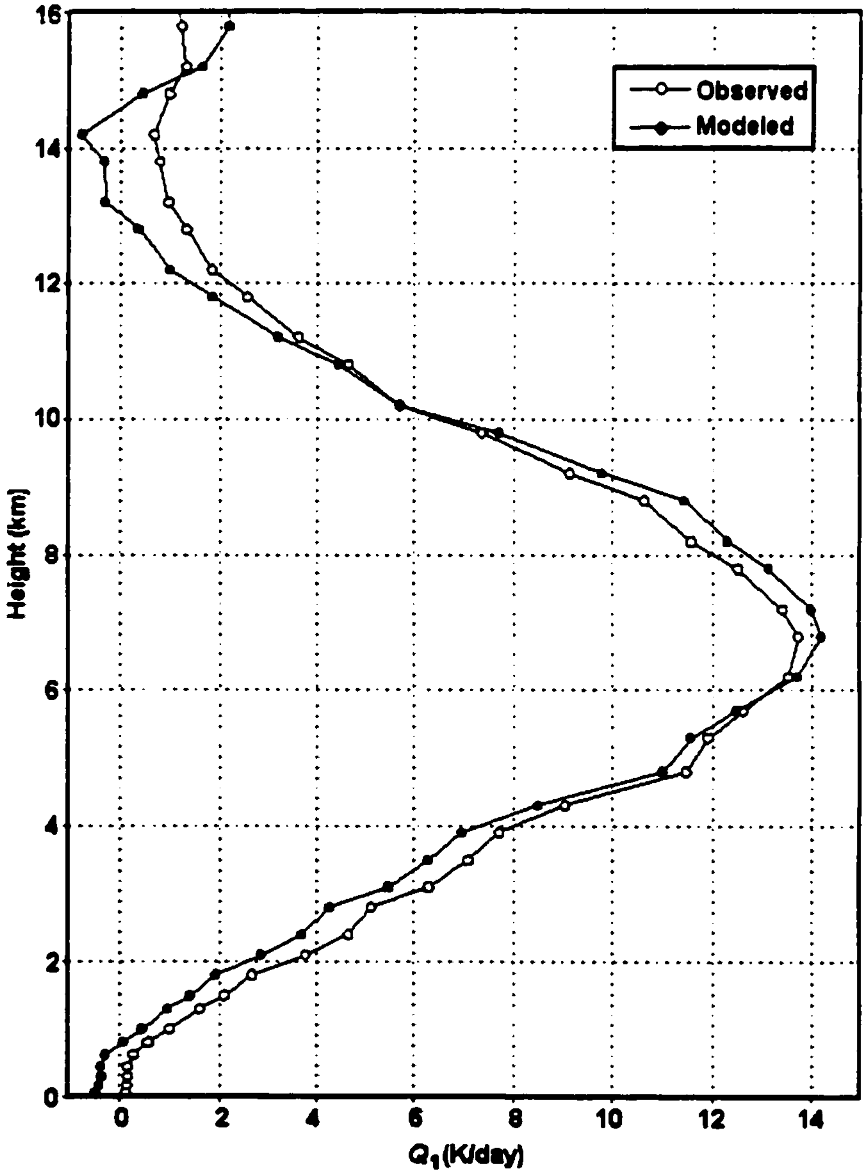

Figure 8.3 – 7-day mean of the observed and modeled (CONTROL simulation) apparent heat source, between 19 and 26 December.

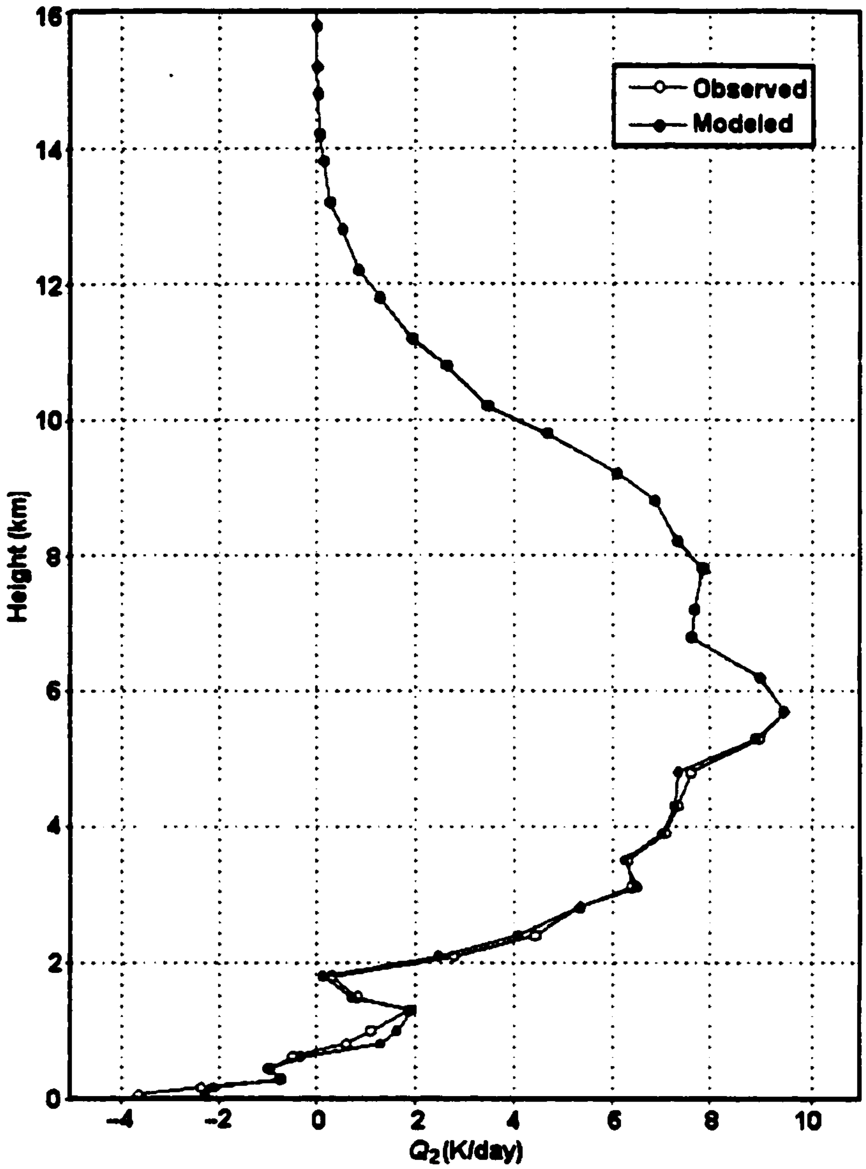

Figure 8.4 – Same as Figure 8.3, except for apparent moisture sink

8.2 – Convective and stratiform Q_1 and Q_2

As discussed in Chapter 2, cloud-resolving models yield partitioning convective systems in their convective and stratiform components. Once the precipitating columns are divided in convective and stratiform, one can calculate the contribution from each class of columns to the apparent heat source and apparent moisture sink.

The resulting Q_1 and Q_2 partitioning from the CONTROL simulation are depicted in Figures 8.5 and 8.6, respectively.

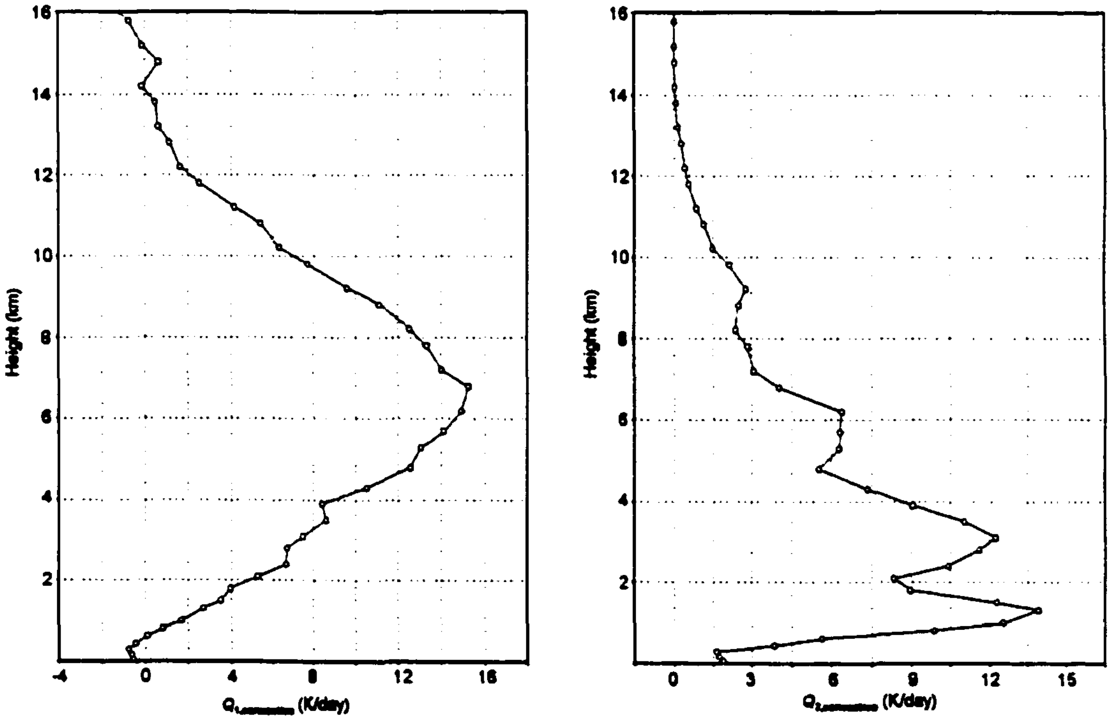

Figure 8.5 – Average profiles of the apparent heat source (left panel) and apparent moisture sink (right panel) averaged over convective columns only. From the CONTROL simulation

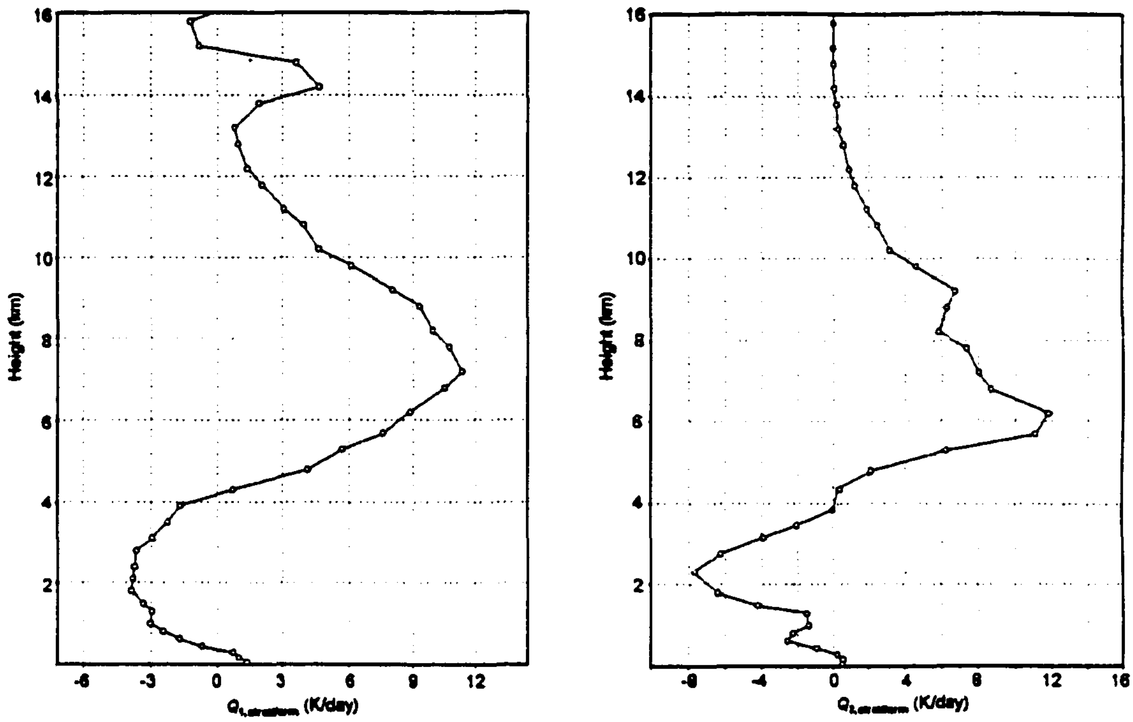

Figure 8.6 – Same as Figure 8.5, except for stratiform columns

Not surprisingly, the warming and drying in the model convective columns extended throughout most of the troposphere, while the stratiform profiles exhibited a dipolar structure, with a sign change occurring about the height of the melting level (roughly 5km). Simulated Q1 and Q2 peaked at different heights, a signature of active convective transport. The results shown in Figures 8.5 and 8.6 show good agreement with other modeling studies in which partitioning was made between convective and stratiform components of cloud systems (e.g., Xu 1996, Alexander and Cotton, 1998), as well as observations of heating rates in tropical convective and stratiform system. A comparison can be made between Figures 8.5 and 8.6 and observed Q_1 and Q_2 in convective and stratiform clod systems during TOGA-COARE depicted in Figure 8.7 (from Yang and Smith, 1999).

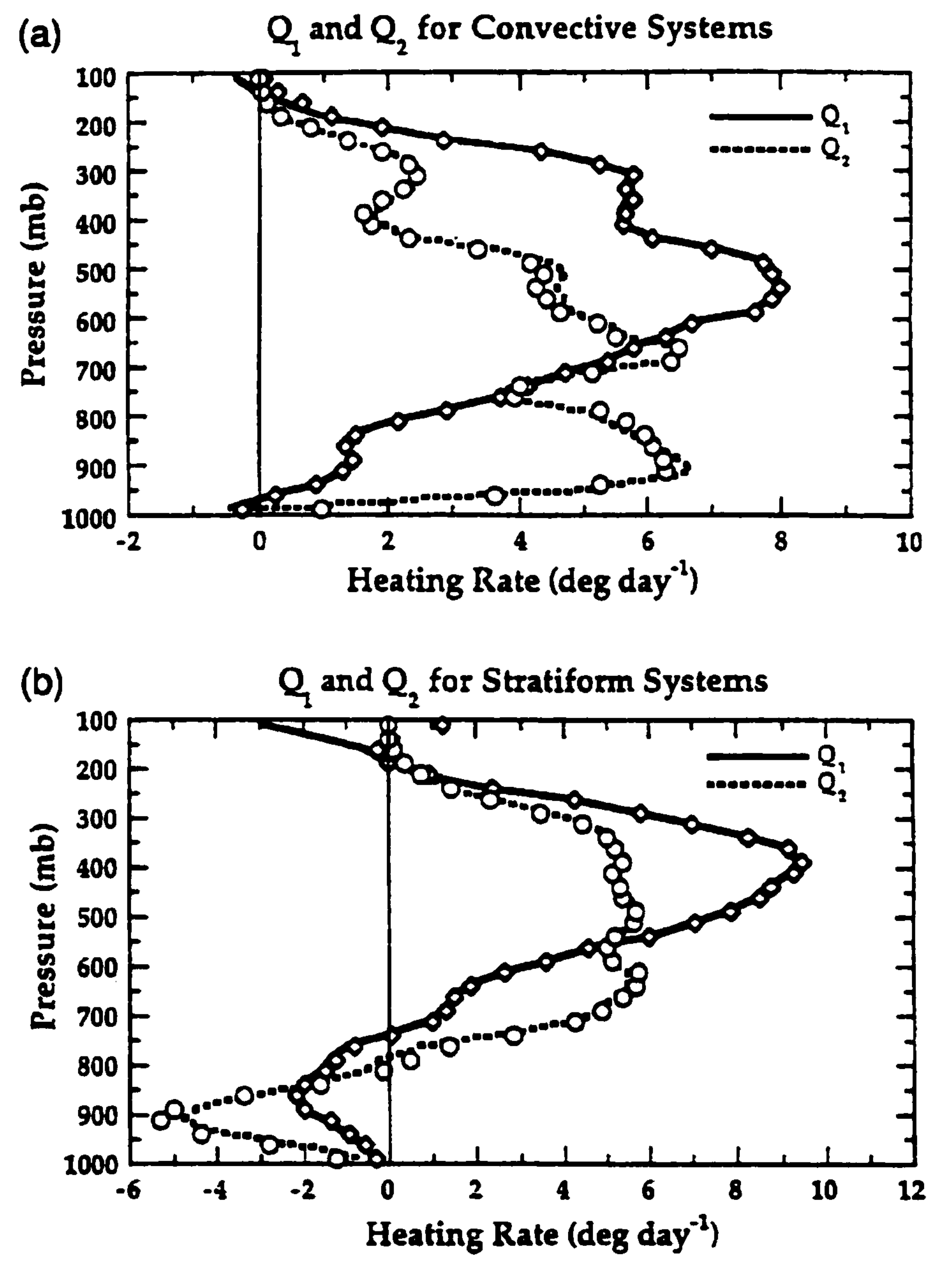

Figure 8.7 - Averaged Q_1 and Q_2 profiles over TOGA COARE IFA for convective (top panel) and stratiform systems (bottom panel). A straight (dashed) line and diamonds (circles) represent Q_1 (Q_2) calculated from two different methods (from Yang and Smith, 1999).

The comparison is obviously limited to qualitative aspects, since the analyzed periods were different (Yang and Smith focused on the study of TOGA COARE convection between 01 and 17 January 1993). The amplitude of the warming and drying was obviously not the same. However, several features are common in the previous Figures, indicating the existence of patterns that were general in the TOGA COARE region, at least for the IOP. For instance, in Figure 8.5 and 8.7, the convective Q_1 exhibits a pronounced peak in mid-levels, although the location was not identical (the maximum modeled convective Q_1 for Case 2 was positioned above 6km, while the peak in the analysis by Yang and Smith 1999 was located below 500mb). Convective Q_2 showed multiple maxima (four peaks in both the right panel of Figure 8.5 and the upper panel of Figure 8.7). The lowest was located at about 1km (Figure 8.5) or approximately 900mb (Figure 8.7). A second peak was found close to the 3km level in Figure 8.5 and about the 700mb level, while a third peak can be noted at roughly 6km (Figure 8.5) or 500mb (Figure 8.7), although the amplitude of the latter was very small in the observations. A last peak appeared right above 9km in the modeled convective Q_2 and at about 300mb in Yang and Smith's observations. Observed and modeled stratiform systems also exhibited a similar behavior. Maximum warming in the left panel of Figure 8.6 occurred at about 7km, which is comparable to the peak warming at 400mb in the lower panel of Figure 8.7. Maximum low-level cooling also appeared at comparable levels in those two Figures (2km in the left panel of Figure 8.6 versus 850mb in the lower panel of Figure 8.7). The most significant differences between observed and modeled Q_1 and Q_2 were found in the profile of the stratiform apparent moisture sink. Along with discrepancies in the shape of the stratiform Q_2 profile, the maximum drying and moistening in the right panel of Figure 8.6 and in the lower panel of Figure 8.7 were not found in the same location.

8.3 – SST Sensitivities

As in most of the fields analyzed in previous chapters, the apparent heat source and the apparent moisture sink were primarily governed by the characteristics of the large-scale forcing.

8.3.1 – Changes due to average SST variations

In general, the greatest sensitivities found were associated with the magnitude of the SST. As expected, increased SSTs generated more warming and drying, while smaller values of Q_1 and Q_2 occurred when the SSTs were decreased. Figures 8.8 and 8.9 respectively show the differences between the apparent heat source and the apparent moisture sink in the simulations SST+, SST- and CONTROL, described in Chapter 5. Variations of the order of 0.5 Kday^{-1} in Q_1 and 1.0 Kday^{-1} in Q_2 were found. It should be pointed out that the maximum Q_1 and Q_2 variations occurred at completely different levels: Q_1 changes were greater in the upper troposphere (above 11km), while Q_2 differences were more pronounced about the 1km level.

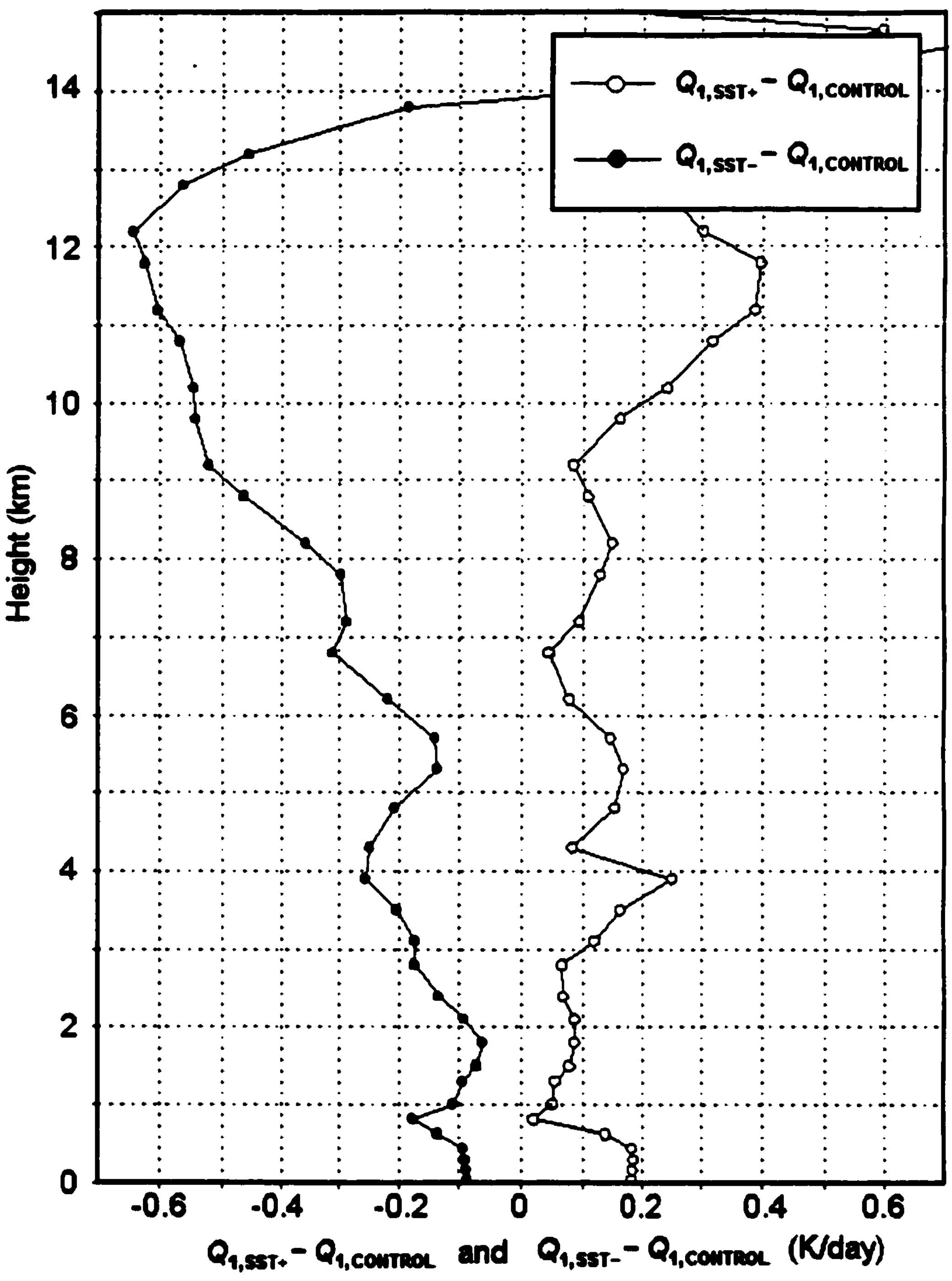

Figure 8.8 - Difference between the averages of the apparent heat source over the atmospheric model domain and the 7-day period in the SST+ and SST- simulations and CONTROL, as a function of height.

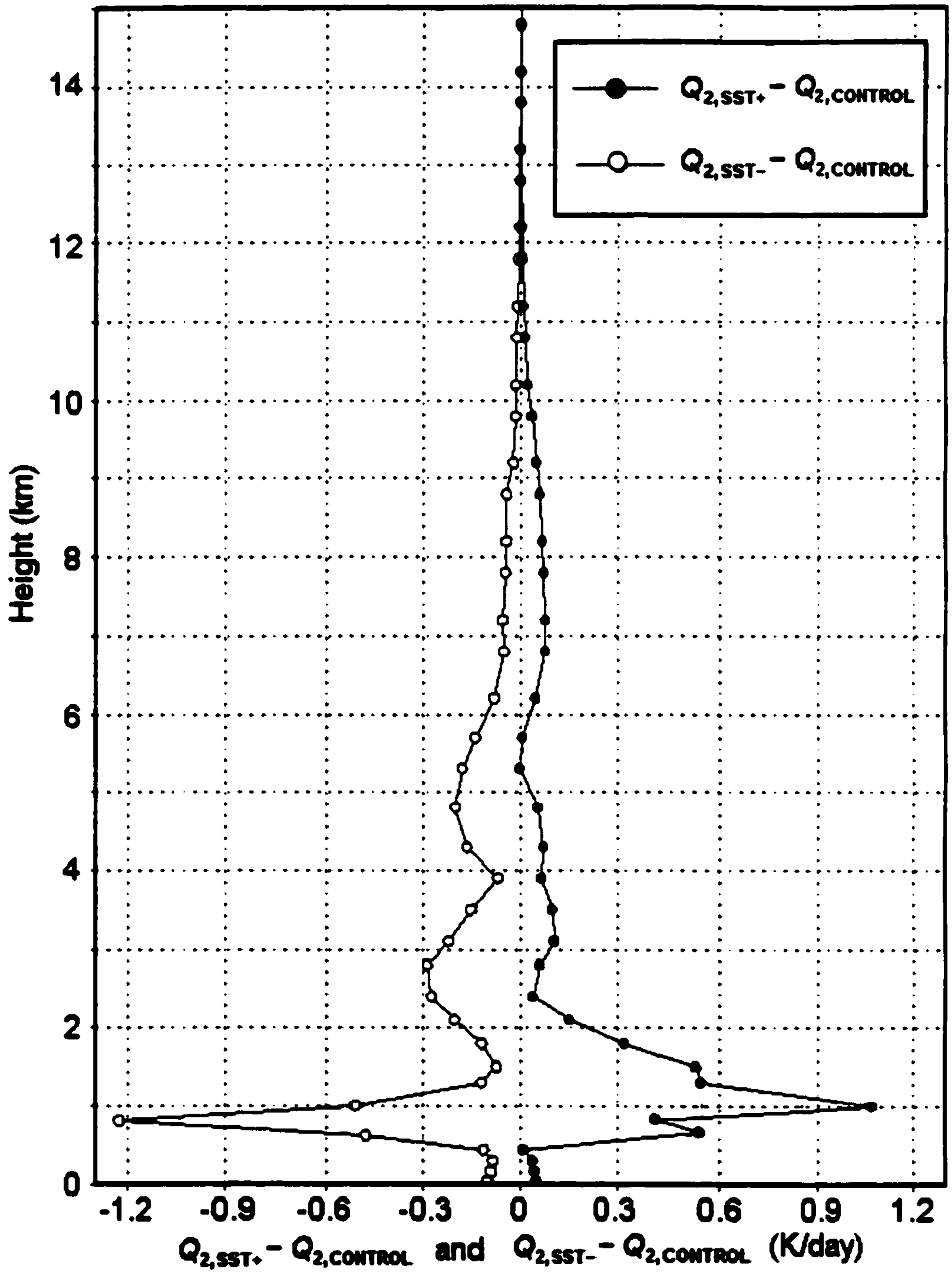

Figure 8.9 – Same as Figure 8, except for the apparent moisture sink.

8.3.2 – Changes due to SST inhomogeneities

In Section 7.3, it was shown that the inhomogeneous forcing, as in the CRM-UOM influences the convective-stratiform partition of the surface precipitation of the simulated cloud systems.

It was also verified that changes in the apparent heat source and apparent moisture sink can be produced in association with increased or decreased SSTs. In fact, smaller, although not less intriguing changes occurred in the average Q_1 and Q_2 profiles when non-uniform SSTs were present. Because they are more realistic, the focus will be on the coupled simulations versus the corresponding uncoupled runs (in which the average SST produced by the CRM-UOM was used) described in the previous Chapter. It will be demonstrated that changes in Q_1 and Q_2 associated with SST inhomogeneities are coherently related to the changes in the convective-stratiform partition of the surface precipitation produced by the simulated cloud systems.

Figure 8.10 depicts the difference between the apparent heat source in the coupled and the uncoupled runs for Case 1. In a very shallow layer close to the surface (less than 500m deep), Q_1 was greater in the uncoupled simulation, as well as in the upper troposphere. In contrast, in most of the troposphere, larger values of Q_1 were produced in the coupled simulation. The same features are found in Figure 8.11, which shows the difference in Q_2 in the coupled and uncoupled runs for the same case.

The difference between the apparent heat source in the coupled and the uncoupled runs for Case 2 is shown in Figure 8.12. As shown in Figure 8.13, Q_2 in the coupled simulation also dominates its counterpart in the uncoupled simulation by a smaller difference (on the order of 0.1 degree per day), although several patterns shown in Figure 8.12 (Q_1 difference) are not present.

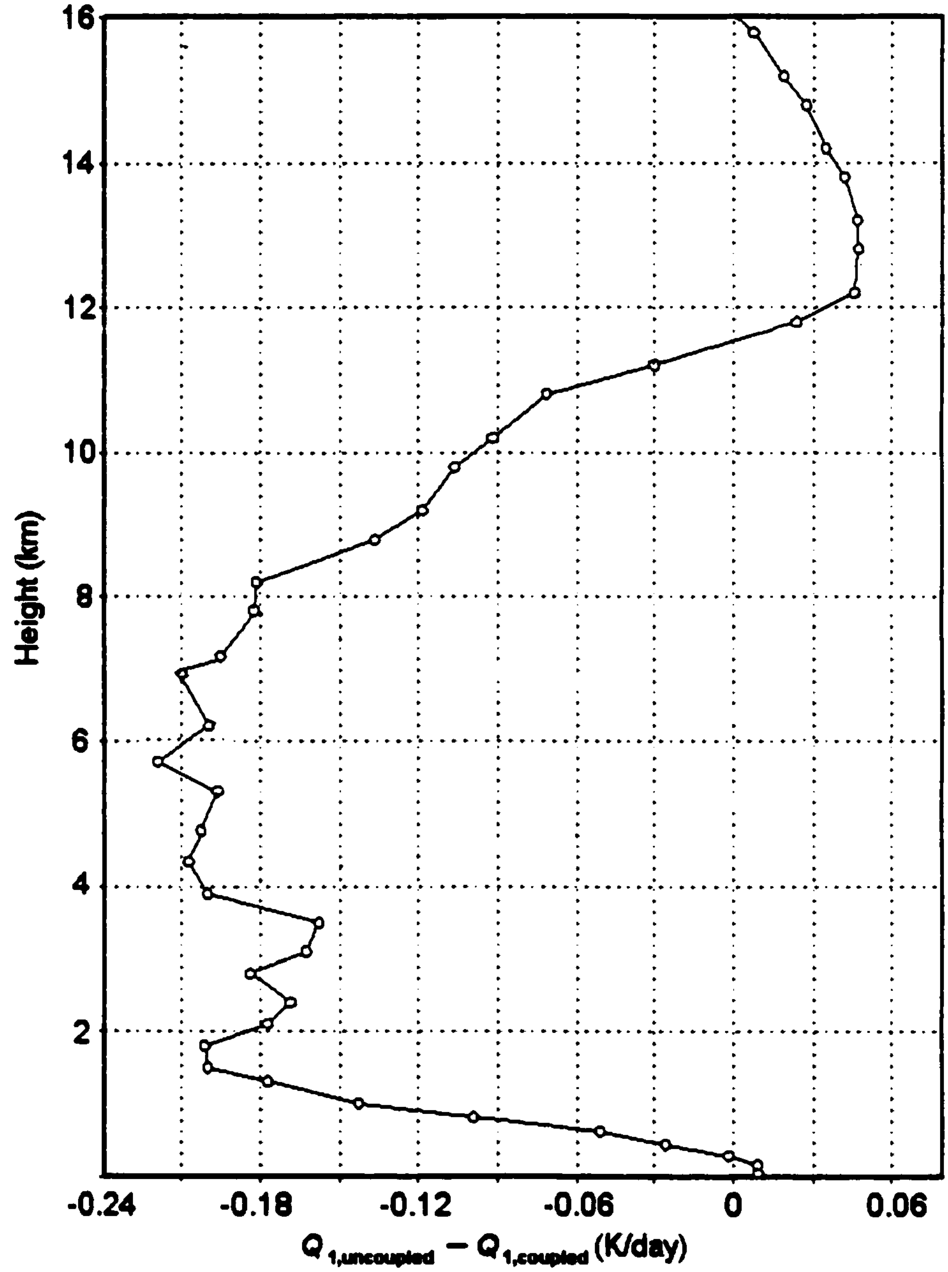

Figure 8.10 - Difference between the averages of the apparent heat source over the atmospheric model domain and the 10-day simulation period in the uncoupled and coupled runs for Case 1, as a function of height.

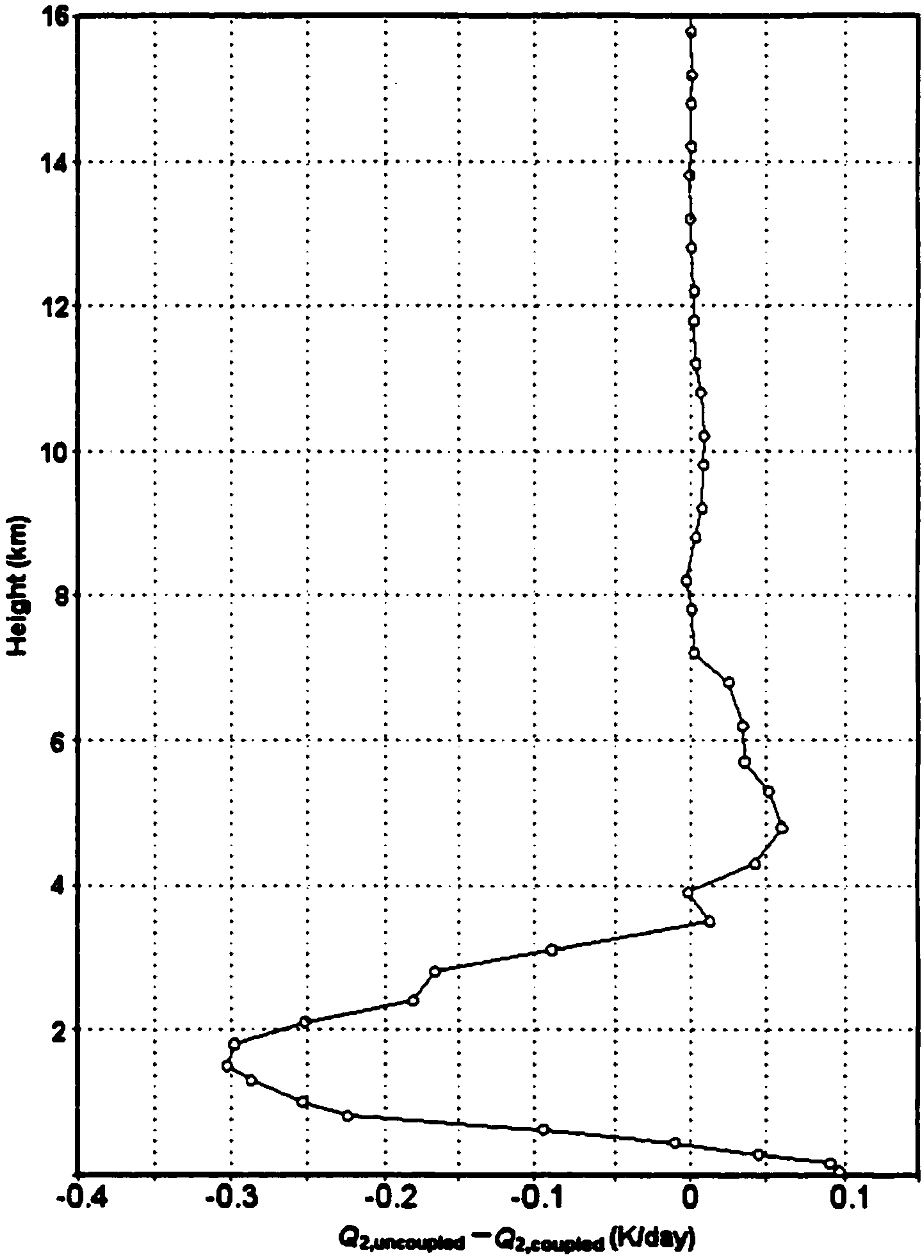

Figure 8.11 - Same as Figure 8.10, except for the apparent moisture sink

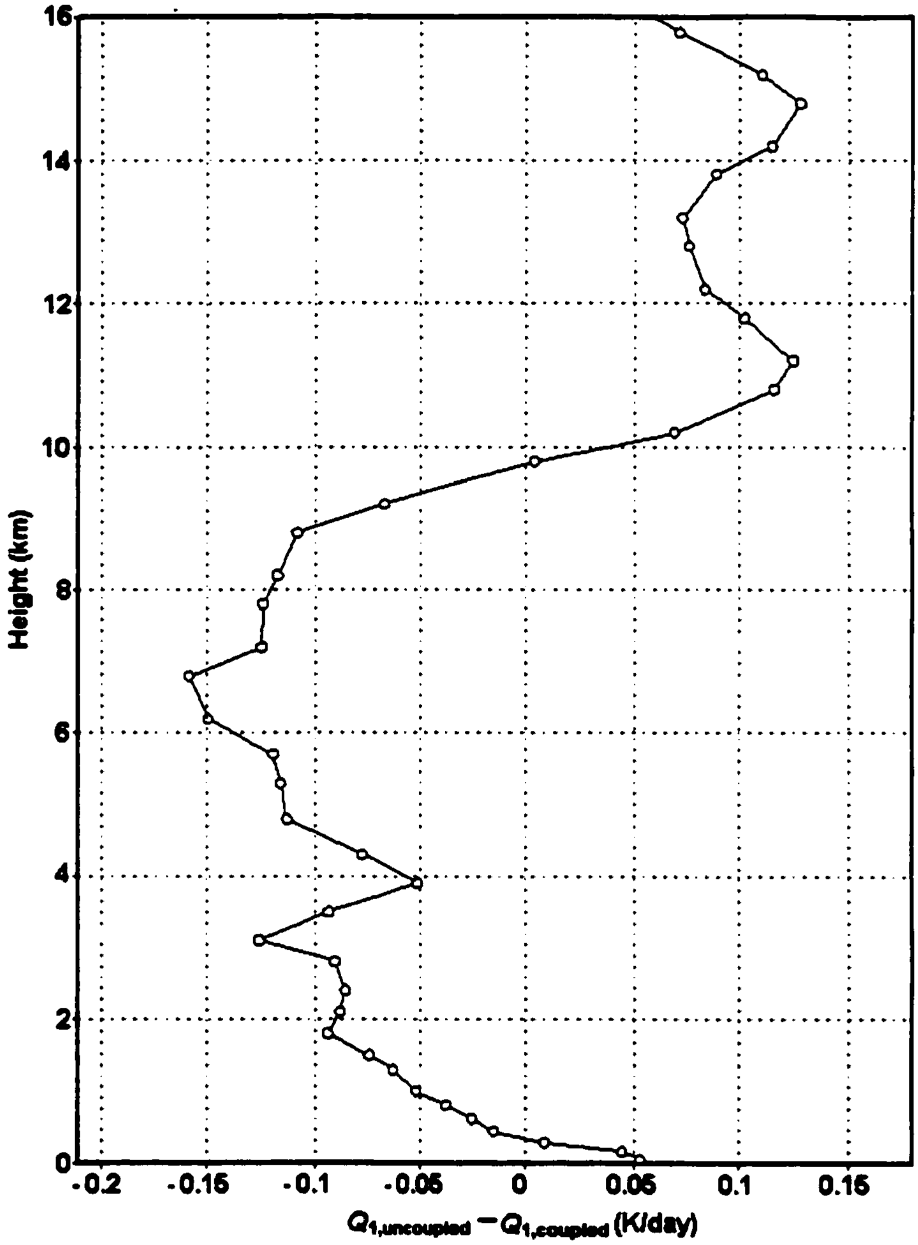

Figure 8.12 - Difference between the averages of the apparent heat source over the atmospheric model domain and the 10-day simulation period in the uncoupled and coupled runs for Case 2, as a function of height.

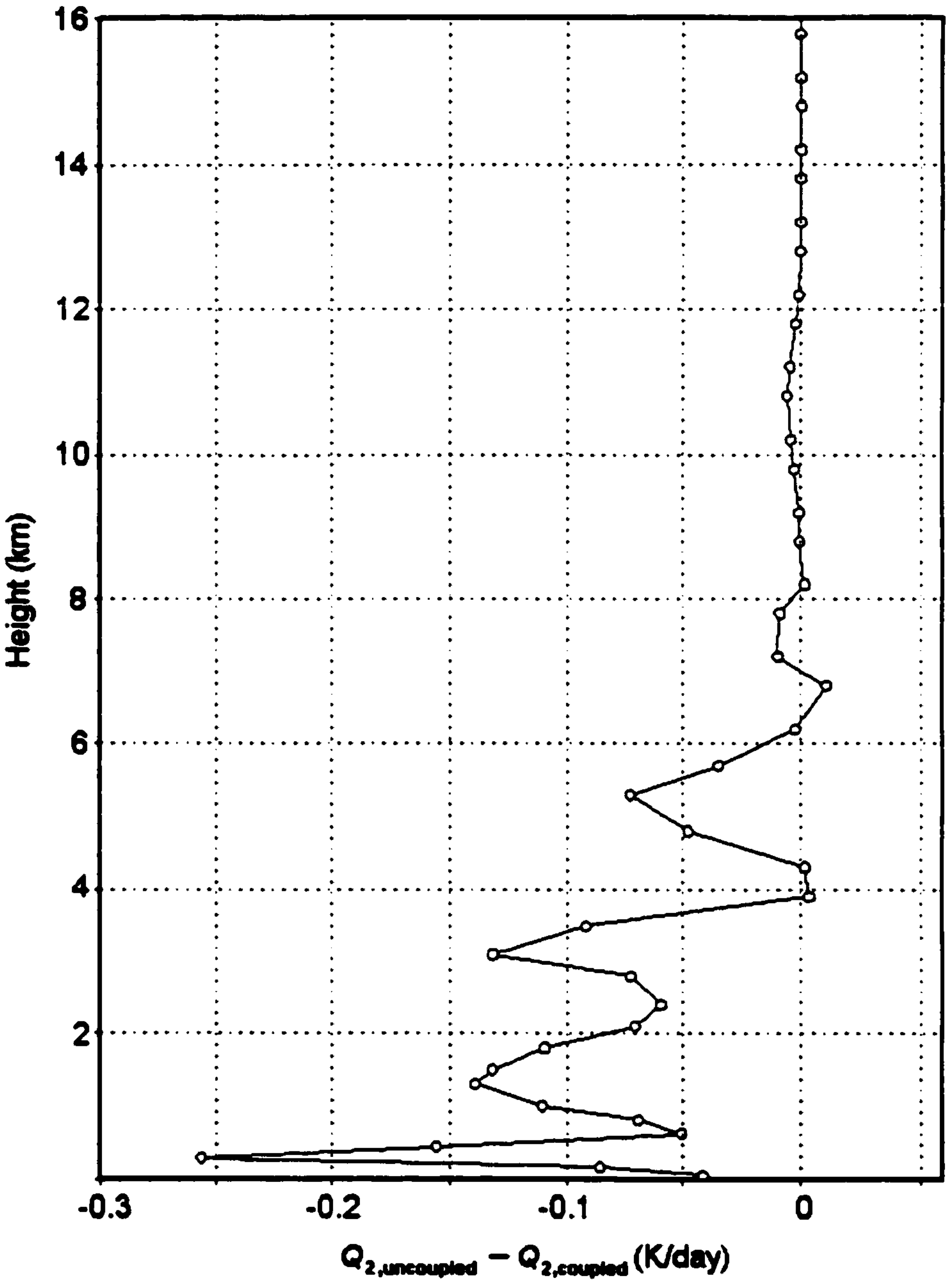

Figure 8.13 - Same as Figure 8.12, except for the apparent moisture sink

8.4 - Analytical Model

In order to explain qualitatively the results in the previous Section, a simple idealization of the apparent heat source profile can be assumed for convective and stratiform regions of precipitating systems. Since convective columns produce warming through the whole troposphere, with the exception of the boundary-layer, which undergoes cooling by the downdrafts, a non-dimensional Q_1 for a convective column can be approximated by a simple formula like:

$$C = \sin\left[\pi\left(\frac{z-h}{L-h}\right)\right], \tag{8.1}$$

where C is the non-dimensional convective heat source, z is the height coordinate, L is the tropopause height and h is the boundary-layer height.

Stratiform precipitation, on the other hand, is associated with warming in the upper troposphere and cooling of the lower troposphere. The sign change in the heating profile is often located by the melting level. Hence, with the assumption (not necessarily true at least for the TOGA-COARE region) that the height of the melting level is half of the tropopause height, a non-dimensional Q_1 for a stratiform column can be written as:

$$S = -\sin\left[2\pi\frac{z}{L}\right], \tag{8.2}$$

where S is the non-dimensional stratiform heat source. Diagrams depicting the idealized profiles given in equations (8.1) and (8.2) are shown in Figure 8.14

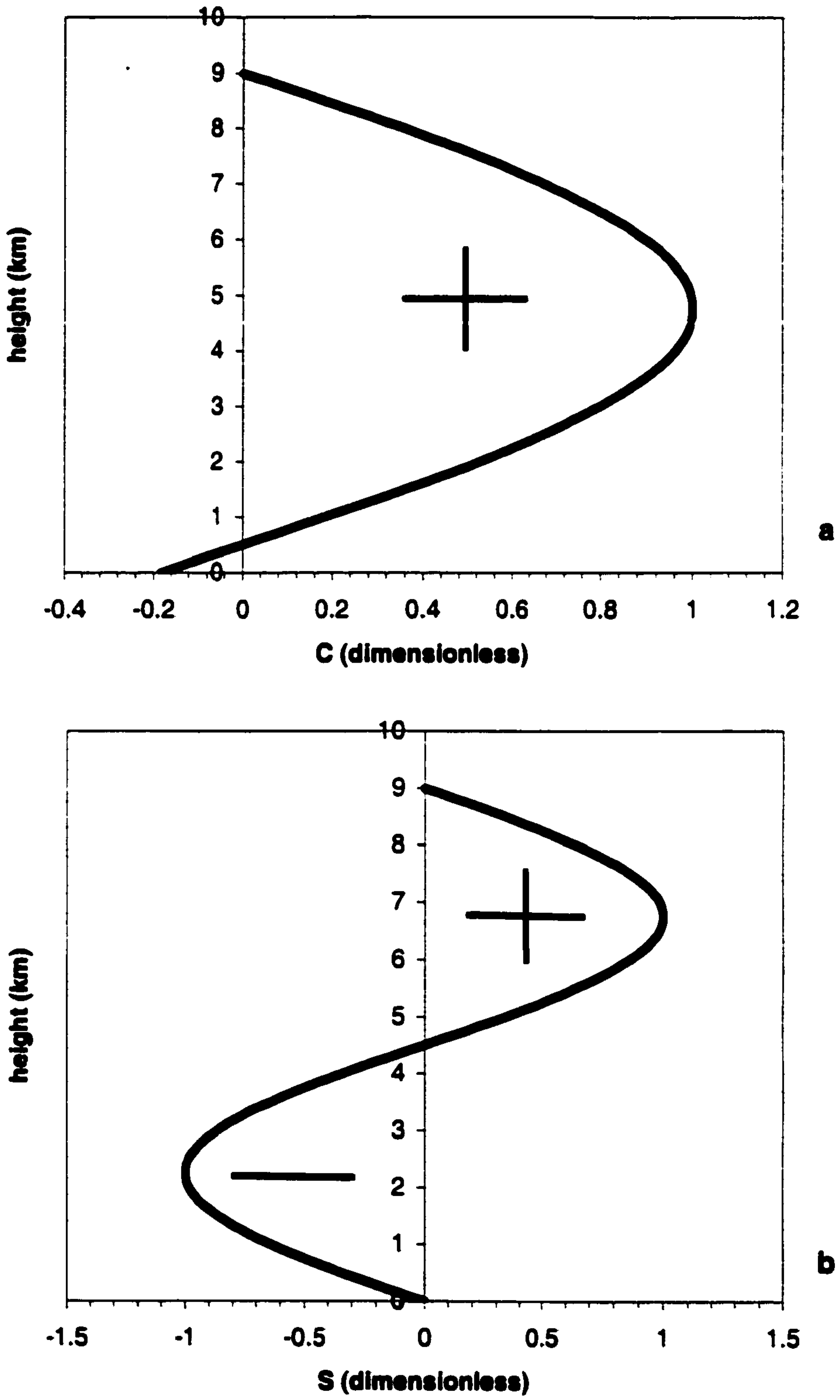

Figure 8.14 - Idealized non-dimensional vertical profiles of the apparent heat source at (a) convective and (b) stratiform columns. Values of L = 9.0 km (providing a melting level height of 4.5 km) and h = 0.5 km were used.

A composite apparent heat source can be written as a linear combination of the two individual "modes" (convective and stratiform), as in equation (8.3):

$$q_{1,0} = aC + bS, \tag{7.3}$$

where $q_{1,0}$ is the non-dimensional heat source at an environment containing convective and stratiform columns, the subscript "0" indicates a "basic state" and a and b are dimensionless coefficients (weights).

Assuming that a certain mechanism (for instance, the change from a homogeneous to a non-homogeneous surface forcing or vice-versa) disturbs the "basic state" of the system, the "disturbed" non-dimensional heat source becomes:

$$q_1 = (a + \delta_c)\, C + (b + \delta_s)\, S, \tag{8.4}$$

where δ_c and δ_s represent relative changes in the contribution from convective and stratiform columns to the total heating, respectively. From (8.3) and (8.4) the perturbation in the apparent heat source can be written as:

$$q_1' = \delta_c C + \delta_s S. \tag{8.5}$$

In order to evaluate the influence of a mechanism that favors the stratiform component to the detriment of the convective elements (a "stratiform disturbance"), the following values are substituted in equation 8.5: δ_c = - 0.01 and δ_s = 0.01. This can represent a proxy for the change from the inhomogeneous forcing (in the coupled runs) to the homogeneous forçing (in the corresponding uncoupled runs), that resulted in a small reduction in the convective rainfall and a small increase in the stratiform precipitation. The resulting perturbation in the dimensionless apparent heat source is shown in Figure 8.15, which qualitatively resembles Figures 8.10 and 8.12.

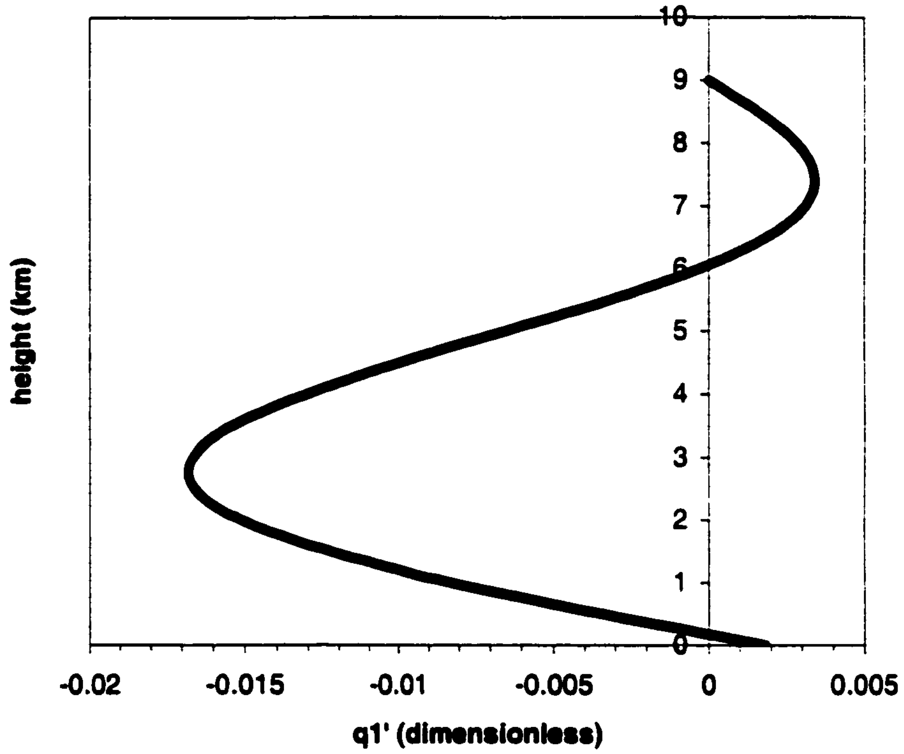

Figure 8.15 - "Stratiform-perturbation" in the non-dimensional apparent heat source, calculated according to equation 8.5.

In both diagrams, a shallow layer (shallower than the subcloud layer) presents less cooling in the stratiform-disturbed state, presumably due to the reduction in the convective downdrafts. Above that layer, up to a level located between the melting layer and the tropopause ("neutral level", referring to the lack of sensitivity of the heat source to the small perturbations in the convective-stratiform partition), there is more cooling in the stratiform-disturbed state than in its undisturbed counterpart. The enhanced cooling in that region is related both to the increased stratiform precipitation and to the reduction of the convective warming. Finally, above the neutral level, the stratiform-disturbed state shows a greater warming. A similar analysis can be done with respect to Q_2.

Chapter 9

CONCERNING THE OCEAN-ATMOSPHERE COUPLING AND THE PARAMETERIZATION OF SURFACE FLUXES

Cai chuva. É noite. Uma pequena brisa	It rains. It is night. A light breeze
Substitui o calor.	Replaces the heat.
P'ra ser feliz tanta coisa é precisa.	One needs so many things to be happy.
Este luzir é melhor	This glow is better.

(Fernando Pessoa)

It is well known that the passage of a convective system brings important changes to the atmospheric boundary-layer and the surface fluxes. According to Young et al. (1995), over the TOGA COARE region, a significant decrease in air temperature, significant increases in the wind speed, sensible and latent heat fluxes, and decreases in the SST, water vapor mixing ratio in the atmospheric surface layer, and sea surface saturation mixing ratio accompany the convective wakes. Saxen and Rutledge (1999) showed that different types of organization of convection are able to produce greatly enhanced surface fluxes during the convectively-active phase.

The objective of this Chapter is to illustrate the importance of several subgrid-scale phenomena to the surface heat fluxes under two deep convective regimes over the warm pool. First, a general discussion of different small-scale processes is made, using a simple bulk formulation for the surface heat fluxes. Then, the dataset generated by the coupled CRM-UOM is used to estimate the effects of such processes.

9.1 – Bulk formulation

Despite the existence of more sophisticated parameterizations, the analysis presented in this Section focuses on simple bulk aerodynamic formulas. In order to simplify all transport coefficients (that can be treated as functions of the wind, atmospheric stability, etc.) are assumed to be constants. According to a very simple bulk formulation, the sensible and latent heat flux over tropical oceans are given, respectively, by:

$$\begin{cases} Q_{s,c} = \rho c_T c_p |\mathbf{V} - \mathbf{v}|(SST - T_a) \\ Q_{l,c} = \rho c_q L |\mathbf{V} - \mathbf{v}|[q_s(SST) - q_a] \end{cases} \tag{9.1}$$

where ρ is the air density, c_T and c_q are the transport coefficients, V is the horizontal wind at a given height above the surface (usually about 10m), T_a and q_a are the temperature and water vapor mixing ratio at that height, v is the surface current, SST is the sea surface temperature, q_s is the saturation mixing ratio, and the subscript c accounts for the inclusion of the ocean currents in the calculation of the fluxes. Commonly, v is neglected in front of V. Accepting this assumption, and using grid-averaged values of those variables, we can approximate (1) by:

$$
\begin{cases} Q_{s,ave} = \bar{\rho} c_T c_p \left|\overline{\mathbf{V}}\right| \left(\overline{SST} - \overline{T_a}\right) \\ Q_{l,ave} = \bar{\rho} c_q L \left|\overline{\mathbf{V}}\right| \left[q_s\left(\overline{SST}\right) - \overline{q_a}\right] \end{cases}, \tag{9.2}
$$

where the subscript *ave* indicates the use of grid-averaged variables.

Because subgrid-scale phenomena can be significant, more accurate formulas can be written as:

$$
\begin{cases} Q_s = \overline{\rho c_T c_p |\mathbf{V}|(SST - T_a)} \cong \bar{\rho} c_T c_p \overline{|\mathbf{V}|(SST - T_a)} = \\ \bar{\rho} c_T c_p \left(\overline{|\mathbf{V}| SST} - \overline{|\mathbf{V}| T_a}\right) \\ Q_l = \overline{\rho c_q L |\mathbf{V}| [q_s(SST) - q_a]} \cong \bar{\rho} c_q L \overline{|\mathbf{V}| [q_s(SST) - q_a]} = \\ \bar{\rho} c_q L \left(\overline{|\mathbf{V}| q_s(SST)} - \overline{|\mathbf{V}| q_a}\right) \end{cases}. \tag{9.3}
$$

If the grid spacing is large, as in general circulation models (GCMs), those sets of formulas can depart significantly from each other, because several important subgrid-scale phenomena are not represented in (9.2), including the gustiness associated with circulations on the meso- and convective-scales. Particularly when convection is active, under weak to moderate large-scale winds, $\overline{|\mathbf{V}|} > \left|\overline{\mathbf{V}}\right|$ and the surface fluxes are enhanced. Also, because the downdrafts associated with convection bring cold and dry air to the surface, the boundary-layer modified by precipitating systems becomes windier, cooler and drier. Hence, negative correlations are established between $|\mathbf{V}|$ and T_a and $|\mathbf{V}|$ and q_a that also contribute to increase the surface heat fluxes. Finally, because precipitation-produced freshwater lenses are often cooler, a third effect can be inferred, namely the one associated with a negative correlation between $|\mathbf{V}|$ and SST. The later effect, in contrast with the former two, acts to reduce the surface heat fluxes. In order to isolate the effects of those two correlations, one can define:

$$\begin{cases} Q_{s,nt} = \bar{\rho} c_T c_p \left(\overline{|\mathbf{V}| SST} - \overline{|\mathbf{V}|}\,\overline{T_a} \right) \\ Q_{l,nq} = \bar{\rho} c_q L \left(\overline{|\mathbf{V}| q_s(SST)} - \overline{|\mathbf{V}|}\,\overline{q_a} \right) \\ Q_{l,nq} = \bar{\rho} c_q L \left(\overline{|\mathbf{V}| q_s(SST)} - \overline{|\mathbf{V}|}\,\overline{q_a} \right) \end{cases} \tag{9.4}$$

and

$$\begin{cases} Q_{s,nsst} = \bar{\rho} c_T c_p \left(\overline{|\mathbf{V}|}\,\overline{SST} - \overline{|\mathbf{V}| T_a} \right) \\ Q_{l,nsst} = \bar{\rho} c_q L \left(\overline{|\mathbf{V}|}\,\overline{q_s(SST)} - \overline{|\mathbf{V}| q_a} \right) \end{cases}, \tag{9.5}$$

where the subscripts *nt*, *nq* and *nsst* account for the neglect of the subgrid-scale variability of the air temperature, the water vapor mixing ratio and the SST.

9.2 – Flux calculations based on the CRM-UOM results

The coupled model described in previous Chapters is a useful tool to evaluate the importance of each of the subgrid-scale processes mentioned in Section 9.1. The entire CRM domain can be conceived as a proxy for a grid column of a GCM, with the mesoscale and convective scales resolved by the CRM representing subgrid scale processes in the GCM. Therefore, the non-bar variables in equations (9.1)-(9.5) are going to be interpreted as CRM grid-point values, and the bar variables as CRM domain averages.

Different values of the heat fluxes were calculated using formulas (9.1)-(9.5) substituting the fields predicted by the CRM. The wind speed, air temperature and water vapor mixing ratio were taken at the first atmospheric level (about 50m). Both c_T and c_q were substituted by $1.4 \cdot 10^{-3}$. The use of this value of the transport coefficients in the bulk equation (9.3) was shown to produce values of both sensible and latent heat flux very close to the ones calculated by the surface parameterization of the CRM.

Tables 9.1 and 9.2 show the 9-day average value of the heat fluxes for cases 1 (between 08 and 16 December) and 2 (between 20 and 28 December), according to formulas (9.1)-(9.5), and the percent difference from Q_l and Q_s (calculated using equation 9.3). As expected, the effects of the surface currents and small-scale processes are more noticeable in the weak wind case. Furthermore, the results indicate that in a relatively long-term average (several days), the effects of the wind speed-water vapor mixing ratio and wind speed-SST correlations are negligible. The positive correlation between the air temperature and the wind speed accounted for an average enhancement of 3.0% in the sensible heat flux in Case 1. However, because the Bowen ratio is small, its average effect on the total surface heat flux can be neglected too. The influence of the surface currents is typically small, accounting for an average reduction of less than 3.0 Wm^{-2} in the total surface heat flux, again in Case 1. In contrast, the effects of gustiness are significant in the multi-day average, particularly if the large-scale winds are weak, producing an increase of 44.0 Wm^{-2} and 12.5 Wm^{-2} in the total surface heat flux in cases 1 and 2, respectively.

Case	Q_s	$Q_{s,ave}$	$Q_{s,c}$	$Q_{s,nt}$	$Q_{s,nsst}$
1	12.20	6.61 (-45.8%)	11.88 (-2.6%)	11.83 (-3.0%)	12.24 (+0.4%)
2	18.20	16.59 (-8.9%)	18.07 (-0.7%)	18.28 (+0.4%)	18.21 (+0.1%)

Table 9.1 - Surface sensible heat flux calculated from the bulk formulas: 9.3 (Q_s), 9.2 ($Q_{s,ave}$), 9.1 ($Q_{s,c}$), 9.4 ($Q_{s,nt}$) and 9.5 ($Q_{s,nsst}$) for cases 1 and 2.

Case	Q_l	$Q_{l,ave}$	$Q_{l,c}$	$Q_{l,nq}$	$Q_{l,nsst}$
1	90.26	51.84 (-42.6%)	88.01 (-2.5%)	90.71 (+0.5%)	90.44 (+0.2%)
2	136.34	125.44 (-8.0%)	135.33 (-0.7%)	136.36 (+0.0%)	136.38 (+0.0%)

Table 9.2 - Surface latent heat flux calculated from the bulk formulas: 9.3 (Q_l), 9.2 ($Q_{l,ave}$), 9.1 ($Q_{l,c}$), 9.4 ($Q_{l,nq}$) and 9.5 ($Q_{l,nsst}$) for cases 1 and 2.

The time evolution of the difference between $Q_{s,c}$, $Q_{s,nt}$, $Q_{s,nsst}$, and $Q_{s,ave}$ and Q_s for Cases 1 and 2 is shown in Figure 9.1. Similarly, the difference between $Q_{l,c}$, $Q_{l,nq}$, $Q_{l,nsst}$, and $Q_{l,ave}$ and Q_l for Cases 1 and 2 is shown in Figure 9.2. The Figures indicate that, despite their small average value, those differences are relatively large at specific times and, under certain circumstances, the ocean currents, and the wind speed-air temperature, wind speed-water vapor mixing ratio and wind speed-SST correlations have to be considered in the calculation of the surface heat fluxes.

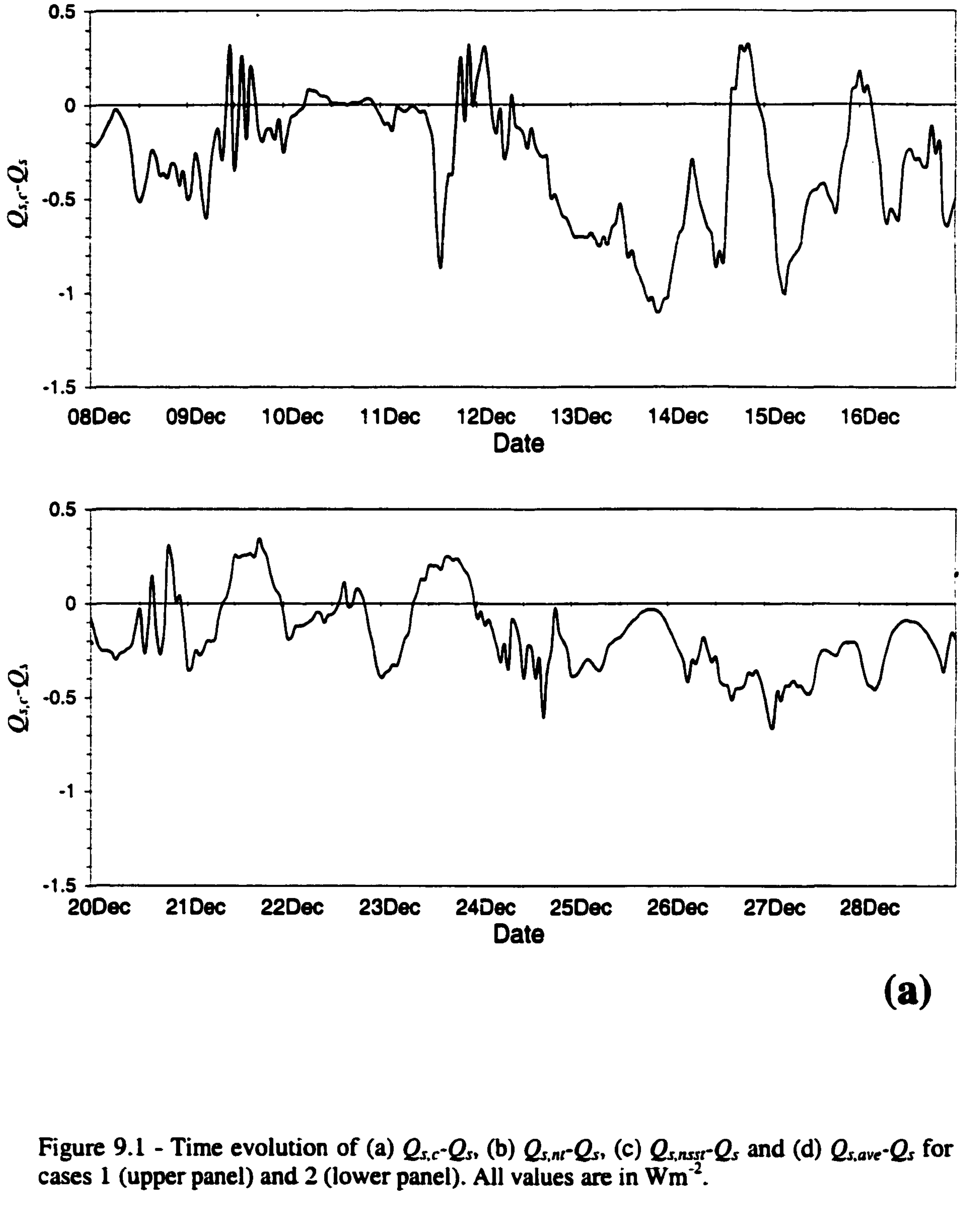

Figure 9.1 - Time evolution of (a) $Q_{s,c}$-Q_s, (b) $Q_{s,nt}$-Q_s, (c) $Q_{s,nsst}$-Q_s and (d) $Q_{s,ave}$-Q_s for cases 1 (upper panel) and 2 (lower panel). All values are in Wm^{-2}.

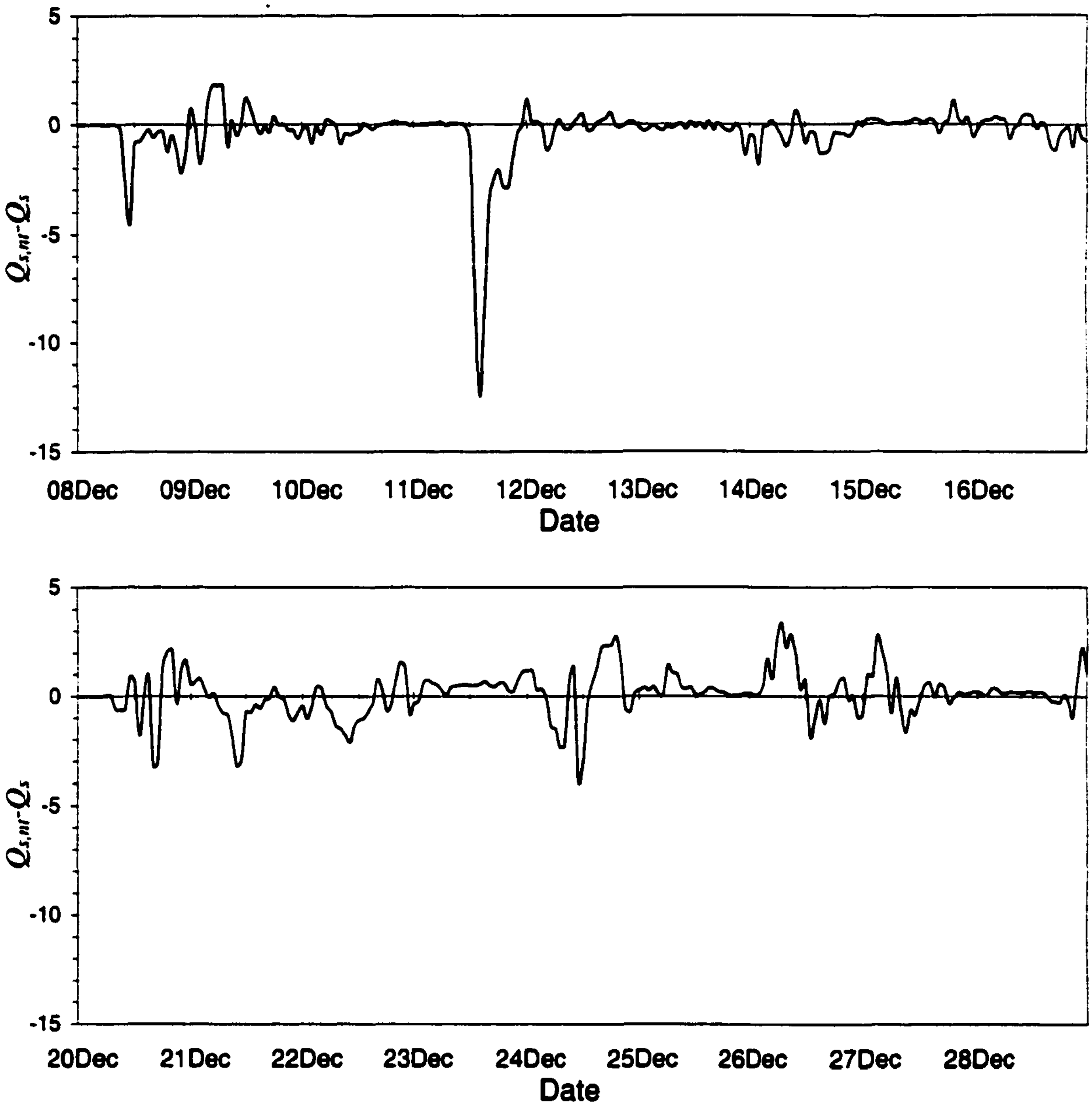

(b)

Figure 9.1 - continuation

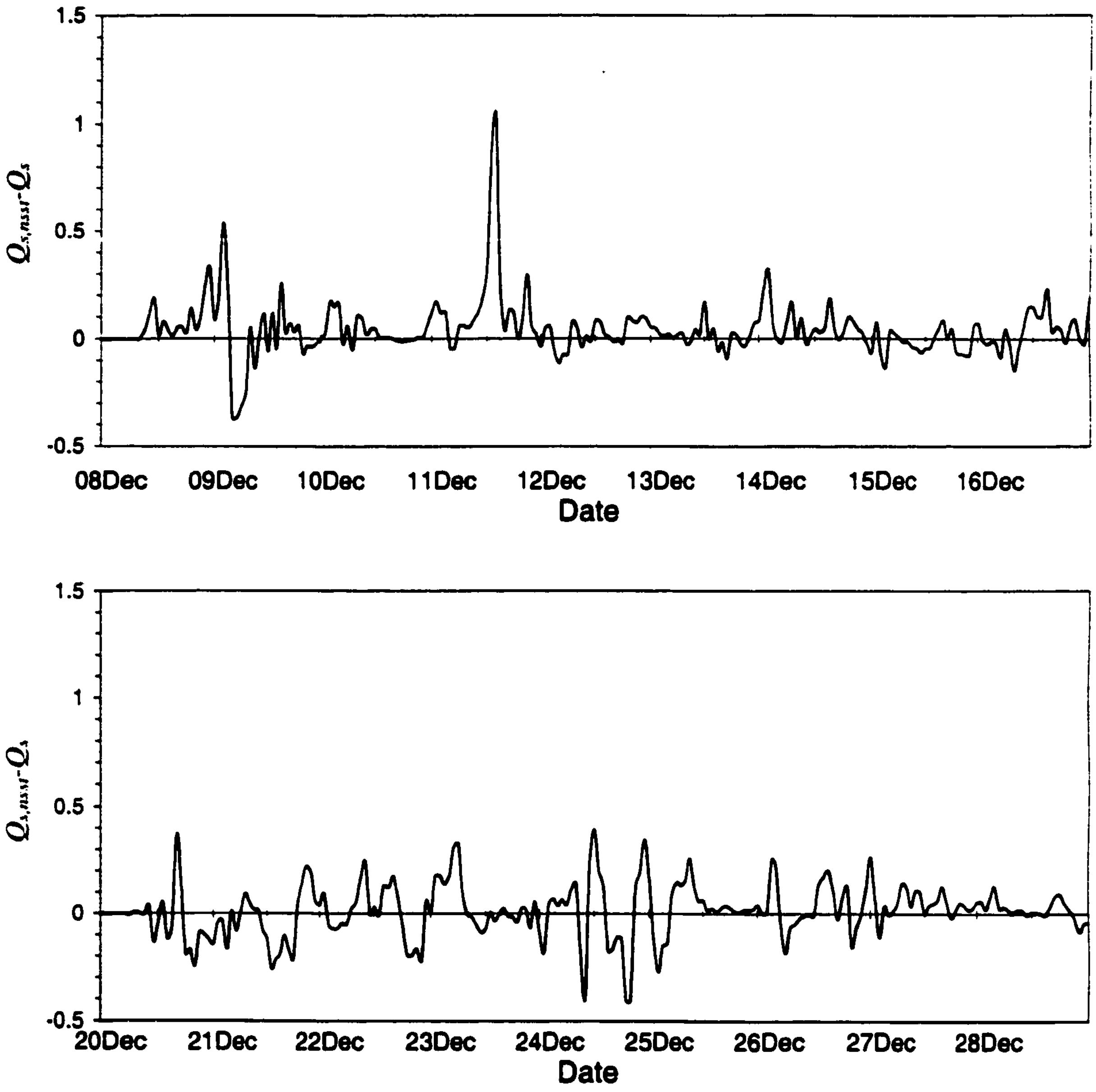

(c)

Figure 9.1 - continuation

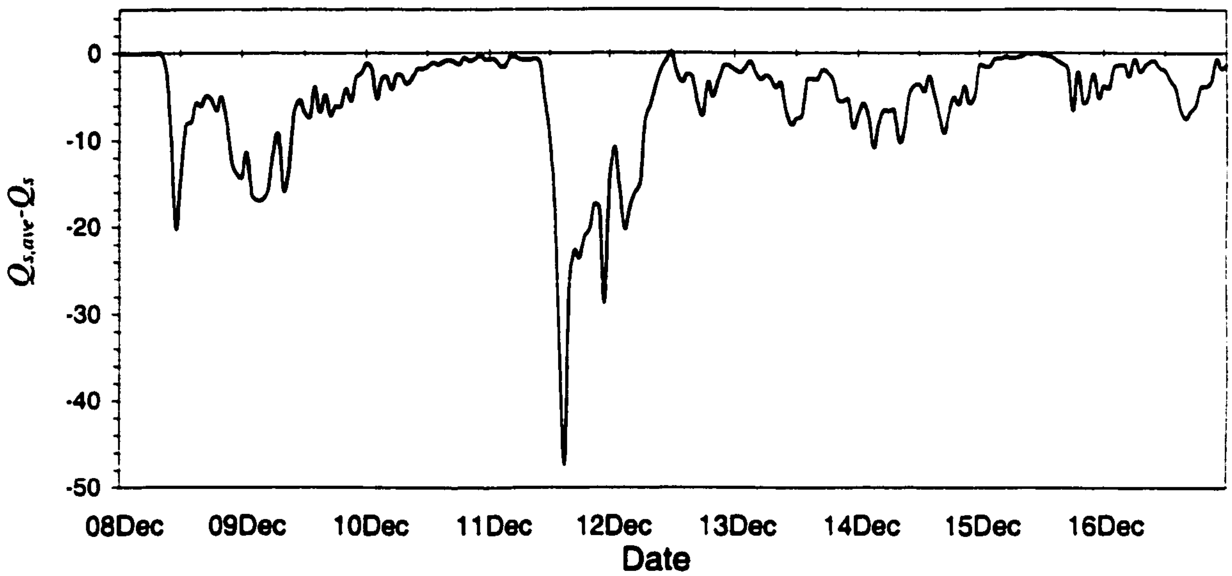

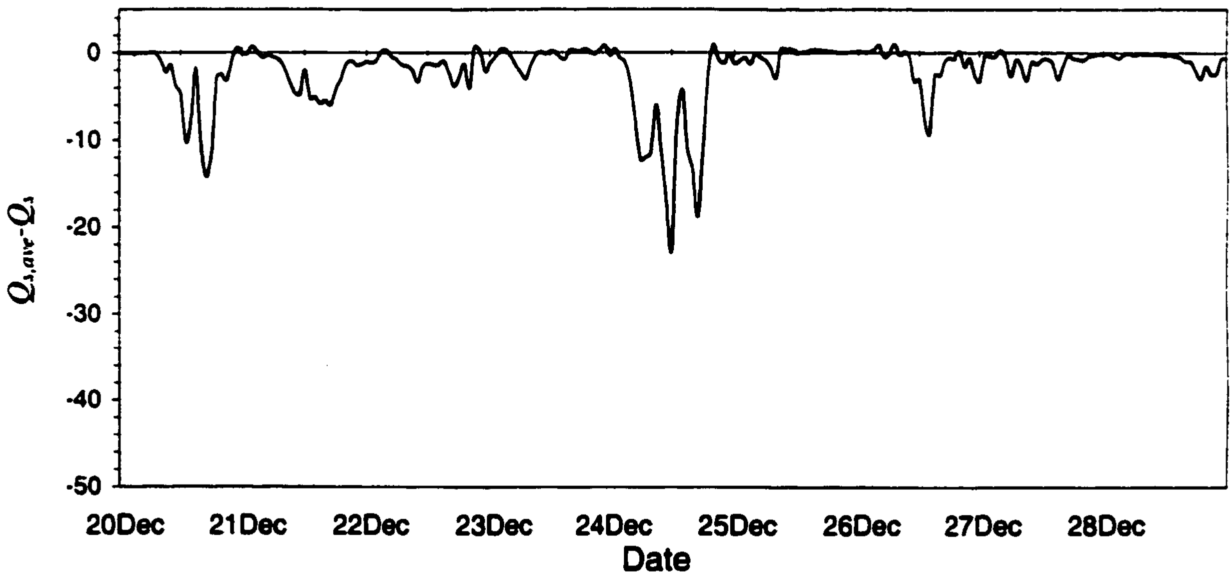

(d)

Figure 9.1 - continuation

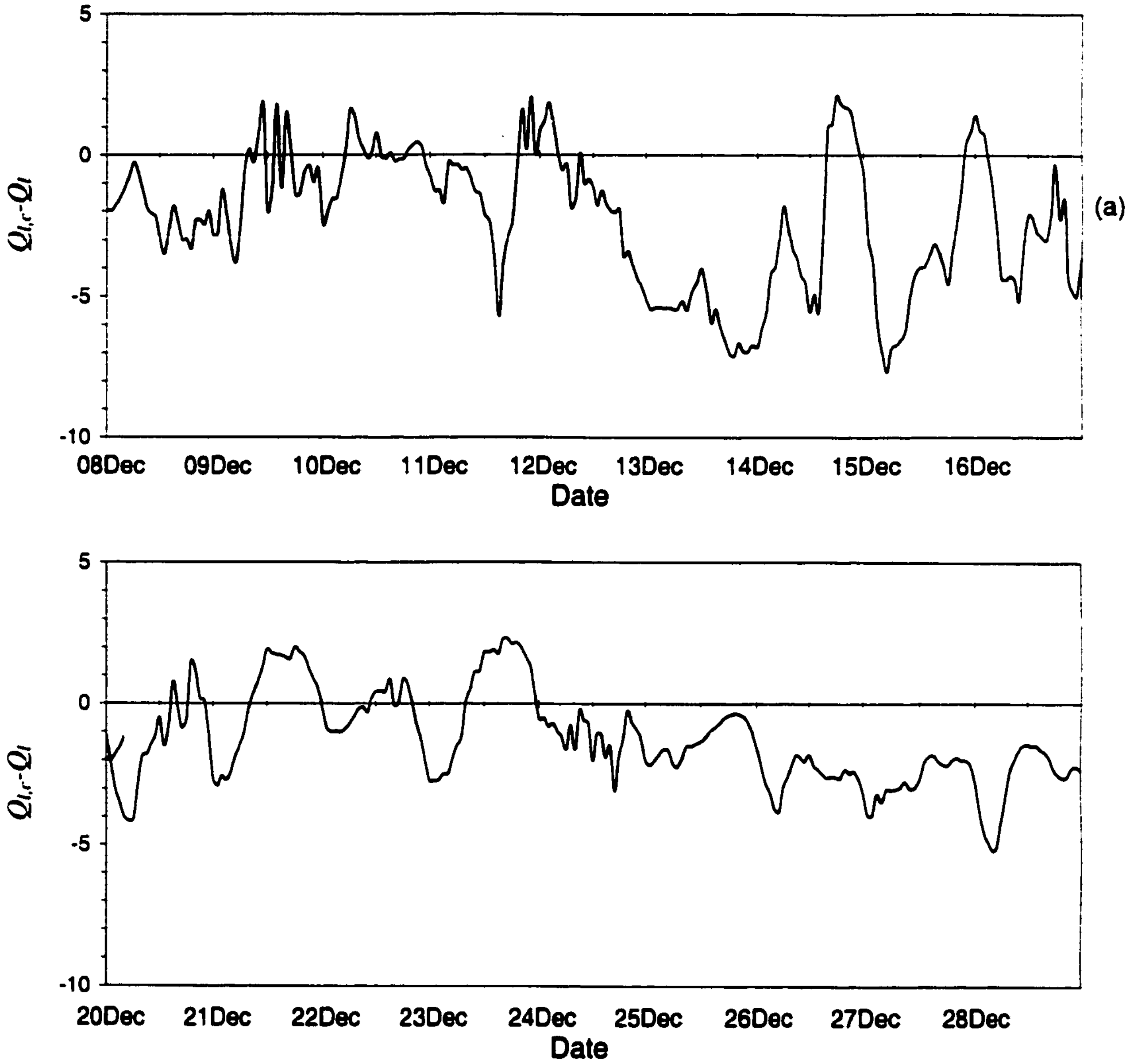

(a)

Figure 9.1 - Time evolution of (a) $Q_{l,c}$-Q_l, (b) $Q_{l,nq}$-Q_l, (c) $Q_{l,nsst}$-Q_l and (d) $Q_{l,ave}$-Q_l for cases 1 (upper panel) and 2 (lower panel). All values are in Wm^{-2}.

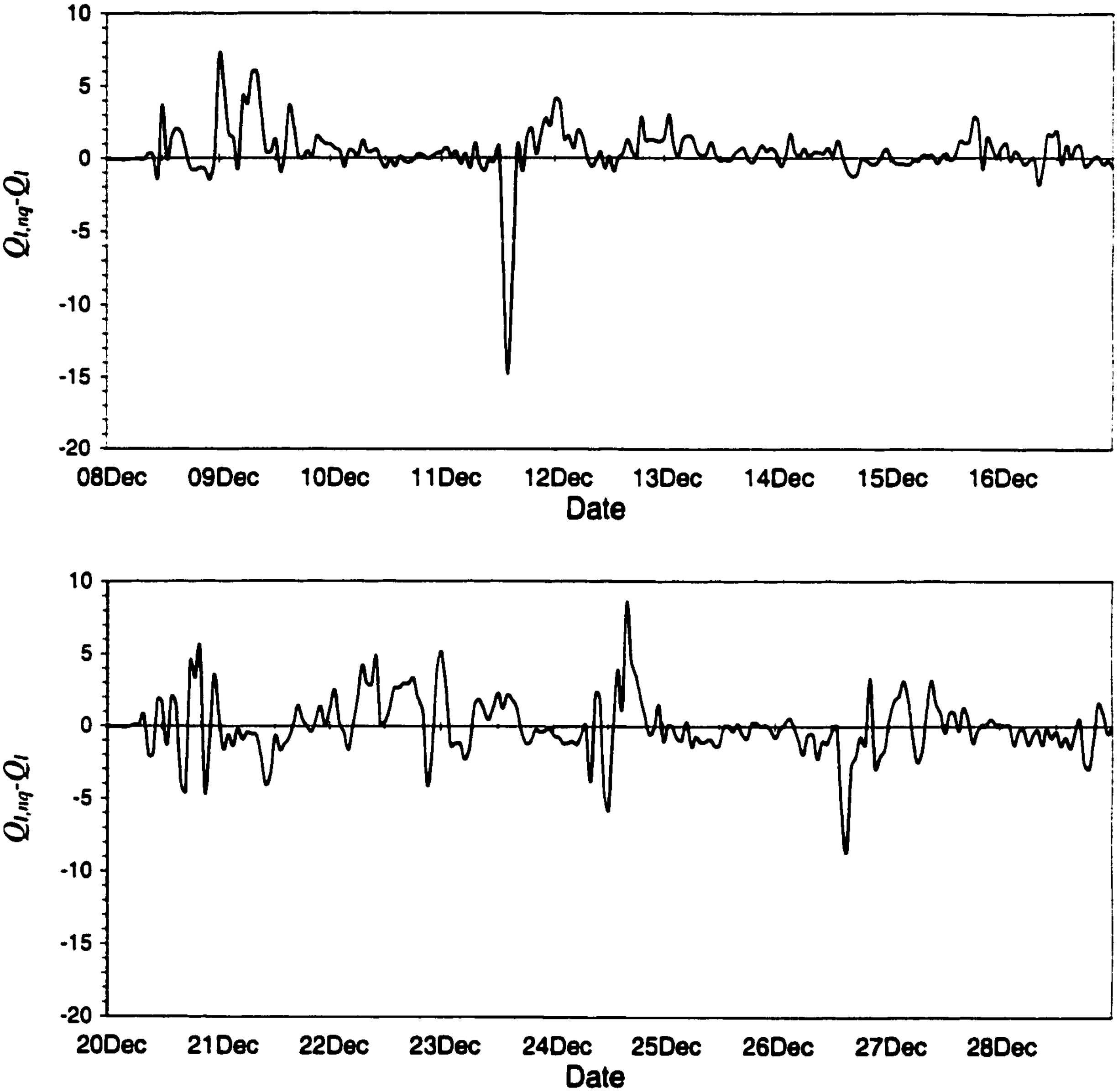

(b)

Figure 9.2 - continuation

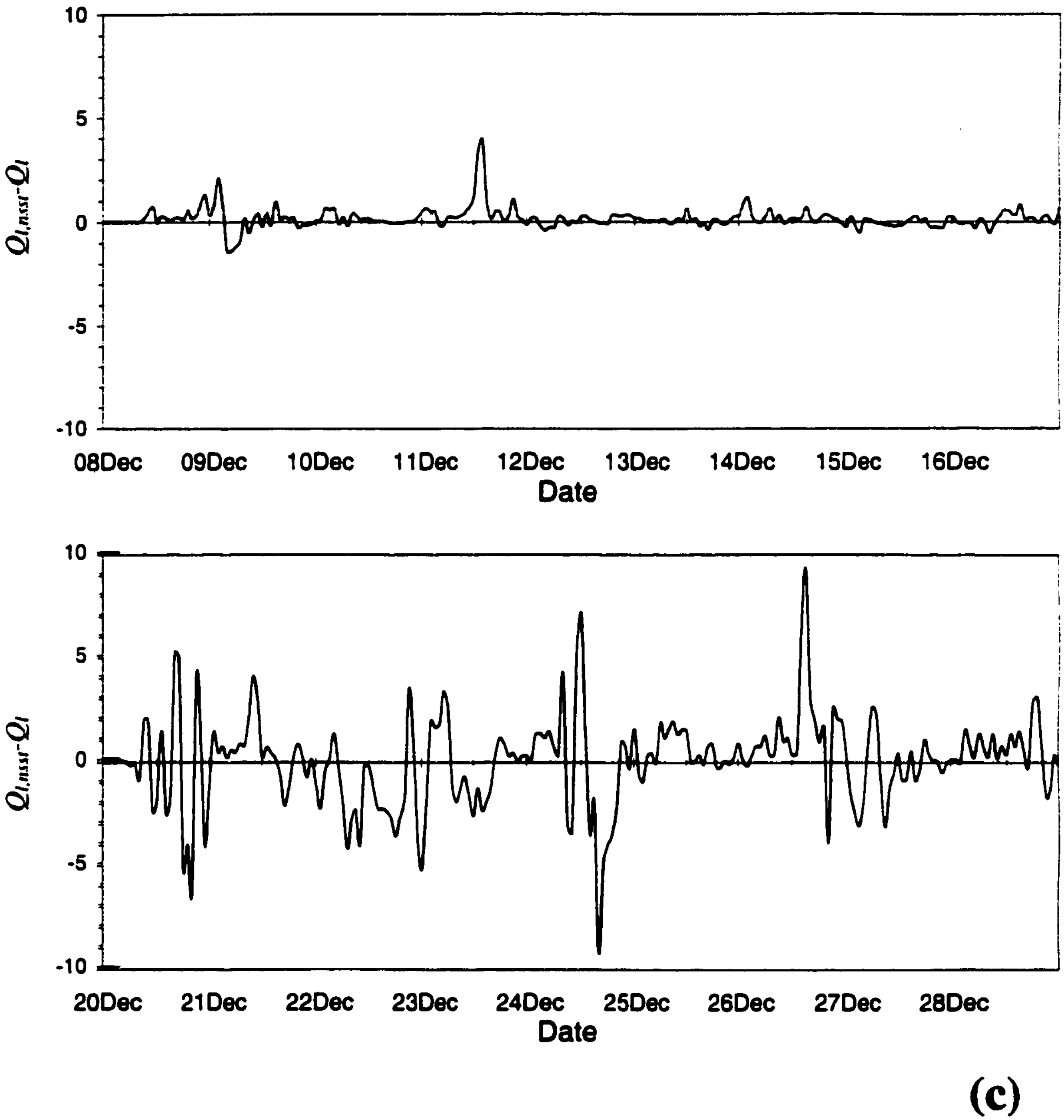

Figure 9.2 - continuation

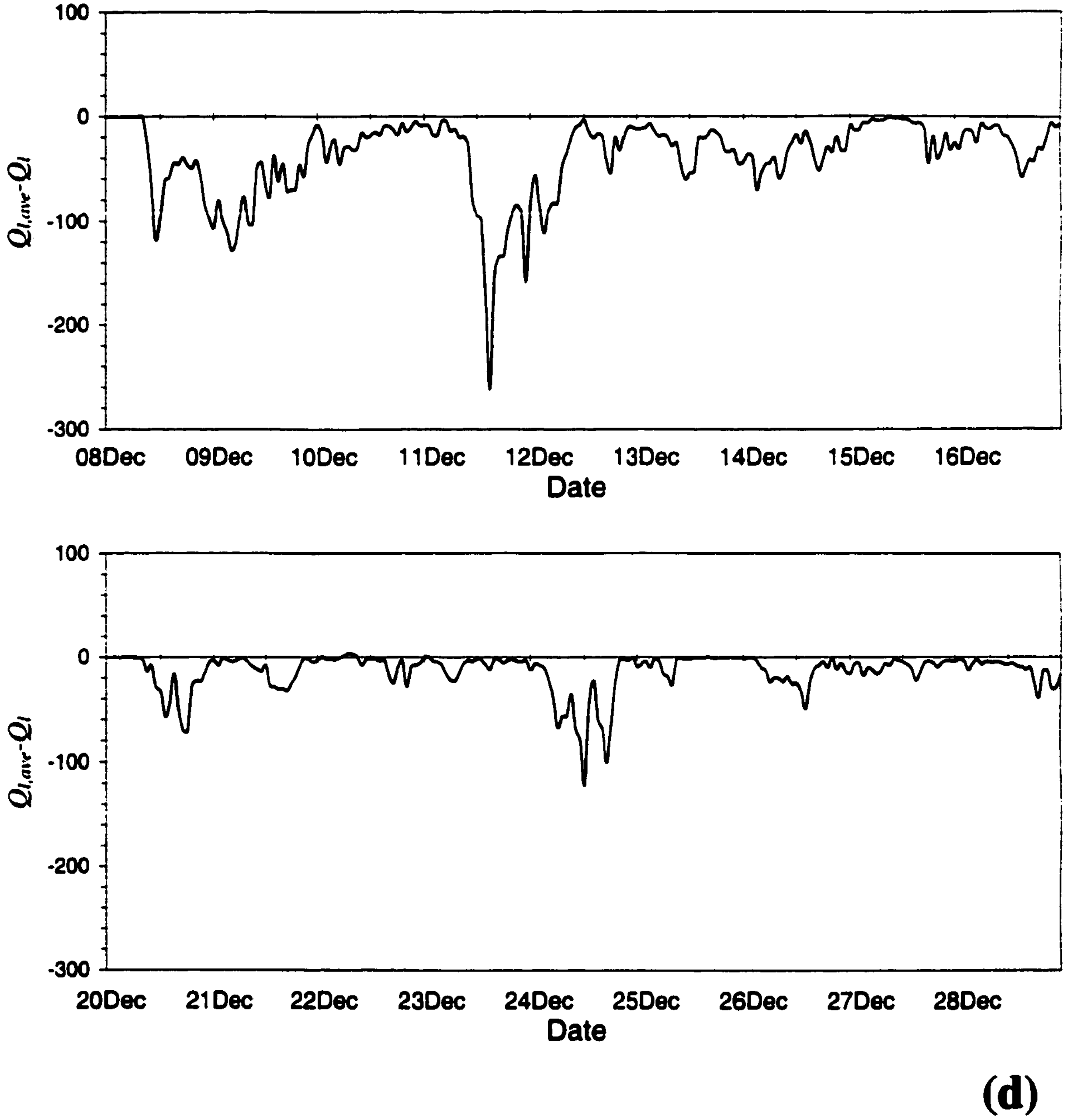

Figure 9.2 - continuation

The ocean currents usually contribute to reduce the surface fluxes, since they tend to align with the surface winds. They accounted for a maximum reduction of 1.1 Wm^{-2} in the sensible heat flux and 7.7 Wm^{-2} in the latent heat flux. This effect is more pronounced after strong precipitation events and during daytime. In both cases, the momentum transport from the atmosphere is limited to a shallow layer that accelerates in the direction of the wind. In a few circumstances, particularly at nighttime, the effect of the currents is to enhance the fluxes, which suggests the existence of a current component opposing the wind. This occurs in association with the mixing of the upper ocean layers with the mixed layer below, which eventually has a bulk current in a direction other than the atmospheric surface flow.

The effects of the wind speed-air temperature and wind speed-water vapor mixing ratio are usually small, related to changes in the heat fluxes of less than 5 Wm^{-2}. The most evident exception was the strong convective event that occurred under a weak wind regime (Case 1, 11 December). During that episode, the correlation between the wind speed and the air temperature accounted for a maximum increase of 12.5 Wm^{-2} in the sensible heat flux and the wind speed-mixing ratio correlation contributed to an increase of 14.8 Wm^{-2} in the latent heat flux.

The variability of the SST and its subgrid-scale correlation with the surface wind speed can have important effects on the surface latent heat flux. In Case 1, this correlation acted to reduce the latent heat flux up to 3.9 Wm^{-2}. In Case 2, the coupled system showed a more complex behavior, with the wind speed-SST correlation changing sign several times. The maximum variation in the latent heat flux in Case 2 was

9.3 Wm^{-2}. The effects of the SST variability on the sensible heat flux were significantly smaller (maximum reduction of 1.0 Wm^{-2}, Case 1).

Among the different phenomena analyzed, gustiness is the one that has the greatest contribution to the surface heat fluxes, particularly when convection is active. In Case 1, the small-scale circulations accounted for an enhancement of up to 47.2 Wm^{-2} in the sensible heat flux and 261.4 Wm^{-2} in the latent heat flux. In Case 2, because the large-scale winds were larger, the contribution from gustiness to the surface heat fluxes was smaller, with a maximum enhancement of 22.7 Wm^{-2} in the sensible heat flux and 121.7 Wm^{-2} in the latent heat flux.

Although exhibiting small average values in both multi-day periods, small-scale effects other than gustiness can also be significant under certain conditions. Therefore, one should consider the parameterization of such small-scale effects in large-scale models, such as GCMs. Recent studies (e.g., Qyan et al., 1998) presented formulations of parameterizations of the effects of the cold, dry downdrafts associated with precipitation on the atmospheric near-surface layer and the surface fluxes. Those parameterizations account for the negative correlations between wind speed and air temperature and between wind speed and water vapor mixing ratio near the surface. In contrast, little attention has been given to the role of the ocean surface currents and SST inhomogeneities. In our simulations, those two effects together produced changes in the total surface heat fluxes of the same order of magnitude (or slightly less) than the changes associated with the cooling and drying of the boundary-layer by convective downdrafts. The present results suggest that the development of a parameterization of such ocean surface processes is needed to obtain more accurate calculations of surface fluxes in

GCMs. Since the momentum transfer from the atmosphere is limited to a shallow layer if the upper ocean is highly stable, the influence of the ocean surface currents has a markedly strong daily variation, and is often amplified in the presence of precipitation. In addition, a significant negative (or even positive) correlation can be established between the SST and the near-surface winds, especially during strong precipitation events.

Chapter 10

LONG-TERM BEHAVIOR OF THE COUPLED SYSTEM

...el tiempo, el agua errante, *el viento vago nos llevo* *como grano navegante.*	...the time, the wandering water, the vague wind took us like a navigating grain ...

Pablo Neruda (Chilean poet)

Air-sea interactions over the WPWP involve physical processes on relatively long intraseasonal timescales (along the interannual to decadal variability). Idealized cloud-resolving simulations of deep convection over tropical oceans often require several days to solve the model transients (e.g., Tao et al., 1999). The characteristics of the oceanic fluid (much greater heat capacity, slower motions and more pronounced low-frequency variability than its atmospheric counterpart) suggest that an ocean model should require even longer times, in order to transient effects to be no longer significant.

In addition, during a cycle of the intraseasonal oscillation, the coupled ocean-atmosphere system undergoes a series of different states. In each of those states, unique kinds of interactions take place. Therefore, limiting the coupled ocean-cloud resolving simulations to timescales of the order of 10 days has obvious shortcomings. The simulations described in previous chapters did not allow the validation of model results against the broad spectrum of regimes found over the warm pool. Although the model was shown to give satisfactory results for two deep convective regimes, there was no evidence that it could properly simulate the suppressed phases of the MJO, in which the SST recovers. Also, chances are that model transients were still not completely resolved by the end of 10-day simulations.

In this chapter, the coupled ocean-atmosphere model described in chapters 4 and 6 is used to simulate the behavior of the warm pool during Case 3, i.e., the 70-day period between 19 December 1992 and 27 February 1993. Some of the characteristics of the atmospheric flow, and the evolution of the sea surface temperature during that period were shown in chapter 3.

As discussed previously, in the long-term runs, the model had a grid spacing twice as large as the one used in week-long simulations. That allowed us to use a smaller number of horizontal grid points and a larger timestep, resulting in the reduction of the computational effort.

In the first section of the present chapter, results from a control simulation are described, and compared to observations. Following, a sensitivity run, in which there was no salinity effect, was carried out, aiming to evaluate the effect of the salt-stratification in the thermal and dynamic characteristics of the warm pool.

10.1 – Case 3 control simulation

In this simulation, the atmospheric model was forced using the observed advective tendencies of temperature and moisture calculated from the TGSA. Nudging terms were added to the momentum, thermodynamic and moisture equations, following the procedure described in Chapter 4. As in previous simulations, random perturbations were imposed to the homogeneous basic state air temperature during the first hour of simulation.

The ocean model was initialized using a vertical profile of temperature, salinity and currents, as observed by the R/V Moana Wave. No forcing terms were added.

10.1.1 – Temperature and moisture biases

Since the atmospheric model was constrained to follow the observed wind, temperature and moisture, good agreement between the model results and the observations was expected, at least regarding those fields. In fact, as in the previous, week or 10-day long simulations, the modeled winds agreed very well with their observed counterparts, thanks to the small relaxation timescale (one hour). Although carried out using a long nudging timescale (one day), the relaxation scheme contributed to limit the temperarure and moistures biases to relatively small values. On average, as depicted in Figure 10.1, the model exhibited a cold, moist bias, with a maximum temperature deficit of about 1.1°C in upper levels and a maximum moisture excess on the order of 0.6 gkg^{-1} at the atmospheric boundary-layer.

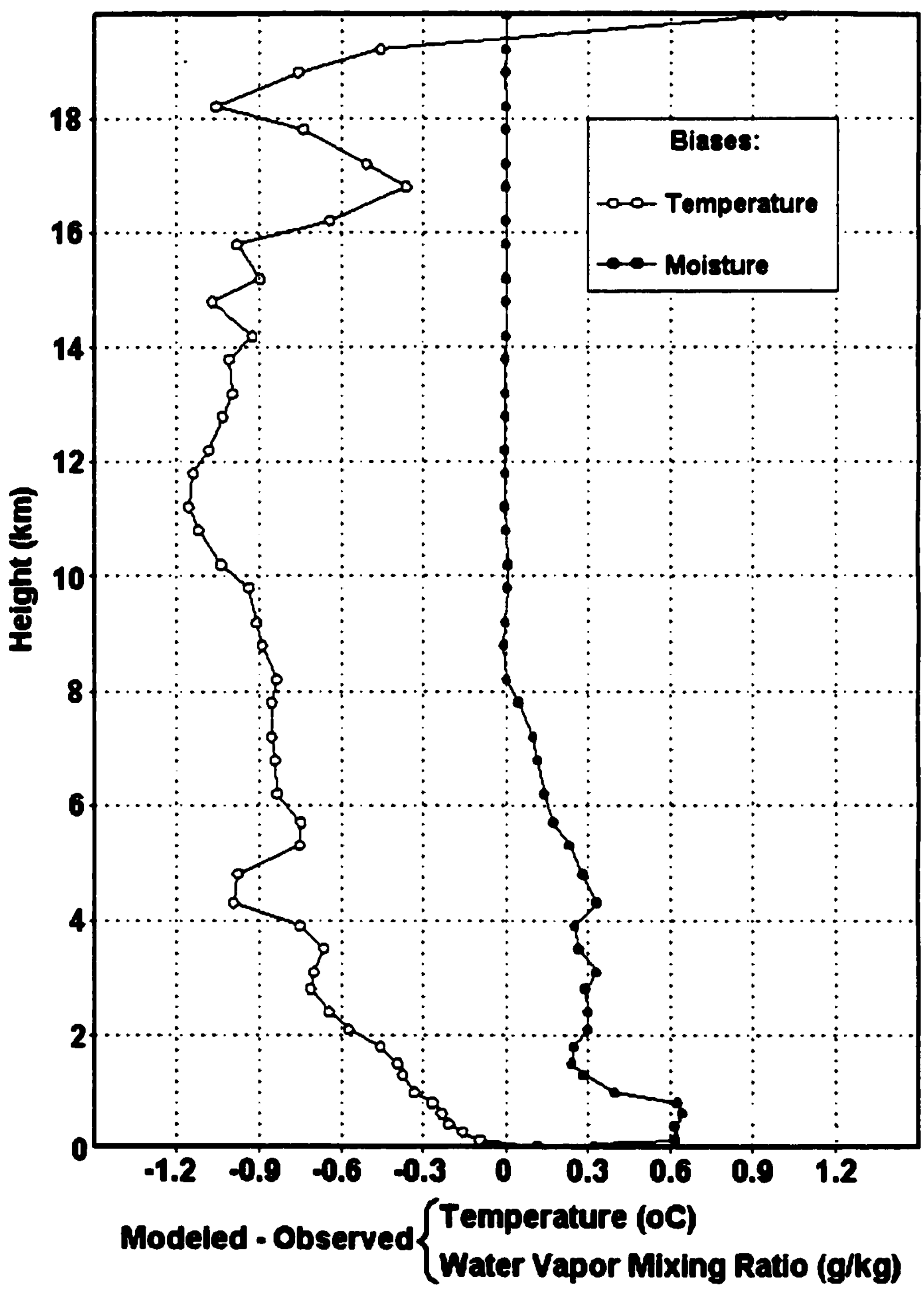

Figure 10.1 – Modeled minus observed temperature (°C) and water vapor mixing ratio (gkg^{-1}) in the control simulation of Case 3.

10.1.2 – Condensate Fields

The modeled total condensate field and the cloud fractional area are strongly correlated with the large-scale advective tendencies of temperature and moisture. The episodes of convective warming and drying in Figures 3.7 to 3.11 are clearly associated with the formation of clouds as depicted in Figures 10.2 (time-height plot of the horizontally-averaged total condensate mixing ratio) and 10.3 (time-height plot of the cloud fractional area). In those Figures, convectively active periods (as the ones on late December, mid-January and late February) correspond to the presence of deep clouds. In contrast, during suppressed periods, cloudiness is either associated with fields of shallow cumuli or virtually absent.

Figure 10.4 shows a comparison between the modeled cloud cover and the observations from the International Satellite Cloud Climatology Project (ISCCP) for the 70-day period between 19 December 1992 and 27 February 1993. Here, a cloudy column in the model is defined as the one containing at least one cloudy grid box, defined in Chapter 5. The model results showed, in general, good agreement with the satellite observations. With the exception of the first day of simulation, during which the model spin-up was not complete, RAMS-POM accurately simulated the observed cloud cover during the convective episodes in late December. It also provided a good representation of the reduction in cloud cover in early January, after the peak WWB, and the cloud variations in mid-February, before the passage of another ISO. Eventually, the model exhibited an exaggerated clearing (for instance, between 11 and 16 January) or covering (for example, between 09 and 11 January). On average, during the 70-day period, the model underestimated the cloud cover slightly; the averaged model cloud cover was 0.7341, versus 0.8011 from the observations.

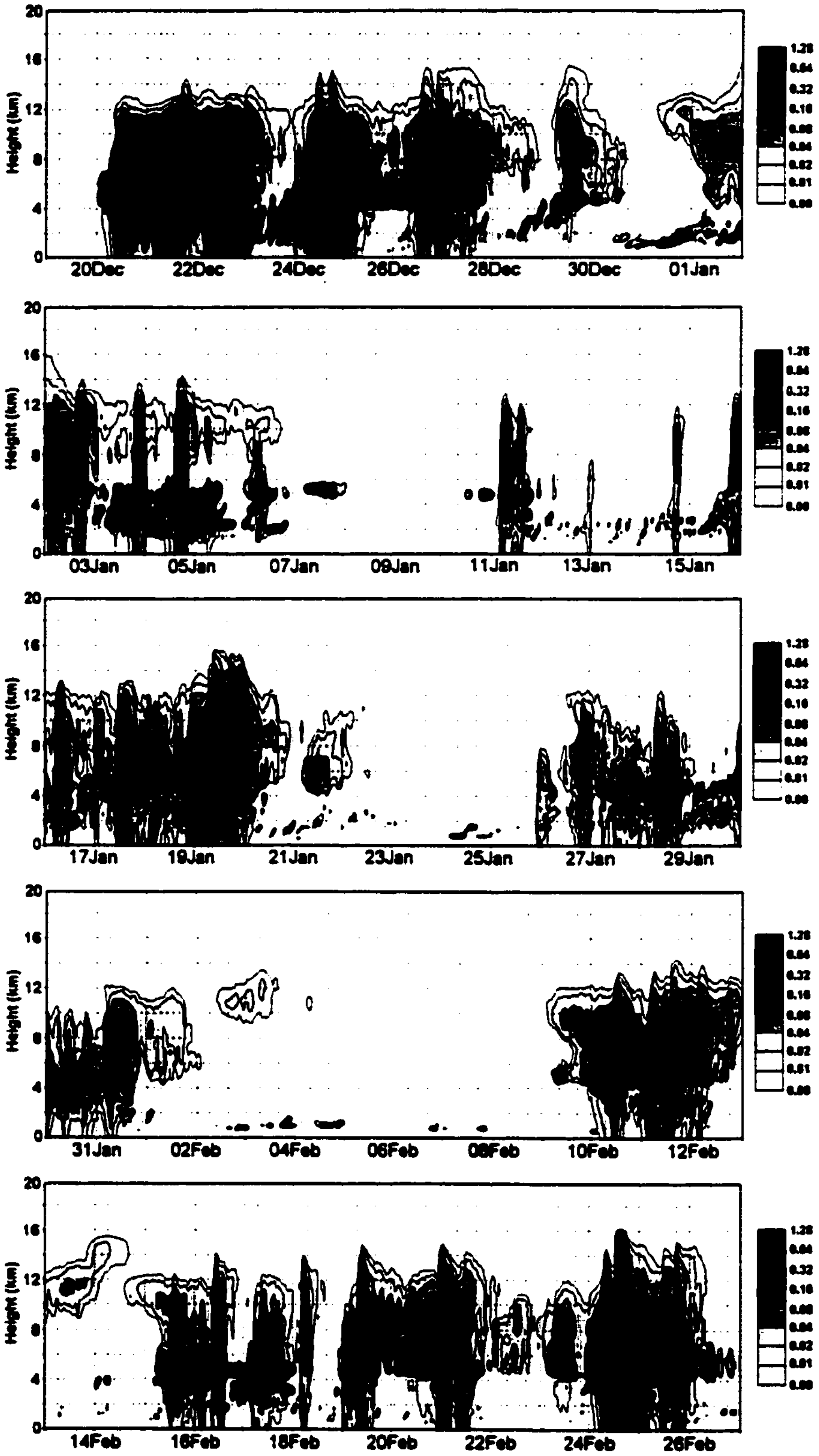

Figure 10.2 – Time evolution of the domain-averaged total condensate mixing ratio (in gkg^{-1}) as a function of height. Contour and gray-shading intervals follow a logarithmic scale starting from 0.01 gkg^{-1}, as indicated in the scale at the right side of each plot.

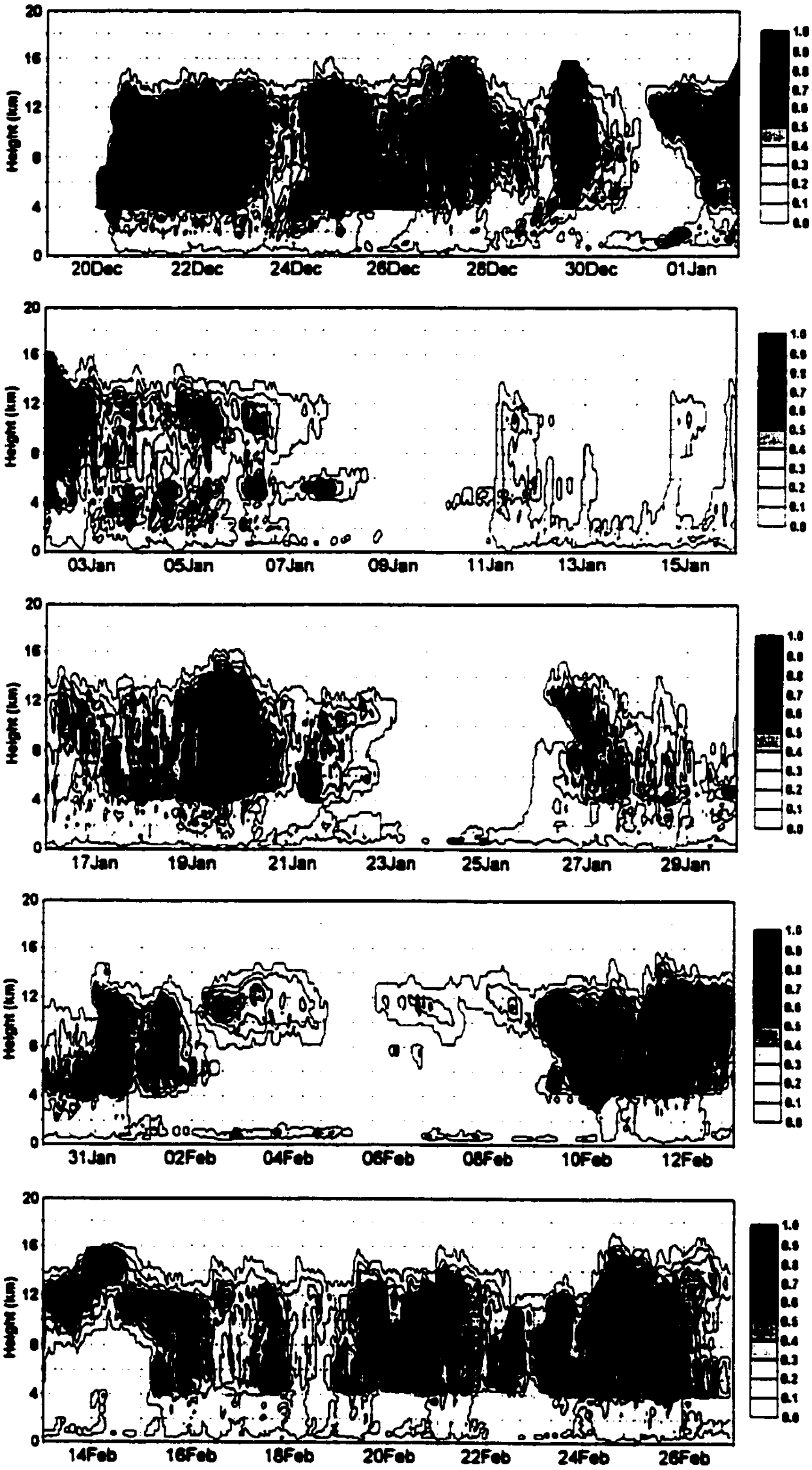

Figure 10.3 – Time evolution of the cloud fractional area (dimensionless) as a function of height. Contour and gray-scale shading intervals are 0.1.

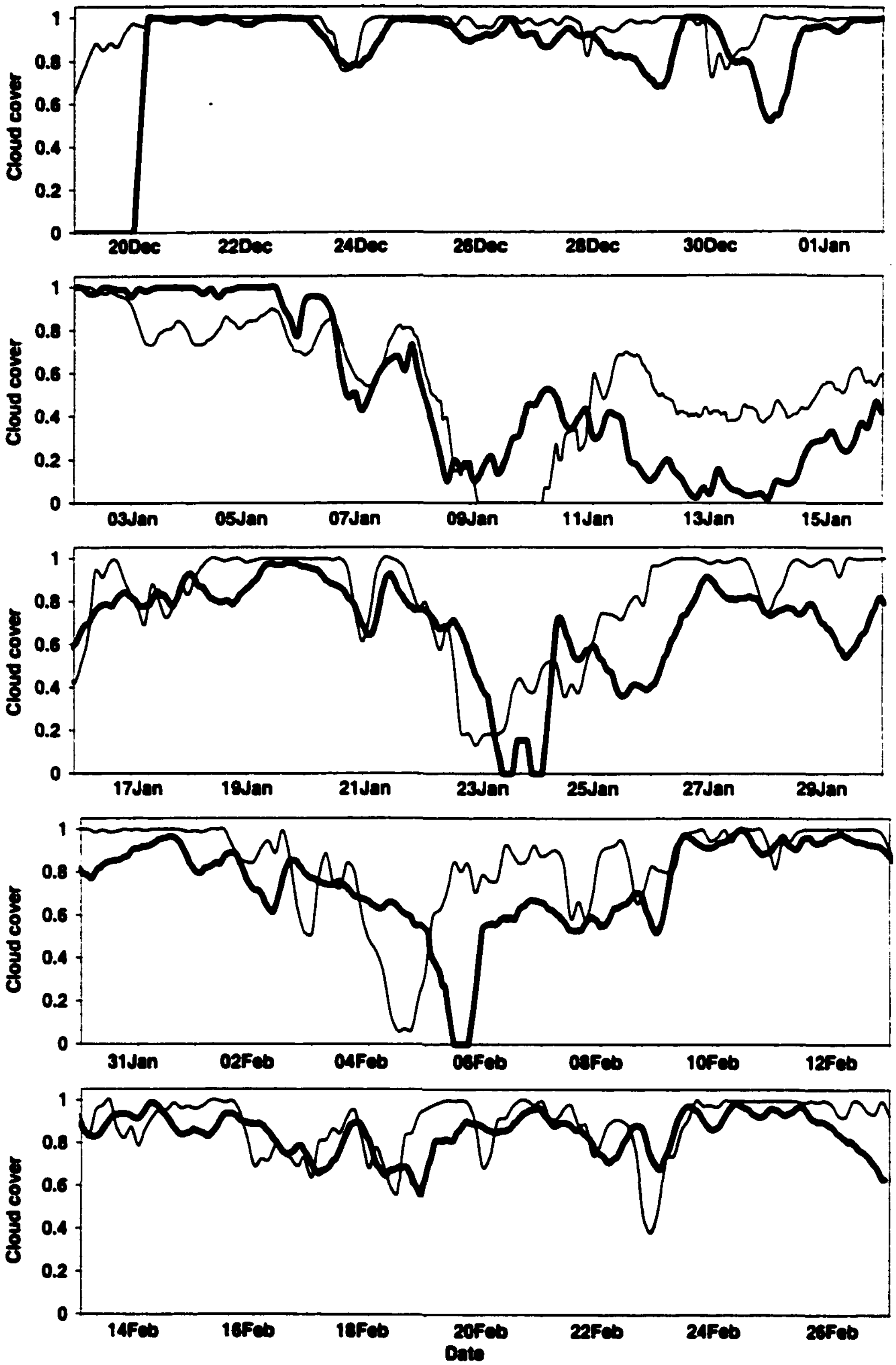

Figure 10.4 – Time evolution of the modeled (thick line) versus ISCCP (thin line) cloud cover over the COARE IFA between 19 December 1992 and 27 February 1993.

10.1.3 – Surface heat fluxes and Precipitation

The simulation of Case 3 provided an opportunity to evaluate the model capability to accurately represent the surface heat fluxes and the surface precipitation in a variety of regimes, including different deep convective regimes, as well as opposite trade wind regimes associated with WWBs or calm winds.

The time-varying domain-averaged modeled surface heat fluxes and precipitation are shown along with their counterparts calculated from COARE IFA observations for the 70-day period between 19 December 1992 and 27 February 1993 in Figures 10.5 to 10.9. Figure 10.5 corresponds to the evolution of those fields during the first couple weeks of that period, which were dominated by strong convective activity, particularly between 19 and 28 December. As discussed by Lin and Johnson (1996b), the sensible heat flux peaked during the period of maximum convective activity. Therefore, a strong correlation can be noted between the sensible heat flux (Figure 10.5a) and the precipitation field (Figure 10.5c). Both the precipitation and the sensible heat flux exhibit maximum values during the most pronounced convective episodes in the period between 19 and 28 December (a comparison can be made between Figure 10.5 and the convective warming and drying panels 3.7c and 3.7d). The latent heat flux, on the other hand, maintained an increasing trend after deep convection and precipitation were suppressed, i.e., after 28 December (Figure 10.5b). Such enhanced evaporation occurred in association with very strong westerly winds, as shown in Figures 3.7a and 3.7b. Between 19 December and 02 January, the model was generally capable of reproducing the observed fields, except that it underestimated the major peaks in the sensible (Figure 10.5a) and latent (Figure 10.5b) heat fluxes during convective episodes, as well as the surface precipitation after 28 December (Figure 10.5c).

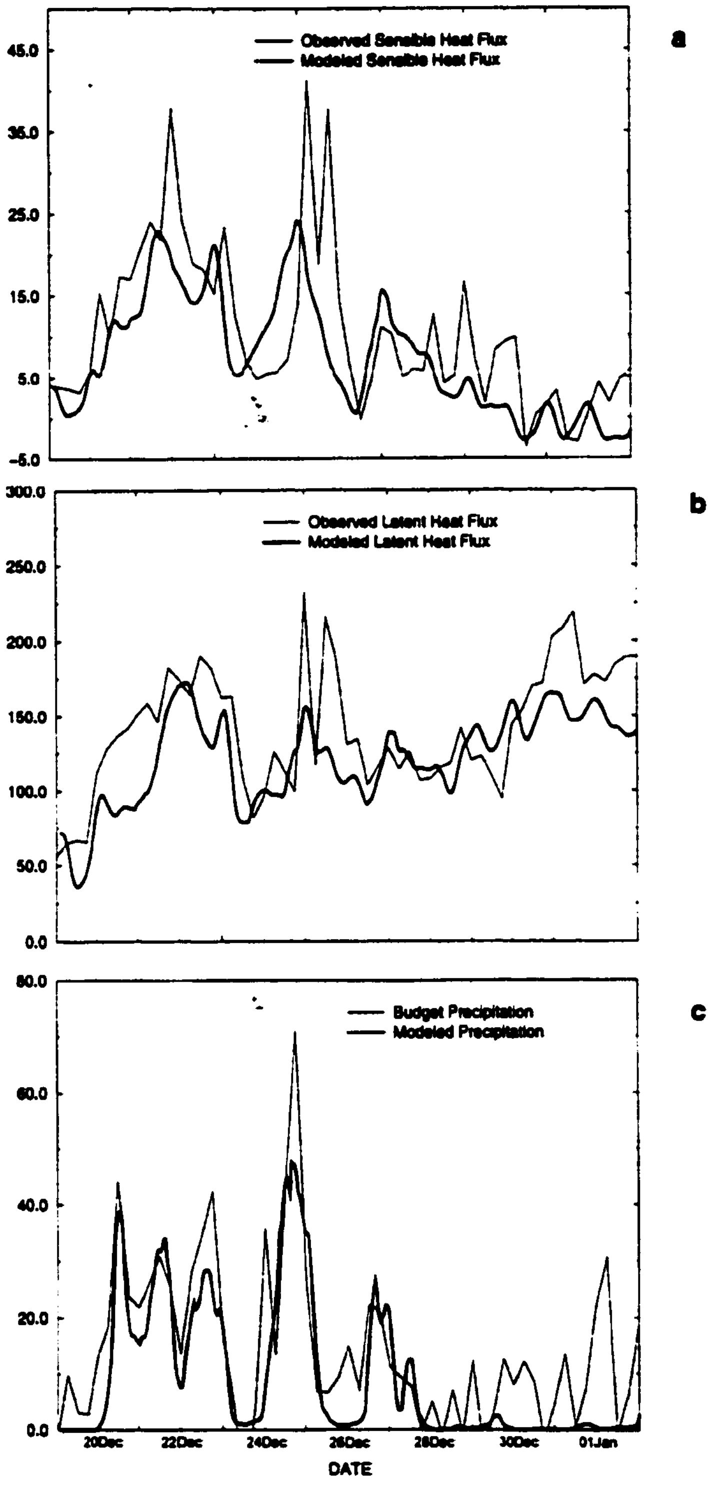

Figure 10.5 – Modeled versus observed (a) sensible heat flux, in Wm^{-2}, (b) latent heat flux, in Wm^{-2}, and (c) surface precipitation, in $mmday^{-1}$ over the COARE IFA between 19 December 1992 and 02 January 1993.

Figure 10.6 depicts the evolution of the sensible heat flux (Figure 10.6a), latent heat flux (Figure 10.6b), and surface precipitation (Figure 10.6c) over the COARE-IFA, between 02 and 16 January 1993, as modeled by RAMS-POM and as calculated from the observations. In association with reduced convective activity, the sensible heat flux was small through that entire 14-day period. The diurnal cycle appears as an important contributor to the variations of the sensible heat flux in time. In general, the results from the coupled simulation showed good agreement with the observations, particularly on days of suppressed convection, when the model was able to properly represent both the magnitude of the sensible heat flux and the amplitude of its diurnal variation (Figure 10.6a). In early January, significant evaporation occurred in association with strong westerly winds, with observed values of the latent heat flux as high as 200 Wm^{-2} for the average over the IFA. As the winds relaxed, the latent heat flux decreased, reaching values below 50 Wm^{-2} less than one week later. By mid-January, evaporation increased again, with values of latent heat flux exceeding 100 Wm^{-2}. The coupled model was able to represent all those trends, although it underestimated the latent heat flux by about 20% during the peak WWB (Figure 3.10b). The budget precipitation was small, especially during the last 5 days of the period. The coupled model simulation provided values of simulated precipitation comparable to its counterparts based on observations between 02 and 05 January and after 11 January. However, it underestimated the budget precipitation during the intermediate period (Figure 3.10c).

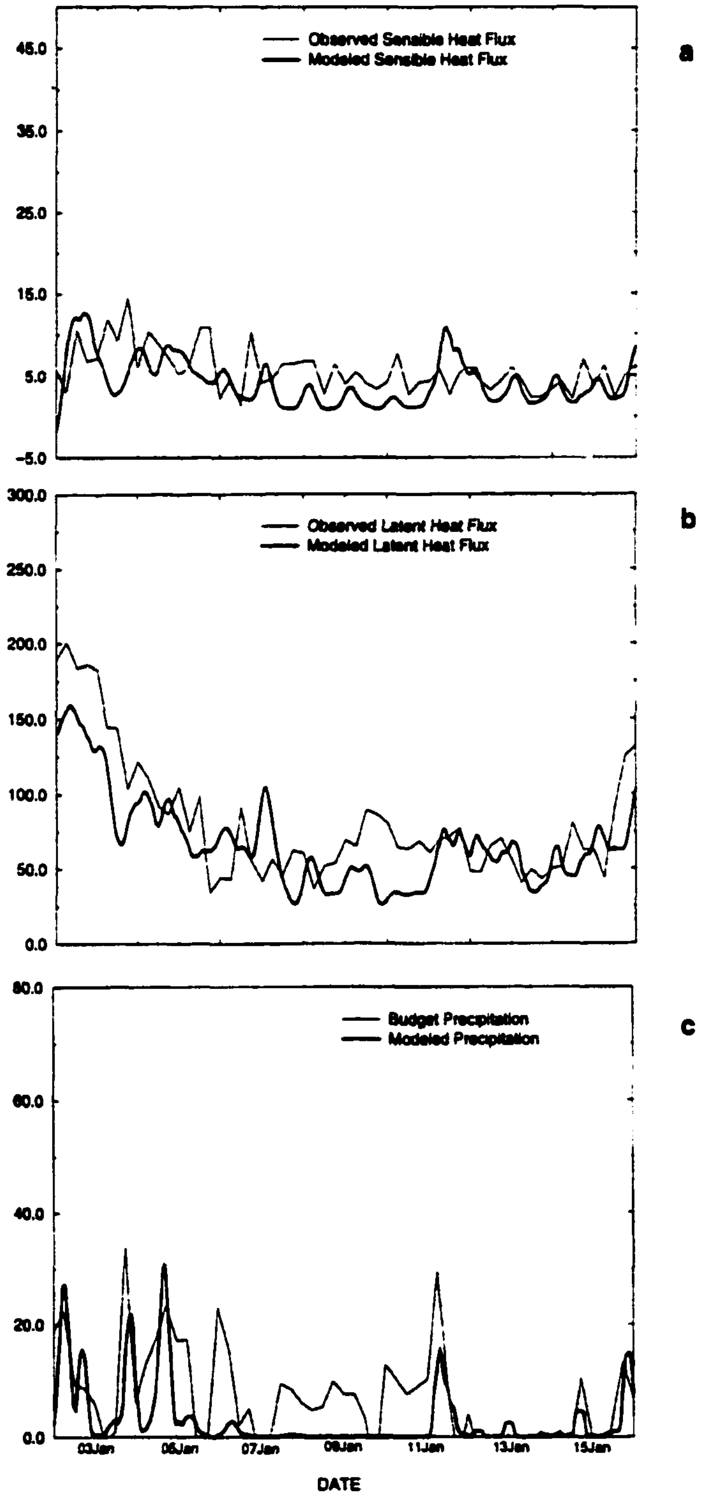

Figure 10.6 – Same as Figure 10.5, except between 02 and 16 January.

Figure 10.7 shows the IFA-averaged surface heat fluxes and precipitation, as calculated from the observations and simulated by the coupled model, from 16 and 30 January. As discussed in Chapter 3, in the first 5 days of that period deep, organized, convection developed. As a result, enhanced sensible heat flux and significant precipitation occurred. Then, convection was suppressed between 21 and 26 January, resulting in reduced sensible heat flux (with a clear diurnal cycle) and virtually no precipitation. The latter part of the two-week period was characterized by some convective activity, accounting for the increase in the sensible heat flux and surface precipitation (Figures 10.7a and 10.7c). The evaporation showed three peaks (on 19, 24, and 28 January). The first peak is associated with a broad peak in the near surface winds (Figure 3.9b) and enhanced convective activity (Figures 3.9c and 3.9d). The other two were heavily related to the strong surface winds (Figure 3.9b). The modeled and observation-derived fields show reasonable agreement for that two-week period.

Most of the period between 30 January and 13 February was dominated by suppressed convection. Consequently, the sensible heat flux was often small, and strongly determined by the diurnal cycle, except in the beginning (between 30 January and 02 February) and the end of the period (between 09 and 13 February), as shown in Figure 10.8a. During the most suppressed days, the model and observed sensible heat flux were in very good agreement. The model also produced latent heat fluxes that agreed well with their observed counterparts during the whole two-week period, as shown in Figure 10.8b. The model precipitation was approximately zero during the entire time interval, except before 01 January and after 09 February. The budget precipitation was also very small, as depicted in Figure 10.8c.

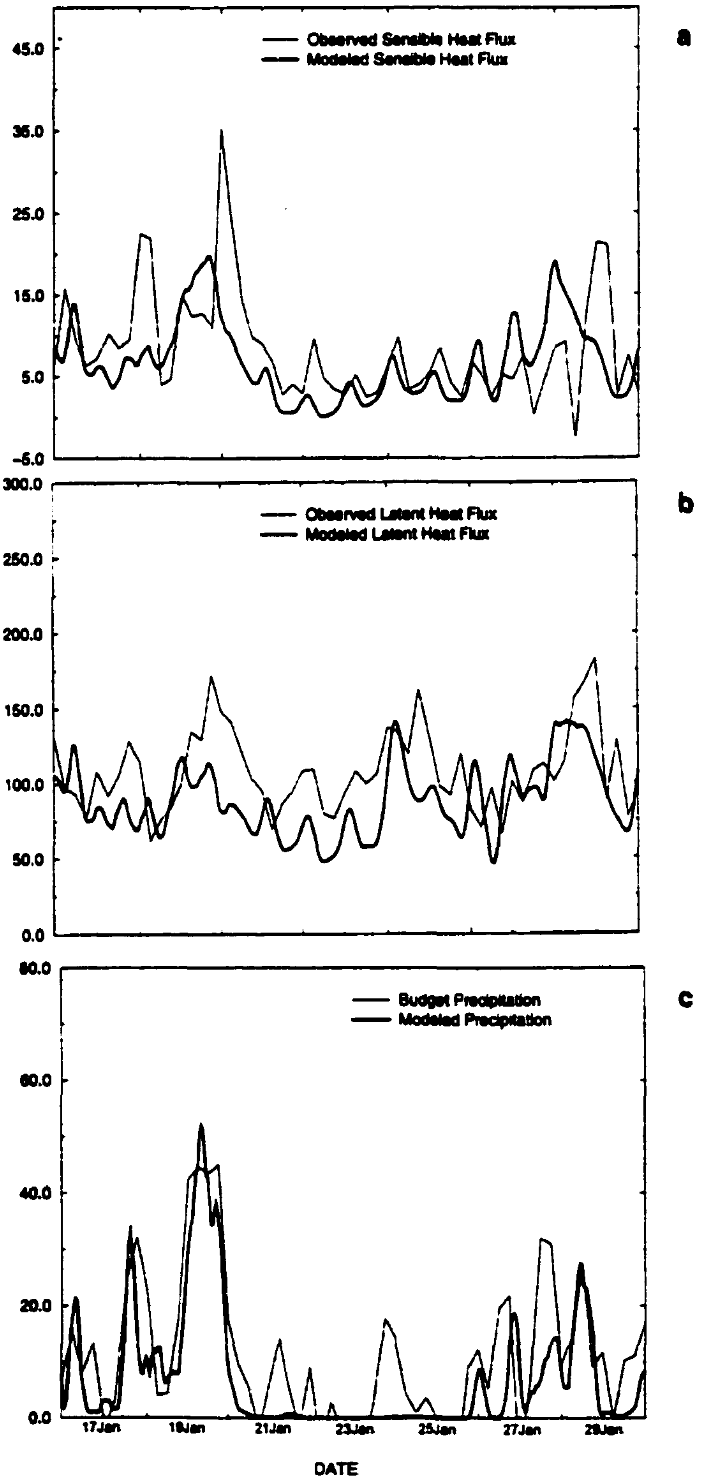

Figure 10.7 – Same as Figure 10.5, except between 16 and 30 January.

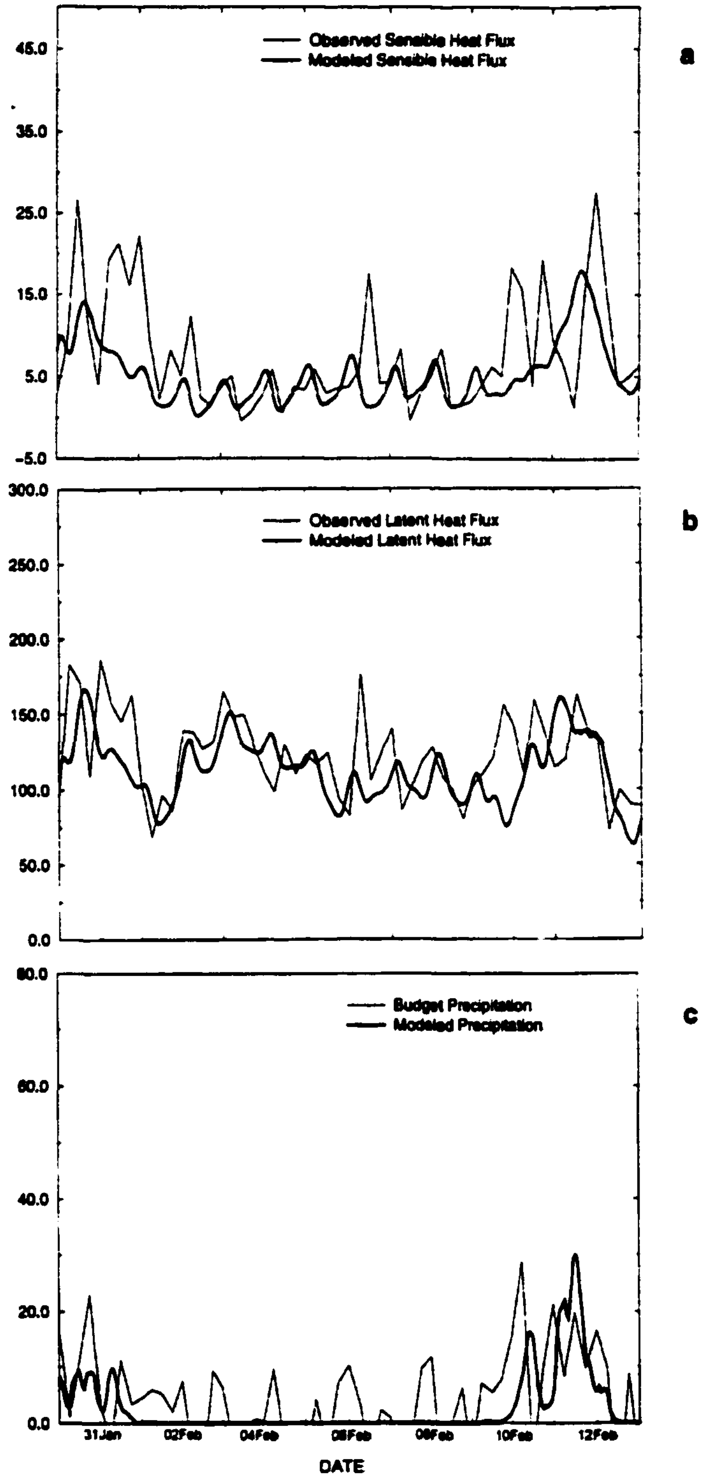

Figure 10.8 – Same as Figure 10.5, except between 30 January and 13 February.

Finally, Figure 10.9 depicts the time evolution of the sensible (Figure 10.9a) and latent (Figure 10.9b) heat fluxes and the surface precipitation (Figure 10.9c) averaged over the COARE IFA between 13 and 27 February. As pointed out in Chapter 3, late during that two-week period, active convection developed under intensifying low-level winds. Sensible and latent heat flux and surface precipitation were highly correlated, peaking during the most convectively-active periods. Although the maxima in the surface heat fluxes were underestimated, particularly in the sensible heat flux, the model was able to correctly represent the major trends in the evolution of all three variables (Figure 10.9).

On average, the model underestimated the surface heat fluxes, producing mean values of 6.0 Wm^{-2} (sensible) and 96.0 Wm^{-2} (latent). The TOGA-COARE data for the 70-day period produced average fluxes of 8.0 Wm^{-2} (sensible) and 112.1 Wm^{-2} (latent). It should be pointed out that, for the case of convection between 19 and 26 December 1992, both sensible and latent heat fluxes were smaller in the present simulation than in the ones for the same period described in previous chapters (5 and 7). The CONTROL uncoupled run described in Chapter 5 produced average fluxes of 18.6 Wm^{-2} (sensible) and 132.8 Wm^{-2} (latent), and the coupled simulation described in Chapter 7 furnished values of 18.5 Wm^{-2} (sensible) and 129.9 Wm^{-2} (latent) for that 7-day convectively active period. The corresponding values for the model in its longterm setup were 11.9 Wm^{-2} (sensible) and 108.7 Wm^{-2} (latent).

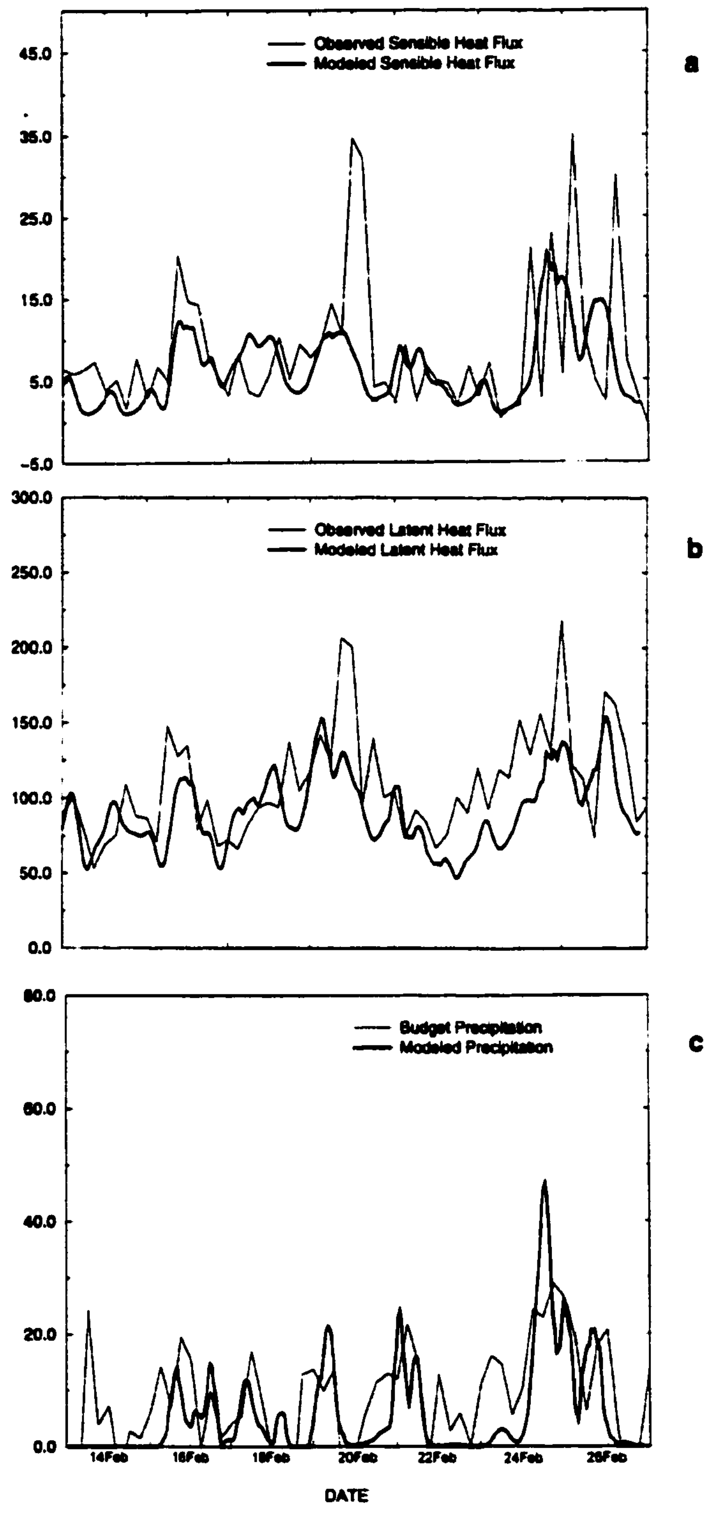

Figure 10.9 – Same as Figure 10.5, except between 13 and 27 February.

The major differences between modeled and observed surface heat fluxes in the simulation using a 2km grid-spacing were found in periods of active convection, when the fluxes were often underestimated. However, the previous simulations, in which a 1km grid-spacing was used, did not show that behavior, which suggests that changes in the model grid-spacing can produce substantial changes in the calculation of the surface fluxes. A possible explanation is that the capability of the atmospheric model in resolving small-scale circulations decreases (increases) as a larger (smaller) grid-spacing is used. Such small-scale circulations are important contributors to the transport of heat and other variables close to the surface, and are often more important when convective is active. Our results suggest that 1km grid-spacing would be a better choice to attain accurate calculations of the transport of heat in cloud-resolving simulations of the deep convective regime over tropical oceans. In our case, however, the use of a coarser resolution was imposed by computer limitations in running 70-day coupled simulations.

The model also underestimated the average IFA rainfall between 19 December 1992 and 27 February 1993, with a modeled value of 6.6 $mmday^{-1}$ versus 8.9 $mmday^{-1}$ from the calculated budget. The smaller modeled precipitation is consistent with a low-tropospheric moist bias and underestimated evaporation. The precipitation was generally better simulated during periods of strong large-scale forcing and deep convection. The underestimation of the precipitation produced by shallower convection can be associated with the parameterization of microphysical processes in that regime (not capable of properly simulating the development of precipitation in a low liquid water content regime), or with the horizontal grid-spacing (not fine enough to resolve circulations on the scale of shallow cumuli).

10.1.4 – Downward Solar Radiation

Along with the surface sensible and latent heat flux, the other major components of the heat budget of the upper ocean are the radiative fluxes. Since the tropical oceans lose thermal energy both through longwave radiative cooling and sensible plus latent heat transfer, the absorption of solar radiation becomes the sole source to maintain the high SSTs at the warm pool. An accurate representation of the shortwave radiation flux is, therefore, strictly necessary to provide a good prediction of the upper-ocean temperatures in the context of a coupled ocean-atmosphere model.

The next couple of Figures compare the modeled downward solar radiation with the data from the ISCCP. Figure 10.10 represents the time evolution of the observed and modeled downward shortwave radiation between 19 December and 27 February. Significant blocking of solar radiation by cloud systems over the COARE IFA occurred during all periods of active convection (late December 1992, mid-January and mid- and late February 1993). In most of the cases, the model was able to produce maximum values of the downward shortwave radiative flux in agreement with the observations.

In order to verify the model capability in simulating the lower-frequency variability of the downward shortwave radiation between 19 December and 27 February, a 5-day moving average was calculated. The corresponding result is depicted in Figure 10.11. The beginning of the simulated period was marked by the occurrence of a vigorous convective episode in late December 1992. As a consequence, the downward shortwave radiative flux at the surface was small, corresponding to the minimum value in the entire 70-day period. As the convective activity diminished and the cloud systems dissipated, the surface downward solar radiation experienced an increasing tendency,

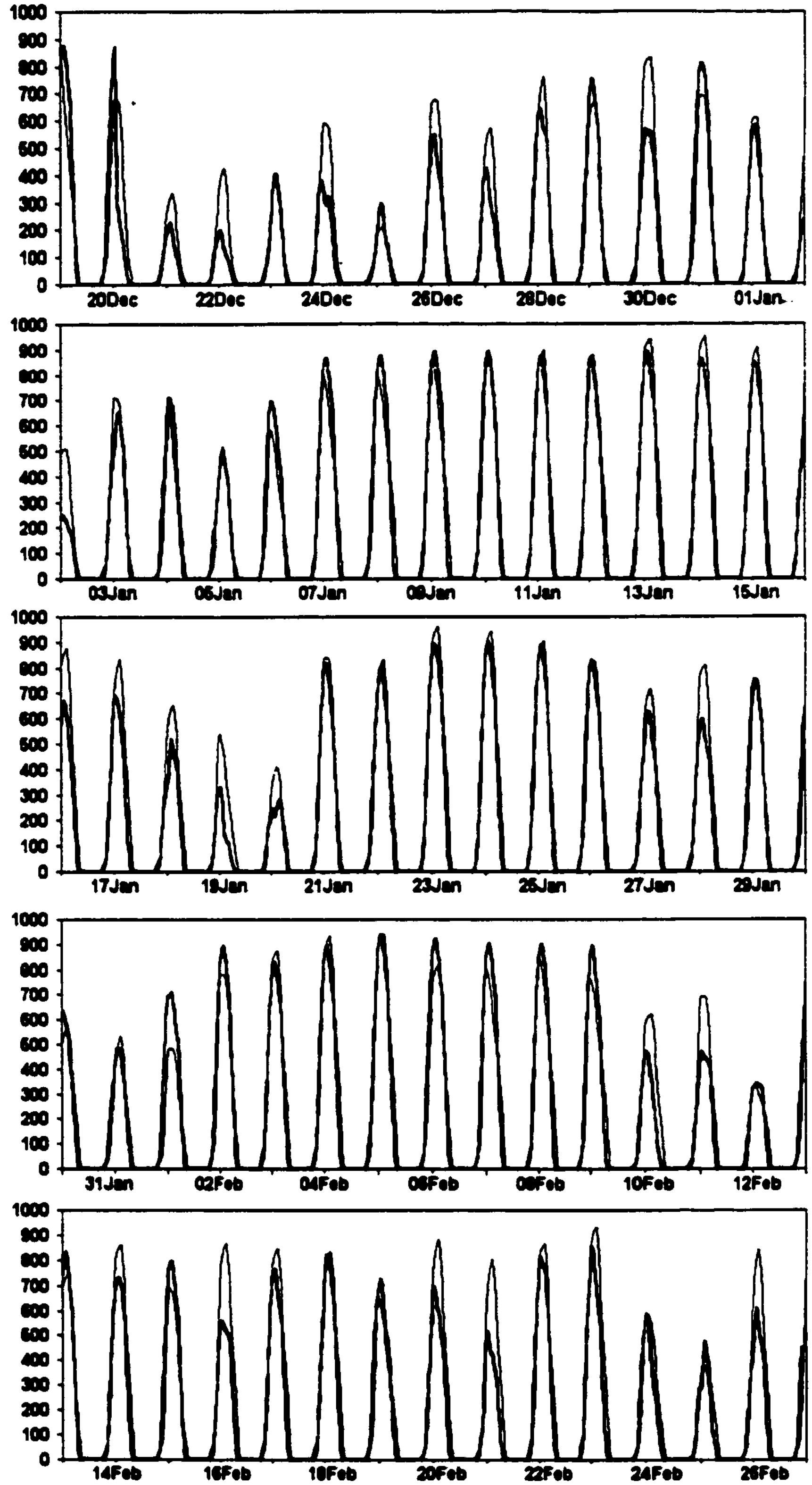

Figure 10.10 – Observed (ISCCP, thin line) and modeled surface downward shortwave radiation (thick line) between 19 December 1992 and 27 February 1993.

peaking on 16 January, according to the observations (2 days earlier, according to the coupled model). This maximum accounted for a dramatic increase in the SST, as will be shown later in this Section. Other maxima of shortwave radiative flux at the surface occurred by late January and early February.

On the average, the model underestimated the net shortwave radiative flux (186.0 Wm^{-2}, modeled, versus 196.4 Wm^{-2}, observed. The errors in the longwave radiative flux were insignificant; the model overestimating the longwave cooling at the ocean surface by 0.8 Wm^{-2}. As a result, the total radiative flux (positive downward) was underestimated by the model by 11.2 Wm^{-2}.

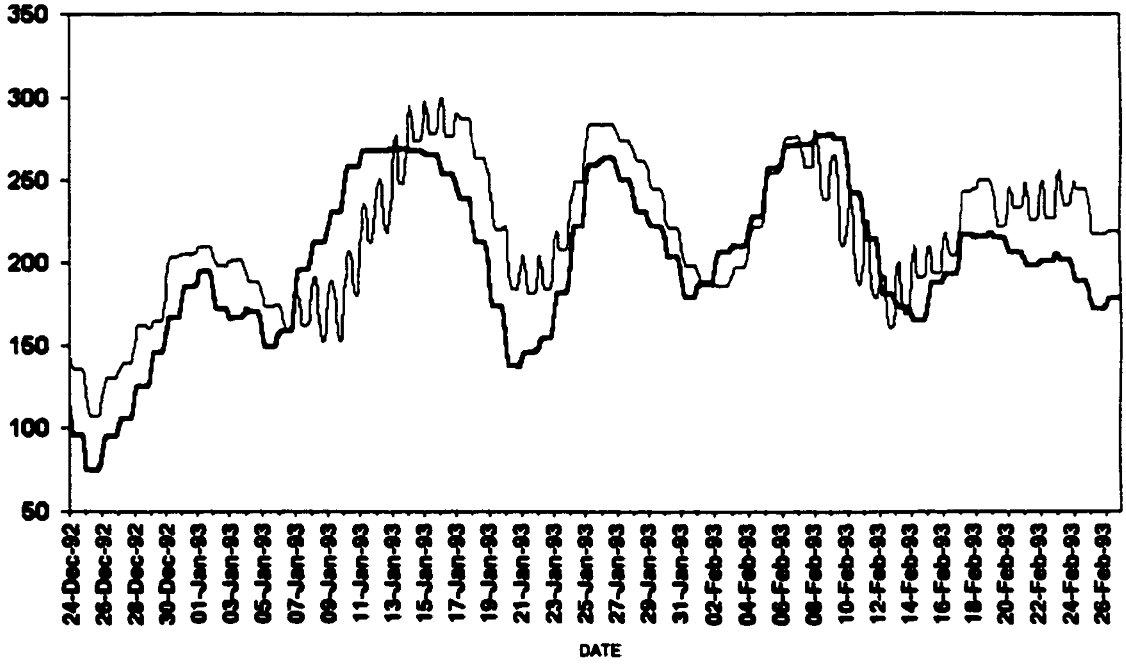

Figure 10.11 – 5-day moving averages of the observed (thin line) and modeled (thick line) surface downward shortwave radiation, between 19 December 1992 and 27 February 1993.

10.1.5 – Sea Surface Temperature

Although the ocean model was forced only by the surface fluxes (momentum, radiation, heat and precipitation), the agreement between the observed and modeled sea surface temperature was reasonable. Good results were achieved because the atmospheric model provided a surface forcing to the ocean model in agreement with the observations, and because the ocean model itself was capable of simulating important aspects of the upper-ocean dynamics in the warm pool, despite limitations due to two-dimensional geometry and the lack of large-scale oceanic forcing.

Figure 10.12 shows the behavior of the average SST over the IFA and its domain-averaged modeled counterpart. In general, the low-frequency trends are well reproduced, although the diurnal cycle was more evident in the simulation than in the observations.

The difference in the amplitude of the modeled and observed diurnal temperature range can be associated with the departure from the observed cloud coverage. As shown previously, the model produced more clearing than observed. The smaller diurnal temperature peak found in the observations is also associated with the poor resolution of the COARE data set. The model often showed peak SSTs at about 04 UTC, while observations were available for comparison at 00UTC, 06UTC, 12UTC and 18UTC. At 06UTC the modeled SST was commonly 0.2 to 0.3°C cooler than the maximum, achieved 2 hours before.

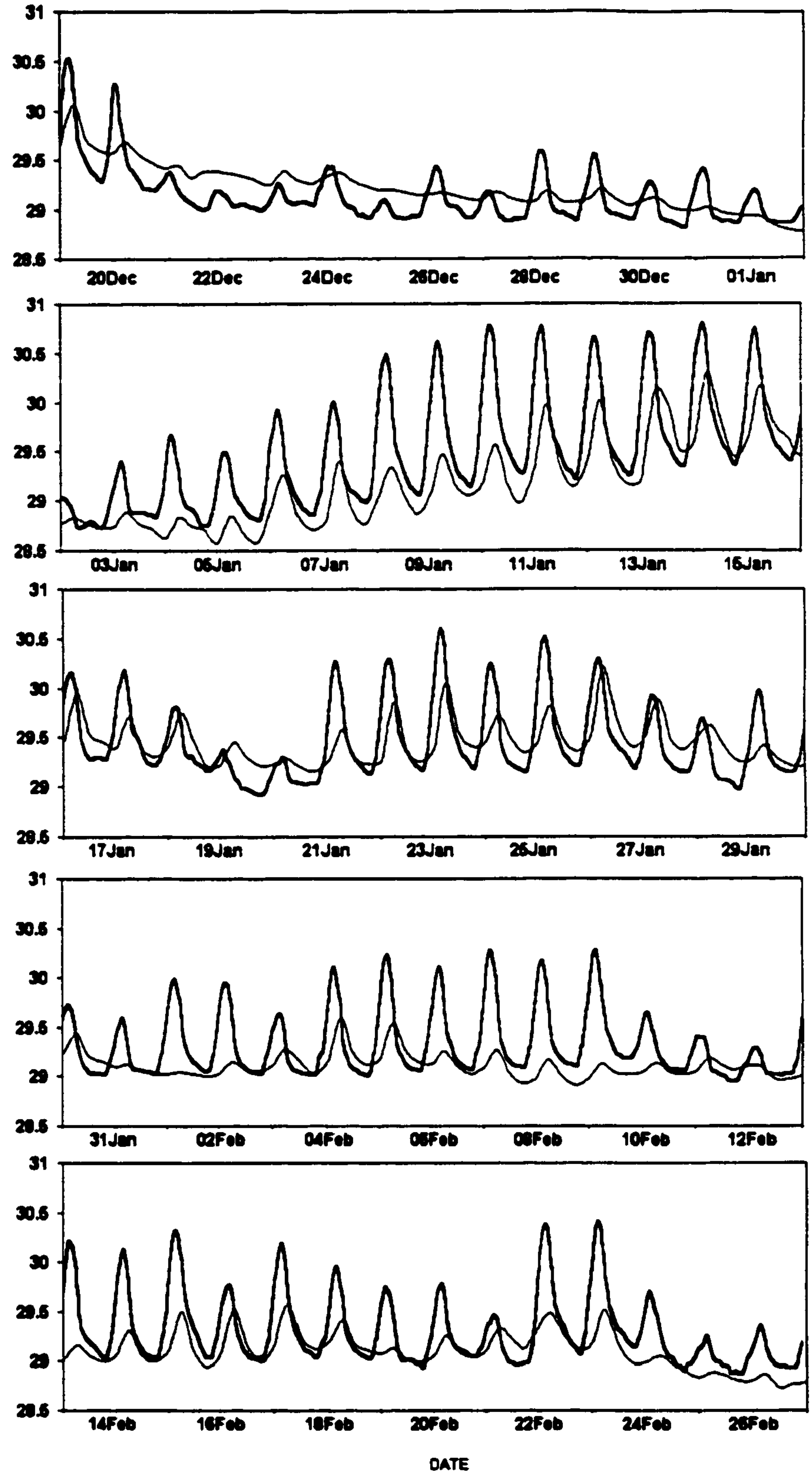

Figure 10.12 – Observed SST, averaged over the IFA (thin line) and modeled SST, averaged over the model domain (thick line), between 19 December 1992 and 27 February 1993.

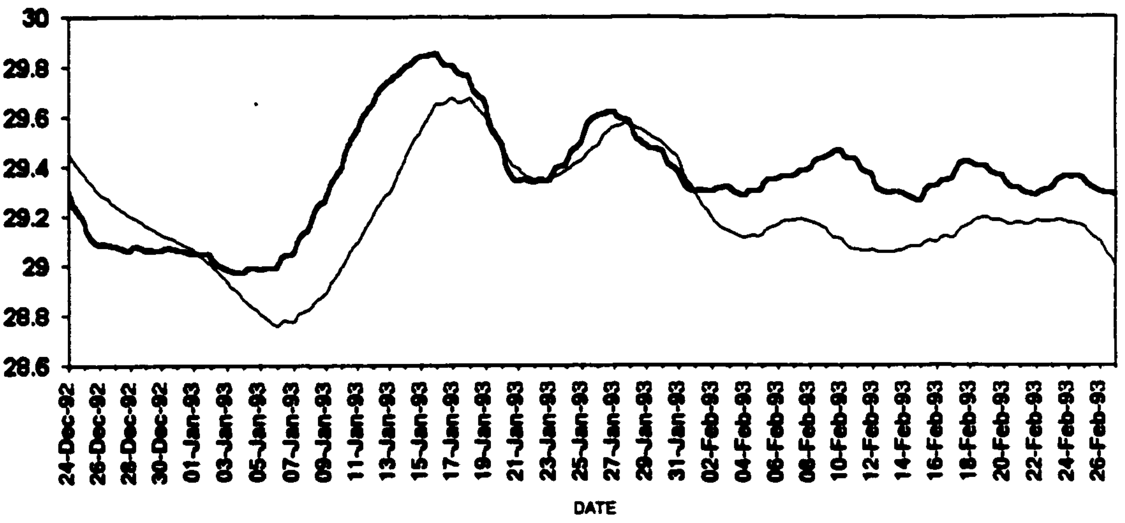

Figure 10.13 – 5-day moving averages of the observed (thin line) and modeled (thick line) SSTs, between 19 December 1992 and 27 February 1993.

Due to the poor time resolution of the observations, a better examination of the model results can be done looking at the SST lower-frequency variability. Figure 10.13 depicts the 5-day moving average of the observed and modeled SSTs for Case 3. Most of the observed trends were well represented by the model, including the prominent warming between 06 and 16 January, and the fluctuations after 04 February 1993. It should be pointed out that all SST tendencies apparent in Figure 10.13 are related to the low-frequency trends in the downward shortwave radiation shown in Figure 10.11, with a phase lag ranging from one to about three days.

The only major difference between the behavior of the modeled and observed SSTs was found in the beginning of the simulation (before 06 January), when the model underestimated the cooling tendency, suggesting that the model spin-up process was not completed yet. In general, there was good agreement between observed and modeled surface temperatures at the ocean, even though processes such as large-scale advection of oceanic fields were not included. It suggests that local surface forcing including radiative fluxes, and heat, momentum water substance transfer at the air-sea interface play a very significant role to the evolution of the upper ocean fields on timescales of the order of several weeks (intraseasonal variability).

On average, the model SST was slightly warmer (29.35°C versus 29.22°C, observed). The model underestimated the sensible plus latent heat flux by 18.1 Wm^{-2}, however it also underestimated the net radiative flux by about 11.2 Wm^{-2}. The resulting difference between the modeled and observed net total heat flux (6.9 Wm^{-2}) is small and compatible with the warm bias (0.13°C) produced by the ocean model. A warming effect of the same order of magnitude can be generated distributing 6.9 Wm^{-2} through a layer about 70m deep, during a period of 70 days.

10.2 – Sensitivity Study

As discussed in previous chapters, many researchers argue that the salt-stratification in the warm pool, with fresher water close to the surface, and a halocline shallower than the thermocline, is important to the maintenance of the large SST values over that region.

A sensitivity test was designed in order to investigate how the haline structure of the warm pool influences its thermal structure. The realistic vertical profile of salinity, based on ship measurements, used in the initialization of the model in the simulation described in the previous Section, was substituted by a constant profile, with a uniform, prescribed salinity of 35.0 psu. The freshwater flux was set to zero throughout the entire simulation, so the constant salinity profile was held constant. As a consequence, the temperature was the only contributor to buoyancy effects.

10.2.1 – Effects on the ocean temperature

The effect of ignoring salinity effects in the time mean of the domain-averaged sea surface temperature was very small. The 70 day-mean of the SST in the control simulation was 29.35°C, versus 29.38°C for the sensitivity experiment.

The three plots in Figure 10.14 provide information on how the different salinity structures influence the thermal evolution of the ocean surface. The upper panel depicts the 5-day moving average of the SST for the control and sensitivity runs. The center panel shows the difference between the SSTs in the two simulations and the corresponding 5-day moving average. The lower panel depicts the 5-day moving average of the net heat flux (positive downward), including effects of shortwave and longwave radiation and sensible and latent heat fluxes, in the two simulations.

Because the statistics of the atmospheric forcing in the two simulations were essentially the same, the SST underwent similar evolution in both cases, as shown in Figure 10.14a. During the suppressed phases, the two simulations produced very similar SST values, and the major differences between the simulated SSTs occurred in the two periods of active convection (late December and mid January). In both cases, the SST was higher in the sensitivity run, in disagreement with the hypothesis that salinity stratification acts to enhance the upper-ocean temperatures in the warm pool.

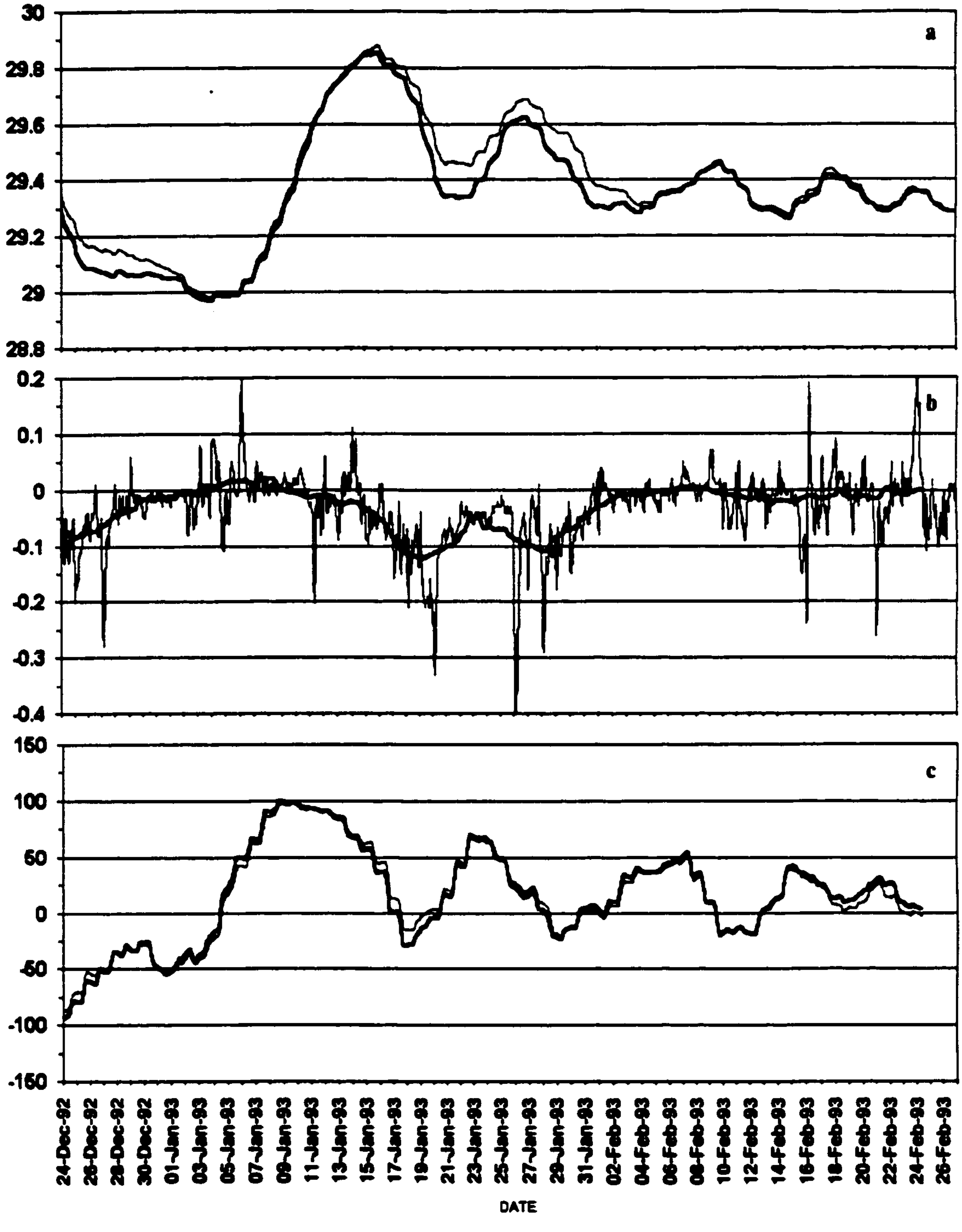

Figure 10.14 – (a) 5-day moving average of the SST in the control (thick line) and sensitivity (thin line) simulations of Case 3. (b) Difference between the SST in the control and sensitivity simulations (thin line) and its 5-day moving average (thick line). (c) 5-day moving average of the net heat flux in the control (thick line) and sensitivity (thun line) Case 3 simulations.

Figure 10.14b shows that the maximum differences between the average SST in the two simulations are no larger than a few tenths of degree. In the 5-day moving average, differences greater than 0.1°C were found to last for several days.

The difference between the net heat flux in the control and sensitivity runs was virtually negligible (average of -0.56 Wm^{-2}), as shown in Figure 10.14c. It is of the same order of magnitude as the heat flux necessary to produce a temperature drop of hundredths of degrees in a 70m deep column of water substance after 70 days but it is too small to account for the temperature differences shown in Figure 10.14b.

Analysis of Figures 10.14b and 10.14c clarifies the physical mechanism associated with the temperature deficit in the salt-stratified case. The SST in the sensitivity run is greater during periods of net surface cooling or small warming. On the other hand, when the upper-ocean experiences significant net warming, the difference between the two simulated SSTs is negligible.

During active periods, large amounts of fresh water are deposited into the ocean by the precipitating systems, resulting in the production of shallow freshwater lenses that are highly stable. The strong stability of the fresh anomalies associated with the significant haline stratification allows the sustenance of an inversion in the vertical profile of temperature close to the surface. This inversion can be very strong in the fresh lenses, as reflected in the average temperature profile. Only the control simulation is able to properly represent this phenomenon. In contrast, in the sensitivity simulation, the mixing of cool rainwater with the warmer water below cannot be prevented because there is no salinity effect on the upper-ocean stability. Hence, the ocean surface tends to remain warmer than in the control case.

The difference in the thermal structure of the ocean mixed-layer in the two simulations (sensitivity minus control) is shown in Figure 10.15. Following the first major convective episode (20 to 28 December), some differences appeared in the evolution of the ocean temperature in the two simulations. In the first panel of Figure 10.15a, at least two layers are distinctive. In the layer above, the temperature in the sensitivity run was warmer on average. In contrast, in the layer below, the ocean temperature was greater in the control simulation. Such a dipolar structure forms because, due to the salt stratification, the upward transport of heat which opposes to the settling of cool rainwater at the ocean surface, is inhibited in the control, but not in the sensitivity simulation. It is apparent that, even four days after the end of the period of active convection, the ocean surface was still warmer in the simulation with no salinity effect. A similar pattern was found after 18 February.

During suppressed periods, such as between 01 and 10 February, there was virtually no difference between the upper-ocean temperature in the two simulations, particularly at nighttime. During daytime, however, under calm winds and suppressed convection, any small difference in the net surface heating rate can cause variations in the shallow, stable near-surface layer. This can be verified in the fourth panel of Figure 10.15. At certain days, such as 03 and 04 February, the ocean was warmer in the sensitivity simulation in the upper 10-20m, as opposed to 05 to 09 February, when the temperature of that layer was greater in the control run. In an average sense, the results

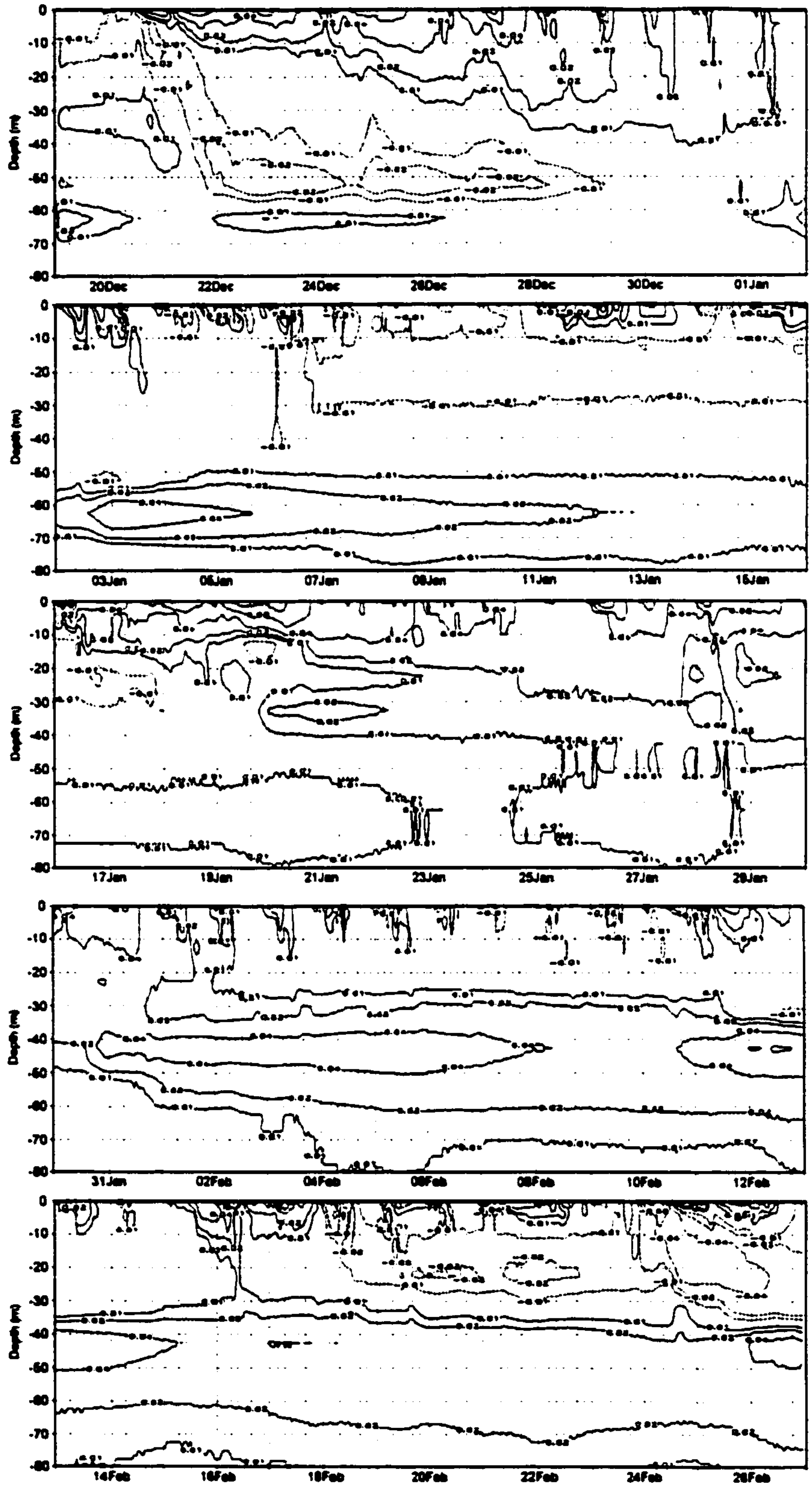

Figure 10.15 – Difference between the ocean temperature in the sensitivity and control simulations (°C) in the upper 80m. See text for comments.

suggest that there is no significant effect of the salt-stratification in the ocean temperature during suppressed periods. During such periods, the thermal stratification appears to be dominant, at least during daytime. In fact, the presence of the highly-stable diurnal warm layer, combined with evaporation, can produce a small salinity inversion, with a saltier, warmer shallow layer sitting over the cooler, slightly fresher water in the mixed-layer below.

A better understanding of the average effect of the salt stratification on the thermal structure of the WPWP can be assessed in a composite analysis of the ocean model data for the different phases of the MJO. Three composite profiles were calculated, one for the convectively active periods, and two for the suppressed periods (daytime and nighttime). The difference between the composite temperatures in the two simulations (sensitivity minus control) is depicted in Figure 10.16.

Most of the differences shown in Figure 10.16 are extremely small, except that, during active periods, in the simulation with no salinity effect, the ocean surface was often warmer by about a tenth of a degree. This contradicts the common belief that the haline stratification at the WPWP helps the maintenance of high SSTs. In fact, our simulations suggest that the relatively fresh upper layers help the SSTs to stay at a lower temperature, by preventing mixing and the consequent destruction of the slight temperature inversion associated with the cooler precipitation.

Although the variability at the near-surface layers is greater during daytime, there is no significant influence of the diurnal cycle coupled to the salinity stratification to modify the average vertical profile of the ocean temperature. This also contradicts the viewpoint that the occurrence of high SSTs relies on the existence of a stable, fresh layer.

If convection (and precipitation) is present, as discussed previously, the tendency is that the salt-stratification helps the upper ocean to remain cooler. Hence, if the salinity stratification acts to favor high SSTs, it would happen primarily during periods of suppressed convection. Such a tendency was not observed in our numerical experiments.

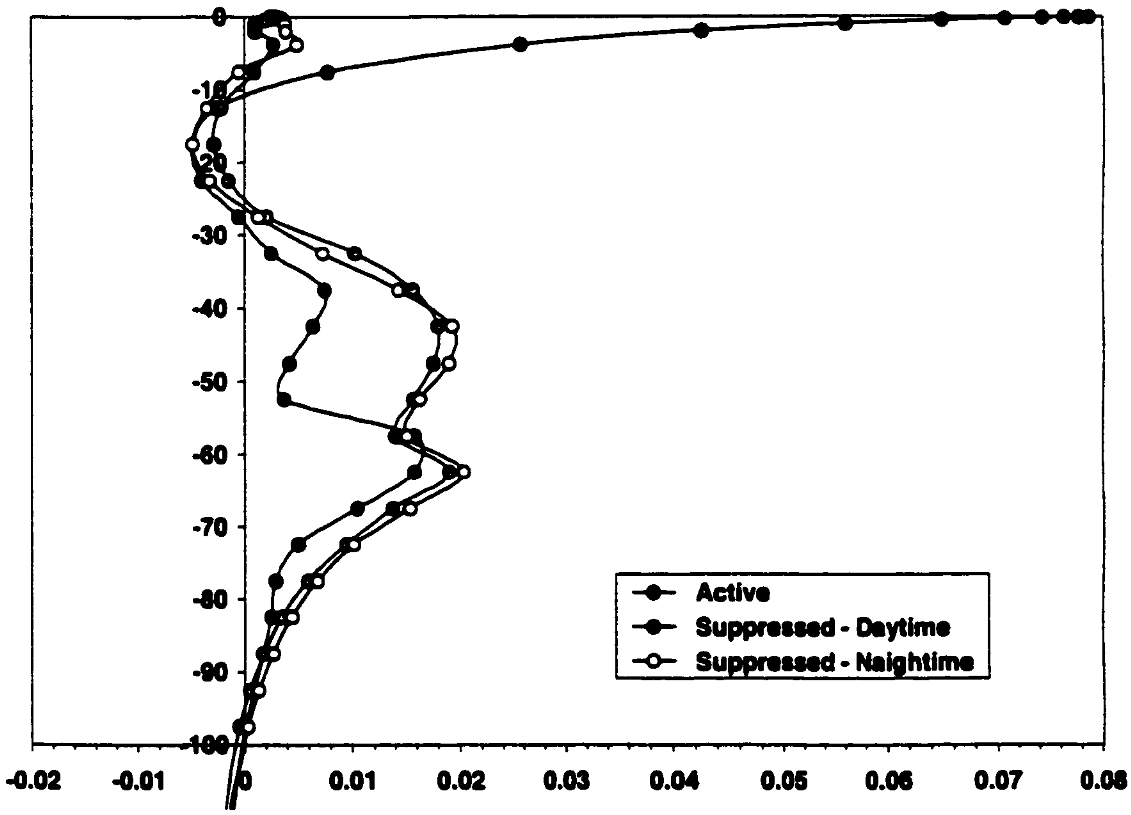

Figure 10.16 – Composite difference between the ocean temperature in the sensitivity and control simulations, in the upper 100m for convectively active cases (black circles), daytime suppressed cases (gray circles) and nighttime suppressed cases (white circles).

Chapter 11

CONCLUSIONS AND FUTURE RESEARCH

No Fim da chuva e do vento	At the End of the rain and the wind
Voltou ao céu que voltou	The moon returned to the sky, and
A lua, e o luar cinzento	The gray moonlight
De novo, branco, azulou.	Again, white, turned blue.

(Fernando Pessoa)

A two-dimensional cloud-resolving model was used to simulate the evolution of convection over the Western Pacific in several cases during the Tropical Ocean Global Atmosphere Coupled Ocean – Atmosphere Response Experiment (TOGA-COARE). In all simulations, the atmospheric model was forced by observed advective tendencies of temperature and moisture, a primary driving mechanism for the development of deep convection, and by observed average winds. In some, the sea surface temperature (SST) was prescribed. In others, an ocean model, coupled to the CRM was used to predict the sea temperature, along other oceanic variables, such as salinity and currents. In the present Chapter, the most important findings are summarized

11.1 – Uncoupled simulations with uniform SSTs

Two-dimensional cloud-resolving simulations of the evolution of tropical convection over the Western Pacific warm pool between 19 and 26 December 1992 were performed with prescribed SSTs. Results from a control simulation showed that the CRM is generally able to represent the response of cloud systems to the large-scale forcing. The strong similarities in the statistics of an ensemble of simulations akin to CONTROL (differing only in the random perturbation introduced in the air temperature field) showed its robustness.

Sensitivity tests were performed in order to evaluate the influence of SSTs on the behavior of the simulated cloud systems. Most of the atmospheric fields were very similar in all simulations, indicating the dominant influence of the prescribed large-scale forcing. For the case of warmer SSTs, the variation of total precipitation was smaller than would be obtained if the extra supply of moisture from the surface were totally converted to precipitation, since part of it was used to moisten the atmosphere (the opposite occurred for the case of cooler SSTs). The results reinforce the point of view that the primary driver for precipitation production is the large-scale circulation rather than the surface fluxes (although in reality the more local, surface forcing, and the more remote, large-scale forcing cannot be separated). Moreover, it agrees with the baseline assumptions of several convective parameterizations, in which the precipitation is estimated based on the characteristics of the large-scale flow.

However, despite the similarities in most of the simulated fields, including the total precipitation, the simulations revealed important sensitivities in the organization of the cloud systems to the imposed SST field. A relationship was observed between the average magnitude of the surface fluxes and the way the cloud systems are separated between their convective and stratiform components. The 7-day mean of the domain-averaged values of the area covered by convective elements and the precipitation associated with them increased by about 17% from the simulation with the lowest SSTs to the simulation with the highest SSTs. Not only were more and stronger convective segments produced as the SST increased, but also compensating subsidence increased, which modified the distribution of cloud coverage and total condensate. Although more cirrus clouds formed in the simulation with larger SSTs, the amount of solar radiation that reached the surface in SST+ was approximately the same as in SST- and CONTROL, in opposition to what is predicted according to the cirrus-thermostat theory. The similar values of surface downward shortwave radiation in CONTROL, SST- and SST+ were primarily due to the reduction (enhancement) of low-level cloud coverage in association with warmer (colder) SSTs.

A similar mechanism has been suggested on a larger scale in the transition between the marine stratocumulus (Sc) and trade wind cumulus (Cu) regimes. In the case of the Sc to Cu transition, a positive feedback occurs between cloud coverage and SST, such that cold (warm) SSTs help to support (destroy) stratiform clouds, increasing (reducing) the fractional cloud area, which favors further cooling (warming) of the sea surface.

Additional research is required to verify whether such a feedback also occurs in the deep convective regime or not. The present study has evident limitations, for example, constraining all the simulations by using the same large-scale forcing is not completely realistic, because the forcing actually depends on the SST, but on a much larger scale. Also, because two-dimensional simulations exclude one of the natural degrees of freedom of convection, downdrafts tend to be exaggerated. Therefore, the observed differences in the convective/stratiform partition and the little impact on the radiative budget might be an artifact of applying the large-scale forcing in a two-dimensional framework. Determining the impact of the two-dimensionality can be investigated using full three-dimensional cloud-resolving simulations. However, nested-grid CRM simulations are required in order to account for the full range of dynamical interaction on multiple scales.

It should be pointed out, however, that there is some evidence that, in reality, surface temperatures can affect the convective-stratiform partition in deep oceanic convection. For instance, Rickenbach et al. (1998) noted that more convective precipitation was found in the TOGA COARE region (78% according to Rosenfeld et al. 1995), where the SSTs are warmer, than in the GATE region (60% according to Cheng and Houze 1979), where the SSTs are cooler.

11.2 – Uncoupled simulations with non-uniform SSTs

A significant variability was observed by several authors in the SST field over the warm pool, with sharp changes occurring on scales of the order of tens of kilometers or less (e.g., Hagan et al. 1997, Soloviev and Lukas 1997, Wijesekera et al., 1999). In order to investigate the influence of SST inhomogeneities of different wavelengths, idealized simulations were performed, in which sinusoidal perturbations were superimposed to the observed average SST.

Despite the similarities among most of the results from the simulations of heterogeneous SST and the ones for the control run, different space-time organizational patterns were observed. Because convection is a very non-linear process, the dominant atmospheric circulations (and precipitation patterns associated with them) can develop on a scale other than the one being forced. Large-scale SST perturbations actually induced circulations at coarse spatial and time scales, while medium-scale inhomogeneities tended to produce convective activity on smaller scales. Small-scale perturbations, however, did not favor convection at similar scales. The simulation where the SST was varied using short wavelengths actually favored larger circulations (on the order of several tens of kilometers). SST disturbances of medium-sized wavelengths were shown to favor the "convective mode" of organization and convective precipitation, while both large and small wavelengths favored a "mesoscale mode" and stratiform precipitation. Because a pattern with fluctuations on extremely small scales is virtually indistinguishable from another with no departures from the mean at all, one expects the existence of a point between, for which the influence of intermediate scales is maximized. The present results suggest that, for deep convection, such a point corresponds to a scale somewhat larger than the one of an individual cumulonimbus cloud. If the system is forced at a wavelength much greater or much smaller than its "natural wavelength", it shows little response. If the spatial scale of the surface forcing is optimum, i.e., corresponds to an average spacing between convective updrafts, the system's response is augmented. A simple analog is the harmonic oscillator forced at large or small frequencies or at frequencies close to its natural mode of oscillation. In the first two cases there is little response from the oscillator, while at the later case there is resonance.

11.3 – Short term coupled simulations

In the Western Pacific warm pool, complex atmosphere-ocean feedbacks are established due to intricate coupling. Dramatic examples of such a coupling, associated with clouds and precipitation at the WPWP are the formation of the barrier-layer (e.g., Lukas and Lindstrom 1991) and the development of a shallow warm-layer (e.g., Fairall et al. 1996), responsible for significant changes in the radiative fluxes to the atmosphere. Because processes associated with atmospheric convection can modify the state of the ocean, one surmises that, in order to model the convection over the WPWP properly, a two-way communication between the atmosphere and the ocean is essential. This was the major motivation in coupling an upper-ocean model (UOM) to a CRM, in agreement with the proposition by Moncrieff et al. (1997) who suggest that coupling CRMs to ocean models is important.

Two convectively active periods were studied, using a two-dimensional cloud-resolving model coupled to an upper-ocean model described in Section 3. In one case (07 to 16 December 1992), the lower troposphere exhibited weak westerlies and the environmental shear was relatively small. The second case (19 to 28 December 1992) was characterized by the presence of moderate eastward winds in low levels and relatively strong westward winds in the upper levels, producing a significantly sheared environment.

In general, the coupled model produced results in good agreement with the observations. In both cases, the model atmospheric component produced temperatures cooler than the observations. In Case 1, the model generated a moist bias, while conversely, a dry bias developed in Case 2. The differences between the modeled precipitation and surface heat fluxes and their counterparts calculated from the COARE dataset in the two simulated periods are both small. As expected the modeled oceanic fields showed a greater departure from the observations, mostly due to the lack of the large-scale advective tendencies of temperature, salinity and momentum.

The coupled model produced a large variability in the simulated upper ocean fields (salinity, temperature and currents), in association with the variable atmospheric forcing. Modeled freshwater anomalies exhibited a behavior similar to the ones observed over the WPWP, as the one described in detail by Wijesekera et al. (1999), including: 1. Deepening with time; 2. High temperature-salinity correlation; 3. Development of a jet in the direction of the wind; 4. Downward motion at the downwind edge and upward motion at the upwind edge of the fresh anomaly.

11.4 – Long term coupled simulations

Air-sea processes over the Western Pacific are strongly modulated by intraseasonal modes. Eventually, the WPWP coupled system can be found in a period of suppressed convection and weak low-level winds, in which the SSTs often experience an increasing trend. In the opposing phase, organized deep convection accompanies strong evaporative and sensible cooling of the upper ocean.

In order to verify the capability of the coupled model to represent the characteristics of the atmospheric flow, including the formation of clouds and precipitation, as well as to predict accurately the oceanic fields, a 70-day simulation was performed, from 19 December 1992 to 27 February 1993. In general, the model provided results in good agreement with the observations, including cloud variables (such as cloud fractional area) observed via satellite and the ocean temperature, despite the fact that no nudging and/or advective tendencies were added to the oceanic variables.

It is possible that the use of a relatively coarse 2km grid-spacing caused the model to underestimate the surface heat fluxes during periods of active convection. During active periods, small-scale circulations are important to enhance the transport of heat and moisture from the ocean surface. Therefore, the use of a resolution coarser than 1km, imposed by computer limitations in running long term coupled simulations, could affect the calculation of the fluxes primarily during convectively disturbed periods.

Since the coupled model was able to simulate the observed cloud coverage, it also provided a good estimate of the downward solar radiation, at least considering a moving average over several days. The agreement between modeled and observed fluxes of shortwave radiation allowed an accurate representation of the SST.

A longterm sensitivity experiment was performed, in which the salinity effect was ignored (in contrast to the simulation previously described that accounted for changes in salinity from precipitation and evaporation). The goal of such experiment was to test the theory that the salt-stratification at the warm pool helps the maintenance of the large SST values over that region. The numerical experiment did not show any evidence to support such a theory. During active periods, when precipitating systems deposit large amounts of cool, fresh rain in the upper ocean, the haline stratification actually allowed the existence of a small temperature inversion, with cooler (but fresher) water sitting over a warmer (and saltier) mixed-layer. During suppressed periods, differences in the SST in the two simulations were indistinguishable.

11.5 – SST influences on the apparent heat source, apparent moisture sink and surface heat fluxes

Analysis of the apparent heat source and apparent moisture sink from the uncoupled, CONTROL simulation, revealed that the atmospheric model, forced by the advective tendencies of temperature and moisture, was capable of simulating the warming and drying associated with deep convection. The strong relationship between the advective forcing of temperature (moisture) and Q_1 (Q_2) relies on the tendency of the tropical atmosphere to exhibit a quasi-moist adiabatic profile. The model was also capable of representing the differences in the Q_1 and Q_2 profiles in convective and stratiform columns.

As expected, increased SSTs (such as the one in SST+) caused a general increase in Q_1 and Q_2. The opposite occurred when the SST was reduced, as in the SST- simulation.

Simulations with non-uniform SSTs, such as the coupled runs, showed smaller sensitivities with respect to the Q_1 and Q_2 profiles. However, those differences could be explained using a simple analytical representation of the apparent heat source and apparent moisture sink in convective and stratiform regions, considering that the inhomogeneous forcing favor the convective component, especially when intermediate SST wavelengths are present.

Simple calculations of the surface heat fluxes were made, using the data generated by the coupled model. The effects of the ocean currents, the wind speed-air temperature, wind speed-water vapor mixing ratio and wind speed-SST correlations and gustiness were evaluated using a bulk formulation. The results showed that, among the different effects analyzed, gustiness produced the greatest changes in the surface heat fluxes. However, although exhibiting small average values in both multi-day periods, the other effects can also be significant under certain conditions. Therefore, one has to consider the issue of the parameterization of such small-scale effects in large-scale models, such as GCMs. Recent studies (e.g., Qian et al., 1998) presented formulations of parameterizations of the effects of the cold, dry downdrafts associated with precipitation on the atmospheric near-surface layer and the surface fluxes. Those parameterizations account for the negative correlations between wind speed and air temperature and between wind speed and water vapor mixing ratio near the surface. In contrast, little attention has been given to the role of the ocean surface currents and SST inhomogeneities. In our simulations, those two effects together produced changes in the total surface heat fluxes of the same order of magnitude (or slightly less) than the changes associated with the cooling and drying of the boundary-layer by convective downdrafts. The present results suggest that the development of a parameterization of such ocean surface processes is needed to obtain more accurate calculations of surface fluxes in

GCMs. Since the momentum transfer from the atmosphere is limited to a shallow layer if the upper ocean is highly stable, the influence of the ocean surface currents has a markedly strong diurnal variation, and is often amplified in the presence of precipitation. In addition, a significant negative (or even positive) correlation can be established between the SST and the near-surface winds, especially during strong precipitation events.

11.6 – Suggestions for future research

Once the coupled system described in this dissertation was built, several modeling studies could be performed with relatively little changes in the model configuration. Further studies using the coupled CRM-UOM will allow a better understanding of the air-sea interaction at the Western Pacific warm pool from timescales ranging from a few hours to intraseasonal or even interannual timescales. Second, the increase in computer power permits the increase in the physical domain of CRMs allowing the simulation of both cloud-scale and large-scale circulations in the same framework, as pointed out by Grabowski et al. (2000). Therefore the present CRM-UOM can be used in the study of basin-scale air-sea coupling. Representing cloud-scale circulations, atmospheric large-scale motions and ocean mixed-layer dynamics in a single framework, it can contribute, for instance, to better understand the physics of the basic and transient states of the Pacific basin. CRM-UOM simulations can also provide data to build physically-based parameterizations of the interaction between convection and the ocean mixed-layer and its effects on the convective organization and the surface fluxes for large-scale models.

Some suggestions of future research are given below, consisting primarily on different applications of the CRM-UOL presented in this dissertation:

- 3-D Simulations: Due to the lack of the third degree of freedom, the 2-D simulations have important limitations in the representation of several aspects of the two-fluid coupled system. In the atmosphere, because two-dimensional simulations exclude one of the natural degrees of freedom of convection, the downdrafts tend to be exaggerated. Therefore, the observed differences in the convective/stratiform partition and the consequences to the radiative budget reported in previous chapters could be influenced by the shortcomings of an imposed large-scale forcing in a two-dimensional framework. Also, in the ocean, the three-dimensionality can be important to the stability and longevity of the shallow low-salinity disturbances. Comparisons between 2-D and 3-D runs for periods of 5 to 10 days using the coupled model will be useful to explore those issues.
- Coupled cloud-resolving simulations of basin-scale circulations: The Walker circulation can be investigated using a slightly modified version of the coupled CRM used in the current studies. A greater number of points in the zonal coordinate can be used, along a slightly coarser grid spacing. Also, instead of using periodic lateral boundary conditions, more realistic closed boundaries can be imposed to the ocean model (allowing the warmer waters to pile up at the western side of the basin), along the application of nudging terms at the

boundaries of the atmospheric model. Simulations using the basin-scale domain must be performed for a timescale of months or longer.

- <u>Parameterization of the effects of an inhomogeneous ocean surface</u>: From the data generated by the coupled CRM, a physically-based parameterizations of the small-scale processes involving deep convection and its interaction with the ocean mixed-layer can be built. Such parameterizations must include both the effects on the warming and drying profiles and the effects on the surface fluxes.

In addition, many idealized simulations can be performed using the atmospheric model only. For example, instead of using real cases, simulated equilibrium states are a valid, alternative approach to investigate SST influences on tropical convection.

Chapter 12

REFERENCES

Alexander, G. D. and W. R. Cotton, 1998: The use of cloud-resolving simulations of mesoscale convective systems to build a mesoscale parameterization scheme. *J. Atmos. Sci.*, **55**, 2137-2161.

Anderson, S. P., R. A. Weller, and R. Lukas, 1996: Surface buoyancy forcing and mixed layer of the western Pacific warm pool: observations and one-dimensional model results. *J. Climate*, **9**, 3056-3085.

Barnett, T. P., 1977: Attempt to verify some theories of El Niño. *J. Phys. Oceanogr.*, **7**, 633-647.

Bjerknes, J., 1966: A possible response of the atmospheric Hadley circulation to equatorial anomalies of ocean temperature. *Tellus*, **18**, 820-829.

Bjerknes, J., 1969: Atmospheric teleconnections from the equatorial Pacific. *Mon. Wea. Rev.*, **97**, 163-172.

Blumberg , A., and G. Mellor, 1987: A Description of a three-dimensional coastal ocean circulation model. In *Coastal and Estuarine Sciences*, **5**, N. Heaps, Ed., Amer. Geophys. Union, Washington, DC.

Bradley, E. F., J. S. Godfrey, P. A. Coppin, and J. A. Butt, 1993: Observations of net heat flux into the surface mixed layer of the western equatorial Pacific Ocean. *J. Geophys. Res.*, **98**, 22521-22532.

Bradley, E. F., 1994: Variability of meteorological variables and air-sea heat, moisture and momentum fluxes during TOGA-COARE. EOS, **75**, 42.

Brown, R. G. and C. Zhang, 1997: Variability of midtropospheric moisture and its effects on cloud-top height distribution during TOGA-COARE. *J. Atmos. Sci.*, **54**, 2760-2774.

Cechet, R. P., 1993: Diurnal SST cycle in the western equatorial Pacific: measurements made aboard the R/V Franklin during TOGA-COARE and pre-COARE cruises. *Bull. Austr. Meteorol. and Oceanogr. Soc.*, **6**, 26-32.

Chang, `C.-P., 1977: Viscous internal gravity waves and low-frequency oscillations in the tropics. *J. Atmos. Sci.*, **34**, 901-910.

Chen, S. S., R. A. Houze Jr., and B. E. Mapes, 1996: Multiscale variability of deep convection in relation to large-scale circulation in TOGA-COARE. *J. Atmos. Sci.*, **53**, 1380-1409.

Chen, S. S. and R. A. Houze, Jr., 1997: Diurnal variation of deep convective systems over the tropical Pacific warm pool. *Q. J. R. Meteorol. Soc.*, **123**, 357-388.

Cheng, C., and R. A. Houze, 1979: The distribution of convective and mesoscale precipitation in GATE radar echo patterns. *Mon. Wea. Rev.*, **107**, 1370–1381.

Chu, P. C., 1993: Generation of low-frequency unstable modes in a coupled equatorial troposphere and ocean mixed-layer model. *J. Atmos. Sci.*, **50**, 731-749.

Clark, T. L., 1977: A small-scale dynamic model using a terrain following coordinate. *J. Comput. Phys.*, **24**, 186-215

Clark, T. L., 1979: Numerical simulations with a three-dimensional cloud model: lateral boundary condition experiments and multicellular severe storm simulations. *J. Atmos. Sci.*, **36**, 2191-2215.

Clayson, C. A., J. A. Curry, and C. W. Fairall, 1995: Determination of surface turbulent fluxes for TOGA COARE: Comparison of in situ measurements and satellite retrievals. *J. Geophys. Res.*, **101**.

Costa, A. A., W. R. Cotton, R. L. Walko, R. A. Pielke Sr., and H. Jiang, 2000: SST sensitivities in multi-day TOGA-COARE cloud-resolving simulations. Submitted to *J. Atmos. Sci.*

Cronin, M., and M. J. McPhaden, 1997: The upper ocean heat balance in the western equatorial Pacific warm pool during September-December 1992. *J. Geophys. Res.*, **102**, 8533-8553

Delcroix, T., G. Eldin, and C. Hénin, 1987: Upper ocean water masses and transport in the western tropical Pacific, *J Phys Oceanogr.*, **17**, 2248-2262.

DeMott C. A. and S. A. Rutledge, 1998a: The vertical structure of TOGA COARE convection. Part I: Radar echo distributions. *J. Atmos. Sci.*, **55**, 2730-2747.

DeMott, C. A. and S. A. Rutledge, 1998b: The vertical structure of TOGA COARE convection. Part II: Modulating influences and implications for diabatic heating. *J. Atmos. Sci.*, **55**, 2748-2762.

Ding, Y. H. and A. Sumi, 1995: Large-scale atmospheric circulation features during TOGA-COARE IOP. *J. Meteorol. Soc. Jpn.*, **73**, 339-351.

Eldin, G., T. Delcroix, C. Henin, K. Richards, Y. du Penhoat, J. Picault, and P. Rual, 1994: The large-scale structure of currents and hydrology along 156°E during the COARE Intensive Observation Period. *Geophys. Res. Lett.*, **21**, 2681-2684.

Emanuel, K. A., 1987: Air-sea interaction model of intraseasonal oscillations in the tropics. *J. Atmos. Sci.*, **44**, 2324-2340.

Fairall, C. W., E. F. Bradley, J. S. Godfrey, G. A. Wick, J. B. Edson, and G. S. Young, 1996a: Cool-skin and warm-layer effects on sea surface temperature. *J. Geophys. Res.*, **101**, 1295-1308.

Fairall, C. W., E. F. Bradley, D. P. Rogers, J. B. Edson, and G. S. Young, 1996b: Bulk parameterization of air-sea fluxes for Tropical Ocean-Global Atmosphere

Coupled Ocean-Atmosphere Response Experiment. *J. Geophys. Res.*, **101**, 3746-3764.

Feng, M., P. Hacker, and R. Lukas, 1998: Upper ocean heat and salt balances in response to a westerly wind burst in the western equatorial Pacific during TOGA COARE. . *J. Geophys. Res.*, **103**, 10289-10311.

Frank, W. M., 1978: Life cycles of GATE convective systems. *J. Atmos. Sci.*, **35**, 1256-1264.

Frank, W. M., H. Wang, and J. L. McBride, 1996: Rawinsonde budget analyses during the TOGA COARE IOP. *J. Atmos. Sci.*, **53**, 1761-1780.

Fu, R., A. D. Del Genio, W. B. Rossow, and W. T. Liu, 1992: Cirrus-cloud thermostat for tropical sea surface temperatures tested using satellite data. *Nature*, **358**, 394-397.

Gadgil, S., P. V. Joseph, and N. V. Joshi, 1984: Ocean-atmosphere coupling over monsoon regions. *Nature*, **312**, 141-143.

Garstang, M., and A. K. Betts, 1974: A review of the tropical boundary layer and cumulus convection: Structure, parameterization and modeling. *Bull. Amer. Meteorol. Soc.*, **55**, 1195-1205.

Garstang, M., and D. R. Fitzjarald, 1999: *Observations of surface to atmosphere interactions in the tropics*. Oxford University Press, 405 pp.

Gill, A. E., 1982: *Atmosphere-ocean dynamics*. Academic Press, New York, 662 pp.

Gill, A. E. and E. M. Rasmussen, 1983: 1982-83 climate anomaly in the equatorial Pacific. *Nature*, **306**, 229-234.

Godfrey, J. S., and E. J. Lindstrom, 1989: The heat budget of the equatorial western Pacific surface mixed layer. *J. Geophys. Res.*, **94(C6)**, 8007-8017.

Godfrey, J. S., R. A. Houze, Jr., R. H. Johnson, R. Lukas, J.-L. Redelsperger, A. Sumi, and R. Weller, 1998: Coupled Ocean-Atmosphere Response Experiment (COARE): An interim report. *J. Geophys. Res.*, **103**, 14395-14450.

Grabowski, W. W., X. Wu, and M. W. Moncrieff, 1996a: Cloud resolving modeling of tropical cloud systems during Phase III of GATE. Part I: Two-dimensional experiments. *J. Atmos. Sci.*, **53**, 3684-3709.

Grabowski, W. W., M. W. Moncrieff, and J. T. Kiehl, 1996b: Long-term behavior of precipitating tropical cloud systems: A numerical study. *Q. J. R. Meteor. Soc.*, **122**, 1019-1042.

Grabowski, W. W., X. Wu, M. W. Moncrieff, and W. D. Hall: 1998a: Cloud resolving modeling of tropical cloud systems during Phase III of GATE. Part II: Effects of resolution and the third spatial dimension. *J. Atmos. Sci.*, **55**, 3264-3282.

Grabowski, W. W., X. Wu, and M. M. Moncrieff, 1998b: Cloud-resolving modeling of tropical cloud systems during Phase III of GATE. Part III: Effects of cloud microphysics. *J. Atmos. Sci.*, **56**, 2384-2402.

Grabowski, W. W., J.-I. Yano, and M. Moncrieff, 2000: Cloud resolving modeling of tropical circulations driven by large-scale SST gradients. . *J. Atmos. Sci.*, accepted.

Graham, N. E., and T. P. Barnett, 1987: Sea surface temperature, surface wind divergence, and convection over tropical oceans. *Science*, **238**, 657-659.

Hagan, D., D. Rogers, C. Friehe, R. Weller, and E. Walsh, 1997: Aircraft observations of sea surface temperature variability in the tropical Pacific. *J. Geophys. Res.*, **102**, 15733-15747.

Harrington, J. Y., 1997: The effects of radiative and microphysical processes on simulated warm and transition season Arctic stratus. Ph.D. dissertation, Atmospheric Science Paper No. 637, Colorado State University, Dept. of Atmospheric Science, 289 pp.

Hendon, H. H. and B. Liebmann, 1994: Organization of convection within the Madden-Julian oscillation. *J. Geophys. Res.*, **99**, 8073-8083.

Hendon, H. H. and M. L. Salby, 1994: The life-cycle of the Madden-Julian oscillation. *J. Atmos. Sci.*, **51**, 2225-2237.

Hildebrand, P. H., 1998: Shear-parallel moist convection over the tropical ocean: a case study from 18 February 1993 TOGA COARE. *Mon. Wea. Rev.*, **126**, 1951-1976.

Hill, G. E., 1974: Factors controlling the size and spacing of cumulus clouds as revealed by numerical experiments. *J. Atmos. Sci.*, **31**, 646-673.

Hodur, R. M., 1997: The Naval Research Laboratory's coupled ocean/atmosphere mesoscale prediction system (COAMPS). *Mon. Wea. Rev.*, **125**, 1414-1430.

Houze, Jr., R. A., 1989: Observed structure of mesoscale convective systems and implications for large-scale heating. *Q. J. R. Meteorol. Soc.*, **115**, 425-461.

Houze, Jr., R. A., 1993: *Cloud dynamics*. Academic Press, San Diego, 573 pp.

Inall, M. E., K. J. Richards, and G. Eldin, 1998: The changing structure of the upper ocean in the western equatorial Pacific during the Tropical Ocean Global Atmosphere Coupled Ocean-Atmosphere Response Experiment. *J. Geophys. Res.*, **103**, 21385-21400.

Jabouille, P., J.-L. Redelsperger and J. P. Lafore, 1996: Modification of surface fluxes by atmospheric convection in the TOGA COARE region. *Mon. Wea. Rev.*, **124**, 816-837.

Jerlov, N. G., 1976: *Marine Optics*, Elsevier, New York, 229pp.

Johnson, R. H., and X. Lin, 1997: Episodic trade-wind regimes over the western Pacific warm pool. *J. Atmos. Sci.*, **54**, 2020-2034.

Jones, C., D. E. Waliser, and C. Gautier, 1998: The influence of the Madden-Julian oscillation on ocean surface heat fluxes and sea surface temperature. *J. Clim.*, **11**, 1057-1072.

Kawamura, R., 1988: Intraseasonal variability of sea surface temperature over the tropical western Pacific. *J. Meteorol. Soc. Jpn.*, **66**, 1007-1012.

Kawamura, R., 1991: Air-sea coupled modes on intraseasonal and interannual time scales over the tropical western Pacific. *J. Geophys. Res.*, **96**, 3165-3172.

Kayano, M. T., and V. E. Kousky, 1999: Intraseasonal (30-60 day) variability in the global tropics: Principal modes and their evolution. *Tellus*, **51A**, 373-386.

Kiladis, G. N., and M. Wheeler, 1995: Horizontal and vertical structure of observed tropospheric equatorial Rossby waves. *J. Geophys. Res.*, **100**, 22981-22997.

Kirk, J. T. O., *Light and Photosynthesis in Aquatic Ecosystems*, Cambridge University Press, New York, 509pp.

Knutson, T. R., K. M. Weickmann, and J. E. Kutzbach, 1986: Global-scale intraseasonal oscillations of outgoing long-wave radiation and 250-mb zonal wind during Northern Hemisphere summer. *Mon. Wea. Rev.*, **114**, 605-623.

Kraus, E. B. and J. A. Businger, 1994: *Ocean-atmosphere interaction*, 2nd Ed. Oxford University Press, New York, 362 pp.

Krueger, S. K., 1988: Numerical simulation of tropical cumulus clouds and their interaction with the subcloud layer. *J. Atmos. Sci.*, **45**, 2221-2250.

Krueger, S. K. and S. M. Lazarus, 1999: Intercomparison of multi-day simulations of convection during TOGA-COARE with several cloud-resolving and single-column models. Preprints, 23rd Conference on Hurricanes and Tropical Meteorology, 10-15 January, Dallas, TX, Amer. Meteor. Soc., 643-647.

Lau, K.-M. and P. H. Chan, 1985: Aspects of the 40-50 day oscillation during the northern winter as inferred from outgoing long-wave radiation. *Mon. Wea. Rev.*, **113**, 1889-1909.

Lau, K.-M. and P. H. Chan, 1986: Aspects of the 40-50 day oscillation during the northern summer as inferred from outgoing long-wave radiation. *Mon. Wea. Rev.*, **114**, 1354-1367.

Lau, K.-M. and P. H. Chan, 1988: Intraseasonal and interannual variations of tropical convection: a possible link between the 40-50 day oscillation and ENSO?. *J. Atmos.Sci..*, **45**, 506-521.

Lau, K.-M. and L. Peng, 1987: Origin of low-frequency (intraseasonal) oscillations in the tropical atmosphere. Part 1: Basic theory. *J. Atmos. Sci.*, **44**, 950-972.

Lau, K. M. and C.-H. Sui, 1997: Mechanisms of short-term sea surface temperature regulation: observations during TOGA-COARE. *J. Climate*, **10**, 465-472.

Leary, C. A., and R. A. Houze, Jr., 1979: Structure and evolution of convection in a tropical cloud cluster. *J. Atmos. Sci.*, **36**, 437-457.

LeMone, M. A., E. J. Zipser, and S. B. Trier, 1998: The role of environmental shear and thermodynamic conditions in determining the structure and evolution of mesoscale convective systems during TOGA-COARE. *J. Atmos. Sci.*, **55**, 3493-3518.

Lewis, S. A., M. A. LeMone, and D. P. Jorgensen, 1998: Evolution and dynamics of a late-stage squall line that occurred on 20 February 1993 during TOGA COARE. *Mon. Wea. Rev.*, **126**, 3189-3212.

Li, X., C.-H. Sui, D. Adamec, and K. M. Lau, 1998: Impacts of precipitation in the upper ocean in the western Pacific warm pool during TOGA COARE. *J. Geophys. Res.*, **103**, 5347-5360.

Li, X, C.-H. Sui, K.-M. Lau, and M.-D. Chou, 1999: Large-scale forcing and cloud-radiation interaction in the tropical deep convective regime. *J. Atmos. Sci.*, **56**, 3028-3042.

Lilly, D. K., 1962: On the numerical simulation of buoyant convection. *Tellus*, **2**, 148-172.

Lim, H., and C.-P. Chang, 1983: Dynamics of teleconnections and Walker circulations forced by equatorial heating. *J. Atmos. Sci.*, **40**, 1897-1915.

Lin, X., and R. H. Johnson, 1996a: Kinematic and thermodynamic characteristics of the flow over the western Pacific warm pool during TOGA-COARE. *J. Atmos. Sci.*,**53**, 695-715

Lin, X., and R. H. Johnson, 1996b: Heating, moistening and rainfall over the western pacific warm pool during TOGA COARE. *J. Atmos. Sci.*, **53**, 3367-3383.

Lindstrom, E., R. Lukas, R. Fine, E. Firing, S. Godfrey, G. Meyers, and M. Tsuchiya, 1987: The western equatorial Pacific Ocean circulation study. *Nature*, **330**, 533-537.

Liou, K., 1986: Influence of cirrus clouds on weather and climate processes: A global perspective. *Mon. Wea. Rev.*, **114**, 1167-1199.

Liu, C., and M. W. Moncrieff, 1998: A numerical study of the diurnal cycle of tropical oceanic convection. *J. Atmos. Sci.*, **55**, 2329-2344.

Louis, J. F., M. Tiedtke, and J. F. Geleyn, 1981: A short history of the PBL parameterizations at ECMWF. Proceedings, Workshop on Planetary Boundary Parameterization, Reading, United Kingdom, ECMWF, 59-79.

Lukas, R., and E. Lindstrom, 1991: The mixed layer of the western equatorial Pacific Ocean. *J. Geophys. Res.*, **96**, 3343-3357.

Lukas, R., P. J. Webster, M. Li, and A. Leetmaa, 1995: The large-scale context for the TOGA Coupled Ocean-Atmosphere Response Experiment. *Meteor. And Atmos. Phys.*, **56**, 3-16.

Madden, R. A., 1986: Seasonal variations of the 40-50 day oscillation in the tropics. J. Atmos. Sci., **43**, 3138-3158.

Madden, R. A., and P. R. Julian, 1971: Detection of a 40-50 day oscillation of the zonal wind in the tropical Pacific. *J. Atmos. Sci.*, **28**, 702-708.

Madden, R. A., and P. R. Julian, 1994: Observations of the 40-50 day tropical oscillation – a review. *Mon. Wea. Rev.*, **122**, 814-837.

Mapes, B. E. and R. A. Houze, Jr., 1995: Diabatic divergence profiles in western Pacific mesoscale cloud systems. *J. Atmos. Sci.*, **52**, 1807-1828.

Maruyama, T., 1971: Vertical section and time sequence of spectra of disturbances over the Line Islands during the years 1957-1958. *J. Meteorol. Soc. Jpn.*, **49**, 146-157.

McBride, J. L., and W. M. Gray, 1980: Mass divergence in tropical weather systems: Part 2, Large-scale controls on convection. *Q. J. R. Meteorol. Soc.*, **106**, 517-538.

McBride, J. L., N. E. Davidson, K. Puri, and G. C. Tyrrel, 1995: The flow during TOGA COARE as disgnosed by the BMRC Tropical Analysis and Prediction System. *Mon. Wea. Rev.*, **123**, 717-736.

Mellor, G., and T. Yamada, 1974: A hierarchy of turbulence closure models for planetary boundary layers, *J. Atmos. Sci.*, **31**, 1791-1806

Moncrieff, M. W., S. K. Krueger, D. Gregory, J.-L. Redelsperger, and W.-K. Tao, 1997: GEWEX cloud system study (GCSS) working group 4: precipitating convective cloud systems. *Bull. Amer. Meteor. Soc.* **78**, 831-845.

Moncrieff, M. W., and E., 1997: Organized convective systems in the tropical western Pacific as a process in general circulation models: a TOGA COARE case study. *Q. J. R. Meteorol. Soc.*, **123**, 805-827.

Mori, K., 1995: Equatorial convection observed by the research vessel Keifu Maru during the TOGA COARE IOP, November 1992. *J. Meteorol. Soc. Jpn.*, **73**, 491-508.

Murakami, T., 1986: Eastward propagation of 30-60-day perturbations as revealed from outgoing long-wave radiation data. *J. Atmos. Sci.*, **43**, 961-971.

Nair, U. S., M. R. Hjelmfelt, and R. A. Pielke, Sr., 1997: Numerical simulation of the 9-10 June 1972 Black Hills storm using CSU-RAMS. *Mon. Wea. Rev.*, **125**, 1753-1766.

Neelin, J. D., I. M. Held, and K. H. Cook, 1987: Evaporation-wind feedback and low-frequency variability in the tropical atmosphere. *J. Atmos. Sci.*, **44**, 2341-2348.

Niiler, P., and J. Stevenson, 1982: The heat budget of tropical ocean warm-water pools. *J. Mar. Res.*, **40**, 465-480.

Ohlmann, J. C., D. A. Siegel, and L. Washburn, 1998: Radiant heating of the western equatorial Pacific during TOGA-COARE. *J. Geophys. Res.*, **103**, 5379-5395.

Olsson, P. Q. and W. R. Cotton, 1998: Balanced and unbalanced circulations in a primitive equation simulation of a midlatitude MCC. Part I: The numerical simulation. *J. Atmos. Sci.*, **54**, 457-478.

Olsson, P. Q., J. Y. Harrington, G. Feingold, W. R. Cotton, and S. M. Kreindenweis, 1998: Exploratory cloud-resolving simulations of boundary-layer Arctic stratus clouds. Part I: Warm season clouds. *Atmos. Res.*, **47-48**, 573-597.

Palmén, E. and L. A. Vuroela, 1963: On the mean meridional circulations in the Northern Hemisphere during the winter season. *Q. J. R. Meteor. Soc.*, **89**, 131-138.

Philander, S. G. H., 1990: El Niño, La Niña, and the Southern Oscillation. Academic Press, 289pp.

Pielke, R. A., W. R. Cotton, R. L. Walko, C. J. Tremback, W. A. Lyons, L. D. Grasso, M. E. Nicholls, M. D. Moran, D. A. Wesley, T. J. Lee, and J. H. Copeland, 1992: A comprehensive meteorological modeling system - RAMS. *Meteorol. Atmos. Phys.*, **49**, 69-91.

Qian, L., G. S. Young, and W. M. Frank, 1998: A convective wake parameterization scheme for use in general circulation models. *Mon. Wea. Rev.*, **126**, 456-469.

Ramanathan, V. and W. Collins, 1991: Thermodynamic regulation of ocean warming by cirrus clouds deduced from observations of the 1987 El Niño, *Nature*, **351**, 27-32.

Rao, G. A., and Bh. V. Ramana-Murty, 1972: Tropical wave disturbances over the regions east of Indian Ocean. *J. Meteorol. Soc. Jpn.*, **50**, 325-331.

Randall, D. A., K.-M. Xu, R. J. C. Sommerville, and S. Iacobellis, 1996: Single-column models and cloud ensemble models as links between observations and climate models. *J. Climate*, **9**, 1583-1697.

Rickenbach, T. M. and S. A. Rutledge, 1998: Convection in TOGA COARE: Horizontal scale, morphology, and rainfall production. *J. Atmos. Sci.*, **55**, 2715-2729.

Riehl, H., 1954: *Tropical Meteorology*. McGraw-Hill Publishers, New York.

Riehl, H., and J. Simpson, 1979: Heat balance of the equatorial trough zone, revisited. *Contrib. Atmos. Phys.*, **52**, 287-305.

Rosenfeld, D., E. Amitai, and D. B. Wolff, 1995: Classification of rain regimes by the three-dimensional properties of reflectivity fields. *J. Appl. Meteor.*, **34**, 198–211.

Roux, F. 1998: The oceanic mesoscale convective system observed with airborne Doppler radars on 9 February 1993 during TOGA-COARE: structure, evolution and budgets. *Q. J. R. Meteorol. Soc.*, **124**, 585-614.

Salby, M. L. and H. H. Hendon, 1994: Intraseasonal behavior of clouds, temperature and motion in the tropics. *J. Atmos. Sci.*, **51**, 2207-2224.

Saunders, P. M., 1967: The temperature at the ocean-air interface, *J. Atmos. Sci.*, **24**, 269-273.

Saxen, T. R., and S. A. Rutledge, 1998: Surface fluxes and boundary-layer recovery in TOGA-COARE: Sensitivity to convective organization. *J. Atmos. Sci.*, **55**, 2763-2781.

Schneider, E. K., and R. S. Lindzen, 1977: Axially symmetric steady-state for instability and climate studies. Part I: Linearized calculations. *J. Atmos. Sci.*, **34**, 263-279.

Short, D. A., P. A. Kucera, B. S. Ferrier, J. C. Gerlach, S. A. Rutledge, and O. W. Thiele, 1997: Shipboard radar rainfall patterns within the TOGA COARE IFA. *Bull. Amer. Meteorol. Soc.*, **78**, 2817-2836.

Siegel, D. A., J. C. Ohlmann, L. Washburn, R. R. Bidigare, C. T. Noose, E. Fields, and Y. Zhou, 1995: Solar radiation, phytoplankton pigments and radiant heating of the equatorial Pacific warm pool. *J. Geophys. Res.*, **100(C3)**, 4885-4891.

Smagorinsky, J., 1963: General circulation experiments with the primitive equations. Part I: The basic experiment. *Mon. Wea. Rev.*, **91**, 99-164.

Smith, R. C., and K. S. Baker, 1981: Optical properties of the clearest natural waters. *Appl. Opt.*, **20**, 177-184.

Soloviev, A., and R. Lukas, 1997a: Observation of large diurnal warming events in the near-surface layer of the western equatorial Pacific warm pool. *Deep-Sea Res.*, **44**, 1055-1076.

Soloviev, A., and R. Lukas, 1997b: Sharp frontal interfaces in the near-surface layer of the ocean in the western equatorial Pacific warm pool. *J. Phys. Oceanogr.*, **27**, 999-1017.

Song, X., C. A. Friehe, and D. Hu, 1996: Ship-board measurements and estimations of air-sea fluxes in the western tropical Pacific during TOGA COARE. *Boundary-Layer Meteor.*, **81**, 373-397.

Soong, S.-T., and W.-K. Tao, 1980: Response of deep tropical cumulus clouds to mesoscale processes. *J. Atmos. Sci.*, **37**, 2016-2034.

Soong, S.-T., and Y. Ogura, 1980: Response of tradewind cumuli to large-scale processes. *J. Atmos. Sci.*, **37**, 2035-2050.

Sprintall, J., and M. Tomczak, 1992: Evidence of the barrier layer in the surface layer of the tropics. *J. Geophys. Res.*, **97**, 7305-7316.

Su, H., S. S. Chen, and C. S. Bretherton, 1999: Three-dimensional week-long simulations of TOGA COARE convective systems using the MM5 mesoscale model. *J. Atmos. Sci.*, **56**, 2326-2344.

Sui, C.-H., K.-M. Lau, Y. N. Takayabu, and D. A. Short, 1997a: Diurnal variations in tropical oceanic cumulus convection during TOGA COARE. *J. Atmos. Sci.*, **54**, 639-655.

Sun, J., J. F. Howell, S. K. Esbenson, L. Mahrt, C. M. Greb, R. Grossman, and M. A. LeMone, 1996: Scale dependence of air-sea fluxes over the western equatorial Pacific. *J. Atmos. Sci.*, **53**, 2997-3012.

Tao, W.-K., and J. Simpson, 1984: Cloud interactions and merging: Numerical simulations. *J. Atmos. Sci.*, **41**, 2901-2917.

Tao, W.-K., and S.-T. Soong, 1986: The study of the response of deep tropical clouds to mesoscale processes: Three-dimensional numerical experiments. *J. Atmos. Sci.*, **43**, 2653-2676.

Tao, W.-K., J. Simpson and S.-T. Soong, 1987: Statistical properties of a cloud ensemble: a numerical study. *J. Atmos. Sci.*, **44**, 3175-3187.

Tao, W.-K., J. Simpson, C.-H. Sui, C.-L. Shie, B. Zhou, K. M. Lau, and M. Moncrieff, 1999: Equilibrium states simulated by cloud-resolving models. *J. Atmos. Sci.*, **56**, 3128-3139.

Tripoli, G. J. and W. R. Cotton, 1981: Use of ice-liquid water potential temperature as a thermodynamic variable in deep atmospheric models. *Mon. Wea. Rev.*, **109**, 1094-1102.

Tripoli, G. J. and W. R. Cotton, 1986: An intense, quasi-steady thunderstorm over mountainous terrain. Part IV: Three-dimensional numerical simulations. . *J. Atmos. Sci.*, **43**, 894-912.

Waliser, D. E., and N. E. Graham, 1993: Convective cloud systems and warm-pool sea surface temperatures: Coupled interactions and self-regulation. *J. Geophys. Res.*, **98**, 12881-12893.

Walko, R. L, W. R. Cotton, J. L. Harrington, M. P. Meyers, 1995: New RAMS cloud micro-physics parameterization. Part I: The single-moment scheme. *Atmos. Res.*, **38**, 29-62.

Wallace, J. M., 1971: Spectral studies of tropospheric wave disturbances in the tropical western Pacific. *Rev. Geophys.*, **9**, 557-611.

Wang, Y., W.-K. Tao, and J. Simpson, 1996: The impact of ocean surface fluxes on a TOGA-COARE convective system. *Mon. Wea. Rev.*, **124**, 2753-2763.

Webster, P. J., 1994: The role of hydrological processes in ocean-atmosphere interactions. *Rev. Geophys.*, **32**, 427-476.

Webster, P. J., C. A. Clayson, and J. A. Curry, 1996: Clouds, radiation, and the diurnal cycle of sea surface temperature in the tropical western Pacific. *J. Climate*, **9**, 1712-1730.

Weickmann, K. M., 1991: El Niño/Southern Oscillation and Madden-Julian (30-60 day) oscillations during 1981-1982. *J. Geophys. Res.*, **96**, 3187-3195.

Wijesekera, H. W., C. A. Paulson, and A. Huyer, 1999: The effect of rainfall on the surface layer during a westerly wind burst in the western equatorial Pacific. *J. Phys. Oceanogr.*, **29**, 612-632.

Wu, X., W. W. Grabowski, and M. W. Moncrieff, 1998: Long-term behavior of cloud systems in TOGA COARE and their interactions with radiative and surface processes. Part I: Two-dimensional modeling study. *J. Atmos. Sci.*, **55**, 2693-2714.

Xu, K.-M. and D. A. Randall, 1996: Explicit simulation of cumulus ensembles with the GATE Phase III data: Comparison with observations. *J. Atmos. Sci.*, **53**, 3710-3736.

Xu, K.-M. and D. A. Randall, 1999: A sensitivity study of radiative-convective equilibrium in the tropics with a convection-resolving model. *J. Atmos. Sci.*, **56**, 3385-3399.

Yamasaki, M., 1975: A numerical experiment of the interaction between cumulus convection and larger-scale motion. *Pap. Meteor. Geophys.*, **26**, 63-91.

Yanai, M., T. Maruyama, T. Nitta and Y. Hayashi, 1968: Power spectra of large-scale disturbances of the tropical Pacific. *J. Meteorol. Soc. Jpn.*, **46**, 308-323.

Yang, S., and E. A. Smith, 1999: Moisture budget analysis of TOGA COARE area using SSM/I-retrieved latent heating and large-scale Q_2 estimates. *J. Atmos. Oceanic Technol.*, *16*, 633-655.

You, Y., 1995: Salinity variability and its role in the barrier-layer formation during TOGA COARE. *J. Phys. Oceanogr.*, **25**, 2778-2807.

You, Y., 1998: Rain-formed barrier layer of the western equatorial Pacific warm pool: a case study. *J. Geophys. Res.*, **103**, 5361-5378.

Young, G. S., S. M. Perugini, and C. W. Fairall, 1995: Convective wakes in the equatorial western Pacific during TOGA., *Mon. Wea. Rev.*, **123**, 110-123.

Zhang, C., and H. H. Hendon, 1997: Propagating and standing components of the intraseasonal oscillation in tropical convection. *J. Atmos. Sci.*, **54**, 741-752.

Ziegler, C. L., T. L. Lee, and R. A. Pielke, Sr., 1997: Convection initiation at the dryline: a modeling study. *Mon. Wea. Rev.*, **125**, 1001-1026.